Development and application of infrared laser heterodyne radiometry for remote sensing of greenhouse gases in the atmospheric column

Jingjing Wang

Thèse de Doctorat

Mention Physics
Spécialité Physique Milieux dilués et optique fondamentale

présentée à *l'Ecole Doctorale en Sciences Technologie et Santé (ED 585)* **de**
l'Université du Littoral Côte d'Opale
et
à l'Ecole doctorale Optique
de University of Science and Technology of China

par

Jingjing WANG

pour obtenir le grade de Docteur de l'Université du Littoral Côte d'Opale

Développement et application de la radiométrie hétérodyne laser dans l'infrarouge pour la télédétection des gaz à effet de serre dans la colonne atmosphérique

Soutenue le 13 décembre 2021, après avis des rapporteurs, devant le jury d'examen :

M. Yao TE, Maître de conférences, Université Paris 6	**Rapporteur**
M. Lei DONG, Professeure, Shanxi University	**Rapporteur**
M. Markus W. SIGRIST, Professeure émérite, ETH Zurich	**Examinateur**
M. Chuanliang LI, Professeur, Taiyuan University of Science and Technology	**Examinateur**
M. Tu TAN, Associate Professeur, AIOFM, Chinese Academy of Science	**Invité**
M. Weidong CHEN, Professeur, Université du Littoral Côte d'Opale	**Directeur de thèse**
M. Xiaoming GAO, Professeur, AIOFM, Chinese Academy of Science	**Co-encadrant de thèse**

Acknowledgments

I am looking forward to the end of my Ph.D. study career, but I also love the learning process during this period. I have felt countless times of frustration and the loss of the sleepless night, but let me learn self-motivation to find a new direction. In my life of experience and scientific research, I have gained a lot of growth and gains, regained the cognition of the world, the understanding of society, the comprehension of responsibility, the definition of failure, the attitude towards scientific research, and the judgment of my ability and defects. Thanks to the good teachers and friends who had a profound impact on my life and study. This thesis was completed under the careful guidance of my tutors, Professors Weidong Chen, Xiaoming Gao, and Tu Tan. I am very grateful to professor Weidong Chen. His deep understanding of the nature of scientific research and his in-depth attention to the details of the experiment have greatly inspired my understanding of scientific research. He also gave me great help and concern in my life and work. I learn from his meticulous scientific research spirit and humorous attitude towards life. Professor Gao plays a vital role in my research topics. He teaches me to take a rigorous and pragmatic attitude towards scientific research and treat my work with high enthusiasm. Thanks to the guidance of Professor Tan on the experimental details. He treats scientific research with a rigorous attitude and explores the unknown with abundant energy, which deeply affected me.

Thanks to Professors Kun Lui and Guishi Wang, Xiaomin Chen, Gong Dong Zhu and Jiaoxu Mei for their beneficial discussion and inspiration, as well as their concern and care for my life and study. Thanks to Yu Wang, Yanan Cao, Shenlong Zha, Jiajing Chen, Yu Zhou, Jingjing Wang, Xing Tian, Rui Wang, Yuan Cao, Tianmei Ke, Zhengyue Xue, Jun Li, Xiaohai Lui, Feiyang Sheng, Nanchang Cui, Ning Wang, Chu Bi, Gang Yang, Yang Dong, etc. for their help and support in the experiment and life.

Thanks to the Eric Fertein, engineer of the Université du Littoral Côte d'Opale and Professor Gunther Roelkens of Ghent University for their help and cooperation.

Thanks to Gaoxuan Wang, Fengjiao Shen, Lingshuo Meng, Junmei Zhang, Bahawal Haq, etc. for their help in my life and study in France and Belgium. I especially thank Shuo Wang and Zhengyun Wang for their continuous support and encouragement and my best friends Yue Sun and Miaomiao Wu for their company and console. Finally, thanks to my parents for their understanding, support, and cultivation.

Table of Contents

List of Figures

List of Tables

List of Abbreviations and Acronyms

A

AC	Alternating Current
AIOFM	Anhui Institute of Optics and Fine Mechanics
ACGS	Atmospheric Carbon-dioxide Grating Spectroradiometer
AK	Averaging Kernel
AOS	Acousto-optic Spectrometer

B

BB	Black Body
BS	Beam Splitter

C

CAPI	Cloud Aerosol Polarization Imager
DFB	Distributed Feedback
TanSat	Carbon Satellite

D

DC	Direct Current
DFB	Distributed Feedback
DAQ	Data Acquisition

E

EC-QCL	External-Cavity Quantum Cascade Laser
EC-LHR	External Cavity Laser Heterodyne Radiometer
ECMWF	European Center for Medium Range Weather Forecasts
EM27/SUN	a Bruker Optics^{TM} potable solar-viewing spectrometer

F

FASCODE	Fast Atmospheric Signature CODE
FC	Fiber Combiner
FoV	Field of View
FSR	Free Spectral Range
FTS	Fourier Transform Spectrometer
FWHM	Full Width at Half Maximum

G

GHGs	Greenhouse Gases
GOSAT	Greenhouse Gases Observing Satellite
GEISA	

H

HWHM	Half Width at Half Maximum
HITRAN	

I

ICL	Interband Cascade Laser
ILS	Instrument Lineshape
IP-NIR-LHR	Integrated Portable Near-infrared Laser Heterodyne Radiometer
I	Iris Diaphragm
IF	Intermediate Frequency
IFS 125HR FT-IR	

L

LBLRTM	Line-By-Line Radiative Transfer Model
LM	Levenberg Marquardt
LPCA	Laboratoire de Physico Chimie de l'Atmosphère

LHR	Laser Heterodyne Radiometer
LHD	Laser Heterodyne Detection
LO	Local Oscillator
LP	Low-Pass
LIA	Lock-In Amplifier
LDC	Laser Diode Controller

M

Mid-IR	Mid-Infrared
Mid-LHR	Mid-Infrared laser heterodyne radiometer
MISO	Mission of Satellite Observation of CH_4 isotope
MAP	Maximum A-posteriori Probability

N

NA	Numerical Aperture
NIR	Near Infrared
NI	National Instruments
NDACC	Network for the Detection of Atmospheric Composition Change
F	Noise Factor
NF	Noise Figure
NEP	Noise Equivalent Power
NASA	National Aeronautics and Space Administration
NOAA	

O

OAPM	Off Axis Parabolic Mirror
OCO-2	Orbiting Carbon Observatory-2
OEM	Optimal Estimation Method

P

PD	Photodetector
PC	Personal Computer
PDF	Probability Density Function

Q

QCL	Quantum Cascade Laser

R

RF	Radio Frequency
RFM	

S

SMOF	Single Mode Optical Fiber
SNR	Signal to Noise Ratio
SR	Stochastic Resonance

T

TCCON	Total Carbon Column Observing Network
THIS	Tunable Heterodyne Infrared Spectrometer

V

VMR	Volume Mixing Ratio

W

WGN	White Gaussian Noise
WM-LHR	Wavelength Modulated Laser Heterodyne Radiometer

Abstract

The increase of greenhouse gases concentration in the atmosphere leads to global warming, which has aroused widespread concern in society. Studying the earth's atmosphere and predicting future climate change are closely related to the accurate observation of greenhouse gas concentrations. At present, the high spectral resolution instruments used to observe column concentration of atmospheric greenhouse gases generally have large sizes and high costs, which are not conducive to monitor the greenhouse gases on a large scale. The laser heterodyne radiometer with high resolution can be made small, low-power consumption, compact and robust. It is conducive to the realization of the mobile observation of atmospheric greenhouse gases in the field.

This thesis mainly focuses on infrared laser heterodyne detection technology and application. The main work and innovations of the thesis are as follows:

An all-fiber dual-channel laser heterodyne radiometer was developed to detect CH_4 and CO_2 in the atmosphere simultaneously. In the device, a fiber optic switch and other fiber optic devices were used to improve the stability and reliability of the measurement system significantly. Continuous observation experiments were performed in Hefei, and the measurement results are approximately consistent with the GOSAT results. The integrated instrument also conducted field observations in Qinghai province. Then, an interband cascade laser based mid-infrared LHR has been demonstrated in an attractive atmospheric window of 3-5 μm, for the first time, in ground-based solar occultation mode. High-resolution (0.0033 cm^{-1}) spectra near 3.53 μm were obtained for simultaneous atmospheric observations of HDO and CH_4. Finally, an external cavity laser based laser heterodyne radiometer for the detection of $^{13}CO_2$ and $^{12}CO_2$ in the atmosphere was developed. The external cavity laser was used as the local oscillator to implement the continuous spectrum measurement in the range of 6248.5 cm^{-1} ~ 6256 cm^{-1}. And the atmospheric transmittance of $^{12}CO_2$ and $^{13}CO_2$ in the entire atmosphere was obtained.

Key Words: Laser heterodyne radiometer; ground-based remote sensing; column-averaged abundances; Mid-infrared (mid-IR); Near-infrared (NIR)

Introduction

Objective

This thesis presents studies, developments, and applications of laser heterodyne radiometer (LHR) based on different local oscillators for the remote sensing of column concentration of CH_4, CO_2, HDO in the atmosphere. This introductive chapter describes the motivation for developing LHR and its characteristics. A brief historical review of LHR techniques and the development state will be described. The main content of each chapter of the thesis is introduced at the end of this chapter.

I Research background

I1 Observation of greenhouse gases (GHGs)

Nowadays, the change of the earth's climate is a common concern of all countries in the world today. Obtaining the actual atmospheric observation data is a key link in the research and prediction of climate change. So, it is essential to improve the monitoring of greenhouse gases such as CO_2 and CH_4 to obtain the most basic research data. Therefore, in-depth research on the sources and sinks of carbon in the atmosphere, prediction of the relationship between global warming trends and atmospheric greenhouse gas concentrations requires high-precision greenhouse gases detection technology and monitoring networks to assess the changes in atmospheric greenhouse gases quantitatively.

The global average sea level has risen by about 20 cm ~ 23 cm [1]. In 2017, IPCC reported in Our Globally Changing Climate nine observational phenomena of changes in the earth (Figure 1) [2]. They are the key indicators representing the warming of the earth's climate. These observations indicate that the temperature of surface air, sea-level temperature, sea level height, tropospheric temperature, ocean heat content, specific humidity, snow in the northern hemisphere, arctic sea ice range, and glacier

accumulation. The mass balance has a consistent long-term trend with global warming. Climate change affects the entire region and all aspects of society, and it is expected that it will be more destructive in the next few decades [3].

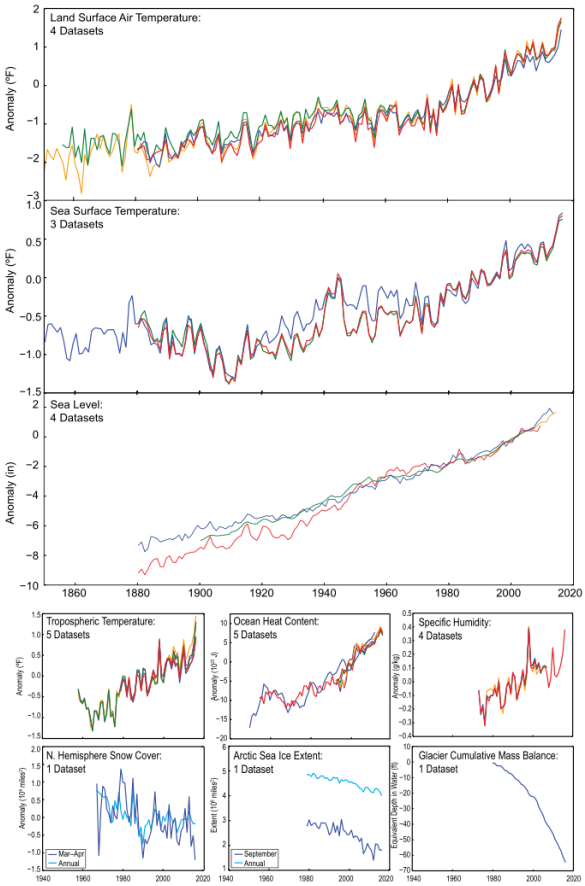

Figure 1 Nine phenomena reflecting global warming [2]

The burning of a large number of fossil fuels has led to an increase in man-made greenhouse gases. The main reasons for the increase in the concentration of greenhouse gases in the atmosphere are the development of modern industry, deforestation, and changes in land use in the past century. When the solar energy reaches the surface and is reflected by the earth, the greenhouse gases in the atmosphere will absorb the corresponding infrared radiation to heat the earth's surface. Therefore, changes in the concentration of greenhouse gases in the atmosphere are one of the reasons for changing the energy balance of the climate system. In 2017, the IPCC reported the radiative forcing of mixed greenhouse gases in Physical Drivers of Climate Change [4]. Figure 2 (a), (b), and (c) show the radiative forcing corresponding

to various greenhouse gases. Figure 2(d) shows the rate of change of these greenhouse gases corresponding to radiative forcing. It can be seen that CO_2 is the most influential greenhouse gas, CH_4 is the second, followed by N_2O, chlorofluorocarbons, and other greenhouse gases. To carry out reliable estimation and research on carbon sources and sinks, long-term observation and research on CO_2 and CH_4 are needed. The concentration of CO_2 and CH_4 in the global atmosphere has far exceeded the value of the pre-industrial atmosphere. Figure 3(a) and (b) are the monthly average concentration data (red circle) and long-term change trend (black line) of CO_2 and CH_4 in the atmosphere published by NOAA in the past thirty years. It can be seen that the concentrations of both in the atmosphere have been increasing in recent years, and they have had an important impact on the greenhouse effect.

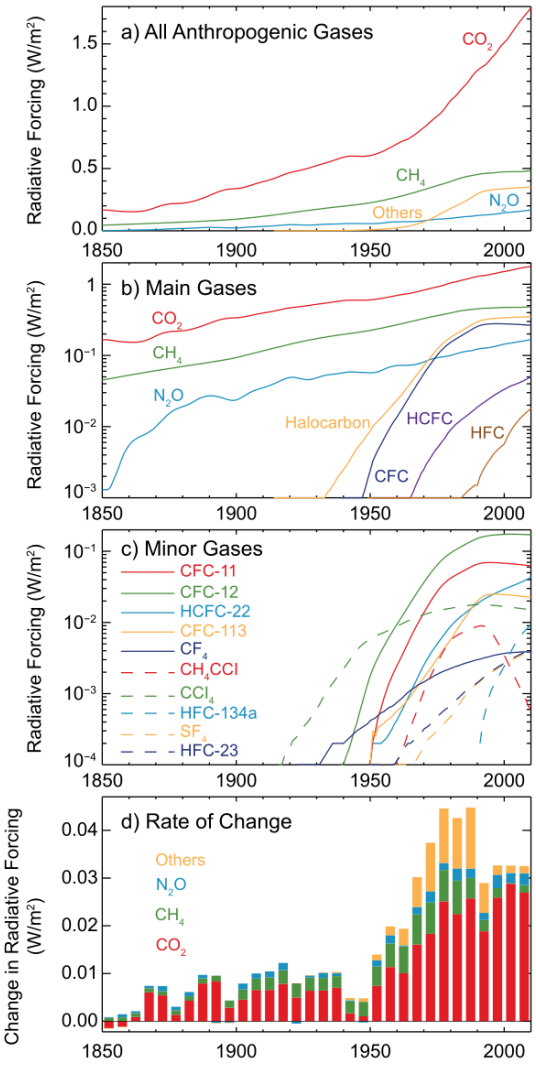

Figure 2 Radiative forcing of mixed greenhouse gases [4]

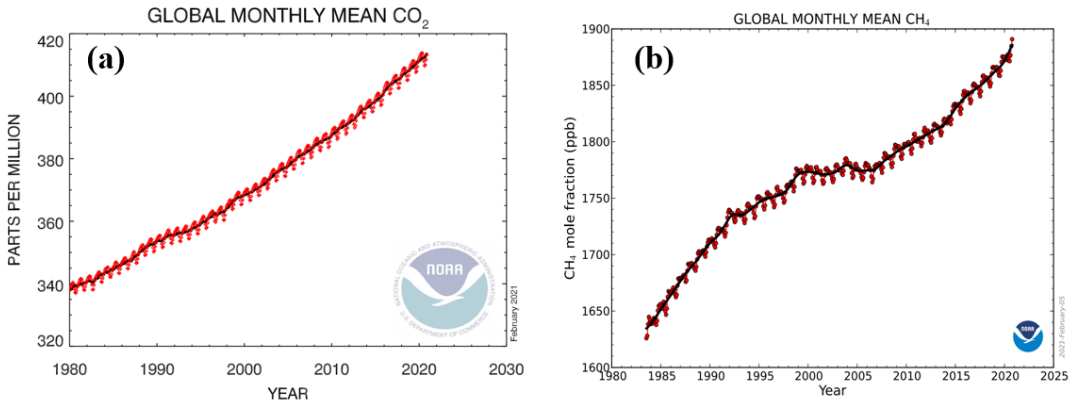

Figure 3 (a) Global monthly average change of CO2 in the atmosphere; (b) Global monthly average change of CH4 in the atmosphere

I2 Current methods for GHGs observation

At present, there are mainly the following methods of observing greenhouse gases (as shown in Figure 4). They are satellite observations, airborne and ball-borne observations, in-situ observations, and ground-based remote sensing observations.

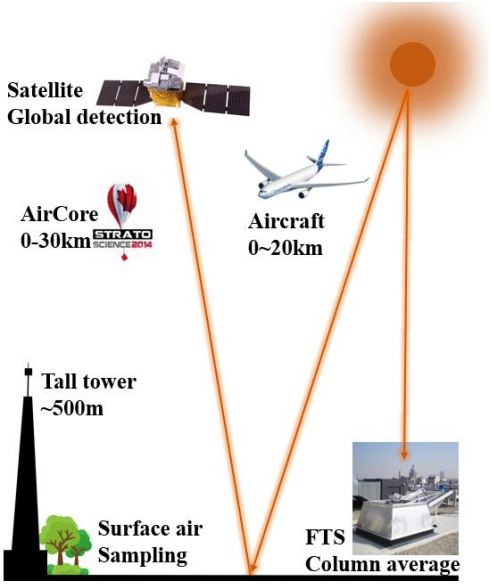

Figure 4 The observation methods of global greenhouse gases

Satellite observation

Satellite observations mainly use space-borne instruments to obtain emission or absorption spectrum information of gas molecules in the atmosphere, thereby reflecting the distribution information of target molecules. Spaceborne observations

can cover a large observation area in a short period. The satellites currently used for greenhouse gas observation include GOSAT satellites, OCO-2 and OCO-3 satellites, and carbon satellites. GOSAT satellite [5-7] was launched to observe the global CO_2 concentration distribution and changes in space and time. It plays a very important role in improving the accuracy of greenhouse gas flux retrieval and estimating the forest carbon budget. It is equipped with measuring instruments such as Infrared Fourier Transform Spectrometer (FTS), cloud, and aerosol imager (CAI). FTS performs spectral detection on the solar shortwave radiation reflected by the earth's surface, clouds, and aerosols and the thermal infrared radiation emitted by the earth's surface. It can measure the atmospheric transmittance spectra of O_2, CO_2, CH_4, and water vapor with a spectral resolution of 0.2 cm^{-1}. Through these absorption spectra, the column concentration and vertical profile of atmospheric greenhouse gases can be retrieved.

The OCO-2 and OCO-3 satellites [8, 9] are used to detect the source and sink information of near-surface carbon. The composition of the OCO-2 satellite. The measurement device it carries is composed of three near-infrared grating spectrometers, which are used to measure the atmospheric transmittance spectrum of sunlight reflected by the earth's surface in the near-infrared band. The Carbon Satellite (TanSat) was launched at the end of 2016 [10-12]. It is equipped with an atmospheric carbon dioxide grating spectroradiometer (ACGS) and cloud aerosol polarization imager (CAPI). Among them, ACGS can detect three channels of the atmospheric absorption spectrum (2.06 μm, 1.6 μm, 0.76 μm), and the highest resolution can reach 0.04 nm.

Airborne and ball-borne observations

This method mainly uses airplanes or balloons to carry greenhouse gas measuring instruments or gas collection devices to detect or sample the gases on each floor. Figure 5 shows a device for detecting greenhouse gases on an airplane equipped with lidar [13]. The Aircore detection technology derived from the ball-borne measurement [14, 15], the principle of the method for sampling the atmosphere is shown

in Figure 6. A weather balloon is used to carry a thin-walled thin-walled stainless steel tube (about 150 m ~ 200 m) into the stratosphere and then descend to sample the atmosphere at altitude. After the balloon lands, a high-precision gas analysis device is used to detect the concentration of sampled gas. This measurement method is a direct measurement of the vertical profile of greenhouse gases. And the measurement results have higher vertical resolution and accuracy. So, it can be better compared and calibrated with the results of satellite and ground remote instruments. However, the experiment preparation project is complicated and costly. Field experiments are easily restricted by objective conditions such as experimental locations and weather changes.

Figure 5 Aircraft equipped with lidar [13]

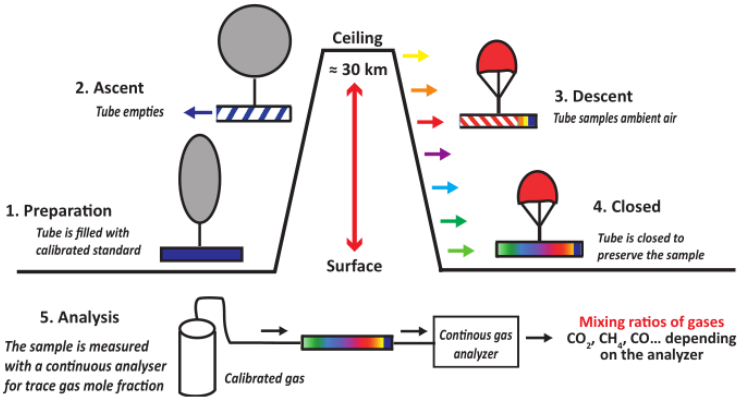

Figure 6 Principle of AirCore sampling method [14]

In situ observation

In the in-situ observation method, the measuring instrument is placed on the surface for fixed-point observation. Compared with other observation methods, this method has high observation accuracy, but it can only provide gas concentration information near the observation point. The NOAA global greenhouse gas observation experiment includes airborne observations, ground observations, and tower observations. The global distribution of observation points is shown in Figure 7. It includes all-weather, long-term measurements on four atmospheric reference observatories and eight observation towers. It collects local air samples for testing in more than 50 locations around the world, regularly uses small aircraft to collect high-altitude air samples, and uses balloons and AirCore sampling systems to measure the vertical profile of greenhouse gases.

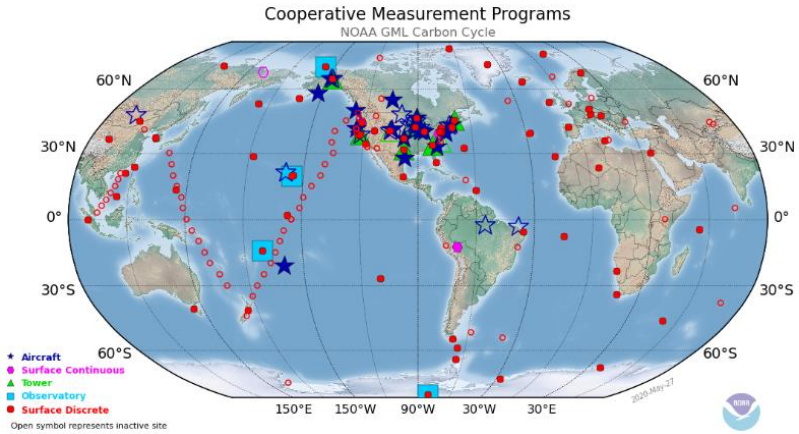

Figure 7 Distribution of NOAA global greenhouse gas observation experiments (https://www.esrl.noaa.gov/gmd/ccgg/about.html)

Ground-based remote sensing observation

The current ground-based remote sensing observation system mainly relies on the Total Carbon dioxide column Observation Network (TCCON). It is an observation network based on the ground FTIR, which records atmospheric absorption spectra in the near-infrared range [16], and can search the average abundance of atmospheric components, including CO_2, CH_4, N_2O, H.F., CO, H_2O, O_2, and HDO. The combination

of observations and in-situ ground-based observations can improve the estimation of greenhouse gas surface fluxes. In addition, it provides essential verification data for the Orbital Carbon Observatory, Sciamachy, and GOSAT [17]. FTIR is a Fourier transform method based on the structure of Michael's interferometer [18, 19], and its spectral resolution can be as high as 0.0095 cm^{-1}. Figure 8 is the FTIR (125HR) at the TCCON observation located in Paris, France. It can be seen that the high-resolution FTIR has a relatively large volume, and the corresponding instrument cost is expensive.

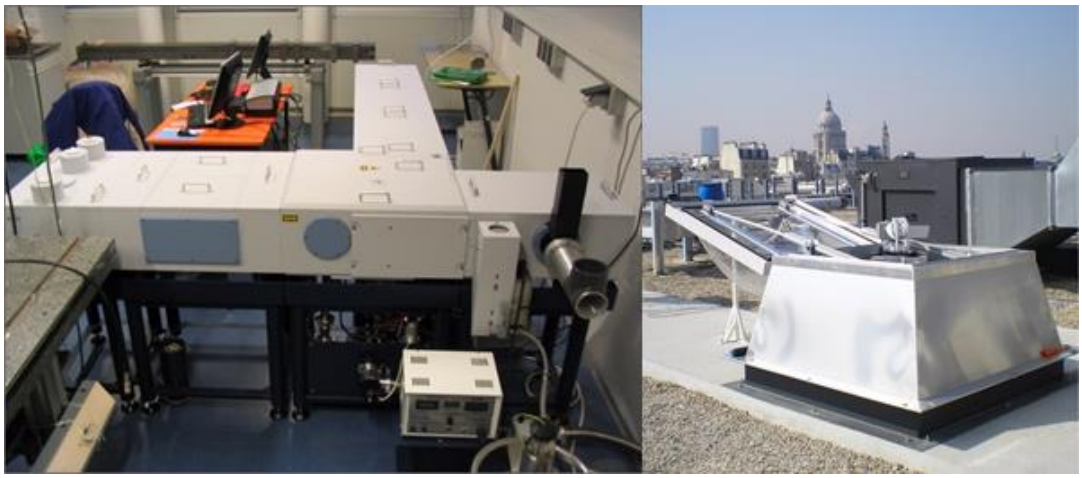

Figure 8 TCCON observation site in Paris (https://tccon-wiki.caltech.edu/Main/Paris)

The observation of greenhouse gases requires the mutual verification and complementation of the above multiple observation methods to more effectively observe the concentration of greenhouse gases in the atmosphere. Among them, ground remote sensing observation is an important observation method. Although satellites can provide observation data on a global scale, satellite observations also have their shortcomings: (1) The spectral resolution of the observation instrument carried by the satellite is relatively low, which will affect the accuracy of the inversion result. (2) Satellite observation data are limited to their lifetime, and long-term continuous observations are not possible. For these defects, ground-based observation instruments can effectively supplement and verify them. Compared with space-borne instruments, ground-based equipment has a simple structure and low cost, and system

calibration is relatively easy. Through the long-term observation experiment process, it has shown excellent stability. The spectral resolution of ground-based instruments is generally high, and the signal-to-noise ratio of the obtained signal is also relatively high. Therefore, ground-based observation data can be used to verify satellite data and be used for long-term local atmospheric composition measurement.

I3 Requirements for ground-based remote sensing

1. High spectral resolution

The spectral resolution of atmospheric remote sensing spectral detection instruments has an important influence on the inversion accuracy of atmospheric molecular concentration profiles. At different heights of the atmosphere, the atmospheric characteristic parameters such as temperature, pressure, and gas concentration are different, causing the width of the molecular absorption spectrum in the atmosphere to vary from 0.003 cm^{-1} to 0.07 cm^{-1}. The spectrum measured by the ground remote sensing instrument is the accumulation of the absorption spectrum at all heights. When the measured spectral resolution is much smaller than the line width of the true absorption spectrum, the true atmospheric transmittance spectrum can be more truly reflected. If two instruments with a spectral resolution of 0.05 cm^{-1} and 0.5 cm^{-1} are used to measure the absorption spectrum with a narrow bandwidth, as shown in Figure 9. It can be seen that the measurement spectrum of the low-resolution instrument will be smoothed. When the actual measurement spectrum resolution is insufficient, there will be a large deviation between the inversion result and the true value. Therefore, to perform accurate atmospheric concentration inversion, the measurement resolution of the instrument is first required to be far smaller than the linewidth of the true atmospheric transmittance. When the measurement resolution of the spectrometer is high enough, it can measure close to the real atmospheric molecular absorption spectrum. Therefore, the study of atmospheric remote sensing detection devices and equipment with the high spectral resolution is of great significance for the observation of atmospheric greenhouse gas concentration

changes.

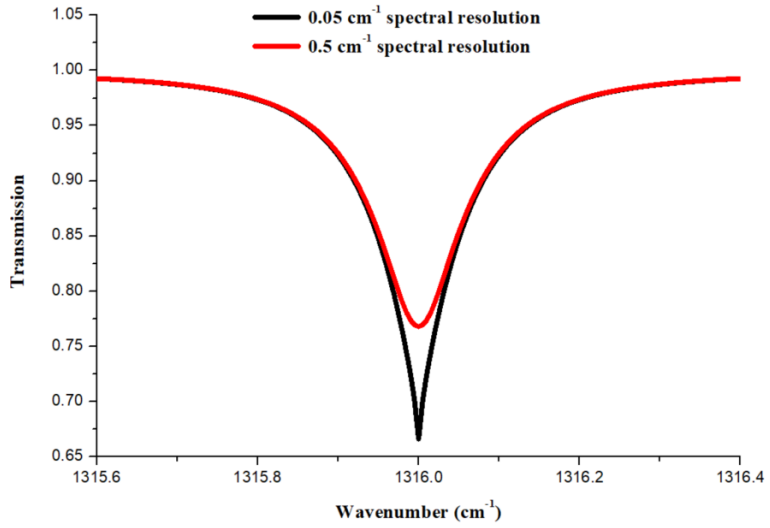

Figure 9 Absorption spectra measured by instruments with different resolutions

2. High SNR

The spectral signal-to-noise ratio for measuring atmospheric transmittance has an important influence on the inversion of gas profile and column concentration. Spectral data with a high signal-to-noise ratio is conducive to the accuracy and uncertainty reduction of gas concentration inversion. In theory, laser heterodyne spectroscopy detection is only limited by the quantum noise of the local oscillator. Therefore, it has the potential to improve the measurement sensitivity to obtain absorption spectra with a higher signal-to-noise ratio.

3. Integrated instrument

The measurement of greenhouse gases must be carried out not only in laboratories and observation stations but also in many remote areas with harsh conditions to achieve local observations of the atmosphere. Therefore, a low-cost, low-power integrated observation instrument is needed to facilitate the expansion of the observation network. In addition, several atmospheric components and physical parameters (such as temperature, wind, etc.) should be measured at the same time in the observation experiment so that the measured data obtained at the same time can be

used for a comprehensive analysis of the atmospheric state. With the development of laser spectroscopy technology, LHR can be used for remote sensing observations with high spectral resolution. It has the advantages of high spectral resolution, low cost, small size, and high mobility. Therefore, it contributes to the general deployment of high-precision observations of greenhouse gases and can be used for comparison between various observation instruments. The laser heterodyne spectrum detection method is different from the traditional direct detection method, and its output signal depends not only on the measured signal light but also on the local oscillator light. The signal power generated by the beat frequency of the signal light and the local oscillator light has a linear relationship with the product of the power of the two. When the laser power of the local oscillator is high enough, the SNR of the detection signal can be close to the SNR under the limit of shot noise. In addition, the spectral resolution of the LHR is determined by the bandwidth of the circuit system and the line width of the laser. The line width of the laser is generally narrow, so its spectral resolution can reach tens MHz. In addition, the optical path system of the LHR is relatively simple, can be implemented in a small space, and has a relatively stable structure (the volume of a typical laser heterodyne device: 60 cm×60 cm×40 cm). Based on these advantages, laser heterodyne spectroscopy technology is used in the remote measurement of atmospheric greenhouse gases increasingly.

II Laser heterodyne radiometer

II1 History

In 1901, in the field of electronic engineering, Reginald Fessenden proposed for the first time that a new frequency could be generated by mixing two or more frequencies into a mixer. In the first stage, the heterodyne experiment in the field of optics was designed by A. T. Forrester, R. A. Gudmundsen et al. in 1955 [20]. They used the light emitted by the mercury lamp Hg5461Å to obtain two emitted lights after Zeeman

splitting. The two beams of light beat frequency on the surface of the SbCs3 photosensitive detector, and a weak beat frequency signal was observed.

The second stage of the development of laser heterodyne technology benefited from the birth of lasers. In the 1960s, with the production of CO_2 gas lasers, He-Ne lasers, and other lasers, lasers were used as local oscillators to construct laser heterodyne measurement systems, which gradually improved the research of laser heterodyne technology. In 1962, A. Javan et al. used two highly coherent laser beat frequencies generated by two He-Ne lasers to obtain optical heterodyne signals [21]. W. S. Read, Y. Ohtsuka et al. split the laser beams emitted by the He-Ne laser and then combined the beams, and finally got the heterodyne signal. On this basis, they studied the angle matching between the beat signal and the combination of the two beams [22, 23]. At the same time, in 1963, G. Lucovsky et al. also conducted in-depth research on the heterodyne detector [24]. M. C. Teich used the laser emitted by the CO_2 gas laser and the reflected laser from a spinning wheel to conduct a beat frequency experiment to study the SNR of the heterodyne signal [25-27]. In 1966, A. E. Siegman made a theoretical analysis of the heterodyne spectrum detection system using a blackbody as the signal light source. He gave the theoretical SNR and the relationship between the detection field angle of the heterodyne system and the observation wavelength [28]. In 1967, F. R. Arams et al. established a laser heterodyne spectrum detection system with a CO_2 gas laser as the local oscillator source[29]. The influence of the electronic parameters in the device on the detection performance was discussed. This enriches the theory and experimental system of heterodyne detection further.

The third stage is the phase of heterodyne detection from laboratory principle research to the preliminary application stage. In 1966, H. Vanbueren first designed a plan to apply heterodyne detection technology to astronomical observations [30]. O. E. Delange compared and studied the laser heterodyne detection method and the direct detection method [31] comprehensively and pointed out the advantages of the heterodyne detection method. D. L. Fried et al. studied the influence of wavefront misalignment caused by an atmospheric disturbance on beat frequency signals [32]. In

1968, H. Nieuwenhuijzen used coherent light and non-phase light to beat the frequency, proposed a method to improve the SNR of heterodyne detection, and studied the detection integration time and detection bandwidth [33]. J. H. McElroy estimated the SNR of a blackbody with a temperature of 5000 K in the vicinity of 10 μm for heterodyne detection [34]. J. Gay used a laser heterodyne device to measure the heterodyne signal of the blackbody radiation at a temperature of 900 K in laboratory and analyzed the SNR ratio of the system [35]. After this stage, the theoretical system and device structures based on laser heterodyne spectroscopy detection are complete.

In the fifth stage, after entering the 21st century, the application of laser heterodyne technology in atmospheric detection has been developed rapidly, and it has also been studied further. In 2000, R. Güsten et al. completed the first-generation heterodyne receiver GREAT [36]. In the same year, D. Weidmann et al. established a laser heterodyne system with a tunable diode laser as the local oscillator source, which realized the detection of SO_2. Since the radiation wavelength is very sensitive to the pump current and temperature of the laser to obtain a high-quality spectrum, they designed a liquid nitrogen cryostat system to control the laser. On this basis, they compared current control and temperature control and found that the effect of temperature control is better. This provides a reference for the control method of laser wavelength [37]. In 2002, G. Sonnabend et al. designed a movable tunable heterodyne infrared spectrometer (THIS), which used a tunable laser as the local oscillator to observe the absorption spectra of different molecules [38]. In the same year, D. Wirtz et al. completed the first test of a tunable laser heterodyne infrared spectrometer based on THIS with a high-power quantum cascade laser. It realizes the detection of a variety of molecules (O_3, NH_3, CH_4, N_2O) [39]. In 2004, B. Parvitte et al. obtained preliminary detection results of O_3 in the atmosphere by a laser heterodyne device using a quantum cascade laser as the local oscillator in the 9 μm area [40]. D. Weidmann et al. established a laser heterodyne spectroscopy measurement system based on quantum cascade lasers [41-43] to perform atmospheric transmittance measurement and concentration inversion of O_3 in the atmosphere. The

high-frequency noise and optical feedback in the system are studied, and the research of laser heterodyne radiometer is perfected. At the same time, the inversion of laser heterodyne spectrum gas concentration is analyzed and introduced in detail. The high-frequency noise and optical feedback in the system are studied, and the inversion of gas concentration using laser heterodyne spectroscopy is analyzed and introduced in detail. They also used the laser heterodyne device to measure the change of gas composition during the combustion process [44], which provides a reference for the extended application of laser heterodyne spectroscopy.

II2 Development states

In recent years, with the development and innovation of lasers, high-speed photodetectors, and detection methods. The cost of laser heterodyne radiometers has gradually decreased. Its volume has become smaller, and the measurement system has become more stable. The spectral resolution is improved further while ensuring that the heterodyne detection spectrum has a high SNR. Due to the urgent need for greenhouse gas observation, laser heterodyne spectroscopy technology has attracted widespread attention, research, and application at present.

D. Weidmann et al. established a laser heterodyne measurement system with ultra-high spectral resolution (0.002 cm^{-1}) based on an external cavity quantum cascade laser (EC-QCL) and observed a variety of gas molecules in the atmosphere (H_2O, O_3, N_2O, CH_4, CCl_2F_3). The wavelength-tunable range of EC-QCL is [1120,1238] cm^{-1}. The schematic diagram of the experimental equipment is shown in Figure 10. The laser light emitted by EC-QCL is reflected by an off-axis parabolic mirror to a beam splitter through an adjustable optical attenuator. The sun tracker tracks the movement of the sun and uses a beam splitter to divide the sun into two beams, which are reflected into the FTIR and transmitted into the LHR. The transmitted sunlight is reflected by two off-axis parabolic mirrors to combine the sunlight with the laser beam. The combined beam of laser and sunlight is focused on the photodetector to generate a beat signal. A wavelength meter and power meter are

used to calibrate the wavelength and power of the laser. The measured spectrum of FTIR and EC-QC-LHR were compared, as shown in Figure 11. As can be seen, when high spectral resolution, narrow field of view, and short measurement time are required, EC-QC-LHR can provide a superior spectral signal for a specific narrow spectral measurement window [45]. In the same year, D. Weidmann et al. also proposed the experimental study of laser heterodyne radiometers using hollow waveguides [46].

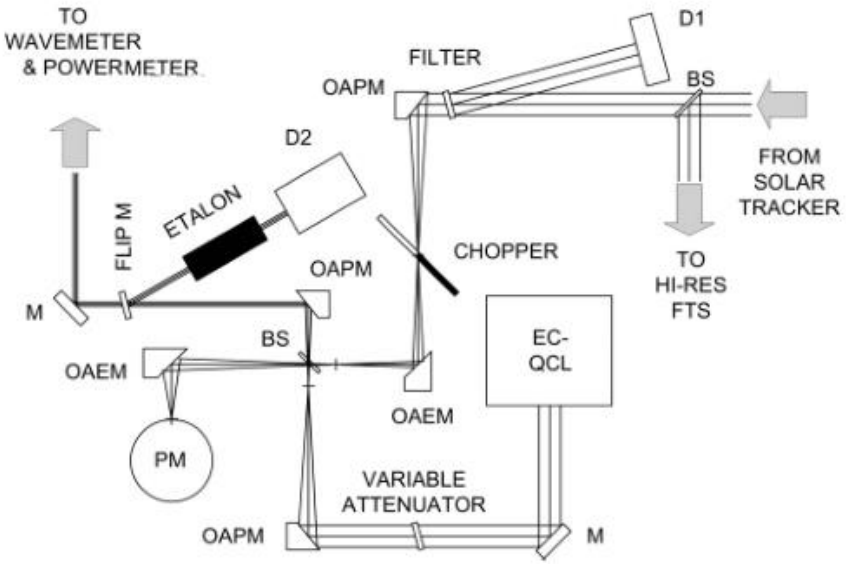

Figure 10 Schematic diagram of mid-infrared laser heterodyne device [45].

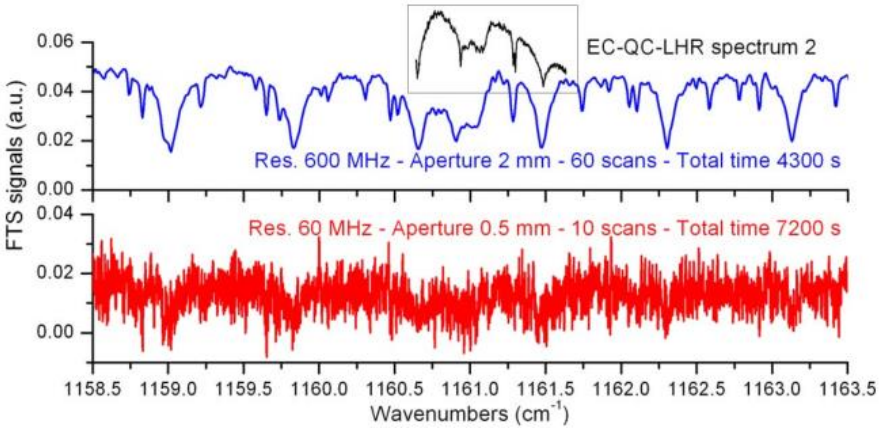

Figure 11 Comparison of LHR and FTIR measurement results [45]

Later, T. Stangier et al. also reported an experimental setup of a compact tunable laser heterodyne radiometer for infrared observation of atmospheric trace gases [47]. The local oscillator source of this device is a QCL laser working in the mid-infrared

band. This device can be used to detect O_3 in the surface atmosphere with a bandwidth of 1.4 GHz. The schematic diagram of the optical path of the device is shown in Figure 12. The green line is the infrared signal light source that can be selected by the stepper motor, the red line represents the signal light, and the blue line is the local oscillator source. When the signal light and laser are beaten on the surface of the I.R. mixer detector, the intermediate frequency (IF) signal was extracted by an acousto-optic spectrometer (AOS) to obtain the measurement spectrum.

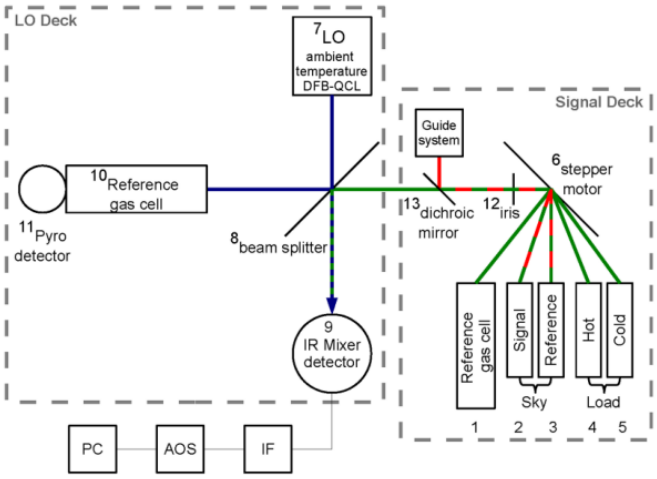

Figure 12 Tunable heterodyne measuring device [47]

A. Hoffmann et al. reported the use of thermal infrared LHR for atmospheric CO_2 measurement in 2016. The experimental schematic diagram and the physical diagram of the device are shown in Figures 13 (a) and (b). Using a QCL laser with a center wavelength of 10.47 μm and output power of 30 mW as the local oscillator, the absorption spectra of CO_2 and H_2O in the range of 1 cm^{-1} were measured. In 2015, they used this device in Didcot, U.K., to measure CO_2 and H_2O in the atmosphere for 8 months. When the spectral resolutions were set as 0.002 cm^{-1} and 0.02 cm^{-1}, the corresponding SNR of the measured spectrum were 113 and 257. It can be seen that for the same laser heterodyne measurement system, the SNR would be correspondingly lost when the spectral resolution was increased. This device and experiment provide an important reference for the use of LHR technology in atmospheric greenhouse gases observation networks or deployment on spaceborne

platforms [48].

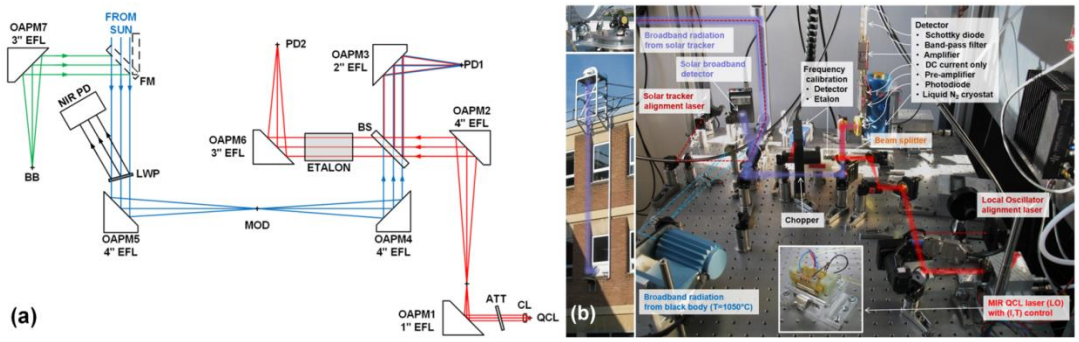

Figure 13 (a) Schematic diagram of LHR; (b) Physical diagram of LHR device [48]

Subsequently, D. Weidmann, A. Hoffmann et al. carried out the mission of satellite observation of CH_4 isotope (MISO) based on the solar occultation mode, combined with laser heterodyne spectroscopy detection technology for spectrum channel optimization and early performance analysis. Figure 14 shows the three-dimensional model of the LHR they designed in the satellite [49]. The volume of the device is about 10×10×30 cm^3. D. Weidmann et al. gradually designed the LHR to be miniaturized, making it suitable for more occasions and applications.

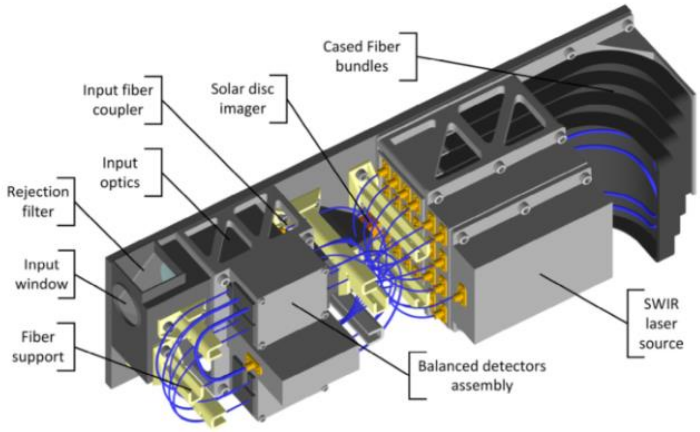

Figure 14 The three-dimensional model of the laser heterodyne radiometer in the satellite [49]

In 2012, A. Y. Klimchuk et al. published their research results on the feasibility analysis of using a tunable diode laser to establish a high-resolution LHR [50]. Then in 2014, A. Rodin, A. Y. Klimchuk et al. used a DFB laser with a center wavelength of 1.651 μm, combined with the fiber-optic devices and a balanced photodetector, to

establish a laser heterodyne measurement system, which can measure the spectrum of CO_2 and CH_4 in the entire atmosphere [51]. The experimental principal structure is shown in Figure 15 (a). The local oscillation laser is divided into two beams with a fiber splitter. One beam passes through the optical attenuator and incident on an input port of the balanced detector. The other laser beam is divided into two beams again. One of them is used for laser wavelength calibration, and the other is combined with sunlight and incident on the other input of the balanced photodetector. Through the amplitude detection and processing of the output signal of the balanced detector, after 10 minutes of averaging, the atmospheric transmittance spectrum of the sunlight around 1.651 μm in the range of 1.1cm^{-1} was obtained (SNR~120), as shown in Figure 15 (b).

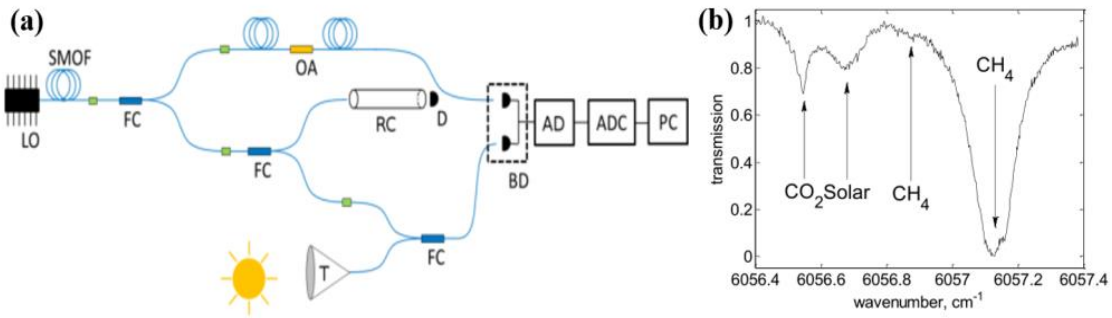

Figure 15 (a) Principal diagram of laser heterodyne radiometer based on balance detection; (b) Measurement spectrum [51]

E. L. Wilson, G. B. Clarke, P. I. Palmer et al. used the DFB laser with a center wavelength of 1.573 μm as the local oscillator source, established an LHR applied to the measurement of the column concentration of CO_2 in the atmosphere. They use optical fiber devices, which greatly reduce the difficulty of optical coupling adjustment and reduce the size of the measurement system. In addition, they analyzed the uncertainty of this system and the potential of the CO_2 column concentration observation network based on LHR to improve global carbon flux estimation[52-54]. The schematic diagram of the system is shown in Figure 16 (a). The two channels of sunlight collected by the light-receiving device on the sun tracker are modulated by a mechanical chopper. One channel is beaten with the local oscillator, and the other is

used for monitoring the intensity of sunlight. The photodetector converts the optical signal into the electrical signal in the radio frequency (IF) range, and then the absorption spectrum of CO_2 in the atmosphere (the measuring range is about 1 cm^{-1}) is obtained after the processing of the R.F. signal, as shown in Figure 16 (b). The physical map of the measuring device is shown in Figure 16 (c).

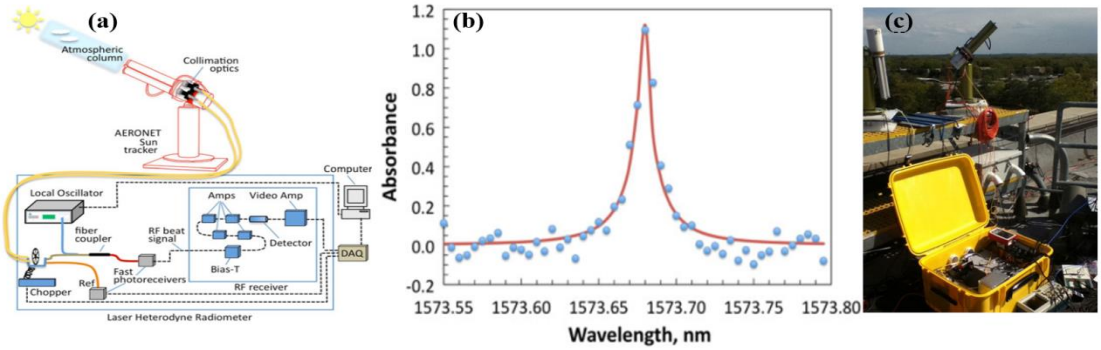

Figure 16 (a) Schematic diagram of laser heterodyne fiber measuring device; (b) Measuring spectrum; (c) Physical picture of measuring device [52]

In 2019, E. L. Wilson et al. integrated the above-mentioned LHR [55] to facilitate the detection of CH_4 and CO_2 in the field. The instrument consists of an LHR chassis and a sun tracker, as shown in Figure 17 (a). The performance of this instrument was proved by two actual measurements in two completely different locations in Alaska and Hawaii. After 15 min or half an hour of data averaging, the processed measurement spectrum is shown in Figure 17 (b) and (c). It can be seen that the measurement range of the spectrum is about 1.1 cm^{-1}, including the absorption spectrum of CH_4 and CO_2 (blue curve), but the absorption of CO_2 is weak, and there is a certain overlap with the absorption of CH_4. In (c) and (d), the concentration of CO_2 and CH_4 is obtained by inversion and fitting of the measured spectrum (orange). Since this mini-LHR is a portable measuring instrument, it is convenient to work with other measuring instruments so that it can be used to characterize the deviation between the immovable column concentration observation instruments. In addition, the LHR can quickly respond to transient events such as methane leaks and can also be used for field studies in designated geographic areas.

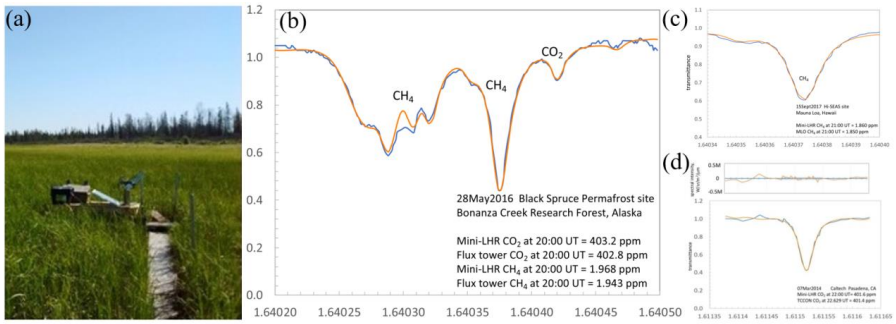

Figure 17 (a) Mini-LHR; (b) Complete measurement spectrum and fitting; (c) Measurement spectrum and fitting of CH_4; (d) Measurement spectrum and fitting of CO_2 [55]

F. Smith et al. also evaluated LHR in numerical weather prediction [56]. The research results show that the multiplexed LHR is a worthy instrument for numerical weather prediction on low-earth orbit and geostationary orbit platforms. It can fill the high-altitude gap of the satellite observation system in operation, so it should be further developed Multiplexing technology, resulting in an instrument that can be used for mid-upper atmosphere detection.

F. Shen et al. built a laser heterodyne measurement system based on EC-QCL lasers to detect atmospheric transmittance around 8 μm [57], and compared them with the FTIR observation results of the Paris Observatory. The CH_4 and N_2O in the atmosphere were detected. The schematic diagram of the device is shown in Figure 18 (a), and (b) is the observation site.

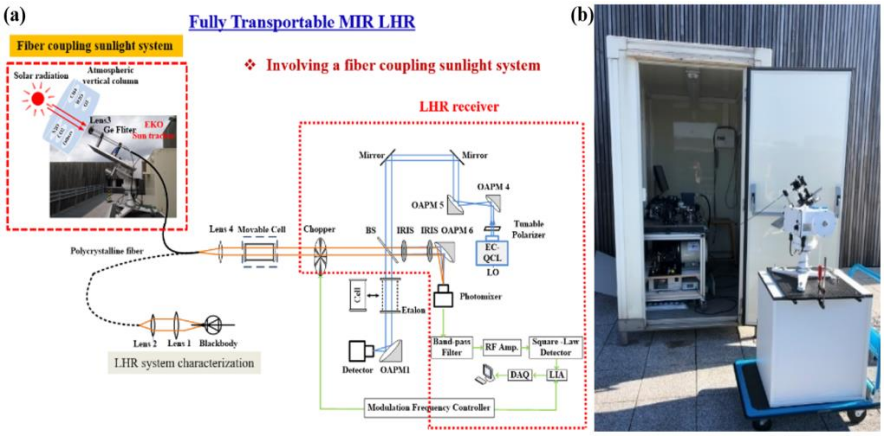

Figure 18 (a) Schematic diagram of EC-QCL-LHR results; (b) Observation site [57]

The above research is mainly based on the direct absorption of sunlight by gas molecules in the atmosphere, and the recent laser wavelength modulation method has also been used in laser heterodyne spectroscopy detection. In 2018, P. Martin-Mateos et al. modulated the wavelength of the local oscillator light to obtain the laser heterodyne spectrum, which improved the SNR of the heterodyne signals. The ratio of the amplitude of the second harmonic to the first harmonic was used to reduce the influence of the laser light intensity on the heterodyne signal [58]. In 2019, P. Martin-Mateos et al. reported on a thermal infrared wavelength modulated laser heterodyne radiometer (WM-LHR) based on an external cavity quantum cascade laser [59]. This WM-LHR system does not require calibration, has an excellent SNR, and does not require an optical chopper.

III Main content of the present PhD thesis

It can be seen from the above-mentioned development history and development status of LHR that based on the advantages of LHR for greenhouse gas remote sensing (small size, low cost, low power consumption, high spectral resolution), it has been developed rapidly in recent years, especially in the near-infrared band.

However, there are still several issues that require further consideration:

(1) In the near-infrared band, DFB lasers are used as the local oscillator source in most of the research work because of their small size, good monochromaticity and operation at room temperature. However, the narrow wavelength scanning range of each DFB laser usually contains only one strong molecular absorption spectrum, which is not suitable for simultaneous measurement of multiple gas molecules in the atmosphere.

(2) At present, most of the research on laser heterodyne detection systems is in the laboratory research stage. Only E. L. Wilson et al. have integrated it for field experiments. The portable laser heterodyne radiometer is of great significance to the construction of the atmospheric greenhouse gas

monitoring network, so further research on the portable laser heterodyne radiometer is needed.

(3) The atmospheric window of 3-5 μm is an attractive spectral region for Mid-infrared atmospheric sounding. However, there is less research on LHR in this band.

The main contents of this thesis are as follows: (1) carrying out the research and application of LHR in the near-infrared band for simultaneous detection of CH_4 and CO_2 in the atmosphere. (2) Miniaturize and integrate the near-infrared LHR to facilitate field applications. (3) Developing a mid-IR LHR in the atmospheric window of 3-5 μm for detection of CH_4 and HDO in the atmosphere. (4) Developing a wide-band measuring LHR based on an external cavity laser for detection of CO_2 and its isotope gases in the atmosphere. The thesis is divided into six parts, and the content of each part is as follows:

Introduction introduces the impact of greenhouse gases (GHGs), and the changing trends, observation methods, requirements for observation devices of the main GHGs. It analyses that the LHRs can meet the urgent needs of high spectral resolution, small size, and low cost for GHGs observation. It describes the history, and research status of LHR. Based on this, it analyzes the issues for further consideration for LHR and summarizes the main content of this paper.

Chapter 1 recalls the basic elements involved in LHR, which include of principle of heterodyne detection, noise in the detection, features of main components in LHR.

Chapter 2 shows a proof of concept of near-infrared laser heterodyne radiometer (NIR-LHR) for simultaneous detection of CH_4 and CO_2 in the atmosphere. The composition structure and system characteristics of NIR-LHR are described in detail. The absorption spectrum of CH_4 and CO_2 in Hefei was detected and analyzed for eight months. The inversion results from the actual observation data are in good agreement with the GOSAT measurement results.

Chapter 3 describes the design of a miniaturized and integrated portable near-infrared laser heterodyne radiometer (IP-NIR-LHR), which was used to conduct

field joint observation experiments in the Dachaidan area, Qinghai Province.

Chapter 4 presents a laser heterodyne radiometer based on an interband cascade laser. The optical structure of the system, the related instruments and devices are presented in detail. The absorption spectra of CH_4 and HDO in the authentic atmosphere are measured, which proved the feasibility of the IC-LHR measurement system.

Chapter 5 presents a laser heterodyne radiometer based on an external cavity laser (EC-LHR). The structure and detection experiments of the device are introduced in detail.

References

[1] W. V. Sweet, R. Horton, R. E. Kopp, A. N. Romanou. IPCC, 2017: Sea level rise. In: Climate Science Special Report: Fourth National Climate Assessment, Volume I. U.S. Global Change Research Program, Washington, DC, USA, 2017: 333-363.

[2] D. J. Wuebbles, D. R. Easterling, K. Hayhoe, T. Knutson, R. E. Kopp, J. P. Kossin, K. E. Kunkel, A. N. LeGrande, C. Mears, W. V. Sweet, P. C. Taylor, R. S. Vose, M. F. Wehner, D. J. Wuebbles, D. W. Fahey, K. A. Hibbard, D. J. Dokken, B. C. Stewart, T. K. Maycock. IPCC, 2017: Our globally changing climate. In: Climate Science Special Report: Fourth National Climate Assessment. U.S. Global Change Research Program, Washington, DC, USA, 2017, 1: 35-72.

[3] D. R. Reidmiller, C.W. Avery, D.R. Easterling, K.E. Kunkel, K.L.M. Lewis, T.K. Maycock, and B.C. Stewart (eds.). USGCRP, 2018: Impacts, Risks, and Adaptation in the United States: Fourth National Climate Assessment. U.S. Global Change Research Program, Washington, DC, USA, 2018, 2: 186.

[4] D. W. Fahey, S. J. Doherty, K. A. Hibbard, A. Romanou, P. C. Taylor, D. J. Wuebbles, D. W. Fahey, K. A. Hibbard, D. J. Dokken, B. C. Stewart, T. K. Maycock. 2017: Physical drivers of climate change. In: Climate Science Special Report: Fourth National Climate Assessment. U.S. Global Change Research Program, Washington, DC, USA, 2017, 1: 73-113.

[5] M. V. Makarova, N. M. Gavrilov, Yu M. Timofeev, A. V. Poberovskii. Comparisons of satellite (GOSAT) and ground-based Fourier spectroscopic measurements of methane content near St. Petersburg. Izvestiya, Atmospheric and Oceanic Physics, 2015,50 (9): 904-909.

[6] Y. Yoshida, N. Kikuchi, and T. Yokota. On-orbit radiometric calibration of SWIR bands of TANSO-FTS onboard GOSAT. Atmospheric Measurement Techniques, 2012,5 (10): 2515-2523.

[7] I. Morino, O. Uchino, M. Inoue, Y. Yoshida, T.Yokota, P. O. Wennberg, G. C. Toon, D. Wunch, C. M. Roehl, J. Notholt, T. Warneke, J. Messerschmidt, D.

W. T. Griffith, N. M. Deutscher, V. Sherlock, B. Connor, J. Robinson, R. Sussmann, M. Rettinger. Preliminary validation of column-averaged volume mixing ratios of carbon dioxide and methane retrieved from GOSAT short-wavelength infrared spectra. Atmospheric Measurement Techniques, 2011,4 (6): 1061-1076.

[8] C. Frankenberg, R. Pollock, R. A. M. Lee, +R. Rosenberg, J. F. Blavier, D. Crisp, C. W. O'Dell, G. B. Osterman, C. Roehl, P. O. Wennberg, D. Wunch. The Orbiting Carbon Observatory (OCO-2): spectrometer performance evaluation using pre-launch direct sun measurements. Atmospheric Measurement Techniques, 2015, 8 (1): 301-313.

[9] Eldering, A. O'Dell, C. W. Wennberg, P. O. Crisp, D. Gunson, M. R. Viatte, C. C. Avis, A. Braverman, R. Castano, A. Chang, L. Chapsky, C. Cheng, B. Connor, L. Dang, G. Doran, B. Fisher, C. Frankenberg, D. J. Fu, R. Granat, J. Hobbs, R. A. M. Lee, L. Mandrake, J. McDuffie, C. E. Miller, V. Myers, V. Natraj, D. O'Brien, G. B. Osterman, F. Oyafuso, V. H. Payne, H. R. Pollock, I. Polonsky, C. M. Roehl, R. Rosenberg, F. Schwandner, M. Smyth, V. V. Tang, T. E. Taylor, C. To, D. Wunch, J. Yoshimizu. The Orbiting Carbon Observatory-2: first 18 months of science data products. Atmospheric Measurement Techniques, 2017, 10 (2): 549-563.

[10] Z. D. Yang, Y. M. Bi, Q. Wang, C. B. Liu, S. Y. Gu, Y. Q. Zheng, C. Lin, Z. S. Yin, L. F. Tian. Inflight Performance of the TanSat Atmospheric Carbon Dioxide Grating Spectrometer, IEEE Transactions on Geoscience and Remote Sensing, 2020, 58 (7): 4691-4703.

[11] Y. H. Ran, X. Li. TanSat: a new star in global carbon monitoring from China, Science Bulletin, 2019, 64 (5): 284-285.

[12] S. P. Wang, A, R. J. van der P. Stammes, W. H. Wang, P. Zhang, N. M. Lu, L. Fang. Carbon Dioxide Retrieval from TanSat Observations and Validation with TCCON Measurements. Remote Sensing, 2020, 12 (14): 19-40.

[13] J. B. Abshire, H. Riris, B. Hasselbrack, G. Allan, C. Weaver, J. Mao. Airborne measurements of CO_2 column absorption using a pulsed wavelength-scanned laser sounder instrument. Conference on Lasers and Electro-Optics/Quantum Electronics and Laser Science Conference, Optical Society of America, 2009: 255-256.

[14] O. Membrive, C. Crevoisier, C. Sweeney, F. Danis, A. Hertzog, A. Engel, H. Boenisch, L. Picon. AirCore-HR: a high-resolution column sampling to enhance the vertical description of CH_4 and CO_2, Atmospheric Measurement Techniques, 2017,10 (6): 2163-2181.

[15] A. Karion, C. Sweeney, P. Tans, T. ewberger. AirCore: An Innovative Atmospheric Sampling System. Journal of Atmospheric and Oceanic Technology, 2010, 27 (11): 1839-1853.

[16] D. Wunch, G. C. Toon, J. F. L. Blavier, R. A. Washenfelder, J. Notholt, B. J. Connor, D. W. T. Griffith, V. Sherlock, P. O. Wennberg. The Total Carbon Column Observing Network. Philosophical Transactions of the Royal Society a-Mathematical Physical and Engineering Sciences, 2011, 369 (1943): 2087-2112.

[17] H. Ohyama, S. Kawakami, T. Tanaka, I. Morino, O. Uchino, M. Inoue, T. Sakai, T. Nagai, A. Yamazaki, A. Uchiyama, T. Fukamachi, M. Sakashita, T. Kawasaki, T. Akaho, K. Arai, H. Okumura. Observations of XCO_2 and XCH_4 with ground-based high-resolution FTS at Saga, Japan, and comparisons with GOSAT products. Atmospheric Measurement Techniques, 2015, 8 (12): 5263-5276.

[18] Y. Yoshida, N. Kikuchi, T. Yokota. Thermal and near infrared sensor for carbon observation Fourier-transform spectrometer on the Greenhouse Gases Observing Satellite for greenhouse gases monitoring. Applied Optics, 2009, 48 (35): 6716-6733.

[19] A. N. Morozov, S. I. Svetlichnyi, S. E. Tabalin. Remote Sensing by Means of Fourier Transform Infrared Spectroscopy. Physical Bases of Instrumentation, 2014, 3 (4): 5-19.

[20] A. T. Forrester, R. A. Gudmundsen, P. O. Johnson. Photoelectric Mixing of Incoherent Light. Physical Review, 1955, 99 (6): 1691-1700.

[21] A. Javan, E. A. Ballik, W. L. Bond. Frequency Characteristics of a Continuous-Wave He-Ne Optical Maser. Journal of the Optical Society of America, 1962, 52 (1): 96-98.

[22] W. S. Read, R. G. Turner. Tracking heterodyne detector. Applied Optics, 1965, 4 (12): 1570-1573.

[23] Y. Ohtsuka. Optical heterodyning with noncritical angular alignment using a pair of ultrasonic light modulators, Japanese journal of applied physics, 1972,11(10):1446.

[24] G. Lucovsky, M. E. Lasser, R. B. Emmons. Coherent light detection in solid-state photodiodes. Proceedings of the IEEE, 1963 , 51 (1): 166-172.

[25] M. C. Teich, R. J. Keyes, R. H. Kingston. Optimum heterodyne detection at 10.6 um in photoconductive Ge: Cu, Applied Physics Letters, 1966, 9 (10): 357-360.

[26] M. C. Teich. Infrared heterodyne detection, Proceedings of the IEEE, 1968, 56 (1): 37-46.

[27] M. C. Teich. Homodyne detection of infrared radiation from a moving diffuse target, Proceedings of the IEEE, 1969, 57 (5): 786-792.

[28] A. E. Siegman. The antenna properties of optical heterodyne receivers, Applied Optics, 1966，5 (10): 1588-1594.

[29] F. R. Arams, E. W. Sard, B. J. Peyton, F. P. Pace. Infrared 10.6-micron heterodyne detection with gigahertz IF capability, IEEE Journal of Quantum Electronics, 1967,3 (11): 484-492.

[30] H. G. Vanbuere. Electronic spectroscopy for astronomical purposes, Bulletin of the Astronomical Institutes of the Netherlands, 1967, 19 (2): 97-106.

[31] O. E. Delange. Optical heterodye detection, IEEE Spectrum, 1968, 5 (10): 77-85.

[32] D. L. Fried. Optical heterodyne detection of an atmospherically distorted signal wave front, Proceedings of the IEEE, 1967, 55 (1): 57-77.

[33] H. Nieuwenhuijzen. Photo-electric mixing of coherent and incoherent light, Bulletin of the Astronomical Institutes of the Netherlands, 1968,19 (5): 391-404.

[34] J. H. McElroy. Infrared heterodyne solar radiometry, Applied optics, 1972, 11 (7): 1619-1622.

[35] J. Gay and A. Journet. Heterodyne detection of blackbody radiation, Applied Physics Letters, 1973, 22 (9): 448-449.

[36] R. Güsten, P. Hartogh, H. W. Hübers, U. Graf, K. Jacobs, H. P. Röser, F. Schäfer, R. Schieder, R. Stark, J. Stutzki, P. van der Wal, A. Wunsch. GREAT - The first-generation German heterodyne receiver for SOFIA, Airborne Telescope Systems, International Society for Optics and Photonics, 2000, 4014: 23-30.

[37] D. Weidmann, D. Courtois. High quality infrared (8 mμ m) diode laser source design for high resolution spectroscopy with precise temperature and current control, Infrared Physics & Technology, 2000, 41 (6): 361-371.

[38] G. Sonnabend, D. Wirtz, F. Schmulling, R. Schieder. Tuneable Heterodyne Infrared Spectrometer for atmospheric and astronomical studies, Applied Optics, 2002, 41 (15): 2978-2984.

[39] D. Wirtz, G. Sonnabend, R. T. Schieder. THIS: a tuneable heterodyne infrared spectrometer, Spectrochimica Acta Part A: Molecular and Biomolecular Spectroscopy, 2002, 58 (11): 2457-2463.

[40] B. Parvitte, L. Joly, V. Zeninari, D. Courtois. Preliminary results of heterodyne detection with quantum-cascade lasers in the 9 mμ m region, Spectrochimica Acta Part a-Molecular and Biomolecular Spectroscopy, 2004, 60 (14): 3285-3290.

[41] D. Weidmann, J. Reburn, K. Smith, Ieee. Infrared heterodyne radiometry using quantum cascade laser as tunable local oscillator: application to atmospheric studies, Conference on Lasers & Electro-Optics/Quantum Electronics and Laser Science Conference, 2007:1476-1477.

[42] D. Weidmann, W. J. Reburn, K. M. Smith. Ground-based prototype quantum cascade laser heterodyne radiometer for atmospheric studies, Review of Scientific Instruments, 2007, 78 (7): 073107.

[43] D. Weidmann, W. J. Reburn, K. M.Smith. Retrieval of atmospheric ozone profiles from an infrared quantum cascade laser heterodyne radiometer: results and analysis, Applied Optics, 2007, 46 (29): 7162-7171.

[44] D. Weidmann, D. Courtois. Passive remote detection in a combustion system with a

tunable heterodyne receiver: application to sulfur dioxide, Journal of Quantitative Spectroscopy & Radiative Transfer, 2004, 83 (3-4): 655-666.

[45] D. Weidmann, T. Tsai, N. A. Macleod, G. Wysocki. Atmospheric observations of multiple molecular species using ultra-high-resolution external cavity quantum cascade laser heterodyne radiometry, Optics Letters, 2011, 36 (11): 1951-1953.

[46] D. Weidmann, T. Tsai, N. A. Macleod, G. Wysocki. Hollow waveguide photomixing for quantum cascade laser heterodyne spectro-radiometry, Optics Express, 2011, 19 (10): 9074-9085.

[47] T. Stangier, G. Sonnabend, M. Sornig. Compact Setup of a Tunable Heterodyne Spectrometer for Infrared Observations of Atmospheric Trace-Gases, Remote Sensing, 2013, 5 (7): 3397-3414.

[48] A. Hoffmann, N. A. Macleod, M. Huebner, D. Weidmann. Thermal infrared laser heterodyne spectroradiometry for solar occultation atmospheric CO_2 measurements, Atmospheric Measurement Techniques, 2016, 9 (12): 5975-5996.

[49] D. Weidmann, A. Hoffmann, N. Macleod, K. Middleton, J. Kurtz, S. Barraclough, D. Griffin, The Methane Isotopologues by Solar Occultation (MISO) Nanosatellite Mission: Spectral Channel Optimization and Early Performance Analysis. Remote Sensing, 2017, 9 (10): 1073.

[50] A. YuKlimchuk, Aleksandr, I. Nadezhdinskii, Y. YaPonurovskii, Y. P. Shapovalov, A. V. Rodin. A high-resolution heterodyne spectrometer for near-IR range on the basis of a tunable diode laser, Quantum Electronics, 2012, 42 (3): 244-249.

[51] A. Rodin, A. Klimchuk, A. Nadezhdinskiy, D. Churbanov, M. Spiridonov. High resolution heterodyne spectroscopy of the atmospheric methane NIR absorption, Optics Express, 2014, 22 (11): 13825-13834.

[52] E. L. Wilson, M. L. McLinden, J. H. Miller, G. R. Allan, L. E. Ott, H. R. Melroy, G. B. Clarke. Miniaturized laser heterodyne radiometer for measurements of CO_2 in the atmospheric column, Applied Physics B-Lasers and Optics, 2014, 114 (3): 385-393.

[53] G. B. Clarke, E. L. Wilson, J. H. Miller, H. R. Melroy. Uncertainty analysis for the

miniaturized laser heterodyne radiometer (mini-LHR) for the measurement of carbon dioxide in the atmospheric column, Measurement Science and Technology, 2014, 25 (5): 055204.

[54] P. I. Palmer, E. I. Wilson, G. L. Villanueva, G. Liuzzi, L. Feng, A. J. DiGregorio, J. Mao, L. Ott, B. Duncan. Potential improvements in global carbon flux estimates from a network of laser heterodyne radiometer measurements of column carbon dioxide, Atmospheric Measurement Techniques, 2019,12 (4): 2579-2594.

[55] E . L. Wilson, A. J. DiGregorio, G. Villanueva, C. E. Grunberg, Z. Souders, K. M. Miletti, A. Menendez, M. H. Grunberg, M. A. M. Floyd, J. E. Bleacher, E. S. Euskirchen, C. Edgar, B. J. Caldwell, B. Shiro, K. Binsted. A portable miniaturized laser heterodyne radiometer (mini-LHR) for remote measurements of column CH_4 and CO_2, Applied Physics B-Lasers and Optics, 2019,125 (11): 211.

[56] F. Smith, S. Havemann, A. Hoffmann, W.Bell, D.Weidmann, S.Newman. Evaluation of laser heterodyne radiometry for numerical weather prediction applications, Quarterly Journal of the Royal Meteorological Society, 2018, 144 (715): 1831-1850.

[57] F. Shen. Development of a Laser Heterodyne Radiometer for Atmospheric Remote Sensing, PhD thesis, Université du Littoral Côte d'Opale, France, 2019.

[58] P. Martin-Mateos, O. E. Bonilla-Manrique, C. Gutierrez-Escobero. Wavelength modulation laser heterodyne radiometry, Optics Letters, 2018, 43 (12): 3009-3012.

[59] P. Martin-mateos, A. Genner, H. Moser, B. Lendl. Implementation and characterization of a thermal infrared laser heterodyne radiometer based on a wavelength modulated local oscillator laser, Optics Express, 2019, 27 (11): 15575-15584.

Chapter 1 Theoretical basis of laser heterodyne technique for ground-based remote sensing of atmospheric greenhouse gases

Objective

This chapter is to describe the principle of laser heterodyne detection, atmospheric transmittance simulation, and the data retrieval method for the atmospheric molecular column abundance with the measurement data from the laser heterodyne radiometer (LHR). These three aspects are the basis and important core for the LHR used in the ground-based remote sensing of atmospheric greenhouse gases (GHGs).

Principle of LHR used in the ground-based remote sensing of atmospheric GHG

In a typical laser heterodyne detection system, the solar radiation is combined with the local oscillator (LO) by a beam splitter. And the two beams are superimposed on a photomixer which can output the photocurrent signal (i_{photo}) containing the information of LO, solar radiation and the beat signal between them. Schematic of the principle of laser heterodyne radiometer used in the ground-based remote sensing of atmospheric greenhouse gases is shown in Figure 1.1. In the optical domain, the optical signals are converted into electrical signals. Through the processing (consisting of the separation of AC and DC, RF signal processing module, heterodyne signal extraction module, and LO scanning) to the electronic signals (in electronic domain), the atmospheric molecular transmittance can be obtained. After the processing of each module, the characteristics of the electronic signals will change accordingly. Therefore, in order to better understand and analyze the process, the signal output from each stage are classified as the intermediate frequency (IF) signal, the low frequency (LF) signal, and heterodyne signal, respectively. The atmospheric molecular column can be inversed by retrieval method from the measured atmospheric molecular transmission.

The critical components of an LHR include the LO, the collection module of solar radiation, the photomixer, the RF signal processing module, and the heterodyne signal extraction module. These modules will be described and analyzed in section 1.1. Data retrieval is based on atmospheric transmittance simulation and solving nonlinear equations by mathematical methods. These two contents will be introduced in sections 1.2 and 1.3, respectively.

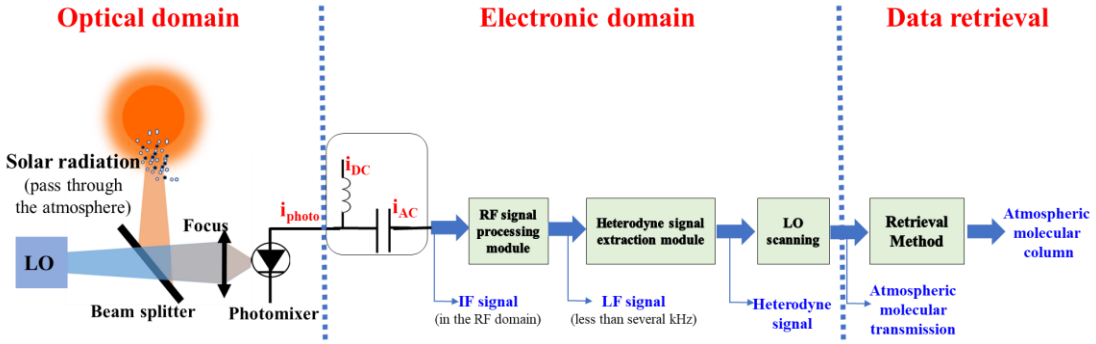

Figure 1.1 Schematic of the principle of laser heterodyne radiometer used in the ground-based remote sensing of atmospheric greenhouse gases; LO: local oscillator; IF: intermediate frequency; LF: low frequency

1.1 Principle of heterodyne detection

The principles of heterodyne detection are explained by J. A. R. Griffith [1] and B. Parvitte [2]. In this section, the principle of the beat of two plane waves is analyzed in the optical domain. Based on the photoelectric conversion principle of photomixer (or photodetector), the IF signal is derived in the electronic domain. This helps understand the IF signal produced by LO and solar radiation, which has complex information of phase, frequency, polarization, et al. Then, the heterodyne receiver will be explained in detail.

1.1.1Two plane waves beating

Any complex wave can be decomposed into plane harmonics waves. Here, two simplest plane harmonic waves are used for the analysis of beat. $\vec{k}_S$ and $\vec{k}_{LO}$ represent the propagation directions of the two plane harmonic waves (signal and LO) in freedom space. Suppose they can be perfectly aligned with the same propagation direction. And they have amplitudes A_S and A_{LO}, angular frequencies ω_S and ω_{LO}, initial phases φ_S and φ_{LO}, linear polarization, respectively. Generally, the photosensitive materials (contained in photodetector) respond to the electric field of electromagnetic waves. So these two plane harmonic waves may be represented by the field $\vec{E}_S$ and $\vec{E}_{LO}$ where:

$$\vec{E}_S = A_S \cos(\vec{k}_S \vec{r} - \omega_S t + \varphi_{S0}) \tag{1.1}$$

$$\vec{E}_{LO} = A_{LO} \cos(\vec{k}_{LO} \vec{r} - \omega_{LO} t + \varphi_{LO0}) \tag{1.2}$$

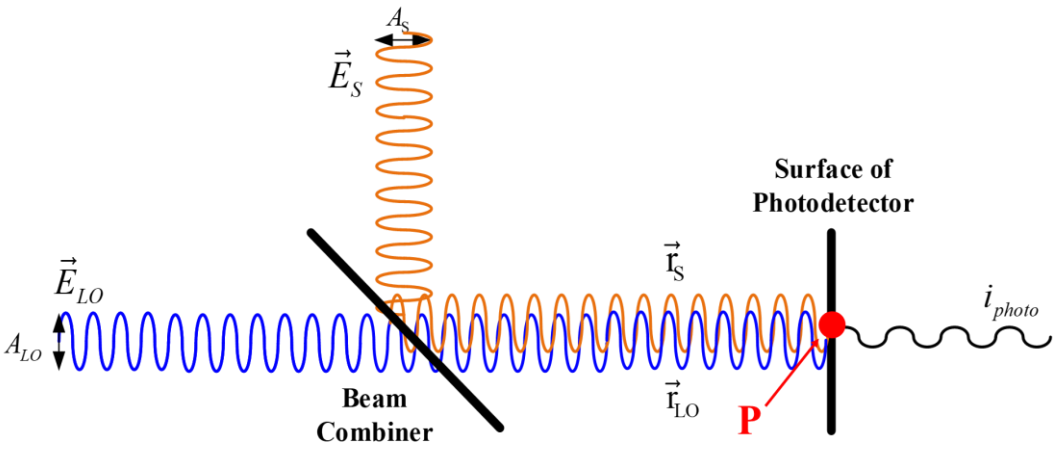

Figure 1.2 Schematic of plane harmonics waves beat principle

Assuming that the phases of two plane waves at point P (on the surface of a photodetector) are φ_S and φ_{LO}, respectively. The electric fields (at point P) of the two plane waves change with time could be expressed as:

$$E_S = A_S \cos(\omega_s t + \varphi_S) \tag{1.3}$$

$$E_{LO} = \mathrm{A_{LO}}\cos(\omega_{\mathrm{LO}}t + \varphi_{\mathrm{LO}}) \tag{1.4}$$

The changing frequency of the electric and magnetic fields of infrared radiation ([780 nm, 1 mm]) is in the range of [300 GHz, 400 THz]. The photodetectors cannot observe the instantaneous value of the change in radiation intensity but can only receive the average value. The average value of the plane wave electric field vector in a period is proportional to the plane wave amplitude A^2, expressed as the following formula:

$$I = \frac{1}{2}\sqrt{\varepsilon/\mu}A^2 \tag{1.5}$$

In the formula, ε is the dielectric constant of the medium, μ is the magnetic permeability in the medium, and $\sqrt{\varepsilon/\mu}$ will be recorded as the proportional coefficient κ. At point P, when the photodetector detects the two plane waves separately to obtain the photocurrent (i_{photo}), which can be expressed as follows:

$$i_{\mathrm{S}} = \alpha \mathrm{K} I_{\mathrm{S}} = \frac{1}{2}\alpha\kappa \mathrm{K} A_{\mathrm{s}}^2 \tag{1.6}$$

$$i_{\mathrm{LO}} = \alpha \mathrm{K} I_{LO} = \frac{1}{2}\alpha\kappa \mathrm{K} A_{LO}^2 \tag{1.7}$$

In the formula, K is the sensitivity of the photodetector, α is the coupling efficiency between the incident light and the photodetector. I_{S} and I_{LD} are the intensity of signal light and LO, respectively. When the signal light and LO reach the point P at the same time, as shown in Figure 1.2, the intensity of the composite wave at point P is:

$$\begin{aligned} I &= (\mathrm{E_S} + \mathrm{E_{LO}})^2 \\ &= \mathrm{A_S}\cos(\omega_s t + \varphi_{\mathrm{S}}) + \mathrm{A_{LO}}\cos(\omega_{\mathrm{LO}} t + \varphi_{\mathrm{LO}})^{\,2} \\ &= I_{\mathrm{s}} + I_{\mathrm{LO}} + 2\sqrt{I_{\mathrm{s}} I_{\mathrm{LO}}}\cos((\omega_{\mathrm{s}} + \omega_{\mathrm{LO}})t + \varphi_{\mathrm{S}} + \varphi_{\mathrm{LO}}) + 2\sqrt{I_{\mathrm{s}} I_{\mathrm{LO}}}\cos((\omega_{\mathrm{s}} - \omega_{\mathrm{LO}})t + \varphi_{\mathrm{S}} - \varphi_{\mathrm{LO}}) \end{aligned} \tag{1.8}$$

The difference frequency or intermediate frequency (IF) component ($\triangle\omega = |\omega_{\mathrm{S}} - \omega_{\mathrm{LO}}|$) is a downward frequency conversion, for example, from the infrared range down to the radio frequency (RF) range if ω_{S} and ω_{LO} are similar in magnitude. A high-speed photodetector with sufficiently high detection speed can respond to the

change of the IF component of the combined light waves. For the sum frequency component ($\omega_S + \omega_{LO}$), since this component changes rapidly, its change period is much shorter than the response time of all photodetectors. Therefore, the response of the sum frequency component is zero. The photocurrent generated by the photodetector at point P for the synthesized light wave can be expressed as:

$$i_p = \alpha K(I_s + I_{LO}) + 2\alpha K\sqrt{I_s I_{LO}}\cos(\triangle\omega t + \triangle\varphi) \tag{1.9}$$

This photocurrent can be divided into the components of DC and AC, denoted as:

$$i_{DC} = \alpha K(I_S + I_{LO} + I_B) \tag{1.10}$$

$$i_{AC} = 2\alpha K\sqrt{I_S I_{LO}}\cos(\triangle\omega t + \triangle\varphi) \tag{1.11}$$

Where I_B is the photocurrent caused by background radiation, based on the above analysis, the following conclusions can be obtained:

1. The DC component can be regarded as the sum of the photocurrent when the LO and signal light are detected independently.
2. The AC component (or IF signal) can indicate the information of intensity, frequency difference, and phase difference of LO and signal light. Only when the electronic bandwidth of a photodetector is larger than $|\omega_S - \omega_{LO}|/2\pi$, the AC component can be detected.
3. Since the magnitude of the photocurrent of the AC component is proportional to the square root of the product of the intensity of LO and signal light when the intensity of signal light is weak, the detection of AC component can be improved by increasing the power of LO.

1.1.2 Photomixer

In order to understand the output signal of the photomixer (photodetector (PD)), we exemplify the principle of a high-speed PD. The schematic diagram of a high-speed PD (Thorlabs, DET08CFC) circuit is shown in Figure 1.3 [3]. The equivalent schematic diagram of PD is inside the dashed box, which is a junction photodiode.

The PD can be equivalent to an ordinary diode, where I_{PD} is the photocurrent, I_D is the dark current, C_J is the junction capacitance, R_{SH} is the shunt resistance, and R_S is the series resistance. This PD is in a reverse-biased state (powered by 5V voltage regulator) and can produce a linear response with applied input light. It works in the photoconductive mode, which reduces the junction capacitance (C_J) in the PD and increases the detection bandwidth ($\Delta f = \frac{1}{(2\pi R_L \times C_J)}$).

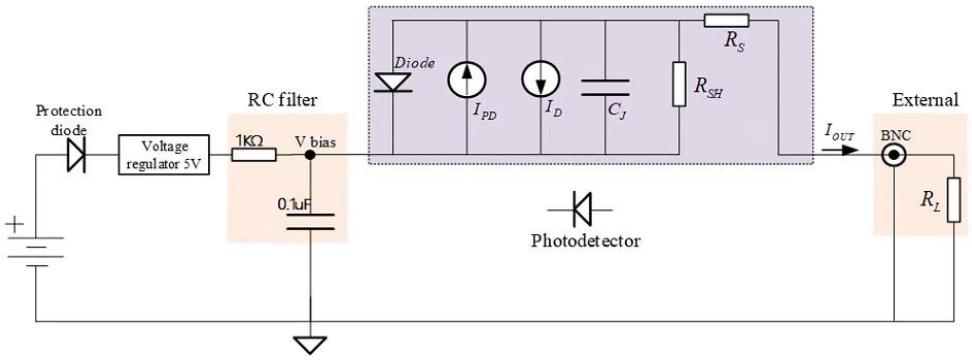

Figure 1.3 Schematic of a high-speed photodetector circuit; The dashed box is the equivalent circuit diagram of PD. I_{PD}: photocurrent, I_D: dark current, C_J: junction capacitance, R_{SH}: shunt resistance, $R_{S:}$ series resistance, $R_{L:}$ Load Resistance.

When signal light and LO incident on the surface of the PD, the output current (I_{OUT}) contains the photocurrent (I_{PD}) and dark current (I_B). The photocurrent is composed of DC and AC components (refer to formula (1.9)). When the dark current is much smaller than the photocurrent, the power of the electrical signal is mostly caused by the AC component. When it is loaded on a load resistance (R_L), the power of the electrical signal can be expressed as:

$$P_{AC} = i_{AC}^2 R_L = 2\alpha^2 K^2 I_S I_{LO} R_L (1+\cos 2(\triangle\omega t + \triangle\varphi)) \tag{1.12}$$

When the average time of detecting the AC component is greater than $\pi/\triangle\omega$, the integral of the AC part is 0, and the above formula can be re-expressed as:

$$P_{AC} = 2\alpha^2 K^2 I_S I_{LO} R_L \tag{1.13}$$

It can be seen that the power of the electronic signal caused by the AC component or IF component is proportional to the intensity of the signal light and LO. The sensitivity (K) of the photodetector, the coupling efficiency (α) between the incident light and the photodetector, and the R_L can influence the amplitude of P_{AC}. In addition, when the dark current is not negligible relative to the photocurrent, the output signal of the PD will have larger background noise

Thermal noise [5] in photomixer is presented as:

$$\left\langle i_J^2 \right\rangle = \frac{4kT_m \cdot \Delta f}{R_m} \tag{1.14}$$

Where the T_m and R_m are the temperatures and the equivalent resistance of a PD. Δf is the bandwidth of the photomixer.

1.1.3 Local oscillator laser beating with solar radiation

Solar radiation is composed of plane waves in infinite states with countless different wavelengths, wave train lengths, phases, polarization states, and various propagation directions. Figure 1.4 shows an understanding of the schematic diagram of LO beat with the solar radiation. Only the solar radiation whose polarization direction and the propagation direction parallel to LO can beat with LO on the PD surface and cause the photocurrent with different frequencies and amplitude.

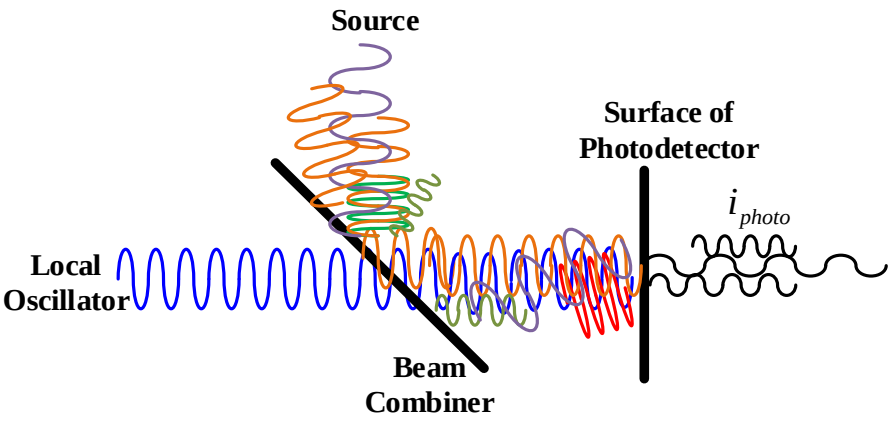

Figure 1.4 Schematic diagram of LO beat with the solar radiation

Assuming that the detection circuit has an ideal rectangular passband, only the IF signal within the passband can be translated from the optical signal to the electrical signal when the two beams of light are beaten. As shown in Figure 1.5, where f_L is the low cutoff frequency of the detection circuit, Δf is the electronic bandwidth, and f_{LO} is the center frequency of LO. The IF signal power is caused by the total power of the optical signal with the frequency distribution in the shadow frequency range. So, this frequency region or electronic bandwidth determines the spectral resolution of the detection.

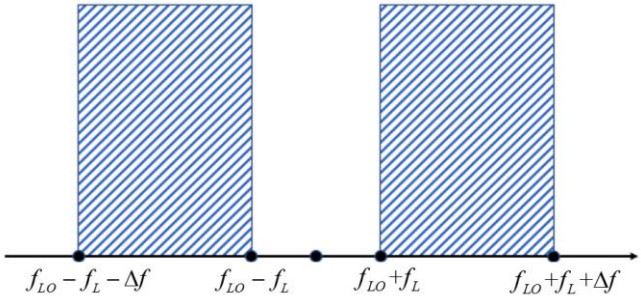

Figure 1.5 Schematic diagram of the frequency distribution of beat signal

1.1.4 Electronic signal processing chain

The next task is to identify the electronic signal converted from the total power of IF signals which distribute in the band of [$f_{LO}-f_L-\Delta f$, $f_{LO}-f_L$] and [$f_{LO}+f_L$, $f_{LO}+f_L+\Delta f$]. PD responds to electrical signals in the radio frequency (RF) domain, so the IF signal (AC component) is also called the RF signal in this paper. In classic laser heterodyne detection, the electrical signals output by a PD will be separated into direct current (i_{DC}) and alternating current (i_{AC}). The DC will be loaded in a DC load resistance (R_{DCL}) and output the DC voltage, indicating the power of LO and solar radiation. The AC signals are in the RF domain, which should be amplified by RF amplifiers, filtered by RF filters, and converted into a low-frequency (LF) signal by a

square-law detector (Schottky diode). This process is called the RF signal processing module, which is shown in Figure 1.6.

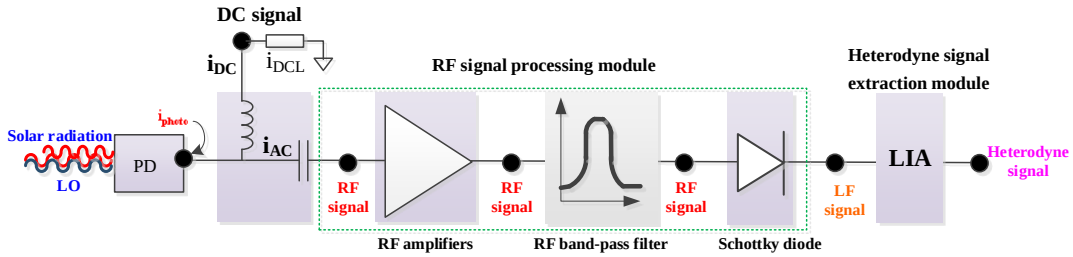

Figure 1.6 Schematic of electronic signal processing chain for heterodyne detection

In the experiment, the amplitude of the LF signal is very small, and more electronic noise is also introduced during the amplification process. Therefore, it is generally necessary to modulate the power of solar radiation and then use a lock-in amplifier to demodulate the low-frequency signal to get the collectible heterodyne signal. When the signal-to-noise ratio is high enough, it is not necessary to modulate the power of the LF signal and directly average the LF signal multiple times to obtain the heterodyne signal as the work[4] of R. Alexander.

1.2 Noise in the heterodyne detection

To process the weaker heterodyne signals to obtain high signal-to-noise ratio (SNR) signals, the noise which is introduced into the heterodyne detection should be understood. The shot noise and thermal noise, the background radiation noise, and the noise from the RF amplifier influence the SNR of heterodyne signals significantly. T. G. Blaney analyzes the noise in heterodyne detection[5] in detail.

1.2.1 Shot noise

The photocurrent passing through the photomixer is used to calculate the shot noise. When the intensity of LO is much greater than the intensity of signal light, the magnitude of this photocurrent mainly depends on the i_{DC}. Due to the generation and

recombination of charge carriers, the noise power will double. Therefore, the mean square of shot noise current $\left\langle i_S^2 \right\rangle$ is expressed [5] as:

$$\left\langle i_S^2 \right\rangle = 4ei_{DC}\Delta f \tag{1.15}$$

Where e is charge. Under the condition of $I_{LO} \gg I_S$ and $I_{LO} \gg I_B$ (where I_{LO} is the intensity of LO, I_S is the intensity of signal light, and I_B is the intensity of background light), the shot noise can be expressed as:

$$\left\langle i_S^2 \right\rangle = \frac{4e^2\eta}{h\nu} I_{LO}\Delta f \tag{1.16}$$

Where η is the quantum efficiency and ν is the photon frequency. In practical applications, when the gain is G, the shot noise is expressed as:

$$\left\langle i_S^2 \right\rangle = \frac{4e^2\eta}{h\nu} I_{LO}G\Delta f \tag{1.17}$$

1.2.2 Thermal noise

Coherent detection thermal noise includes any radiation source within its detection range and will be coherently detected by the receiver. When the signal frequency is within the receiver bandwidth, it will be heterodyne amplified. These radiations may be signals or background, and they will all produce mean square noise currents[5]:

$$\left\langle i_T^2 \right\rangle = \frac{4\eta^2 e^2}{h\nu} \beta I_{LO}\delta_B\Delta f \tag{1.18}$$

Where $\delta_B = \left[\exp\left(\frac{h\nu}{kT_B}\right) - 1\right]^{-1}$ and β (≤ 1) is the coefficient.

1.2.3 Background radiation noise

Noise in the total background radiation $\left\langle i_{BT}^2 \right\rangle$: the radiation frequency is outside the receiver frequency but within the detection bandwidth of the photodetector, then the noise current will be generated. In addition, within the heterodyne receiving bandwidth, radiation outside the solid angle of the receiver can also cause noise

currents. The noise is a complex function of wavelength, total spectral interval, detector area, temperature, and field of view angle. Because these noises are not related to the laser, they will not be amplified by heterodyne and can be ignored when the laser power is large enough.

1.2.4 Noise in radio frequency amplifier

The noise of the RF amplifier can be expressed [5] as:

$$\left\langle i_A^2 \right\rangle = \frac{4kT_A \cdot \Delta f}{MR_A} \tag{1.19}$$

Where T_A and R_A are the noise temperature and input resistance of the RF amplifier; k is Boltzmann's constant (1.3807×10^{-23} J/K); M is the coefficient indicating the impedance mismatch between the mixer and the amplifier (generally $M \leq 1$)

1.3 Features of main components

1.3.1 Antenna characteristics

For a single planar mixing device, to effectively mix the signal light and the LO on the photosensitive surface, it is necessary to keep the wavefronts of the signal light and the LO in phase. When the LO irradiates the mixer (the area is A), only the radiation from the solid angle (Ω) around the normal can be effectively detected. The antenna formula[5] is expressed as:

$$\Omega A = \lambda^2 \tag{1.20}$$

Where λ is the wavelength. Therefore, for a mixer with a mixing area A=1 mm^2, the alignment angle between the signal light and the LO should be better than 0.6° (λ = 10 μm). When the effective photosensitive surface diameter of the mixer is 80 μm, and the detection wavelength is 1.653 μm, the angle at which the signal light and the LO need to be aligned should be better than 1.5°.

1.3.2 Thermal radiation detection

Assuming that a blackbody with a temperature of T_S is full of the field of view of the heterodyne system (considering using a telescope to receive the radiation), the maximum power that can be obtained is given by Siegman:

$$P_{\max} = h\nu\delta_S d\nu \tag{1.21}$$

Where $\delta_S = \left[\exp\left(\frac{h\nu}{kT_S}\right) - 1\right]^{-1}$ and $d\nu = \Delta f$ is the receiving bandwidth. If the area of the telescope's objective lens is A_T and the observed solid angle of the heat source is Ω_S, the received optical power is:

$$P_{rec} = \beta h\nu\delta_S \cdot \Delta f \tag{1.22}$$

Among them, when $\Omega_S \geq \frac{\lambda^2}{A_T}$, β =1. When $\Omega_S < \frac{\lambda^2}{A_T}$, $\beta = \frac{A_T\Omega_S}{\lambda^2}$. Assuming that in the case of full thermal background (T_S>T_B), the field of view of the detection system to the signal source is small ($\Omega_S < \frac{\lambda^2}{A_T}$), the obtained SNR is:

$$S_{vo} = \frac{2\eta\beta\delta_S}{1 + 2\eta\beta\delta_S + 2\eta(1-\beta)\delta_B}\sqrt{\Delta f \cdot \tau} \tag{1.23}$$

1.3.3 Local oscillator

1. Requirements for the local oscillator

In many actual measurement systems, the main noise source (except the noise of the local oscillator) comes from the RF amplifier. To obtain the ultimate performance, the power of the local oscillator should be increased to make $\left\langle i_S^2 \right\rangle + \left\langle i_T^2 \right\rangle \gg \left\langle i_A^2 \right\rangle$. Within the quantum noise limit ($\left\langle i_S^2 \right\rangle \gg \left\langle i_T^2 \right\rangle$), the lowest power of the LO [5] is:

$$I_{LO} > \frac{kT_A \cdot R_\lambda}{eMGR_A} \tag{1.24}$$

Where k = 1.3807×10^{-23}J/K, assuming that M = 0.9, R_λ = 0.8, R_A =50 Ω, T_A=303 K, G = 10^5. Under this condition, the power of the laser should be greater than 4.6 nW.

2. Laser wavelength scanning modes

The laser wavelength scanning mode has an important influence on the instrument line-shape (ILS) function. In order to select a simpler ILS function, the measurement spectrum under the laser wavelength continuous scanning mode and the laser wavelength point-by-point scanning mode was compared. The experimental setup of laser wavelength scanning mode is shown in Figure 1.7. The laser for the measurement of CH_4 is modulated by a FOS. One output of FOS is detected by PD2 for the reference signal of LIA. The other output was collimated and pass through a cell which is full of pure CH_4, then was detected by PD1. The signals form PD1 was demodulated by the LIA. When setting different programs to control the laser output wavelength mode, the absorption spectra in different modes can be collected.

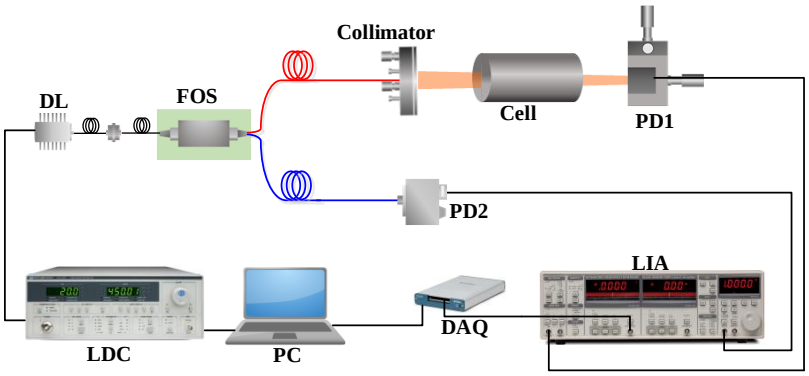

Figure 1.7 Experimental setup of laser wavelength scanning mode; DL: DFB laser (CH_4); FOS: fiber optic switch; LDC: laser diode controller; Cell: the absorption cell is filled with pure methane gas; PD: photodetector; LIA: lock-in amplifier; DAQ: data acquisition card; PC: personal computer.

(1) Continuous scanning mode

In this mode, the laser wavelength was scanned by a continuous triangular wave. The scanning period was set as 10 s, the sampling rate was 1k, and 12000 points were

collected per cycle. The frequency of FOS was set as 125 Hz. The absorption spectra were demodulated under different parameters of LIA shown in Figure 1.8. It can be seen that when the integration time of LIA changes, the shape of the absorption spectra can be changed greatly. When the laser heterodyne absorption spectrum is obtained in this way, it will cause the distortion of the atmospheric absorption spectrum. We can regard this deformation as a component of the ILS function and re-correct it in data processing, but this complicates the ILS function and introduces errors that are likely to occur during correction.

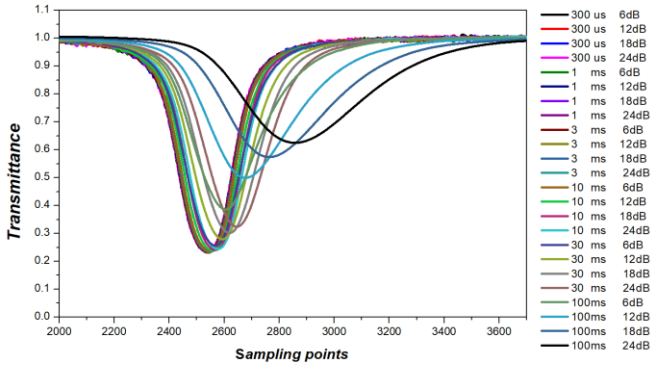

Figure 1.8 Absorption spectra under different parameters in continuous scanning mode

(2) Point-by-point scanning mode

On this condition, the laser wavelength was scanned point-by-point, and the data of absorption spectra were collected one by one. The frequency of FOS was also set as 125 Hz. The absorption spectra were obtained under different parameters of LIA shown in Figure 1.9, which also contains a direct absorption spectral. As you can see that these spectra basically coincide. So with the point-by-point scanning mode, the shape of the absorption spectrum can not be affected by different parameters of LIA. This scanning mode can be used in LHR when the chopper frequency is low.

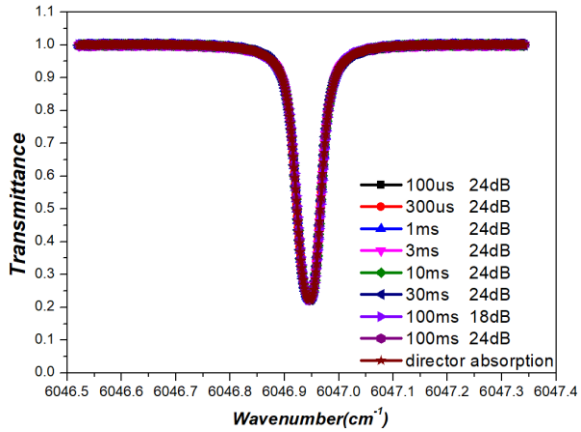

Figure 1.9 Absorption spectra under different parameters in point-by-point scanning mode

In the continuous scanning mode, the entire absorption spectrum will be low-pass filtered in LIA. Different integration time and roll-off settings change the cut-off frequency and the orders of the low-pass filter in LIA, which can impact the shape of the entire spectrum. In the point-by-point scanning mode, the LIA processes the individual heterodyne signal (rectangular wave sequence) corresponding to each laser wavelength. The low-pass filter only affects the shape of the rectangular wave sequence and will not affect the entire absorption spectrum. Therefore, in the experiment, the laser point-by-point scanning method was used to obtain the laser heterodyne absorption spectrum. This simplifies the ILS function of LHR and makes the ILS function mainly depend on the electronic passband of LHR. This also makes the spectral resolution mainly depends on the electronic bandwidth.

1.3.4 Signal light

The signal light source used in heterodyne detection can be equivalent to a blackbody with a specific temperature. The blackbody radiation formula is expressed as follows:

$$B_\lambda = \frac{2hc^2}{\lambda^5\left[\exp\left(\frac{hc}{k\lambda T}\right)-1\right]} \tag{1.25}$$

Where B_λ is the radiant intensity at λ, c is the speed of light of 2.99792×10^8 m/s,

h is the Planck constant of 6.62607004×10^{-34} m^2kg/s, and k is the Boltzmann constant of 1.3806×10^{-23} J/K, T is the absolute temperature of the blackbody.

For ordinary light sources such as thermal light sources and gas-discharge light sources, due to the violent movement of atoms and continuous collisions with each other, the radiation process of the atomic system is easily interrupted, so the light emission is intermittent, and the time interval for each light emission is the time interval for each collision. The direction and initial phase of the electric field vector of multiple radiations generated by each atom or molecule are also irregular. The radiation of an ordinary light source can be regarded as the superposition of light waves with infinite kinds of electric field vectors, and there is no polarization characteristic. Several signal light sources commonly used in experiments include artificial blackbody, carbon-silicon rod, halogen lamp, xenon arc lamp, and so on.

It is generally believed that solar energy comes from the nuclear fusion reaction of hydrogen atoms, and the energy released during the nuclear fusion process is converted into solar radiation energy. The diagram of the sun is shown in Figure 1.10, which can be divided into the sun's interior and the solar atmosphere. Its interior is composed of the core zone, the radiation zone, and the convective zone. The solar atmosphere contains the photosphere, chromosphere, and corona. Most of the electromagnetic energy of the earth comes from the visible region of the photosphere, the sun, with an average temperature of about 5800 K, and the radiation spectrum is a continuous spectrum. Radiant light contains various wavelengths from rays to radio waves. Because of the non-quantized electronic transition, most of the solar energy is stored in the continuous spectrum. The temperature of the sun reaches a minimum (approximately 4000 K) at the height of the layer where the cooler gas is concentrated. These gases can absorb the corresponding electromagnetic radiation so that the emission spectrum of the sun has a spectral structure. Among them, the continuous absorption of visible light and infrared spectrum is produced by the absorption of negative hydrogen ions, which is called the Fraunhofer spectrum.

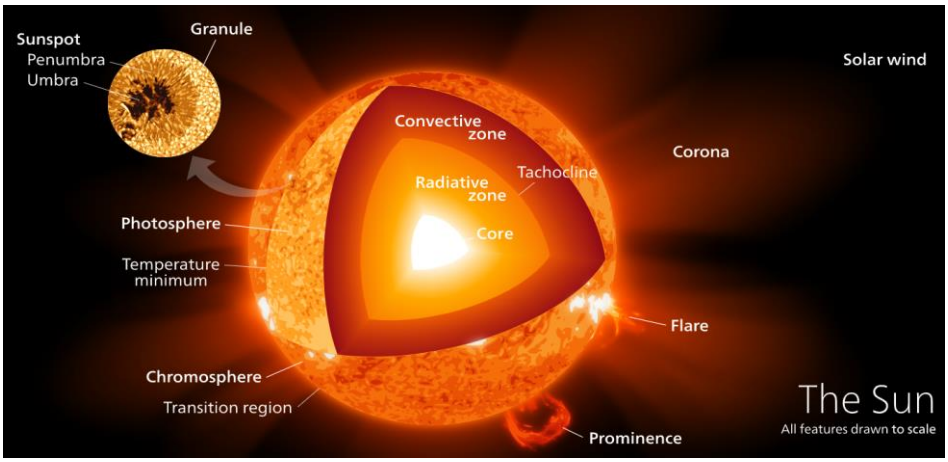

Figure 1.10 Diagram of solar (https://commons.wikimedia.org/wiki/File:Sun_poster.svg)

On the top of the earth's atmosphere, the distribution of solar radiation with wavelength is called the solar spectrum, as shown in the yellow area in Figure 1.11. The black solid line in Figure 1.11 is the simulated blackbody spectrum at a temperature of 5250 K according to the Planck formula. The red area is the solar radiation at sea level. It can be seen that the solar radiation is strongly absorbed by the earth's atmosphere, adding more absorption line structures.

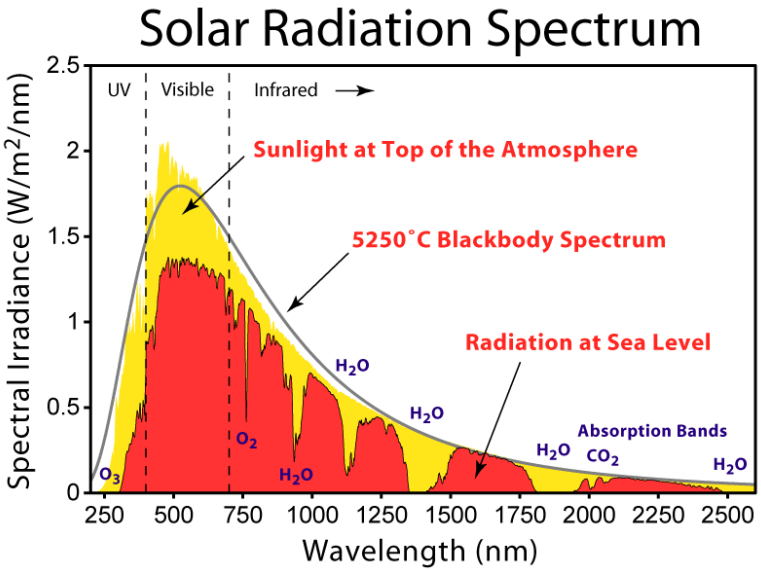

Figure 1.11 Solar radiation spectrum (https://commons.wikimedia.org/wiki/File:Solar_Spectrum.png)

1.3.5 Photomixer characteristics

Photovoltaic detectors are referred to as PV detectors (Photovoltaic) or photodiodes. These devices have the characteristics of low dark current, high-speed response, low electronic noise, and good linearity of photoelectric response. Its working mode can be divided into photovoltaic mode and photoconductive mode. In a photovoltaic way, the applied bias voltage of the PN junction is zero. When light is incident, the generated photocurrent has a linear relationship with the intensity of incident light. In the photoconductive mode, a reverse voltage is applied to the diode, which is beneficial to increase the responsivity of the detector.

1. Spectral sensitivity and quantum efficiency

Spectral sensitivity is the ratio of the photocurrent output by the photodetector to the received optical power at a specific wavelength when the photodetector is in the linear region. It describes the photoelectric conversion efficiency and is a macro parameter. The spectral sensitivity (unit is A/W) can be expressed as follows:

$$R_\lambda = \frac{i}{P_\lambda} \tag{1.26}$$

Quantum efficiency is a microscopic concept. It is defined as the ratio of the number of electrons produced per second to the number of photons incident. The higher the ratio, the better. The conversion relationship between spectral sensitivity and quantum efficiency can be expressed as:

$$\eta = \frac{hc}{e\lambda} R_\lambda \tag{1.27}$$

In the formula, h is Planck's constant, c is the speed of light, λ is the wavelength, and e is the elementary charge.

2. Noise Equivalence Power (NEP)

The output signal of the photodetector contains the photocurrent (I) generated by the useful signal and the noise current (I_N) caused by the background light and detector defects. They all produce power on the load resistance (R_L), and the ratio of the two is defined as the SNR of the photodetector as shown in the following equation:

$$S_{NR} = \frac{I^2 R_L}{I_N^2 R_L} = \frac{I^2}{I_N^2} \tag{1.28}$$

For a single optoelectronic device, the SNR is related to factors such as the incident light power and the light-receiving area. The response to infinitely weak signal light is likely to be submerged in noise. It is impossible to distinguish whether the signal light is received from the output signal. Therefore, the noise equivalent power (unit: W) is used to represent the lower limit of a detector's detection performance. It is defined as the optical signal power when the SNR of a detector output signal is 1, as shown in the following formula:

$$NEP = \Phi\big|_{I=I_N} \tag{1.29}$$

The smaller the noise equivalent power, the more sensitive the device, and the weaker the radiation can be detected. However, the actual detection limit of the device is related to the detection technology. NEP is just a sign of the detection capability of a detector.

The detection degree (D, the unit is W^{-1}) represents the obtainable SNR for per unit radiant power on the detector, which can be expressed as the following formula:

$$D = \frac{1}{NEP} \tag{1.30}$$

3. Other parameters

Other parameters of the photodetector include the area and shape of a photosensitive surface, the shunt resistance and junction capacitance of a photodiode, the applied

voltage and operating temperature required during operation. The photodetector needs to be selected and operated within the specified range of these parameters.

1.3.6 RF signal processing module

The beat signal directly output by the PD is feeble and distributed in the RF band, so low-speed data acquisition cannot collect this signal. Therefore, the beat signal needs to be amplified, filtered, converted, etc., before being collected. Figure 1.12 shows each device's physical diagram and beat signal conversion process in the RF signal processing circuit. The output current signal from the PD can be divided into a DC part (i_{DC}) and an AC (i_{AC}). The DC part is the sum of the PD's responses to signal light and LO. The AC part reflects the beat information. Therefore, a Bais-Tee is used to separate the i_{DC} from the i_{AC}. The i_{DC} is loaded on a 50-ohm resistor welded on the Bais-Tee to generate a DC voltage signal which can be collected directly. The i_{AC} within the response range of the PD is very small and can be affected by laser noise significantly. Therefore, Three RF amplifiers are used to amplify the power of the AC part, and the total magnification is about 10^6 times. Due to the material properties, mechanical properties, laser relaxation properties of the laser, and the noise of the laser driver, the noise power introduced by the laser is much greater than the power of the beat signal within some particular RF bands. Then an RF high pass filter and an RF low pass filter are used to filter out the noise in these bands. On the other hand, these RF filters reduce the measurement bandwidth and improve the spectral resolution of the measurement system. The retained beat signal is converted to a low-frequency signal by a Schottky diode. The low-frequency signal has the same frequency as the chopping frequency, and it will be demodulated by a lock-in amplifier (LIA) with the same reference frequency. The output of LIA is the laser heterodyne signals.

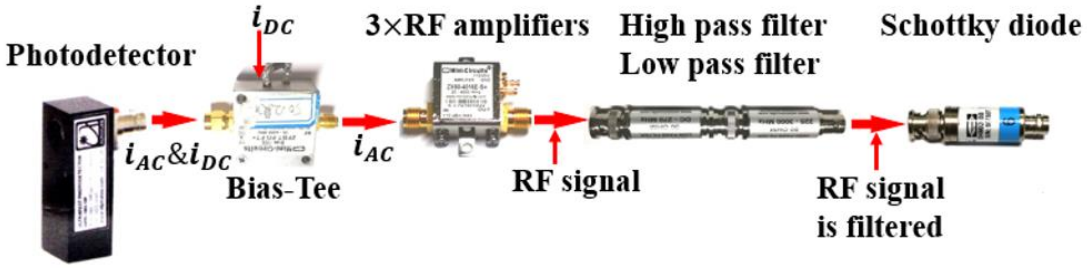

Figure 1.12 Physical diagram of the RF signal processing circuits

1. Bias-tee

The ideal T-type biaser (Bias-tee) can be regarded as composed of ideal capacitors and inductors. The perfect capacitor allows AC signals to pass through but prevents DC bias. The ideal inductance blocks AC signals but allows DC signals to pass. In the experiment, the characteristic impedance of Bias-tee is 50 Ω, the bandwidth is from 0.1 MHz to 4.2 GHz, and the insertion loss is 0.6 dB. The curves of Bise-Tee insertion loss and its isolation with the signal frequency are shown in Figure 1.13 (a) and (b). It can be seen that in the 2 GHz range, this device can effectively separate the DC signal from the AC signal.

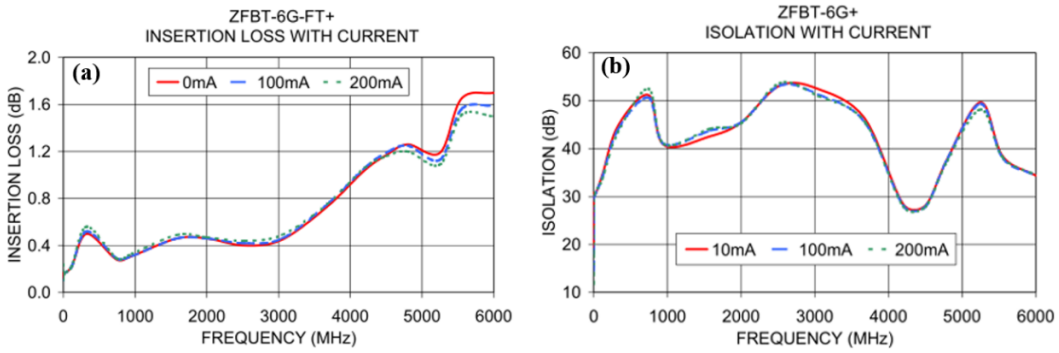

Figure 1.13 (a) Insertion loss changes with signal frequency; (b) Isolation changes with signal frequency

2. RF amplifier and RF filter

Since the phase and polarization state of blackbody radiation are irregular, the power spectrum distribution of the beat signal is similar to the power spectrum distribution of white noise. While amplifying the beat signal, the RF amplifiers amplify the original noise and introduce its noise. An RF amplifier is mainly composed of

resistors, capacitors, and transistors. The noise figure (NF), noise temperature (T), and noise factor (F) can be used to indicate the noise performance of an electronic system, and the relationships between the three are expressed as follows:

$$NF = 10\log F \tag{1.31}$$

$$F = \frac{T}{T_0} + 1 \tag{1.32}$$

where T0 = 290 K. The noise factor of a system composed of n stages can be described as:

$$F = F_1 + \frac{F_2 - 1}{G_1} + \ldots + \frac{F_n - 1}{G_1 \bullet G_2 \ldots G_{n-1}} \tag{1.33}$$

It can be seen that an increase in the temperature of the RF amplifier will lead to a rise in the noise figure, so heat dissipation of the device is required in the experiment. In addition, the first-stage noise factor of the RF amplifier has the most significant impact on the final signal. Therefore, an RF amplifier with a small noise figure should be used as much as possible in the first stage of amplification. In the experiment, the RF amplifiers have an NF of 3.9 dB. The gain curve and noise figure curve of the RF amplifiers are shown in Figure 1.14 (a) and (b), respectively. The gain of the RF amplifier decreases with the increase of frequency, and the noise figure increases with the rise of the frequency, so the RF signal in the lower-frequency band should be used. So, a bandpass filter of 290 MHz ~ 3 GHz was used in the experiment.

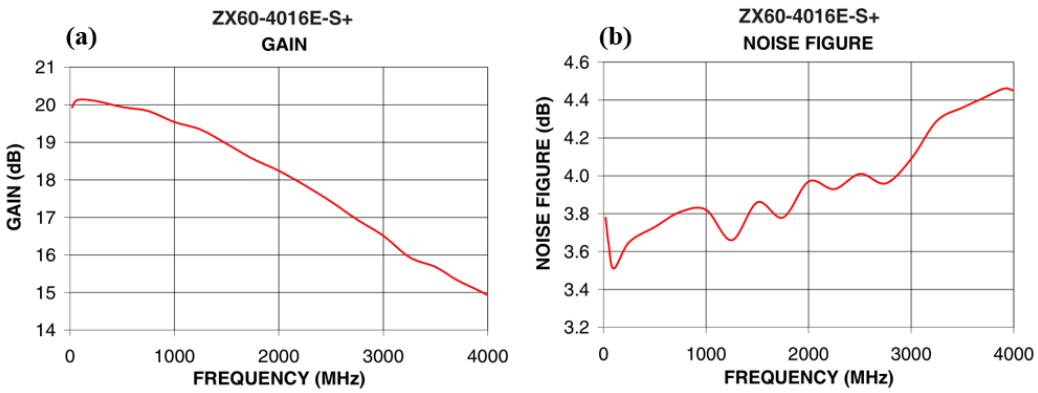

Figure 1.14 (a) Gain curve; (b) Noise figure curve

3. Schottky diode

The Schottky diode is a diode with low turn-on voltage and high-speed switching. The signal conversion schematic diagram is shown in Figure 1.15. DC signals were modulated into the high-frequency signal on the left. After pass through a Shottky diode, the DC signals are recovered.

In the experiment, the Schottky diode is used as a square-law detector for small signals. Its working bandwidth is from 100 kHz to 2 GHz with a sensitivity of 1 mV/μW. Its input signal voltage is from 10 μV to 5 V (corresponding to the input power from -50 dBm to +20 dBm), and it also has an extremely flat frequency response.

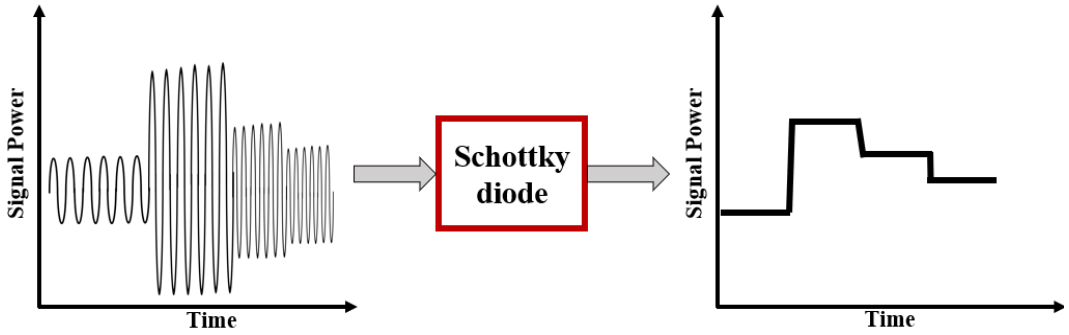

Figure 1.15 Signal conversion schematic of Schottky diode

1.3.7 SNR analysis in laser heterodyne detection chain

1. SNR of the output from the photomixer

In the near-infrared band, the general heterodyne detector is a PIN-type InGaAs photodetector, which works at room temperature. There are four kinds of noises in the photovoltaic detector of the PIN tube: thermal noise, generated-composite noise, shot noise, and 1/f noise. Combining the causes of various noises explained above and the characteristics of heterodyne detection, it is concluded that thermal noise and shot noise are the main influencing factors. Because the beat signal is in the RF range, the other two types of noise are related to the frequency and are relatively small in the RF range and can be ignored. The following analysis is carried out on the two types of noise with greater impact.

Substituting the output current of the photodetector into the expression of shot

noise, the power of shot noise can be obtained as:

$$\begin{aligned} P_{sn} &= i_{SN}^2 R_L \\ &= \sqrt{2e\ i_{AC} + i_{DC} + i_D\ \Delta f}^{\ 2} R_L \\ &= \alpha e R_L \mathrm{K} \Delta f\ \sqrt{I_S I_{\mathrm{LO}}} \cos\ \triangle\omega t + \triangle\varphi\ + 2\ I_S + I_{Lo}\ + i_D \end{aligned} \tag{1.34}$$

Where Δf is the detection bandwidth which is determined by the RF filter bandwidth. The thermal noise power can be calculated within the detection bandwidth at room temperature as:

$$P_{NT} = 4kT\Delta f = (5.5T + 1509)\Delta f \tag{1.35}$$

When a bandwidth of 1 GHz is used for detection, the thermal noise power will be calculated as 1.647×10^{-11} W. According to actual conditions, suppose that the power of signal light is ten pW in the beat frequency bandwidth (ΔB), the intensity of the LO is 3 mW, the photoelectric coupling efficiency is 1, the responsivity K of the photodetector is 1, and the dark current is 1.5 nA in the experiment. Then the power of shot noise is calculated approximately to be:

$$P_{sn} = 0.14\times10^{-15} \cos(\triangle\omega t + \triangle\varphi) + 1.6\times10^{-19} + 4.8\times10^{-11} + 1.224\times10^{-17} \tag{1.36}$$

Under this condition, the shot noise is greater than the thermal noise, but they are in the same order of magnitude.

2. SNR of the output from the RF amplifiers

The SNR (Sp) at the output of the RF amplifier can be expressed as [5]:

$$S_p = \frac{\left\langle i_{AC}^2 \right\rangle}{\left\langle i_S^2 \right\rangle + \left\langle i_T^2 \right\rangle + \left\langle i_{BT}^2 \right\rangle + \left\langle i_J^2 \right\rangle + \left\langle i_A^2 \right\rangle} \tag{1.37}$$

When the power of the local oscillator is large enough, except for shot noise and thermal noise, other noises can be ignored, and the following equation is obtained:

$$S_p = \frac{\eta I_S}{2h\nu\Delta f\,(1 + \eta\beta\delta_B)} \tag{1.38}$$

Within the quantum noise limit ($h\nu \gg kT_B$), the above formula is written as:

$$S_p = \frac{\eta I_S}{h\nu\Delta f} \tag{1.39}$$

3. SNR of the output from LIA

When the passband of the RF amplifier is an ideal rectangular passband, and the bandwidth is f_0 ($f_0 \ll \Delta f$) and $S_p \ll 1$, after the square rate detection of the beat signal, the SNR of the output voltage is:

$$S_{vo} = S_p \frac{1}{\sqrt{2}} \left(\frac{\Delta f}{f_0} \right)^{1/2} \tag{1.40}$$

If the output filter is a first-order RC filter circuit, then $f_0 = 4\tau^{-1}$ where $\tau = RC$, therefore, under the condition of the quantum limit state, the SNR of the output signal of the photoconductive mixer [5] is expressed as:

$$S_{vo} = \frac{\eta I_s}{h\nu\Delta f} \sqrt{2\Delta f \cdot \tau} \tag{1.41}$$

Summary

This chapter mainly introduces the basic theory of laser heterodyne spectroscopy detection technology which provides a theoretical basis for the establishment of laser heterodyne radiometers.

References

[1] J. A. R. Griffith. Laser heterodyne spectroscopy, Philosophical Transactions of the Royal Society a-Mathematical Physical and Engineering Sciences, 1982, 307 (1500): 563-571.

[2] B. Parvitte, V. Zeninari, C. Thiebeaux, A. Delahaigue, A. D.Courtois. Infrared laser heterodyne systems, Spectrochimica Acta Part A, 2004, 60 (5): 1193-1213.

[3] Data sheet of DET08CFC_M.

[4] Rodin, A. Klimchuk, A. Nadezhdinskiy, D. Churbanov, M. Spiridonov. High resolution heterodyne spectroscopy of the atmospheric methane NIR absorption, Optics Express, 2014, 22 (11): 13825-13834.

[5] T. G. Blaney. Signal-to-noise ratio and other characteristics of heterodyne radiation receivers, Space Science Reviews, 1975,17 (5): 691-702.

[6] A. E. Siegman. The antenna properties of optical heterodyne receivers, Applied Optics, 1966, 5(10):1588-1594.

Chapter 2 Proof of concept near-infrared laser heterodyne radiometer (NIR-LHR)

Objective

In this Chapter, the development of a proof of concept near-infrared laser heterodyne radiometer based on two DFB lasers (NIR-LHR) is presented. The developed NIR-LHR was tested in Anhui Institute of Optics and Fine Mechanics, Science island, Hefei, China. Ground-based measurements of CH_4 and CO_2 in the atmospheric column were performed.

2.1 Introduction

Carbon dioxide (CO_2) and methane (CH_4) are key greenhouse gases emitted by human activities, accounting for ~76% and ~16% of total greenhouse gases emissions at the global scale [1]. However, current knowledge about the sources and sinks of both gases is still insufficient for reliable climate predictions. Current space-based observations, though useful for quantification of the sources and sinks on large scales, suffer from limited precision, limited density of observations, and biases related to details of atmospheric scattering properties [2]. Whilst ground-based observations (such as TCCON [3]), usually equipped with Fourier transform spectrometer (Bruker, IFS125HR) with ~0.01 cm^{-1} spectral resolution, can provide column-averaged abundances with high precision and accuracy, however, the shortfalls (such as large dimensions and high cost of maintenance) limit further expansion of the observing network. Over the last decade, portable FTIR spectrometers (Bruker, EM27/SUN) with 0.5/0.2 cm^{-1} spectral resolution, which sacrifices the spectral resolution for portability, have proven to be a promising complement to the ground-based observations [4-6]. With the objective to develop a portable instrument maintained with high spectral resolution (< 0.01 cm^{-1}), a

preliminary setup of a high-resolution laser heterodyne radiometer (LHR) for ground-based atmospheric remote sensing was developed.

Early LHR based applications, employing carbon dioxide (CO2) gas lasers or lead-salt diode lasers as the local oscillators [7-8] for the mid-infrared spectral region, where many important atmospheric species exhibit fundamental rotational-vibrational absorptions. More recently, quantum cascade lasers (QCLs) and inter-band cascade lasers (ICLs) offered more reliable alternatives to traditional local oscillators in the mid-infrared region with the merits of room-temperature, operation wide spectral tuning range, compactness, and robustness. Over the past decade, the QC-LHR and IC-LHR have been successfully developed for atmospheric observations of different species [9-13]. However, limited by the lack of matured fiber optical components or optical waveguides in the mid-infrared spectral region, further integration of the optical module is currently difficult. LHR using telecommunication distributed feedback (DFB) diode lasers as local oscillators operating in the near-infrared spectral region exhibit their unique advantages. Combined with single-mode optical fibers, couplers, and attenuators, the NIR-LHR can be made small, low-power consumption, compact and robust, which make it a promising instrument for ground-based observations [14-18].

In the present work, an all-fibered NIR-LHR is demonstrated in ground-based solar occultation mode. A 1x2 fiber optical switch is employed as an alternative modulator to a traditional chopper, which makes the system more stable and compact. By employing two DFB lasers (1.6 μm and 1.65 μm) as the local oscillators, measurements of column-averaged abundances and mixing ratio in the dry air of atmospheric CO_2 and CH_4 were performed over six months in our laboratory (Hefei, China, 31.9°N 117.16°E). The experimental details, data processing, as well as analysis results and validation through comparison with GOSAT results will be presented and discussed.

2.2 Proof of concept setup of NIR-LHR

The experimental setup of the fibered NIR-LHR is schematically shown in Figure 2.1. Solar radiation containing atmospheric absorption information is captured by a custom-made solar tracker equipped with a fiber collimator (Thorlabs, FC/APC 1550), then chopped by a 1x2 fiber optical switch (Angiltron, CL1x2) for lock-in amplification of the heterodyne signals. One output arm of the optical switch is coupled with a local oscillator centered at ~1.6 μm (DL1, NEL) through a fiber coupler (FC1), and then connected to a high-speed photodetector (PD1, Thorlabs, DET08CFC, 5 GHz) for CH_4 heterodyne detection. The other arm is separated by a 5% : 95% fiber splitter (FS3), where the 5% part is connected to PD (Thorlabs, PDA20CS2) for tracking the solar power and generates the reference signal, while the rest part is coupled with a local oscillator centered at ~1.65 μm (DL2, NEL) through FC2, and then connected to another high-speed photodetector (PD2) for CO_2 heterodyne detection. Before the two laser beams are combined with the solar radiation, 10% of the power of lasers are split by the fiber beam splitters (FS1, FS2) and enters the wavelength meter (WM1, WM2) for the real-time laser wavelength. The beat signals generated from PD1 and PD2 are processed by two Radio frequency (RF) processing modules (RM1 and RM2), where the DC component and AC component (RF signal) are extracted through a bias-Tee (Mini-Circuits) for monitoring local oscillator powers and further RF processing. During RF processing, the RF signals are first amplified by three amplifiers (Mini-Circuits, ZX60), then filtered by a band-pass filter, and finally converted to low-frequency signals by a Schottky diode (HEROTE, DHM020BB) which is demodulated at first harmonic using a lock-in amplifier (Stanford Research Systems, SR830) for the heterodyne signal. The experiment of primary NIR-LHR is shown in Figure 2.2, and the solar tracker is installed on the track mount fixed to the laboratory window.

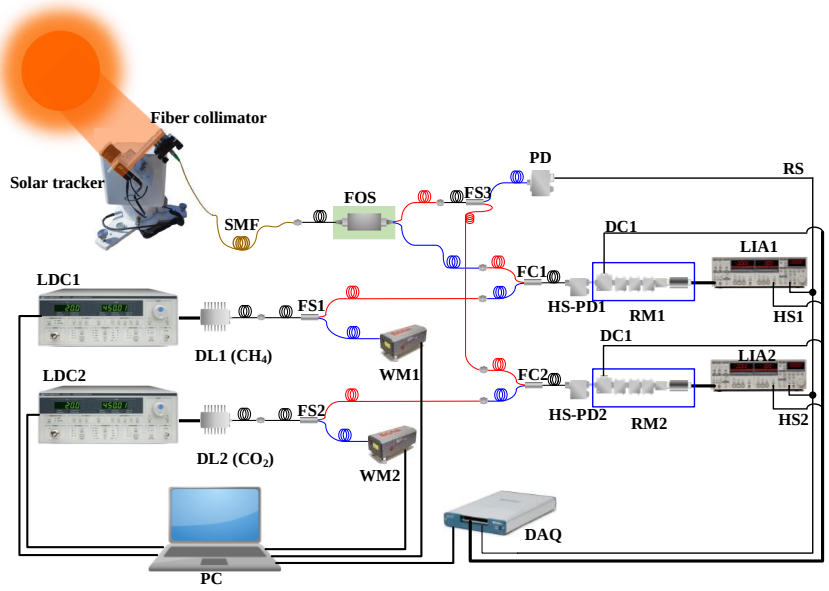

Figure 2.1 Schematic diagram of the measurement system; SMF: single-mode fiber; LDC: laser diode controller; DL: DFB laser; FOS: fiber optic switch; FS: fiber splitter; WM: wavelength meter; FC: fiber coupler; PD: photodetector; HS-PD: high-speed photodetector; RM: radio frequency processing module (it consists of a bias-Tee, three RF amplifiers, RF band-pass filters and a Schottky diode in sequence); DC: DC signal; HS: heterodyne signal; LIA: lock-in amplifier; RS: reference signal; DAQ: data acquisition card; PC: the personal computer

Figure 2.2 Experiment of NIR-LHR

2.3 Key modules involved in NIR-LHR

2.3.1 Collection and modulation of solar radiation

In the solar tracker (shown in Figure 2.3(a)), a camera is used to obtain the image of the sun (Figure 2.3(b)) and is controlled by two stepping motors and a deceleration drive

system to move following the solar. The tracking accuracy can reach 4×10^{-6} rad [19], which is much smaller than the divergence angle of sunlight (9.6×10^{-3} rad). So it can meet the requirements of the laser heterodyne measurement system.

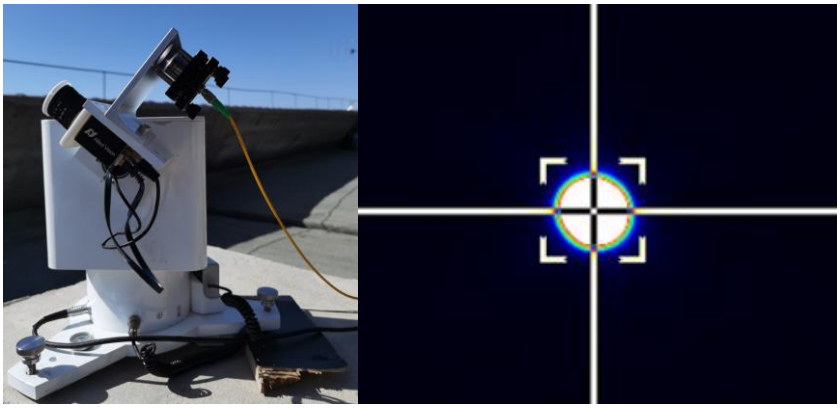

Figure 2.3 (a) Solar tracker in NIR-LHR; (b) Solar image

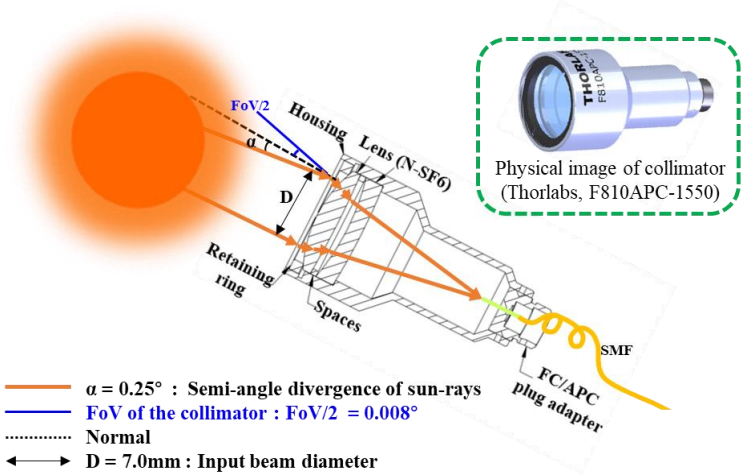

Figure 2.4 Collection principle of solar radiation

The fiber collimator installed on the solar tracker is shown in Figure 2.4. Its material is fused silica with a working wavelength in the range of 1050 nm to 1620 nm. It is resistant to high temperatures and can be exposed to sunlight. This fiber collimator has no moving parts, so it has a compact structure. It has an FC/PC connector and a numerical aperture of 0.24. Its surface reflectance changes with wavelength as shown in Figure 2.5, there is very low reflectivity in the range of 1000 nm to 1600 nm, which is

beneficial for filtering out the sunlight in other bands.

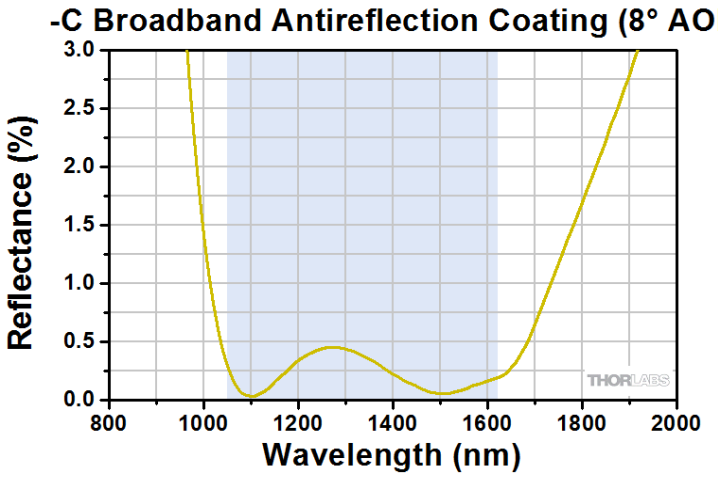

Figure 2.5 Surface reflectance of the fiber collimator changes with wavelength

The collected soler power is transmitted by a single mode fiber (SMF-28-J9,5m) with an interface of FC/APC. In the experiments conducted in Hefei, when there are no clouds in the field of view (0.016°) of the fiber collimator, the collected solar power can vary from 5 μW to 8 μW in the time of day.

Unlike traditional mechanical chopper, a fiber optic switch (Figure 2.6 (a)) capable of high-speed switching is used to modulate the sunlight. It has the advantages of compact structure, low power consumption, long service life, and shock resistance. The FOS is based on the principle of magneto-optical rotation to switch the input sunlight between two output channels. Its best working band is from 1520 nm to 1580 nm. The duty cycle and modulation frequency can be set by the drive circuit of FOS. The duty cycle is usually set as 50:50 and the modulation frequency can be set form 100 Hz to 2000 Hz. The modulated sunlight signals output from the two channels of the FOS are shown in Figure 2.6 (b). It can be seen that the output intensity of the two channels is similar and the modulation ratio can reach more than 90%. The actual output power of each channel is about 310 nW.

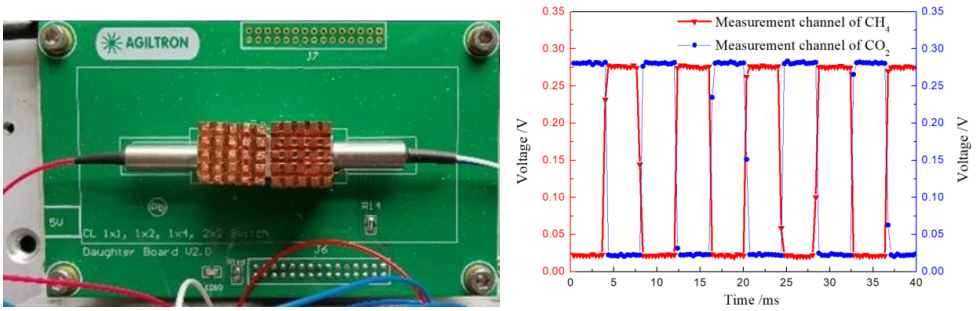

Figure 2.6 (a) Fiber optical switch; (b) sunlight signal modulated by optical switch

2.3.2 Near-infrared DFB laser

The DFB laser used is a 14-pin butterfly package containing a semiconductor laser chip, photodiode monitoring circuit, integrated TEC, and a thermistor. The PID temperature controller controls the temperature components integrated into the package, which can provide accurate temperature measurement and regulation for the chip. Therefore, the driver of this type of laser can be made in small volumes to reduce the size of the LHR device. The model of the DFB laser is: NEL NLK1U5FAAA (1625 nm~1670 nm), and the physical diagram is shown in Figure 2.7. The laser diode controller of model LDC-3724B are used to control the output of DFB lasers.

Figure 2. 7 Physical diagram of DFB lasers

Figure 2.8 High-speed photodetector (DET08CFC)

In the continuous scanning mode, the entire absorption spectrum will be low-pass filtered in LIA. Different integration time and roll-off settings change the cut-off frequency and the orders of low-pass filter in LIA, which can impact on the shape of entire spectrum. In the point-by-point scanning mode, the LIA processes the individual

heterodyne signal (rectangular wave sequence) corresponding to each laser wavelength. The low-pass filter only affects the shape of the rectangular wave sequence, and will not affect the entire absorption spectrum. Therefore, in the experiment, the point-by-point scanning method was used to obtain the laser heterodyne absorption spectrum. This makes the ILS function mainly depend on the electronic passband of LHR and makes the spectral resolution mainly depends on the electronic bandwidth.

2.3.3 Near-infrared photomixer

The high-speed photodetector (HS-PD, shown in Figure 2.8) with a electronic bandwidth of 5 GHz was selected as the heterodyne mixture. Its parameters are shown in table 2.1. Its response sensitivity near 1600 nm is about 1 A/W and it has low noise equivalent power and small dark current. In order to achieve the maximum coupling and matching, the fiber jumper with connectors of FC/APC and FC/PC was used between the fiber combiner and the high-speed photodetector.

Table 2.1 Parameters of DET08CFC

Parameters	**value**
Bandwidth (GHz)	5.0
Spectral Range (nm)	800~1700
Sensitive Area (Dia.μm / mm^2)	80/0.005
Noise Equivalent Power ($W/Hz^{1/2}$)	2×10^{-15}
Dark Current (nA)	1.5
Material	InGaAs

2.3.4 Data acquisition

The software of LabVIEW was used to program the laser wavelength and the acquisition of heterodyne absorption spectrum. The programs and acquisitions for the measurement of CH_4 and CO_2 are similar. For one measurement, the flow chart of the laser heterodyne absorption spectrum acquisition program is shown in Figure 2.9. We set two ranges for the drive currents to the DFB laser. The first range is from I0 to I1, and the current increment interval is i1. The second range is from I2 to I3, and the

current increment interval is i2. After a new diver current is injected into a DFB laser, there is a wait time (t ms) to wait for the laser wavelength to stabilize. After that, the signals of DC signal, heterodyne signal (HS), reference signal (RS) and laser wavelength can be collected and averaged. Next, determine whether the current (I) is greater than the maximum value of the first segment of drive current (I1). If I < I1, the next step is to set a new drive current I = I0 + i1 into the DFB laser and perform the wait, collect, average until I ⩾ I1. Then a new driver current I = I2 + i2 is set to the DFB laser and performs the data acquisition in the second current range. When I ⩾ I3, all averaged data and corresponding currents will be save to obtain a laser heterodyne absorption spectrum.

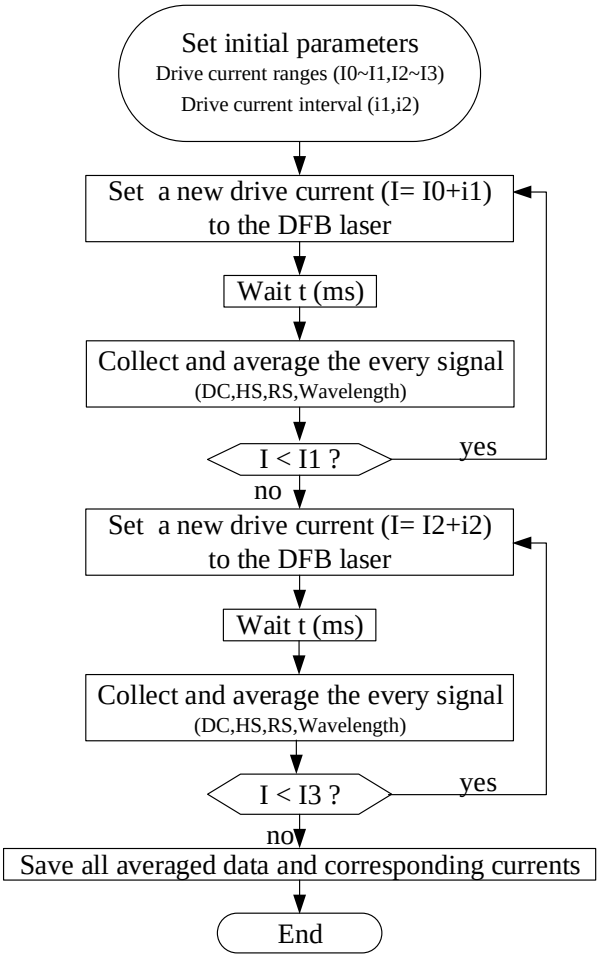

Figure 2.9 Flow chart of the laser heterodyne spectrum acquisition program; DC: DC signal; HS: heterodyne signal; RS: reference signal

2.4 Characteristics of RF signal

We used a spectrum analyzer to measure the spectrum of the RF signals after being amplified on four different input conditions, as shown in Figure 2.10. The curves 1), 2), 3), and 4) in which represent the measured spectrum under four conditions respectively: laser and blackbody (BB) light are input at the same time, the only laser is input, without any light input, only blackbody light is input. From the results, there is a large amount of RF noise in the band from 10 MHz to 200 MHz, and according to analysis, these RF noises mainly come from laser. Comparing the four results, the RF signal caused by the blackbody radiation is minimal. So the RF filters are needed to remove the RF noise below 200 MHz. For example, the frequency band in the red box in the Figure 2.10 can be used by the subsequent circuit.

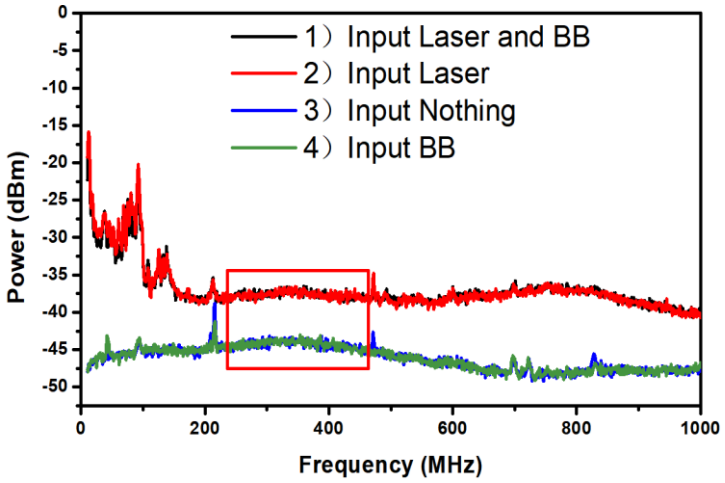

Figure 2.10 RF signal power spectrum

A high-pass RF filter above 290 MHz and a low-pass RF filter below 580 MHz are selected to do further research. Under different drive currents, the frequency spectrums of the RF signals were measured as shown in Figure 2.11. The RF signals increase with the increase of the drive currents. The actual passband of the filter is not consistent with the nominal passband. Figure 2.12 is obtained by calculating the areas of the spectrum curves with the horizontal axis (represent the size of heterodyne

signals) under different driving currents. The areas which can represent the size of beat signals increase with the increase of the driving currents. There is a large background of 0.7 V in the beat signals. When this background is converted, a larger DC bias will be generated.

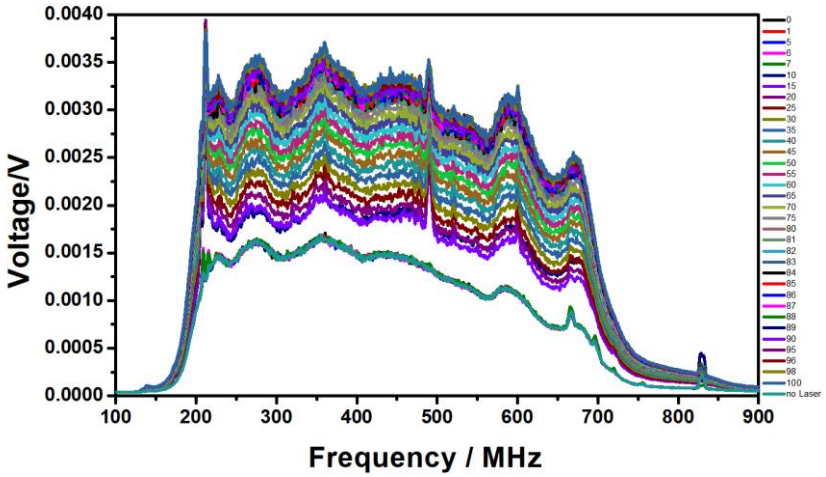

Figure 2.11 Spectrums of beat signals under different drive currents

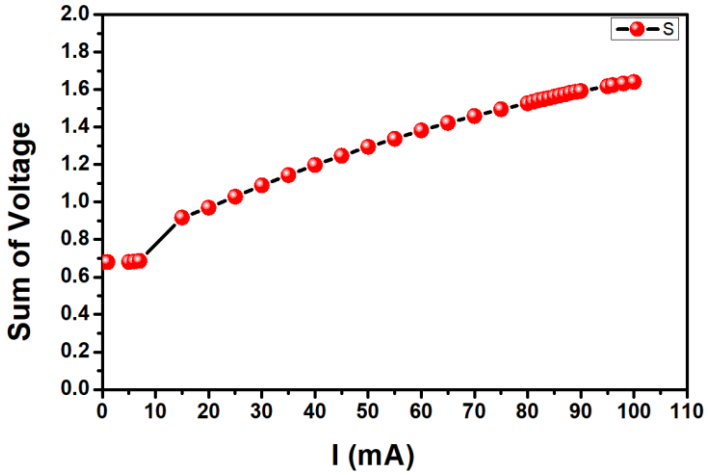

Figure 2.12 Areas of the spectrum curves with the horizontal axis under different driving currents

It can be seen from Figure 2.12 that the power spectrum of the beat signal isn't distributed uniformly. Figure 2.13 shows the spectrum under different filter bandwidths. The energy distributions contained in different bandwidths are different. Figure 2.14 shows the areas that were calculated from the data of Figure 2.13. The blue curve indicates the changes of areas with nominal bandwidths and the green

curve represent the changes of areas with the measured bandwidths. From the blue curve, the signal gradually increases as the bandwidth increases, but there is no strict linear relationship. But from the green curve that there is an obvious linear relationship between the measured bandwidths and the signals. The turning point of the green curve is caused by the uneven distribution of the spectrum signal. Therefore, it should be calculated based on the actually measured beat signal spectrum instead of the nominal bandwidths when determining the instrument function and the instrument's spectral resolution.

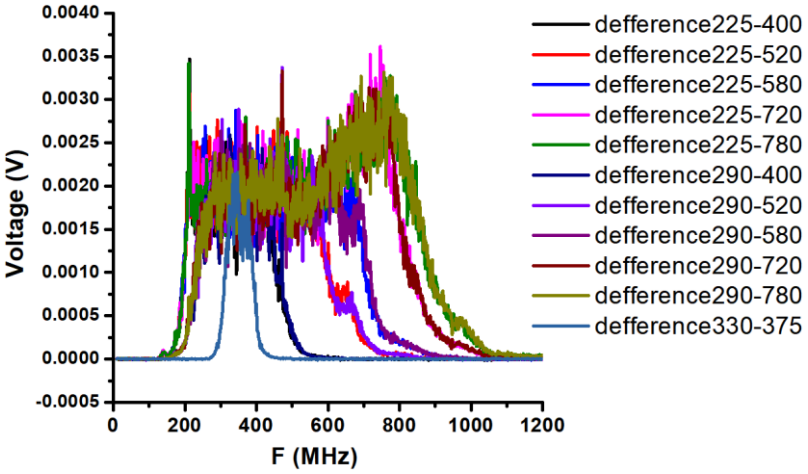

Figure 2.13 Spectrum of beat signals under different filter bandwidths

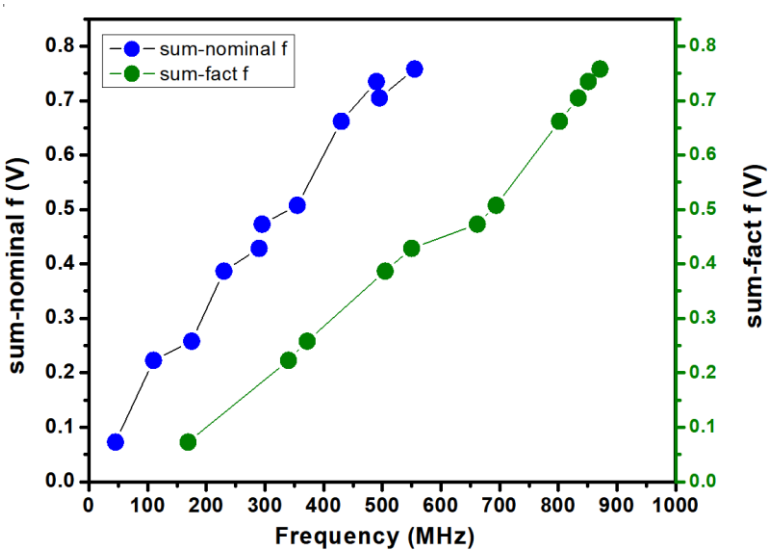

Figure 2.14 Changes of areas with measured bandwidths and nominal bandwidths

2.5 Measurements in laboratory with different resolutions

2.5.1 Measurement with resolution of 0.0073 cm^{-1} and 0.0083 cm^{-1}

When the band-pass filters of [290, 400] MHz (passband ~220 MHz) and [395, 520] MHz (passband ~250 MHz) were used in the system, the ILS functions can be obtained from the spectrum analysis data of RF signals. In particular, a wavelet denoising method was employed in the data processing to avoid introducing additional noises to the data retrieval. In Figure 2.15, (a) and (b) are the ILS functions for measuring CH_4 and CO_2, respectively, and the calculated spectral resolutions are 0.0073 cm^{-1} (CO_2) and 0.0083 cm^{-1} (CH_4).

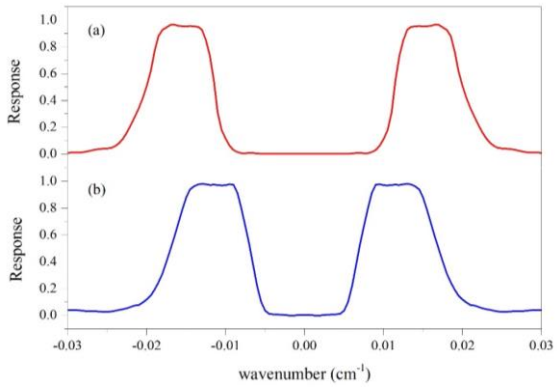

Figure 2.15 The ILS functions, (a) The ILS function for measuring CH_4, (b) The ILS function for measuring CO_2.

Table 2.2 Parameters in the experiments with the resolution of 0.0073 cm^{-1} (CO_2) and 0.0083 cm^{-1}(CH_4)

Parameters	**DFB laser (CH_4)**	**DFB laser(CO_2)**
drive current range (I0~I1)	0 mA ~ 100 mA	
Drive current increased interval (i1)	0.1 mA	
Wait time (t)	300 ms	
Sensitivity, integration time, roll-off of LIA	500 μV, 30 ms, 24 dB	
Sampling frequency	2 kHz	
Number of samples for every averaged signal	1000	

The data acquisition parameters in the experiment with the resolution of 0.0073 cm^{-1} (CO_2) and 0.0083 cm^{-1}(CH_4) are shown in Table 2.2. The corresponding signals

are shown in Figure 2.16, which were measured on April 17, 2019. And one typical scan time is about 4 minutes.

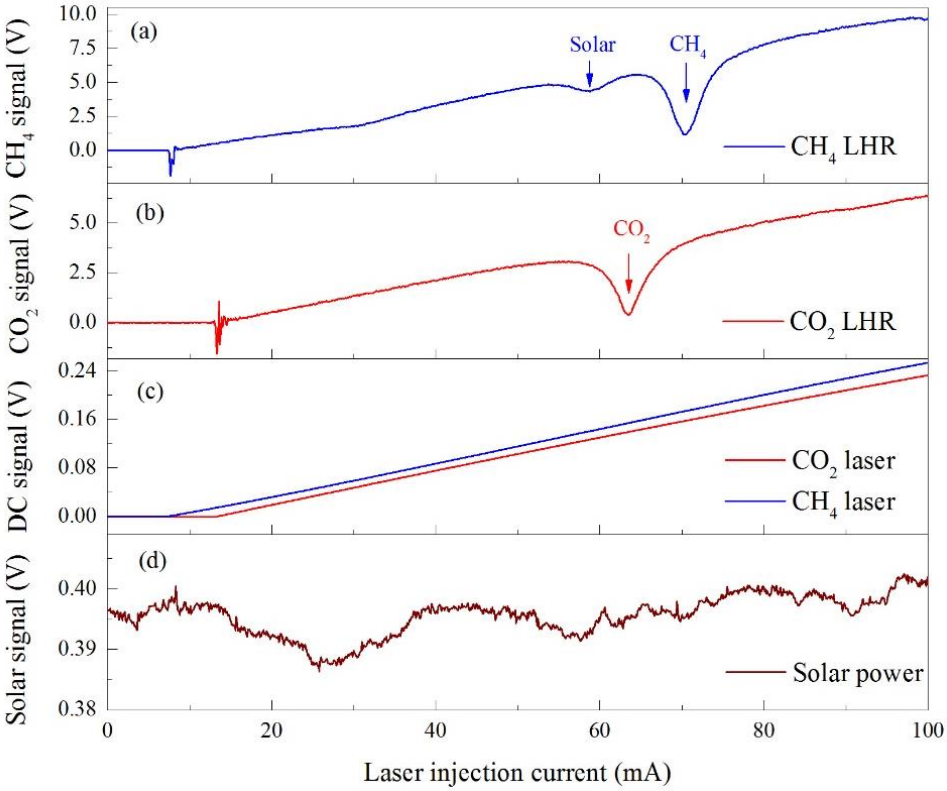

Figure 2.16 Example of raw signals acquired in one scan on April 17, 2019. (a) (b) the CH_4 and CO_2 NIR-LHR signals; (c) DC signals for monitoring the power of the two local oscillators (lasers for CO_2 in red, for CH_4 in blue); (d) Amplitudes of the signals of the solar power.

2.5.2 Measurement with a resolution of 0.00442 cm^{-1}

When the band-pass filters of [330, 375] MHz were used in the system, the actual electronic bandwidth (3 dB bandwidth) of the measurement system is about 66.3 MHz. The ILS functions (shown in Figure 2.17) can be obtained according to the frequency spectrum analysis data. The upper figure is the ILS function of the CH_4 measurement channel, and the other figure is the ILS function of the CO_2 measurement channel. The ordinate is the response amplitude of the system to the RF signal, and the abscissa represents the difference between the radiation frequency in the solar spectrum and the laser with a fixed radiation frequency. The calculated response bandwidth of the system

is about 132.6 MHz, and the spectral resolution is about 0.00442 cm^{-1} for CH_4 and CO_2. The power of the RF signal in this bandwidth is about 0.15 μW, and this power will be changed into low-frequency signals by the Schottky diode.

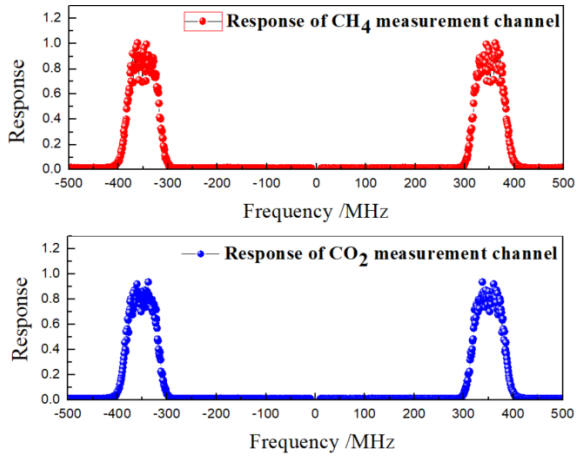

Figure 2.17 The ILS functions for the measurement of CH_4 and CO_2

Table 2.3 Parameters in the experiment with the resolution of 0.00442 cm^{-1}

Parameters	**DFB laser (CH_4)**	**DFB laser(CO_2)**
First drive current range (I0~I1)	0 mA ~ 20 mA	0 mA ~ 20 mA
Drive current increased interval (i1)	0.5 mA	0.5 mA
Second drive current range (I2~I3)	31 mA ~ 110 mA	60 mA ~ 100 mA
Drive current increased interval(i2)	0.1mA	0.1mA
Wait time (t)	300 ms	
Sensitivity, integration time, roll-off of LIA	200 μV, 30 ms, 24 dB	
Sampling frequency	2 kHz	
Number of samples for every averaged signal	1000	

The main experiment parameters are shown in Table 2.3. The data acquisition of the first drive current range was used to detect the background value of the output of LIA. The other range was used to detect the absorption signals. During the experiment, the cumulus cloud's occlusion of sunlight will reduce the heterodyne signal or even reduce it to zero. Therefore, it is necessary to monitor the changes in the intensity of solar radiation to reduce the interference of the cloud. In the process of spectrum collection, the standard that the fluctuation of sunlight intensity does not exceed 10% of

its average value was used to screen out the effective measurement spectrum. Adjust the parameters of LIA according to the power of sunlight to improve the SNR of the heterodyne signals.

Figure 2.18. shows one measurement data for CH_4 and CO_2 in the atmosphere, and the corresponding experiment parameters are in Table 2.3. The measurement data of heterodyne signals of CH_4 and CO_2 in the atmosphere are shown in Figure 2.18 (a) and (b). The corresponding wavenumber data are shown in Figures 2.18 (c) and (d), respectively. The two DFB lasers have wavenumber variations of 0.97 cm^{-1} (CO_2) and 1.83 cm^{-1} (CH_4). When the drive current changes 0.1 mA, the average wavenumber changes about 0.00245 cm^{-1} (CO_2) and 0.00234 cm^{-1} (CH_4), and they are smaller the spectral resolution (0.00442 cm^{-1}).

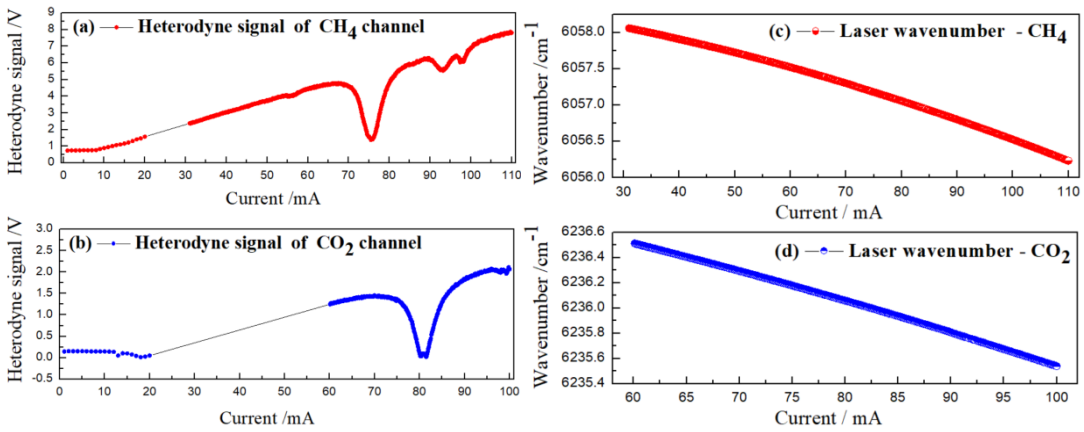

Figure 2.18 One measurement data, (a) the heterodyne signal for the measurement of CH_4 in the atmosphere; (b) the heterodyne signal for the measurement of CO_2 in the atmosphere; (c) laser wavenumber of DFB laser - CH_4; (d) laser wavenumber of DFB laser - CO_2.

Figure 2.18 (a) and (b) show that the measured signal has different background values, which should be subtracted. After normalization and wavelength calibration of the two absorption spectra, the transmittances of CH_4 and CO_2 in the atmosphere were obtained, which are shown in Figures 2.19 (a) and (b).

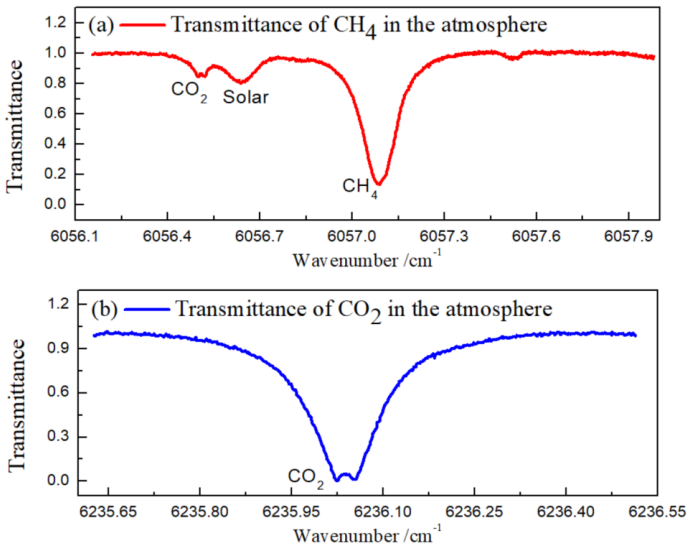

Figure 2.19 (a) The transmittance spectrum of CH_4 in the atmosphere; (b) The transmittance spectrum of CO_2 in the atmosphere.

2.5.3 Comparative and analysis of spectra with different resolutions

It can be seen from Figure 2.16 (b) and Figure 2.18 (b) that when the spectral resolution is higher, a finer spectral structure can be measured. The position of the strongest gas absorption is consistent with the position of the absorption line recorded in the Hitran database. In Figure 2.19 (a), there are three strong methane absorption lines (interval about 0.01 cm^{-1}) on the right side of the strongest methane absorption line (6057.0795 cm^{-1}). Therefore, the methane absorption peak is asymmetric, and the absorption line width is relatively wide. An absorption line (6056.508 cm^{-1}) of CO_2 was also recorded in the transmittance spectrum, showing a double-peak phenomenon. The center position of the solar spectrum (6056.636 cm^{-1}) is the same as the measurement results of the FTS. The SNR of the CH_4 absorption signal in this spectrum is 197, the SNR of the absorption signal at the CO_2 weak absorption line is 35, and the SNR of the solar spectrum is 44.

Due to the relatively low atmospheric pressure in the stratosphere, the true absorption spectrum linewidth of CO_2 in the atmosphere is narrow. When the absorption linewidth is narrower than the bandwidth of the passband filter and is

smaller than the low cut-off frequency, the double peaks will appear in the measurement spectrum, according to the principle of laser heterodyne. Figure 2.19 (b) shows the transmittance of CO_2 (6236.0369 cm^{-1}) with an SNR of 209. And there is a bimodal in it.

In the ILS function, the center distance of the passband is 705 MHz, so the center distance (expressed by $\triangle\upsilon_{ILS}$) of the two frequencies generating the heterodyne signal in the solar radiation is 0.0235 cm^{-1}. From the measured spectrum, the distance between the double peaks (expressed by $\triangle\upsilon_m$) is 0.0275 cm^{-1}. Theoretically, $\triangle\upsilon_m$ should be equal to $\triangle\upsilon_{ILS}$, but they differ by 0.004 cm^{-1}. Compare this deviation with the spectral resolution (0.0044 cm^{-1}). This deviation is within the allowable deviation range of the measurement system. The absorption of CH_4 includes four absorption lines with similar intensities. The distribution range is 0.0474 cm^{-1}, which is wider than $\Delta\upsilon_{ILS}$. Due to the overlap of four absorption lines, there is no bimodal in the transmittance of CH_4.

2.6 Results

2.6.1 Data processing

Before data retrievals, the raw NIR-LHR signals need to be pre-processed, including intensity normalization and wavenumber calibration. For intensity normalization, the offset of the NIR-LHR signal is first subtracted, which equals to the mean value of the NIR-LHR signal before the laser emitting light. Then, the NIR-LHR signal is divided by the DC signal ((a) / $(c)_{blue}$ and (b) / $(c)_{red}$ in Figure 2.16) to normalize the power variations caused by the local oscillator. It should be noted that, if large solar power fluctuations appeared in the scan, the NIR-LHR data would no longer be considered for further analysis.

Since the laser currents are scanned in the point-by-point mode, it is convenient to calibrate the wavenumber by using a wavelength meter (Bristol, 621B). However, the laser wavenumber may slightly change during the measurements (Figure 2.20 (a)).

In order to accurately identify the wavenumber shift, as shown in Figure 2.20 (b), the correlation coefficient of the reference signal (calculated using the forward model) and the real signal is calculated by moving the real signal, where the moving step can be defined as an arbitrarily small length by using interpolation method. Finally, the wavelength shift can be precisely determined by the location of the maximum correlation coefficient (inset of Figure 2.20 (b)). Especially, the proposed correlation method still works at low SNR. After intensity normalization and wavenumber calibration, the processed data is now ready for data retrievals.

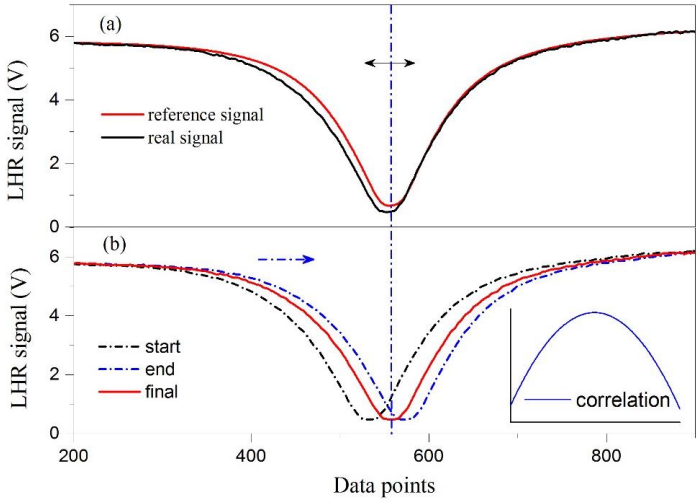

Figure 2.20 Principle of the wavenumber shift identification. (a) Wavenumber shift between the reference signal and real signal; (b) The process of calculating the wavenumber shift, the inset shows the result of correlation coefficients.

2.6.2 Retrieval of X_{CH4} and X_{CO2}

Considering the balance between SNR and spectral resolution, the band-pass filters with [290, 400] MHz and [395, 520] MHz were chosen for the detections of CO_2 and CH_4 in the long-term observation. The two DFB lasers' center wavenumbers are around 6238.78 cm^{-1} (CO_2) and 6046.96 cm^{-1} (CH_4). The data inversion part of the work is mainly completed by G. WANG. The following briefly describes the inversion process to verify the working performance of the measurement system of NIR-LHR.

In order to describe the data retrieval process more clearly, the data acquired on April 17, 2019 are chosen as a representative. The pressure and temperature profiles used for the data retrieval are shown in Figure 2.21, which were obtained from China Meteorological Data Service Center (CMCC), National Centers for Environmental Prediction (NCEP) and the European Centre for Medium-Range Weather Forecasts (ECMWF). Data from 0.2km to 55 km (blue dots) were interpolated from the data of Hefei observation station (NECP), while the data above 55 km (pink dots) were interpolated from the typical zonal mean profiles in April (obtained from ECMWF), and the surface data (red star) were obtained from CMCC. Note that the atmosphere is separated to 45 layers from surface (30 m altitude) to 78 km with an altitude grid of 0.5, 1, 2, 4 and 6 km, separately. For the *a prior* profiles of CO_2 and CH_4, typical mid-latitude daytime profiles were used in the retrieval, while the water vapor profile was interpolated from the upper air data from CMCC. Besides the atmospheric parameters, a solar position calculation program is also compiled to determine the real-time solar zenith angle, and the relative deviation was found to be less than 0.1% by comparison with the NOAA (National Oceanic and Atmospheric Administration) solar calculator.

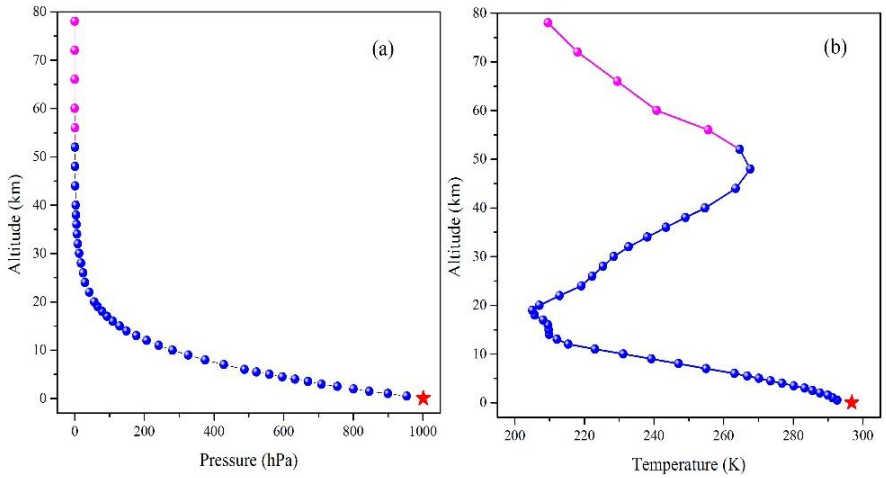

Figure 2.21 Pressure (a) and temperature (b) profiles used for the data retrieval on April 17, 2019, which are interpolated based on the data from CMCC (red star), NDACC (blue dots) and ECMWF (pink dots)

Table 2.4 Definition of the state vector used in the data retrieval

State vector	*a priori*	Error	Description
$x1$ (CH_4)	1	10%	Scale factor of the *a prior* profile for CH_4 retrieval.
$x2$ (CO_2)	1	10%	Scale factor of the *a prior* profile for CO_2 retrieval.
a	a0	100%	Polynomial coefficients of the baseline, where a0, b0,
b	b0	100%	and c0 are calculated by using a second-order
c	c0	100%	polynomial fit of the ratio of the pre-processed
S_1	Sa0	10%	Parameters for describing the Gaussian like solar
S_2	Sb0	10%	spectrum in CH_4 retrieval, where S_1 defines the peak
S_3	Sc0	10%	height, S_2 defines the peak position, S_3 defines the
S_4	Sd0	10%	peak width, and S_4 defines the offset.

The LM iterative process is considered to be converged when $\Delta\chi^2/\chi^2$ < 1E-3 within an upper limit of 20 iterations. In a well-conditioned retrieval, the ultimate cost function (χ^2) should be close to the size of the measurement vector (m). The retrieval results of CO_2 and CH_4 are shown in Figures 2.22 (a), 2.22 (b) and Figures 2.23 (a), 2.23 (b), respectively, where the pre-processed NIR-LHR data, the fitted spectrum, baseline and residuals are presented with an interval of 0.001 cm^{-1}. The iterative processes are shown in the inset of Figures 2.22 (a) and Figures 2.23 (a), where χ^2/m equals to ~1 is obtained after 7 and 6 iterations, respectively. After the iterations, the retrieved CH_4 and CO_2 profiles are calculated by multiplying the retrieved scale factor with relative *a priori* profile. Based on the retrieved CH_4 and CO_2 profiles, the total column abundance of CH_4 and CO_2 is calculated to be ~412.7 ppm (or ~8.2E21 molecules/cm^2) and ~1.886 ppm (or ~3.74E19 molecules/cm^2), respectively. By using the water vapor profile obtained from CMCC, the mixing ratio in dry air (X_{CH4} and X_{CO2}) are calculated to be ~415 ppm and ~1.897 ppm, respectively. For calculating the X_{CH4} and X_{CO2} more accurately, real-time retrieval of NIR-LHR spectrum of the water vapor will be performed in the future.

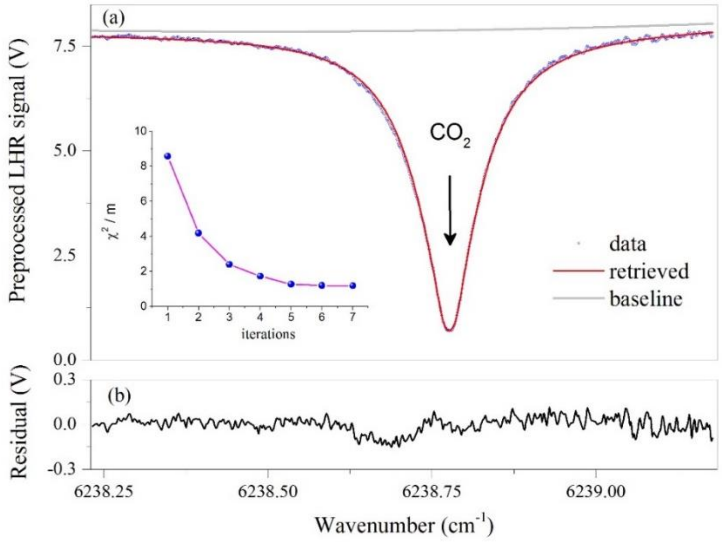

Figure 2.22 Retrieval results of CO_2 on April 17, 2019. (a) Preprocessed (blue dots), baseline (gray line) and fitted (red line) NIR-LHR spectra and the iteration process (inset); (b) the residuals.

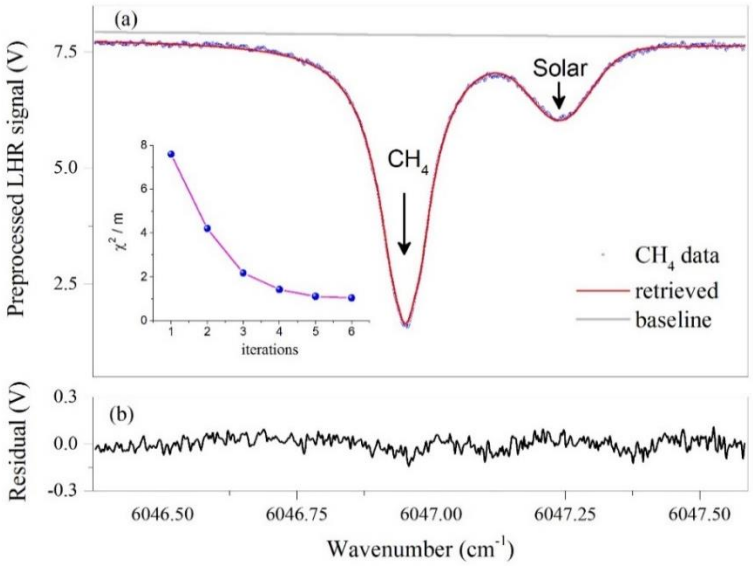

Figure 2.23 Retrieval results of CH_4 on April 17, 2019. (a) Preprocessed (blue dots) and fitted (red line) NIR-LHR spectra, baseline (gray line) and the convergence of the iteration process (inset); (b) the residuals

The consecutive measurement results on April 17, 2019 shown in Figures 2.24 (a) and 2.24 (b) indicate a standard deviation of ~6 ppb (part per billion) for X_{CH4} and ~1 ppm (part per million) for X_{CO2}, respectively. It should be noted that, only the measurement results from 11:00 am to 13:00 pm were analyzed in this study, because the timestamp

of NCEP and CMCC data was 12:00, and the atmospheric parameters were considered stable during this time period. The factors affecting the detection accuracy of the NIR-LHR can be sorted as errors resulted from system noises and retrieval errors. For further improvement of the measurement accuracy, efforts will be focused on improving the signal to noise ratio of the NIR-LHR signals, building appropriate covariance matrices, so as to employing more reasonable *a priori* profiles for the data retrievals.

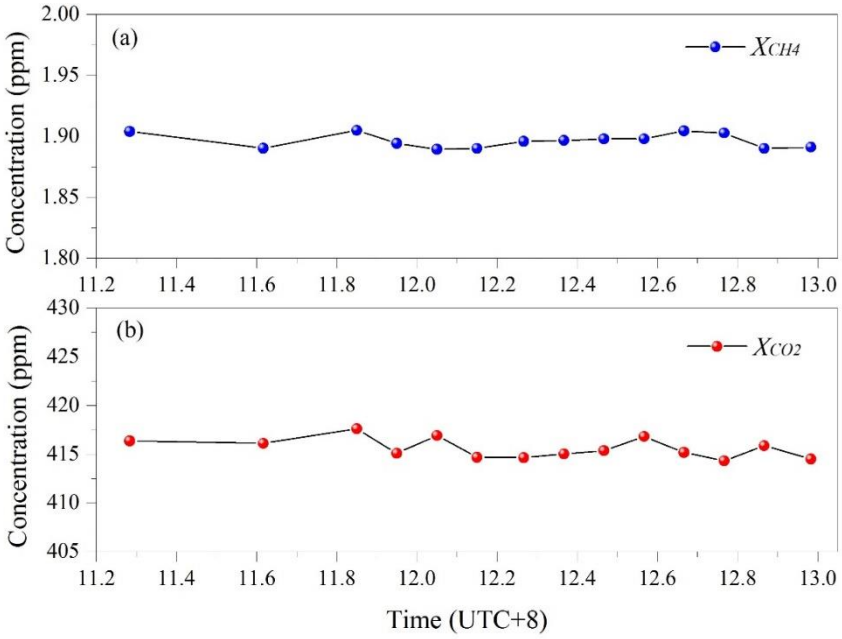

Figure 2.24 Retrieval results of the X_{CH4} and X_{CO2} from 11:00 to 13:00 on April 17, 2019. (a) X_{CH4} results versus time; (b) X_{CO2} results versus time

2.6.3 Validation with GOSAT measurements

In order to evaluate the results of the NIR-LHR, comparisons with GOSAT data were performed in the sunny days during the period from October 2018 to May 2019. Figures 2.25 (a) and 2.25 (b) show the time series of the daily averaged NIR-LHR retrieval results (with standard deviation as the error bar) and GOSAT results of X_{CH4} and X_{CO2}, where the GOSAT results were selected within a 3 degree radius of the observation site (Hefei, China, 31.9°N 117.16°E). The standard deviations are found

to be in the range of [3,17] ppb for X_{CH4} and for [0.7,2.2] ppm for X_{CO2} during the measurements, which correspond to an uncertainty region of 0.15%-0.7% for X_{CH4} and 0.17%-0.5% for X_{CO2}, respectively. As seen from the Figure 2.25 (a), for the measurements of X_{CH4}, there is a bias of ~10 ppb between the NIR-LHR results and GOSAT results, which means that the X_{CH4} is underestimated from the GOSAT measurements. The probable reason may be the existence of methane sources around the observation site. While for the measurements of X_{CO2} (shown in Figure 2.25 (b)), the NIR-LHR results are in good agreement with the GOSAT results. In the future, longer term analysis will be carried out for the study of seasonal and annual variations of atmospheric CO_2 and CH_4.

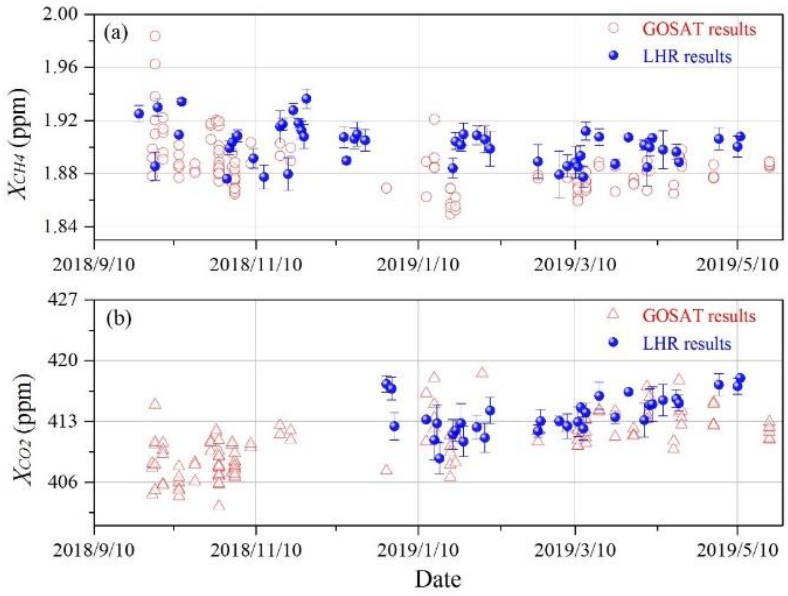

Figure 2.25 Time series of the NIR-LHR data retrieval results and GOSAT results. (a) NIR-LHR results (blue sphere) and GOSAT results (circle) of X_{CH4}; (b) NIR-LHR results (blue sphere) and GOSAT results (up triangle) of X_{CO2}.

Summary

An all fibered NIR-LHR has been developed for operation in ground-based solar occultation mode. A 1x2 fiber optical switch is employed to modulate solar radiation, which makes the system more stable and compact. High resolution NIR-LHR spectra

of atmospheric CO_2 and CH_4 were obtained by employing two DFB lasers (1.6 μm and 1.65 μm) as the local oscillators. After power calibration, the wavenumbers were precisely calibrated using a correlation correction method. Subsequently, an OEM and RFM based retrieval algorithm was developed for retrieval of the vertical profiles, column-averaged abundances and mixing ratios in dry air of atmospheric CO_2 and CH_4. Finally, the long term NIR-LHR results were validated by comparing the GOSAT results during the same time period, which indicates a uncertainty region of 0.15%-0.7% for X_{CH4} and 0.17%-0.5% for X_{CO2}, respectively. The NIR-LHR demonstrated in this manuscript has great potential to be a portable and high spectral resolution instrument for atmospheric multi-component gases sensing.

References

[1] Edenhofer O, Pichs-Madruga R, Sokona Y, Farahani E, Kadner S, Seyboth K, Adler A, Baum I, Brunner S, Eickemeier P, Kriemann B, Savolainen J, Schlömer S, von Stechow C, Zwickel T and Minx JC. IPCC, 2014: Climate Change 2014: Mitigation of Climate Change. Contribution of Working Group III to the Fifth Assessment Report of the Intergovernmental Panel on Climate Change. Cambridge University Press, Cambridge, United Kingdom and New York, NY, USA 2015.

[2] Hase F, Frey M, Blumenstock T, Groß J, Kiel M, Kohlhepp R, Mengistu Tsidu G, Schäfer K, Sha MK and Orphal J. Application of portable FTIR spectrometers for detecting greenhouse gas emissions of the major city Berlin. Atmospheric measurement techniques, 2015, 8(7): 3059–68.

[3] Wunch D, Toon GC, Blavier J-FL, Washenfelder RA, Notholt J, Connor BJ, et al. The Total Carbon Column Observing Network. Philosophical Transactions of the Royal Society A: Mathematical, Physical and Engineering Sciences, 2011, 369 (1943): 2087–112.

[4] Frey M, Hase F, Blumenstock T, Groß J, Kiel M, Mengistu Tsidu G, Schäfer K, Sha MK, and Orphal J. Calibration and instrumental line shape characterization of a set of portable FTIR spectrometers for detecting greenhouse gas emissions. measurement science and technology, 2015, 8 (7): 3047–57.

[5] Gisi M, Hase F, Dohe S, Blumenstock T, Simon A and Keens A. XCO2-measurements with a tabletop FTS using solar absorption spectroscopy. measurement science and technology, 2012, 5 (11): 2969–80.

[6] Tian Y, Sun Y, Liu C, Xie P, Chan K, Xu J, Wang W and Liu C. Characterization of urban CO_2 column abundance with a portable low resolution spectrometer (PLRS): Comparisons with GOSAT and GEOS-Chem model data. Science of The Total Environment, 2018, 612:1593–609.

[7] Sonnabend G, Wirtz D, Schmülling F, Schieder R. Tuneable Heterodyne Infrared Spectrometer for atmospheric and astronomical studies. Applied Optics, 2002, 41(15): 2978–84.

[8] Weidmann D, Courtois D. Infrared 7.6-μm lead-salt diode laser heterodyne radiometry of water vapor in a CH_4-air premixed flat flame. Applied Optics 2003, 42 (6):1115–21.

[9] Weidmann D, Reburn WJ, Smith KM. Ground-based prototype quantum cascade laser heterodyne radiometer for atmospheric studies. Review of Scientific Instruments, 2007, 78 (7): 073107.

[10] Weidmann D, Wysocki G. High-resolution broadband (>100 cm^{-1}) infrared heterodyne spectro-radiometry using an external cavity quantum cascade laser. Optics Express, 2008, 17 (1):248–59.

[11] Weidmann D, Perrett BJ, Macleod NA, Jenkins RM. Hollow waveguide photomixing for quantum cascade laser heterodyne spectro-radiometry. Optics Express, 2011, 19 (10):9074–85.

[12] Tsai TR, Rose RA, Weidmann D, Wysocki G. Atmospheric vertical profiles of O3, N_2O, CH_4, CCl_2F_2, and H_2O retrieved from external-cavity quantum-cascade laser heterodyne radiometer measurements. Applied Optics, 2012, 51 (36):8779–92.

[13] Wang J, Wang G, Tan T, Zhu G, Sun C, Cao Z, Chen W and Gao X. Mid-infrared laser heterodyne radiometer (LHR) based on a 353 μm room-temperature interband cascade laser. Optics Express 2019, 27 (7): 9610–9.

[14] Wilson EL, McLinden ML, Miller JH, Allan GR, Ott LE, Melroy HR and Clarke GB. Miniaturized laser heterodyne radiometer for measurements of CO2 in the atmospheric column. Applied Physics B: Lasers and Optics, 2013, 114(3):385–93.

[15] Wilson EL, DiGregorio AJ, Riot VJ, Ammons MS, Bruner WW, Carter D, Mao JP, Ramanathan A, Strahan S E, Oman LD, Hoffman C, and Garner RM. A 4 U laser heterodyne radiometer for methane (CH_4) and carbon dioxide (CO_2) measurements from an occultation-viewing CubeSat. measurement science and technology, 2017, 28 (3): 035902.

[16] Rodin A, Klimchuk A, Nadezhdinskiy A, Churbanov D, Spiridonov M. High resolution heterodyne spectroscopy of the atmospheric methane NIR absorption. Optics Express, 2014, 22 (11):13825–34.

[17] Kurtz J, O'Byrne S. Multiple receivers in a high-resolution near-infrared heterodyne spectrometer. Optics Express, 2016, 24 (21): 23838–48.

[18] Guo X, Zheng F, Li C, Yang X, Li N, Liu S, Wei J, Qiu X and He Q. A portable sensor for in-situ measurement of ammonia based on near-infrared laser absorption spectroscopy, Optics and Lasers in Engineering, 2019,115:243–8.

[19] S.Huang. The design and related data analysis of full band solar spectral radiometer. Hefei. University of Science and technology of China, 2018.

Chapter 3 Integrated portable near-infrared laser heterodyne radiometer (IP-NIR-LHR)

Objective

In this Chapter, for the further development of field experiments, the development of an integrated portable near-infrared laser heterodyne radiometer (IP-NIR-LHR) based on two DFB lasers is presented. Ground-based measurements of CH_4 and CO_2 in the atmospheric column of Dachaidan (in Qinghai province, China.) were performed.

3.1 Introduction

In order to avoid the interference of pollution emissions in urban areas, observation experiments on the atmospheric background are usually carried out in areas with less human activities. A variety of locations, long-term, and high-quality atmospheric observation data are beneficial to studying the Earth's climate change. At present, the Total Carbon Column Observing Network (TCCON) observation network with high-resolution ground-based FTIR as the observation instrument provides a large amount of research data for the observation of CO_2, CH_4, and other atmospheric molecules in the global atmosphere. However, the current observation network is relatively sparse and still lacks a large number of ground-based observations.

For the FTIR, the higher resolution, the larger volume and the higher cost. Bruker's EM27/SUN is a portable FTIR suitable for long-term measurements in remote areas. This device is shown in Figure 3.1 (a). In addition, the LHR is a low-power consumption, small-sized, high-resolution atmospheric remote sensing observation instrument that can be used. Based on the research of the signal in the LHR measurement system, an integrated portable near-infrared laser heterodyne radiometer for the remote sensing of atmospheric CO_2 and CH_4 was developed, which is shown in Figure 3.2 (b). Table 3.1. shows the comparison between the FTIR and IP-NIR-LHR.

The EM27/SUN Series spectrometers provide a very compact and robust design, relatively low weight. They are highly portable and hence ideally suited for long term

measurement campaigns in remote areas with little infrastructure. It can detect lower resolution atmospheric transmittance. However, for absorption spectra with a narrow linewidth of the absorption spectrum, measuring instruments with a high spectral resolution are required. Therefore, there is a strong demand for portable observation instruments with lower cost, low power consumption, and high spectral resolution, which is convenient for long-term multi-site observation of atmospheric background in remote areas.

Table 3.1 Comparison between Bruker FTIR and LHR

Parameters	**IFS 125HR FT-IR**	**EM27/SUN (NIR)**	**IP-NIR-LHR**
Spectral range	10 ~ 50000 cm^{-1}	5000 ~14500 cm^{-1}	Cover 1 ~ 2 cm^{-1}
Spectral resolution	Maximum 0.001 cm^{-1} (30 MHz)	Maximum 0.5 cm^{-1} (15000 MHz)	0.00442 cm^{-1} (126 MHz)
Species	CO_2 CH_4 H_2O NO_2 etc.	CO_2 CH_4	CO_2 CH_4
Main composition	CAM Tracker Optics bench Vacuum pump Computer	EM 27/SUN Computer	Solar Tracker IP-NIR-LHR Computer
Weight	~ 680 kg	~ 25 kg	~ 20 kg
Dimension	0.39×1.71×0.97~ 0.39×5.13×0.97 m	~ 0.62×0.36×0.457 m	~ 0.5×0.4×0.4 m (Without Solar tracker)
Power consumption	~ 2250W	~ 80 W	~120W

Figure 3.1 (a) Device of EM27/SUN; (b) Device of IP-NIR-LHR

3.2 Integrated design

Based on the research in chapter 2, the schematic diagram of the IP-NIR-LHR was designed (shown in Figure 3.2). The fiber structures (consisting of the solar tracker,

fiber collimator, SMF, FOS, FS0, FS1, FC1, FS3, FC3) used for the generation of the heterodyne signal and the reference signal are the same as Figure 2.1. The radio frequency processing module is also the same as the description in chapter 2. In this design, in order to integrate all the control modules into a small box, two laser diode controllers (LDC1, LDC2), two-wavelength meters, and two lock-in amplifiers are needed to be miniaturized.

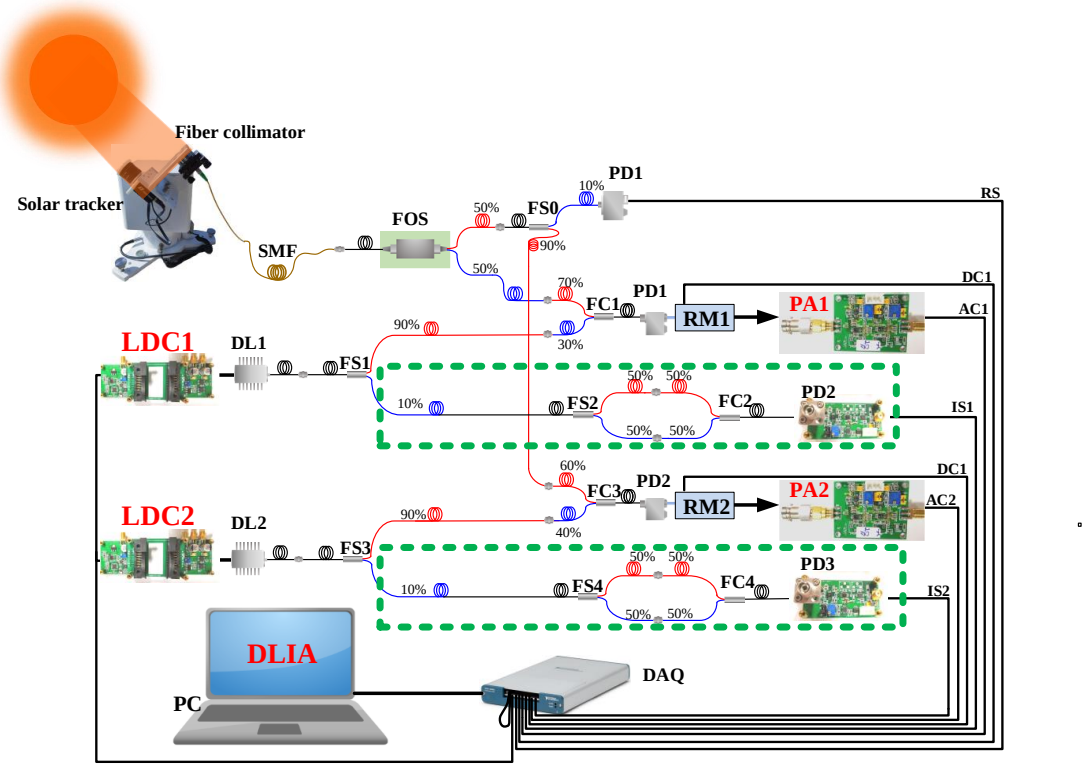

Figure 3.2 Schematic diagram of the IP-NIR-LHR**;** SMF: single-mode fiber; LDC: laser diode controller; DL: DFB laser; FOS: fiber optic switch; FS: fiber splitter; FC: fiber coupler; PD: photodetector; HS-PD: high-speed photodetector; RM: radio frequency processing module; RS: reference signal; DC: DC signal; AC: AC signal; IS: interference signal; DAQ: data acquisition card; PC: the personal computer; DLIA: digital lock-in amplifier. The percentages in the figure are the optical power splitting ratios of the corresponding device

Connect the outputs of the two-beam splitters (FS2, FS4) and the inputs of the two-beam combiners (FC2, FC4), respectively; when the lengths of the two arms are not equal, the interference signals (IS1, IS2) related to the wavelengths of two DFB lasers will be generated in the photodetector (PD2, PD3), which were used to calibrate the wavenumbers. Select the difference in fiber length according to the laser wavelength.

Two preamplifiers (PA1, PA2) were designed to amplify the low-frequency signals from the two Schottky diodes. The outputs signals (AC1, AC2) were collected by the data acquisition card and translated to the personal computer. Two digital lock-in amplifiers were programmed in the PC to demodulated the AC1 and AC2. Other signal processing methods and laser scanning modes are the same as those introduced in Chapter 2. The data in laser heterodyne absorption spectrum was collected point by point.

The integrated box (shown in Figure 3.3) was divided into two layers. The lower layer was equipped with power converters, optical fiber paths, optical fiber switch, and DAQ. The upper layer was equipped with laser drive circuits, DFB lasers, two radio frequency processing modules, two preamplifiers, and power modules, etc. The outputs of the optical fiber were connected to the corresponding photodetectors on the upper layer. Each module will be described in detail below.

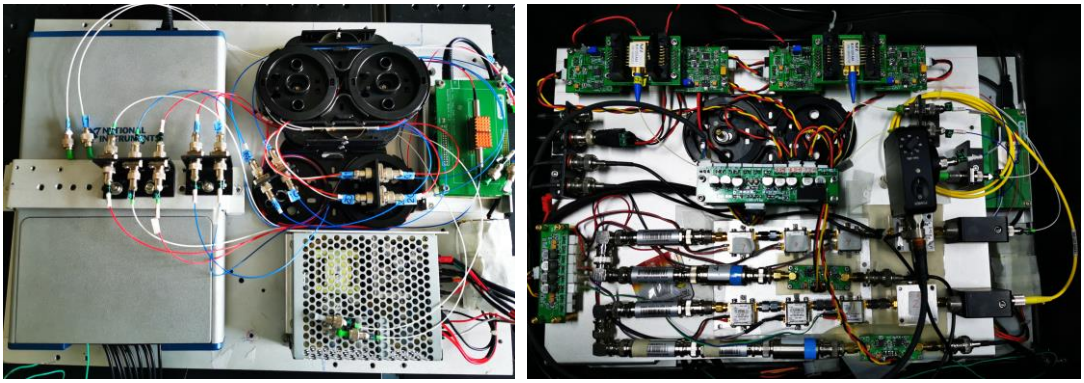

Figure 3.3 Internal physical map of IP-NIR-LHR

3.3 Design description of key modules

3.3.1 Design of laser controller

A schematic diagram of the internal composition of the DFB laser is shown in Figure 3.4. Pins 1 and 2 belong to the internal thermistor; pins 4 and 5 are the positive and negative electrodes of the internal photodiode; pins 6 and 7 are the internal thermoelectric controller (TEC). The combination of TEC and thermistor can control the working temperature of the laser diode (LD). Pin 12 is the cathode of the LD, and

pins 11 and 13 are the anode of the LD. Therefore, a temperature control module, a current source control module, and a current source module are designed to control the output of the DFB laser. The connection between these modules and DFB is shown in Figure 3.5.

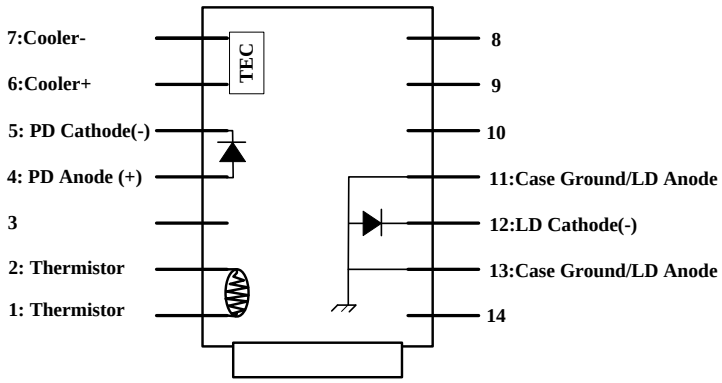

Figure 3.4 Schematic diagram of the internal composition of the DFB laser

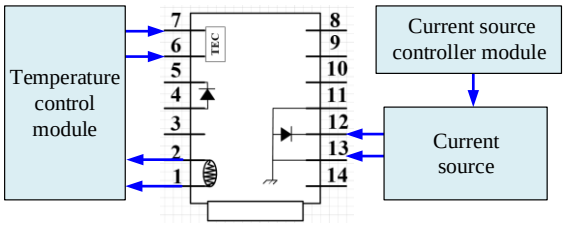

Figure 3.5 Control scheme of DFB laser

In the design, a Howland Current Source (HCS) circuit is used as the current source of the laser diode. Howland proposed the first HCS circuit in 1962 to convert the voltage to current. Due to the influence of voltage compliance, an improved version of HCS was proposed and widely used [1, 2]. The most important requirement in the system is to ensure that the injected current (also called the source current) has a constant amplitude over a wide frequency range, so high output impedance is required. Figure 3.6 is an improved HCS schematic [3]. This circuit includes a negative feedback circuit and a positive feedback circuit to make the output resistance infinite. It is necessary to match the resistances R1, R2, R3, R4, R5, so the output current has nothing to do with the load.

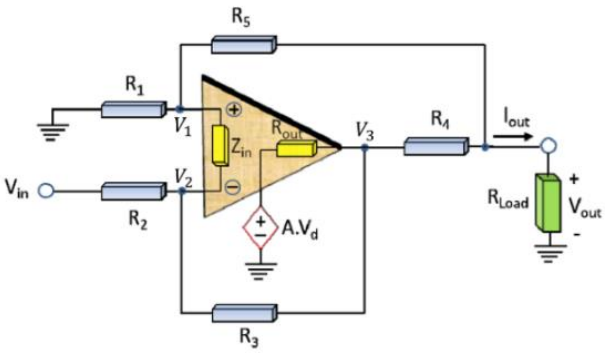

Figure 3.6 Improved HCS schematic

The laser temperature control module was designed based on a TEC power drive chip. When setting the working temperature of the LD, a fixed voltage value (v1) is set through an adjustable resistor. At the same time, the thermistor will also output the voltage (v2) corresponding to the real-time operating temperature of the LD. A comparator circuit is used to compare v1 and v2, and the output signal is input to the TEC power drive chip to control the heating and cooling of the TEC inside the laser. According to the cooling and heating of the TEC, the thermistor's response to the working temperature, and the feedback control of the circuit, the working temperature of the LD is stabilized at the desired value. The physical map of the homemade DFB laser control circuit is shown in Figure 3.7. The current source control module is composed of a personal PC and DAQ card, which will be introduced below.

Figure 3.7 Physical map of homemade DFB laser control circuit

3.3.2 Digital lock-in amplifier (DLIA) and data acquisition

1. Hardware parts

The voltage (AC signal) of the output from the Schottky diode was generally lower than 2 mV and accompanied by a lot of voltage noise and a strong bias that is much

larger than the signal's amplitude. In order to improve the SNR and remove the bias of the AC signal to make a DAQ card can collect it, it should be appropriately filtered and amplified before being collected. So, the preamplifier is designed. Its schematic diagram and PCB diagram are shown in Figure 3.8 and Figure 3.9.

During the spectral scanning, the amplitude and bias of the AC signal will continuously change with the change of laser power. This should be considered when setting the magnification. The AC signal frequency is generally the same as solar radiation's modulated frequency (125 Hz ~ 2000 Hz). This is the passband frequency of the filter circuit.

Firstly, a precision, low-noise, low-input-bias operational amplifier (A1: OPA1177) is used to form a low-pass filter circuit to isolate DC voltage and filter the high frequency noise. This can prevent the saturation in subsequent amplifier circuit. Then, two-stage instrumentation amplifiers (A2, A3: AD8223) are used to amplify the signal. A potentiometer is used to adjust the gain according to the actual signal. The amplification of each stage can reach 200 times. For each level of amplification, the DC bias voltage will also be amplified. Therefore, the amplifiers (A4, A5) are used to fine-tune the output bias voltages of A2 and A3 to make the output bias voltage is around zero volts. This processing makes the AC signal have enough SNR and voltage value to be collected by a DAQ card.

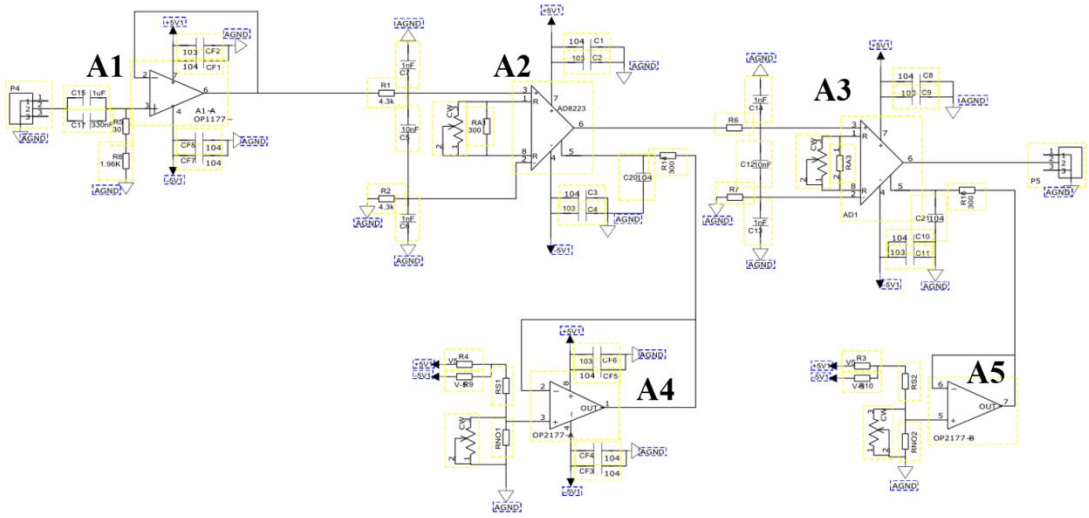

Figure 3.8 Design schematic diagram of the preamplifier

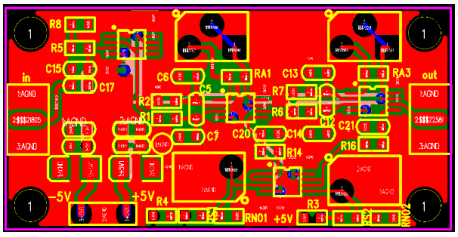

Figure 3.9 PCB diagram of the preamplifier

In the experiment, the preamplifier amplifies the AC signal about 10,000 times, removes the DC offset and most of the high-frequency noise. In the process of spectral scanning, when the laser output power is different, the preamplifier will output signals of different amplitudes shown in Figure 3.10. When different voltages are input to the HCS, the DFB laser outputs different laser power. The greater the input voltage, the greater the output power of the laser. Here the value of voltage is used to express the relative magnitude of laser power. In Figure 3.10, the output of the preamplifier filters out most of the high-frequency noise to make the waveform of the AC signal visible. The AC signal is approximated as a series of square waves signal. When the input voltage is 2.27 V, the AC signal is the smallest, which corresponds to the signal at the absorption peak in the absorption spectrum. When the input voltage is 4.56 V, the laser output wavelength is far away from the gas absorption center, and the amplitude of the square wave signal is larger. When other voltages are input into the HCS, the square wave signals correspond to the signals on the increased side of the absorption spectrum. So as the voltage increases, the amplitude of the square wave signal increases.

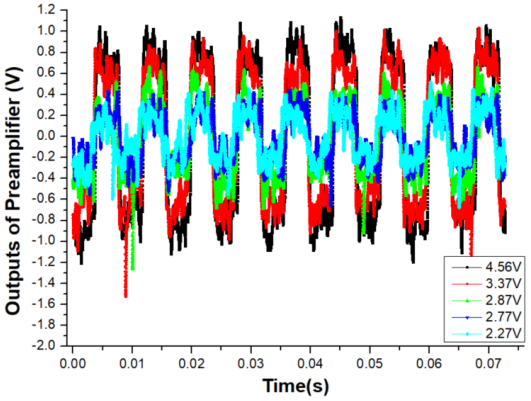

Figure 3.10 Output of the preamplifier under different voltages

2. Software parts

LabVIEW software and DAQ card were combined to collect all data (RS, DC1, DC2, AC1, AC2, IS1, IS2) and program two digital lock-in amplifiers (DLIA), which were used to demodulate the signals of AC1 and AC2 to heterodyne signals in the spectrum. The flow chart of the spectrum signal acquisition and processing program is shown in Figure 3.11 (on the right).

Before the spectrum acquisition, the initial parameters should be set in the software shown in Table 3.2. The output analog voltage of the DAQ card is input to the HCS circuit board to control the drive current of the LD. The drive current of the LD has a linear relationship with the input analog voltage. When the analog voltage changes, the output wavelength and power of the LD change. The analog voltage was set by the software. Because the signal at the absorption peak of an absorption spectrum is the smallest, its corresponding SNR is the lowest, while the baseline part and both sides of the absorption peak have relatively large signal values, and the corresponding SNR is relatively large. Therefore, the collection of an absorption spectrum was divided into three sections, the baseline part 1, the absorption peak part 2, and the baseline part 3, respectively corresponding to V0 ~ V1, V1 ~ V2, V2 ~ V3. The number of p1 and p2 are the spectrum points collected per volt, p1 corresponding to the range of V0 ~ V1, V2 ~ V3, p2 corresponding to V1 ~ V2.

Table 3.2 Initial parameters of IP-NIR-LHR

Parameters	**Values**
Voltage set range V0 ~ V1 ~ V2 ~ V3	-3V ~ 2.5V ~ 3V ~ 5V
Number of spectrum points collected per volt p1,p2 (p1 correspond to V0 ~ V1, V2 ~ V3, p2 correspond to V1 ~ V2)	80, 90
Chopper frequency (Hz), Acquisition rate (kHz)	500, 50
DLIA(phase offset, taps, lowpass frequency)	10, 1700, 0.1
Number of samples to calculate each heterodyne signal n1, n2 (n1 correspond to V0 ~ V1, V2 ~ V3, n2 correspond to V1 ~ V2)	50k, 100k
Range of the data segment to average the output by DLIA s1 ~ e1, s2 ~ e2 (s1 ~ e1 correspond to V0 ~ V1, V2 ~ V3, s2 ~ e2 correspond to V1 ~ V2)	2 k ~ 50 k, 2 k ~ 100 k

In the experiment, the chopper frequency was set as 125 Hz, 250 Hz, 500 Hz, and 1000 Hz, depending on the situation. Generally, it was set as 500 Hz, and the acquisition rate was set as 50 kHz. The flow chart of one of the digital lock-in amplifier (DLIA) principles is shown on the left in Figure 3.11. The input of the DLIA is the AC signal (shown in Figure 3.11). After the seven signals are collected, the reference signal's frequency, phase, and amplitude can be calculated. The amplitude can reflect the solar radiation power. A sine wave and a sine wave with a phase difference of 90° can be generated according to the RS's frequency and phase. After these two signals multiplied with the AC signal, the two results were filtered by two low-pass filters and squared respectively. A heterodyne signal (HS) can be obtained by adding these two squared signals, taking root mean square, and averaging. The collected signals of DC1, DC2, IS1, and IS2 were averaged and got the corresponding average. Input the analog voltage to the HCS circuit board, carry out data acquisition and processing, and cycle point by point. The laser heterodyne absorption spectrum can be got finally. Figure 3.12 shows the software interface

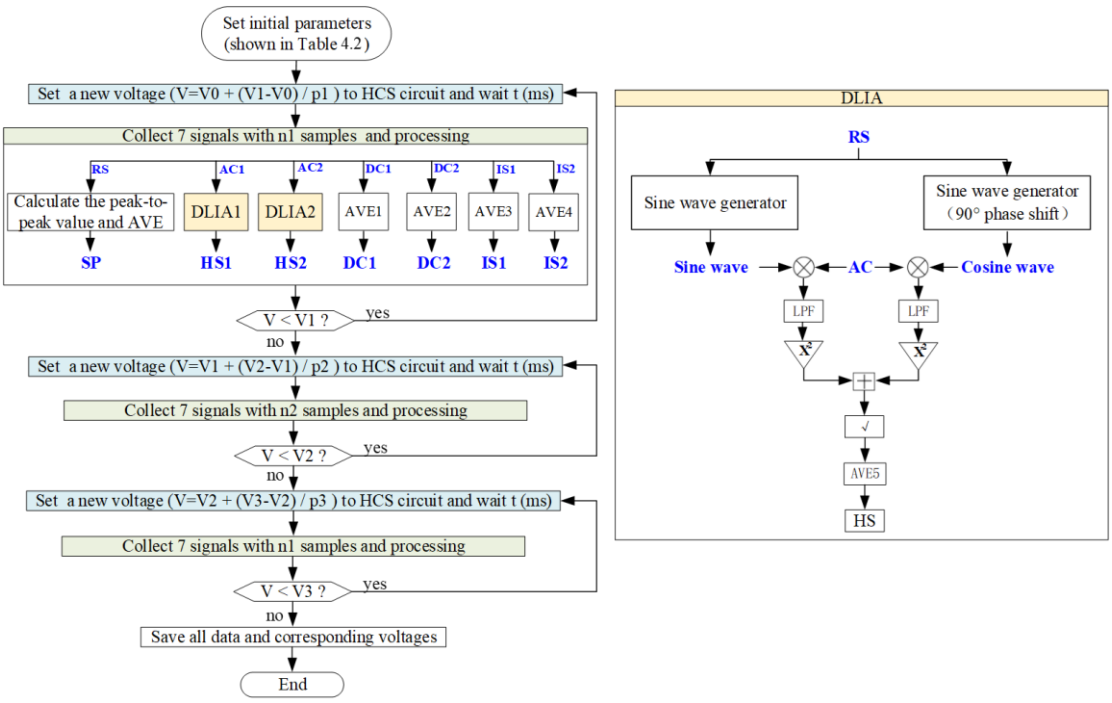

Figure 3.11 Flow chart of the spectrum signal acquisition and processing program (right); flow chart of digital lock-in amplifier (DLIA) principle (left); RS: reference signal of the modulated solar radiation; SP: solar radiation power; AC: AC signal; DC: DC signal; IS: interference signal;

DLIA: digital lock-in amplifier. The initial parameters (V0, V1, V2, V3, p1, p2, n1, n2, etc.) are shown in Table 3.2. AVE: calculate the average of data group; LPF: low-pass filter; X^2: calculate the square of a data group; HS: heterodyne signal

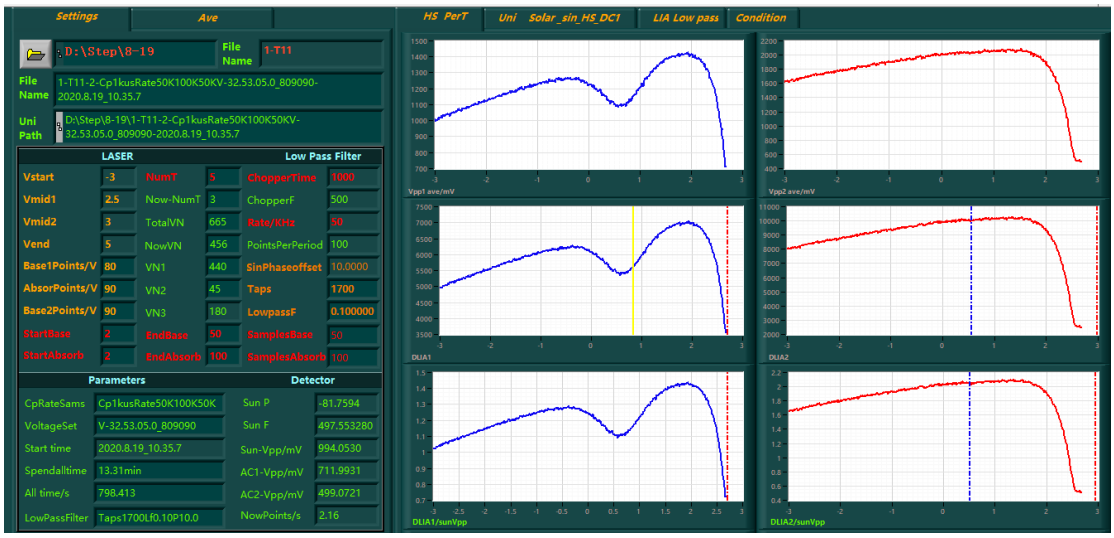

Figure 3.12 Software interface

3.4 Performance

3.4.1 Calibration of laser wavelength

The structure diagram of the optical fiber that generates the laser interference signals is shown in the two green dotted frames in Figure 3.2. Two laser beams of the same wavelength propagating in two optical fibers with different lengths will generate interference signals. Suppose the optical path difference is ΔL, the laser amplitude is A, and the wavelength is λ, the interference signals V_{IF} in the photodetector can be expressed as follows:

$$V_{IF} = \beta \frac{A^2}{2} \cos(2\pi \frac{\Delta L}{\lambda}) \tag{3.1}$$

Supposed that the wavenumber corresponding to the maximum value in a sinewave is k_1, the minimum value is k_2, and the next maximum value is k_3. $k_1 < k_2 < k_3$, then the following equation can be obtained:

$$\begin{cases} \Delta L k_1 = N_1 \\ \Delta L k_2 = N_2 + 0.5 \\ \Delta L k_3 = N_3 \end{cases} \tag{3.2}$$

Among them N_1 N_2 and N_3 are the integer multiples of the optical path difference to the wavelength. The optical path difference can be expressed as:

$$\Delta L = \frac{N_2 - N_1 + 0.5}{k_2 - k_1} = \frac{\Delta N_{21} + 0.5}{\Delta k_{21}} \tag{3.3}$$

ΔN_{21} is an integer and Δk_{21} is the difference between the corresponding wavenumbers at the peaks and troughs of the two interference signals. Record the wavelength data and interference signal measured by the wavelength meter at the same time. The interference signals are shown in Figure 3.13. Evaluate whether the laser wavelength is stable by observing the quality of the interference signal. The calculation of Δk_{21} is shown in Figure 3.14. The average value of the wavenumber difference is 0.01172 cm^{-1}, and the standard deviation is 0.0009 cm^{-1}. Assign ΔN_{21} to 0，1，2，3…… to calculate ΔL. The difference between the lengths of the two arms of the optical fiber splitter is about 0.3 m, with a core refractive index of 1.4682, the estimated value of the optical path difference is 44, Only ΔN_{21} is 0 can the optical path be 42.82, small difference from the estimated value of optical path difference, therefore, it is obtained that ΔN_{21} is 0 and ΔN_{31} is 1 in this optical path difference, and the wavenumber difference corresponding to each two maximum and minimum values in the interference image is 0.011677 cm^{-1}, the wavenumber difference between each two maximum and minimum values in the interference image is 0.011677 cm^{-1}.

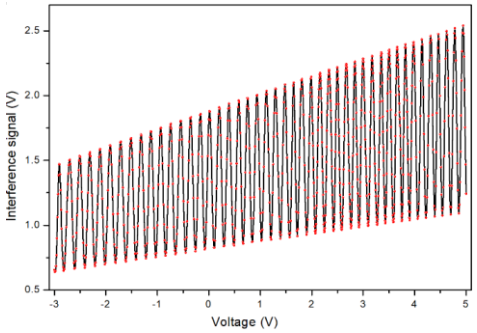

Figure 3.13 Interference signal

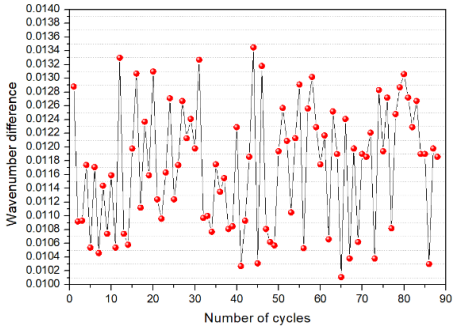

Figure 3.14 Difference between the wavenumber corresponding to the crests and troughs

3.4.2 Performance of DLIA

In order to verify the detection performance of the digital lock-in amplifier (DLIA), the DLIA and the analog lock-in amplifier (SR830, ALIA) are used to extract the heterodyne signal in the heterodyne detection system at the same time. The measurement result is shown in Figure 3.15 and Figure 3.16. It can be seen by comparison that the DLIA designed in this chapter can extract heterodyne signals.

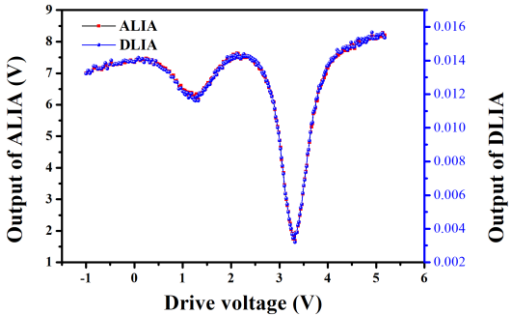

Figure 3.15 Measurement spectrum of CH_4 when ALIA (SR830) and DLIA are used for simultaneous demodulation

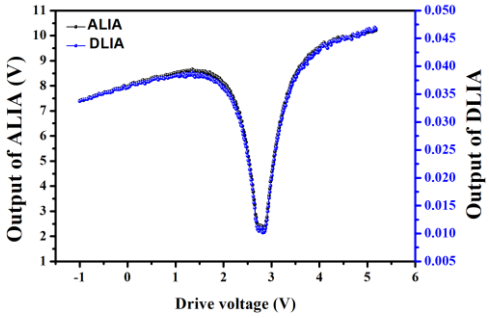

Figure 3.16 Measurement spectrum of CO_2 when ALIA (SR830) and DLIA are used for simultaneous demodulation

In the process of using the DLIA to demodulate the heterodyne signal, it is necessary to filter the result of the multiplication of the original signal and the sine wave. The low-pass filter will affect the output signal. Therefore, the filter's passband will contain a part of the noise signal, which is relatively small compared to the heterodyne signal. This signal and the heterodyne signal will be output by the DLIA. When the sunlight is weak, the heterodyne signal decreases, and it is larger than the heterodyne signal. Figure 3.17 shows the changes in the output of the DLIA with the decrease of sunlight intensity. When the sunlight intensity is zero, the output of the DLIA is not zero. The signal produced by noise can change the absorption depth of the absorption spectrum, so this background needs to be subtracted. Before collecting heterodyne signals, the first is to set the needed parameters of DLIA and then collect a group of background signals without solar radiation input. The average value of this background signal can be regarded as the lowest point of the absorption spectrum. After the complete spectrum is obtained, it needs to subtract the lowest point.

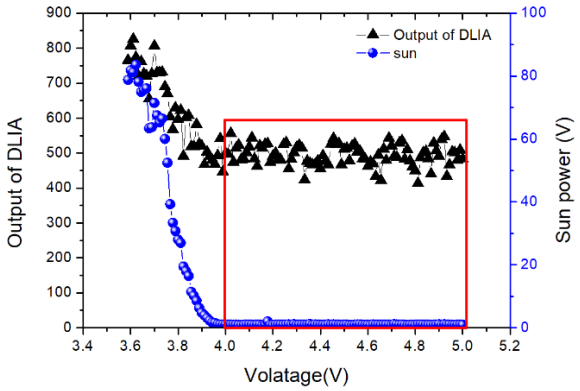

Figure 3.17 Changes in the output of the DLIA with the decrease of sunlight intensity

3.5 Field observation in Dachaidan

3.5.1 Field experiment

A 20-day observation was conducted in the Dachaidan District, Haixi Mongolian-Tibetan Autonomous Prefecture in Qinghai Province

(37.7442°N,95.3424°E). The atmosphere in this area is less affected by human activities and can be used as an atmospheric background observation site shown in Figure 3.18 (a) and (b).

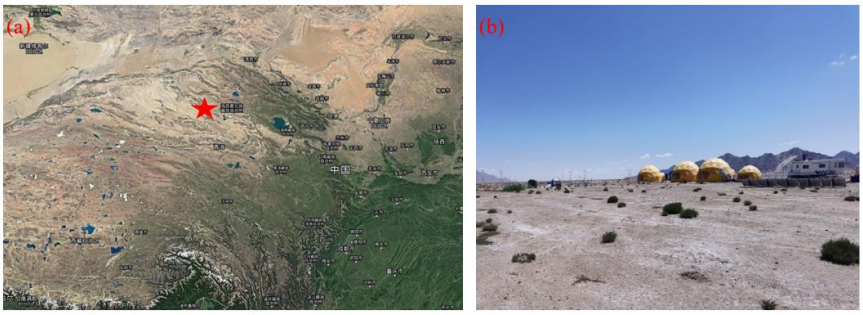

Figure 3.18 (a) Observation location; (b) Observation site

The observation state of the instrument in the experiment is shown in Figure 3.19 The single-mode fiber transports the solar radiation collected by the solar tracker light-receiving device into the IP-NIR-LHR for detection. To prevent wind, sand, and rainy weather at any time, the IP-NIR-LHR is placed in a tent to work.

Figure 3.19 Observation status of the instrument

3.5.2 Signal correction and filtering

The instrument can only work on sunny days. There are nine kinds of weather conditions during the measurement shown in Figure 3.20. Obstructions on the collected solar radiation path will interfere with the detection of heterodyne signals or reduce the SNR.

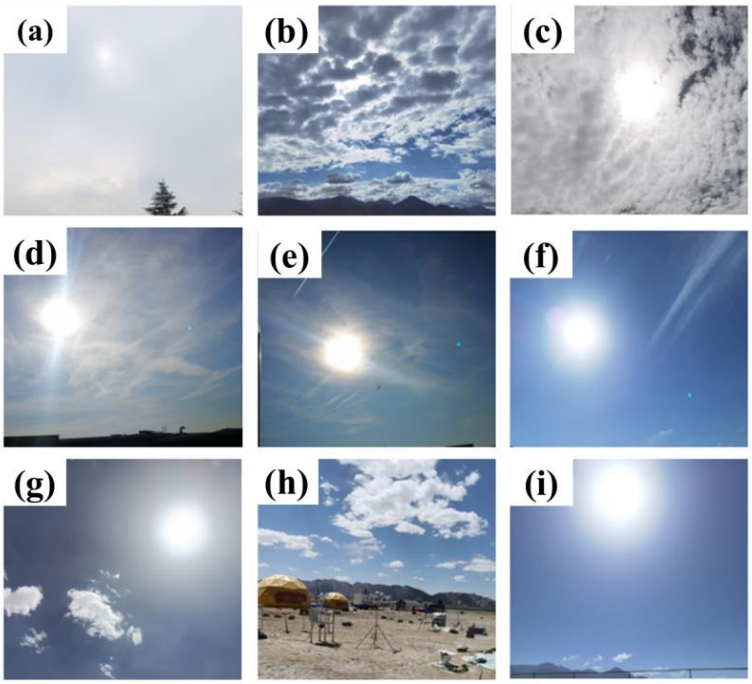

Figure 3.20 Weather conditions during the measurement

The flying bird can cover the detection field quickly shown in Figure 3.20 (e), which will affect several points in the absorption spectrum. These points can be directly removed when they are not near the absorption peak. The best weather conditions are shown in Figure 3.20 (i). In many situations, there are clouds in the sky, so the interference of the cloud to the heterodyne signal measurement is inevitable. To collate more available measurement data, the influences of the cloud are divided into the following situations to deal with separately.

(1) In cloudy weather, as shown in Figure 3.20 (a) and (b), the solar tracker cannot work in this case, and the measurement cannot be performed.

(2) When the sunlight is very strong and can pass through dense clouds, as shown in Figure 3.20 (c), the solar tracker only tracks the sun occasionally. Only a few heterodyne signals are valid, and a complete absorption spectrum cannot be obtained.

(3) The sky is covered with clouds, as shown in Figure 3.20 (d), (e), and (f). In this situation, the power (5 mW) of sunlight can still be collected and is relatively stable. The thin clouds will drift with the wind, and the collected sunlight intensity will weaken the heterodyne signal, which will distort the spectrum. Therefore, in this case,

it is necessary to eliminate the slight amplitude fluctuation of the heterodyne signal.

(4) For sunny weather, the sunlight is strong, but floating clouds in the sky will block the sunlight. Due to the collection device has a small field of view, the collected sunlight can generally pass through the gap between the clouds, as shown in the distribution of clouds in Figure 3.20 (g). Then the heterodyne signal is greatly affected by the cloud layer.

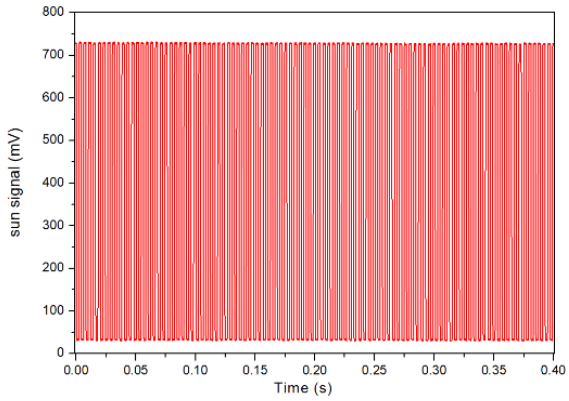

Figure 3.21 A group of sunlight signal data corresponding to a heterodyne signal

Based on the analysis of the working conditions of IP-NIR-LHR in the above several kinds of weather. It is necessary to eliminate the influence of the cloud on the sunlight intensity in the heterodyne signal. Figure 3.21 shows a group of sunlight signal data corresponding to a heterodyne signal. In this short period (0.4 s), the sunlight intensity remains unchanged. The average value of the peak-to-peak value of this group of data is regarded as the sunlight intensity, which corresponds to each heterodyne signal in the spectrum.

Figure 3.22 is a group of sunlight intensity fluctuations during the measurement process that have a greater impact on the heterodyne signal; (a) is the sunlight fluctuations during the spectrum measurement process; (b) is the DC signal indicating the laser power; (c) is the heterodyne signal demodulated by the DLIA; (d) is the heterodyne signal after removing the sunlight intensity. From Figure 3.22 (a) and (c), the fluctuation of the heterodyne signal is basically the same as the fluctuation of the sunlight intensity. From Figure 3.22 (d) and (b), the baseline signal increases with the increase of laser power. The sunlight fluctuations are basically eliminated

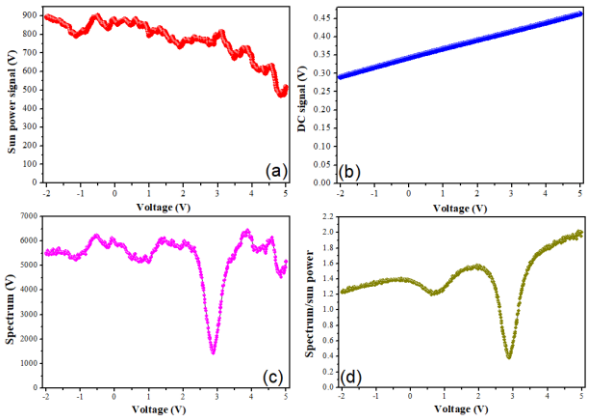

Figure 3.22 (a) Change of sunlight intensity; (b) DC signal; (c) Heterodyne signal; (d) Heterodyne signal after removing sunlight intensity.

3.5.3 Spectral comparison with FTIR

Take the methane absorption spectrum as an example, use the center position of the absorption spectrum to determine the corresponding wavenumber, and combine the interference data to perform wavelength correction on the heterodyne spectrum to obtain the wavelength-calibrated CH_4 absorption spectrum, as shown in the red curve in Figure 3.23. The black curve in Figure 3.23 is taken from the high-resolution FTIR measurement spectrum. Because the measurement time and location of the two spectra are inconsistent, the absorption position of CH_4 in the two spectra is the same, and the spectral absorption depth measured by FTIR is deeper than that measured by IP-NIR-LHR. However, the solar spectrum in the two spectra almost overlaps, because the solar spectrum is not affected by time and location, which also shows the validity of the instrument measurement data.

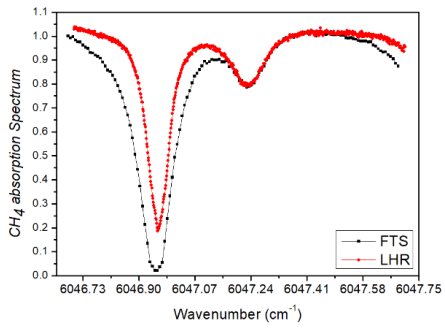

Figure 3.23 Measured spectrum of IP-NIR-LHR and FTIR in the same waveband

3.5.4 Atmospheric transmittance in a day

Conducted field surveys according to local weather conditions, Figure 3.23 shows the measurement results of atmospheric transmittance of CH_4 and CO_2 on August 18th, before 14:00 in the morning, the absorption depth of CH_4 and CO_2 in the atmosphere gradually increased with time, and the absorption depth of the two in the afternoon gradually decreased with the passage of time. The absorption spectrum changes slowly from 11:00 to 14:00 at noon, and changes quickly at other times. The time for the instrument to collect a spectrum varies with the change of sunlight intensity, In the range of 5 min to 10 min, the signal-to-noise ratio of the spectrum can be obtained as about 250 (the SNR of the spectrum is obtained by dividing the absorption peak depth by the variance of the baseline), The atmospheric transmittance of CH_4 and CO_2 with a spectral resolution of 0.00442 cm^{-1}.

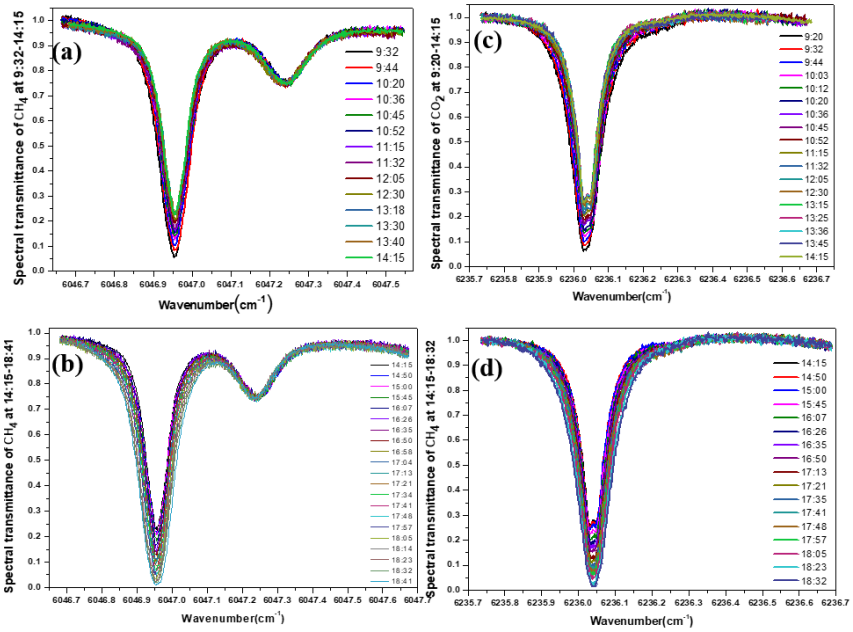

Figure 3.24 (a) Change of atmospheric transmittance of CH_4 before 14:15; (b) Change of atmospheric transmittance of CH_4 after 14:15; (c) Change of atmospheric transmittance of CO_2 before 14:15; (d) Changes in atmospheric transmittance of CO_2 after 14:15

3.6 Retrieval results

The transmittance of CH_4 and CO_2 measured at 9: 32 on the same day was inverted through the inversion algorithm. The fitting results of the two measured transmittances

obtained by iterative calculation are shown in Figure 3.25 (a) (c), respectively. Figure 3.25 (b) (d) is the residual difference between the measured transmittance of CH_4 and CO_2 and the simulated transmittance. It can be seen that the calculation result and the measured spectrum can be well fitted. The absolute value of the residual error is larger in the area with larger wave number and the absorption peak. This is due to the lower laser output power in the area with larger wave number, which reduces the signal-to-noise ratio, while the sunlight is absorbed at the absorption peak, the signal-to-noise ratio of the heterodyne signal here is lower than the signal-to-noise ratio where there is no absorption. From the inversion of the measured spectrum of CH_4 and CO_2, the column concentration of CH_4 gas below 24 km is 2.695×10^{19} molecular/cm^2, and the column concentration of CO_2 gas is 5.804×10^{21} molecular/cm^2. This part of the inversion work is mainly done by myself. The inversion principle and process are explained in appendix 1 and appendix 2.

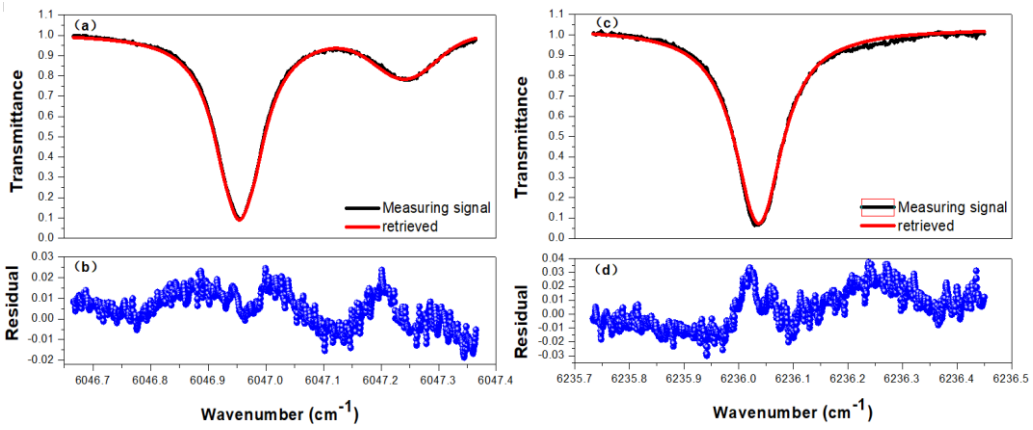

Figure 3.25 (a) Fitting result of the entire atmosphere CH_4 transmittance measurement spectrum; (b) Residual of the CH_4 simulation transmittance and the measured transmittance; (c) Fitting result of the entire atmosphere CO_2 transmittance measurement spectrum; (d) Residual difference between CO_2 simulated transmittance and measured transmittance.

Summary

This chapter introduces the development of IP-NIR-LHR, designs the laser diode current control circuit and temperature control circuit, combined with the radio frequency amplifier to make the spectral resolution of the measurement system reach 0.00442 cm^{-1}. The laser wavelength calibration structure is constructed by using the

optical fiber combiner and the optical fiber splitter. The preamplifier is designed to block, filter and amplify the weak voltage signal output by the RF signal processing circuit. Combined with the digital lock-in amplifier, the collected signal is demodulated, and finally the heterodyne signal is averaged. When the sky is cloudless, the entire layer of atmospheric transmittance of CH_4 and CO_2 with a signal-to-noise ratio of about 250 can be obtained every 3 minutes. This instrument is the first high-resolution portable laser heterodyne detection instrument in China, and its ability to observe in the field has been verified through experiments in the Dachaidan area. The next step is to perform secondary temperature control on this instrument, further optimize the internal structure, and improve the stability of its measurement. Improve the data acquisition and processing software to enable unattended observation.

References

[1] F. Seoane, R. Bragós, K. Lindecrantz. Current source for multifrequency broadband electrical bioimpedance spectroscopy systems, A novel approach. International Conference of the IEEE Engineering in Medicine and Biology Society, IEEE, 2006: 5121-5125.

[2] F. Seoane, R. Macias, R. Bragos, K. Lindecrantz. Simple voltage-controlled current source for wideband electrical bioimpedance spectroscopy: circuit dependences and limitations, Measurement Science and Technology, 2011, 22 (11): 115801.

[3] P. Bertemes-Filho, A. Felipe, C. V. Vincence. High accurate howland current source: output constraints analysis, Circuits and Systems, 2013, 4 (7): 451-458.

Chapter 4 Mid-infrared laser heterodyne radiometer based on an interband cascade laser (IC-LHR)

Objective

In this Chapter, the development of a mid-infrared (mid-IR) laser heterodyne radiometer based on an interband cascade laser (IC-LHR) is presented. The developed IC-LHR was tested in Anhui Institute of Optics and Fine Mechanics, Science island, Hefei, China. Ground-based measurements of CH_4 and HDO in the atmospheric column were performed.

4.1 Introduction

Initial LHRs, employed carbon dioxide (CO_2) gas lasers as local oscillators, focused in the 8~12 μm atmospheric window, where numerous important atmospheric species exhibit fundamental rotational-vibrational absorptions. However, the CO_2 lasers suffered from line-tuned spectral tunability. As an alternative, lead-salt diode lasers offered better frequency choice and frequency tuning ability but lacking reliability and optical powers and suffering from the requirement of LN_2 temperature cooling [1,2]. The quick development of quantum-cascade lasers (QCLs) offers an ideal alternative to the traditional local oscillators in the mid-infrared region with the merits of room-temperature operation, wide spectral tuning range, compactness, and robustness. Over the last decade, the QC-LHR applications for atmospheric observation have been successfully developed [3-8]. At the same period, the application of LHR for passive sensing of atmospheric CO_2 and CH_4 in the shortwave infrared band (around 1.6 μm) is also investigated, where telecommunication distributed feedback lasers are employed as the local oscillators. Combined with single-mode optical fibers, couplers, and attenuators, the system can be made small, low-power consumption, compact and robust [9-12].

The atmospheric window of 3-5 μm is another attractive spectral region for

mid-infrared atmospheric sounding. However, commercially available QCLs operate generally in the [4,12] μm spectral region, which led to a "mid-infrared gap" in the QC-LHR applications. Since the first demonstration in 2008 [13], interband cascade lasers (ICLs), lasing in continuous-wave (cw) mode at room temperature at the spectral region between 3 and 6 μm, open a new spectral window for mid-infrared sensing. ICLs offer room-temperature operation, compactness, high spectral purity with much lower electrical power consumption compared with QCLs.

So, in this chapter, an ICL based LHR (IC-LHR) for atmospheric sounding is demonstrated. Simultaneous heterodyne detection of atmospheric water vapor (HDO) and methane (CH_4) near 3.53 μm has been performed in ground-based solar occultation mode. The experimental details and result analysis will be presented and discussed.

4.2 An IC-LHR operating at 3.53 μm

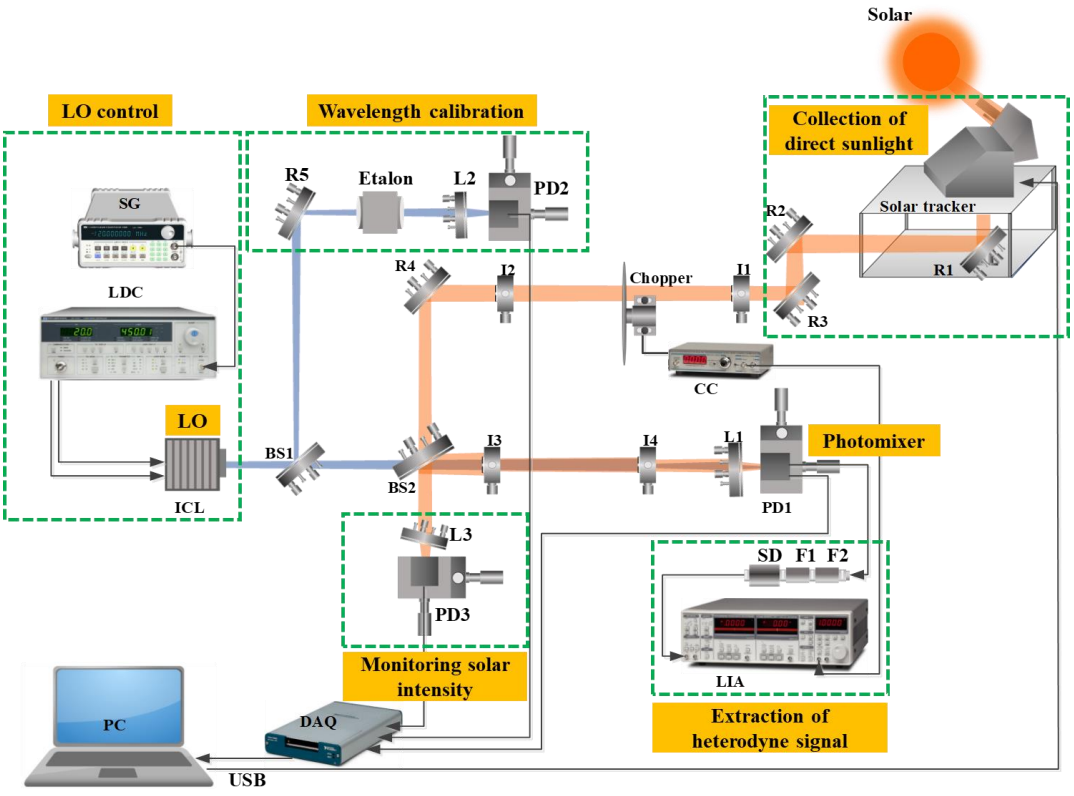

Figure 4.1 Schematic of the developed mid-IR IC-LHR. SG: signal generator (SP-F120); LDC: laser diode controller (ILX Lightwave, LDC-3724C); ICL: interband cascade laser; BS: beam splitter; I: iris diaphragm; R: reflector; L: lens; CC: chopper controller; PD: photodetector (PD1 is used as a photomixer); SD: Schottky diode; F: filter; LIA: lock-in amplifier (SR830); USB:

Universal Serial Bus; PC: a personal computer; DAQ: data acquisition card (NI 6366). Thick blue line: laser path; thick orange line: sunlight path; thin black line: electric signal flow direction

Figure 4.2 The physical image of IC-LHR

The developed IC-LHR is schematically shown in Figure 4.1. And Figure 4.2 shows the physical image of IC-LHR. It is composed of a collection module of direct sunlight associated with a solar tracker, a modulation module of solar radiation, and ICL, a photodetector, and a heterodyne signal extraction module, as well as a frequency metrology module (in our case, a wavelength correction module and the absorption lines of CH_4 and HDO retrieved from the Hitran database were used).

1. Collection and monitoring of solar radiation

Solar radiation containing atmospheric absorption information was captured with the help of a homemade solar tracker and reflected into the system by the reflectors (R1, R2, R3). And then, it was chopped at 2 kHz for lock-in amplification of the LHR signal by a chopper controlled by an SR540 chopper controller. The two iris diaphragms (I1, I2) and two reflectors (R3, R4) were used to mark and adjust the solar light path to be collinear with the laser path. After a 50T/50R beam splitter (BS2), the reflected solar

beam was directed to PD3 focused by L3 (f = 25 mm, ZnSe) for monitoring solar intensity fluctuation during the measurement.

2. Combination of LO and solar radiation

A beam splitter (BS2) was employed as a mixing device to combine the reflected solar radiance with the light beam from an ICL used as the local oscillator (LO). The output mode of ICL was controlled by a laser diode controller and a signal generator. The combined beams were focused on a high-speed mercury cadmium telluride photodetector (PD1, Vigo PV-2TE-4 with a custom preamplifier), which had both DC ([0,1] MHz, for monitoring the ICL power) and AC ([1 kHz,100 MHz], for LHR detection at radio-frequency (RF)) by L1 (f = 25 mm, ZnSe). The iris diaphragms of I3 and I4 were used to assist in adjusting the collinearity of LO and solar radiation.

3. Extraction of the heterodyne signal

The solar radiation containing atmospheric absorption information was down-converted to the RF domain via PD1, followed by a band-pass filter (consisted of F1: 10 MHz~3 GHz and F2: DC~60 MHz) employed to determine RF detection bandwidth which defines the instrument lineshape (ILS) of the LHR system. Subsequently, the RF signal after the band-pass filter was converted to a DC signal by a Schottky diode (HEROTE, DHM020BB) and demodulated at first harmonic using a lock-in amplifier (Stanford Research Systems, SR830) with the chopping frequency as reference. LHR signal can ultimately be obtained by tuning the laser frequency across the target molecular absorption lines.

4. Wavelength calibration

A small fraction of the ICL beam reflected by BS1 was used for wavelength calibration: a flip mirror (R5) directed the ICL beam either to a 50.8 mm germanium etalon (with a free spectral range of ~0.0246 cm^{-1}) followed by PD2 recording etalon fringe signal or

to a wavemeter (Bristol Instruments, 621) for absolute frequency measurements or for relative frequency metrology.

5. Data record

A personal laptop equipped with a DAQ card (National Instruments, USB-6366) and LabVIEW software was employed for data acquisition and instrument control (solar tracker controlling, frequency tuning, and wavenumber reading). Signals from 5 channels were recoded: the in-phase (X) and quadrature (Y) outputs of the lock-in amplifier for phase compensation of the LHR signal by using the angle sum and difference identities (trigonometric identities), the DC output of PD1 for tracking the ICL power, the signal from PD2 for the relative wavelength calibration, and the signal from PD3 for tracking the solar power variation.

4.3 Features of the key devices involved in the IC-LHR

4.3.1 Characteristics of the ICL

The used local oscillator was a distributed feedback ICL (shown in Figure 4.3(a)) operating around 3.53 μm and mounted on TO-66. There was a collimator lens to shape the output beam. The thermal image of the collimated laser beam at 3.0 m distance from the laser facet is shown in Figure 4.3(b). Around the 3.53 μm, the output power spectrum of the ICL is shown in Figure 4.3(c). This laser can be coarsely tuned ~10 cm^{-1} by tuning the temperature at a constant current or precisely tuned over ~1 cm^{-1} by tuning the injection current at a constant temperature.

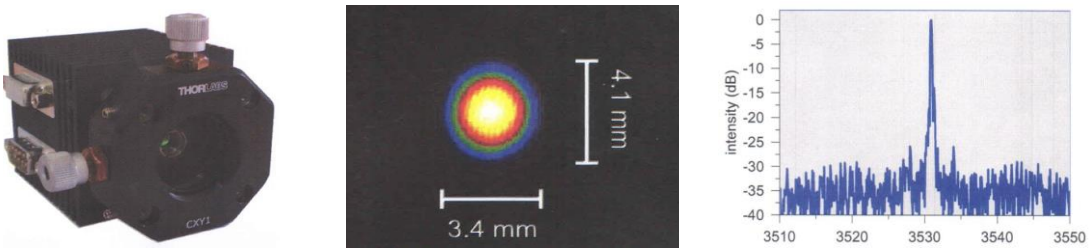

Figure 4.3 (a) Distributed feedback ICL mounted on TO-66 with TEC, cap, and collimating lens (consist of a lens (f = 12.7 mm, ZnSe) and a lens mount Thorlabs, CXY1); (b) Thermal image of

the collimated laser beam at 3.0 m distance from the laser facet; (c) Output power spectrum of the ICL around 3.53 μm.

The relationships between laser wavenumber, laser power, and laser injection current are shown in Figure 4.4. During LHR measurement, the laser temperature and current were set at 14 °C and 30 mA to probe the CH_4 and HDO absorption lines located around 2831.92 cm^{-1} (CH_4 @ 2831.9199 cm^{-1} with a spectral line intensity of 1.622 × e^{-21} cm/mol; HDO @ 2831.841 cm^{-1} with a spectral line intensity of 3.014×e^{-24} cm/mol. The data are retrieved in HITRAN database). The frequency tuning of the laser could be performed by changing the laser current point-by-point via laser controller or scanning the injection current with a common function waveform (such as sinusoidal or triangle waveform).

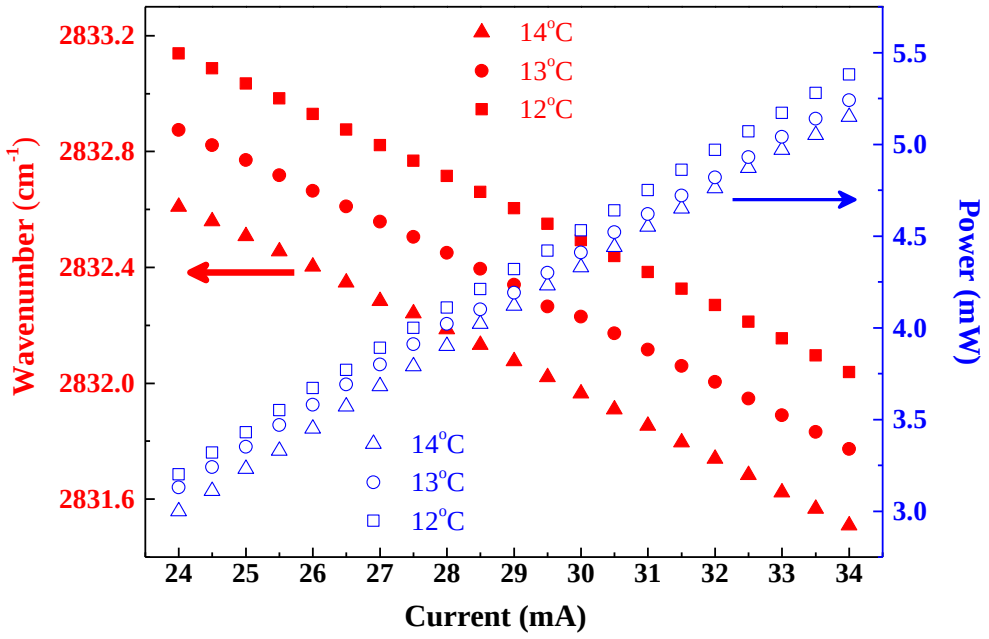

Figure 4.4 Relationships between laser wavenumber (solid red symbols), power (blue hollow symbols), and laser injection currentt

4.3.2 Solar tracker in freedom space

The solar tracker used in IC-LHR was designed by T. Tan and Y. Cao. It can track the solar steadily and reflect the direct sunlight into the LHR. In the process of tracking, the path of the beam incident on the LHR by the sun tracker remains unchanged. Its X-axis and Y-axis tracking accuracy were 0.068° and 0.06°. Figure 4.5 (a) shows the

propagation of the sunlight beam in the solar tracker. The solar tracker working principle is as follows: Combine the Labview application to get the local time and the local longitude and latitude through the external GPS module. According to the information of the time, the latitude and the longitude, the elevation, and the azimuth of the sun are calculated and converted into the number of pulses for driving stepper motors S1 and S2. In this way, the amount of movement of the stepper motor is controlled separately. When the CCD image sensor collects the solar spot (as shown in the set in Figure 4.5 (a)), the offset of the center position of the spot can be obtained through image processing, which can be converted to the number of pulses to control the stepper motors finely. The homemade solar tracker is shown in Figure 4.5 (b).

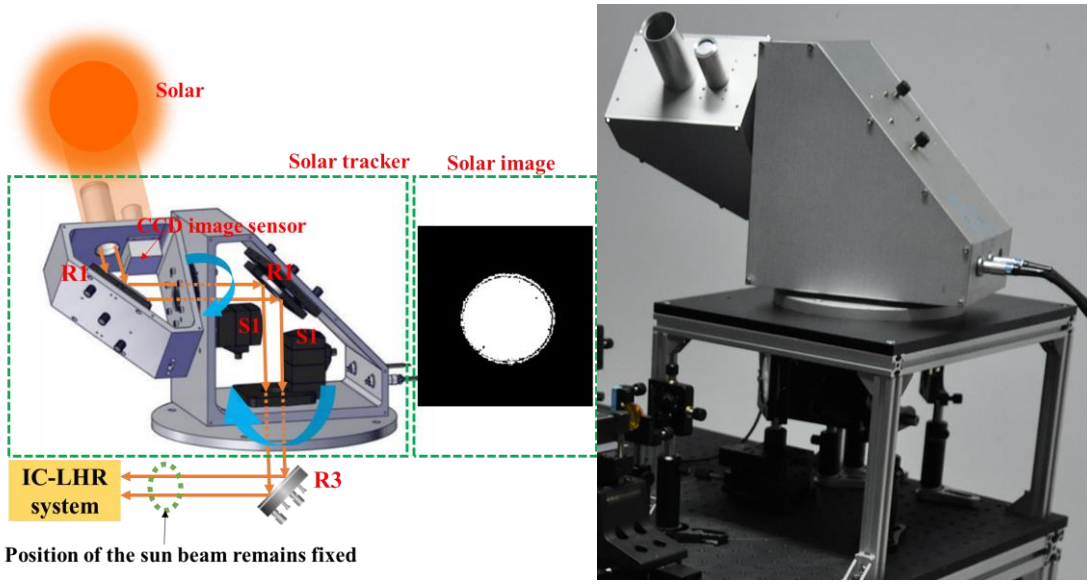

Figure 4.5 (a) Propagation of the sunlight beam in the solar tracker. R (R1, R2, R3): reflector; S (S1, S2): stepper motors. (b) Homemade solar tracker.

R1, R2, and R3 reflected the solar beam into the IC-LHR system. In the experiment, the position of the solar beam should remain fixed. This plays an important role in the beat between the laser and the solar beam in freedom space. In order to verify the stability of the reflected beam of the solar tracker, another CCD image sensor (size: 38 mm × 38 mm, pixel: 5120 × 3840) was placed at the position of the IC-LHR system to collect the coordinates of the center of mass of the solar spot. We used this solar tracker to track the solar for two hours and obtained the drift of the

center particle of the CCD sensor on the X-axis and the Y-axis. The results are shown in Figure 4.6.

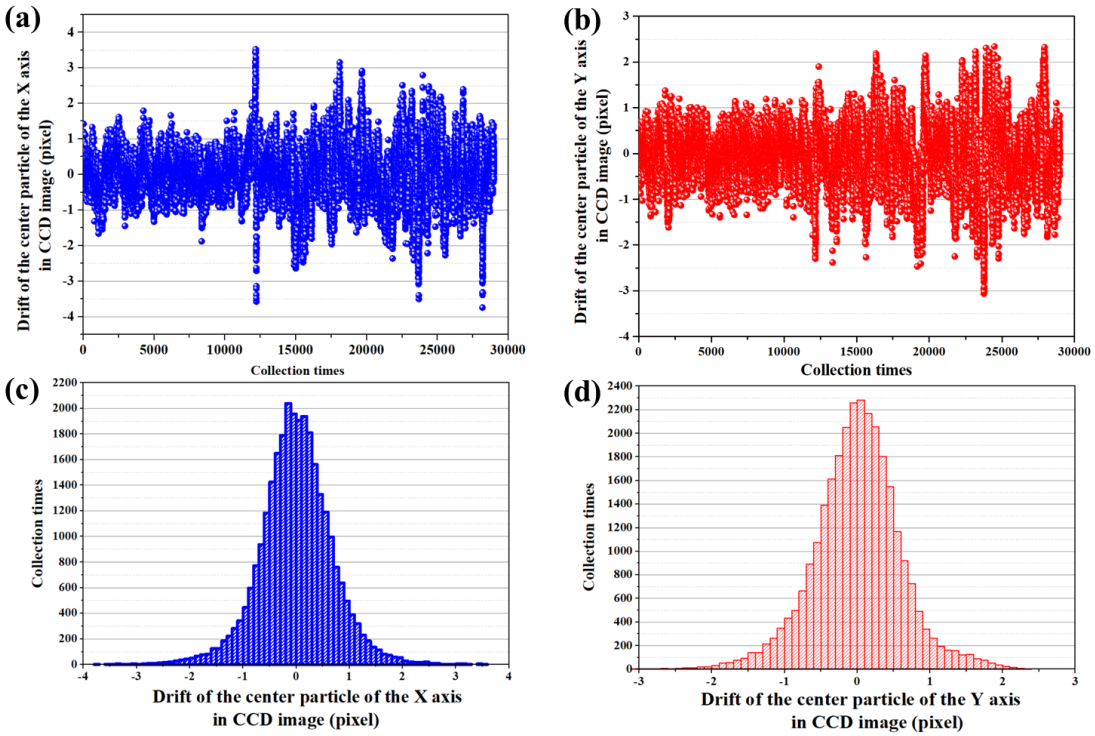

Figure 4.6 Drift of the center particle of the CCD sensor on the X-axis and the Y-axis

The angle between every two pixels is 0.01°. The deviation of the X-axis and Y-axes are similar to the Gaussian distribution and are mainly distributed in the interval of [-0.01°, +0.01°]. This can basically meet the needs of the beat between the laser and the solar radiation.

4.3.3 Mid-infrared photomixer

The Photomixer (Vigo, PC-2TE-4-0.1×0.1-TO8-wBaF2-70) is made of HgCdTe, of which descriptions are shown in Table 4.1. It is a photovoltaic detector that has high-performance features in the range of 2.3 ~ 4.2 μm spectrum range and two-stage thermoelectrically cooled. The physical image and mechanical layout of the mid-infrared photomixer are shown in Figure 4.7(a) and (b). The FOV of 70° and the active area of 0.1×0.1 mm^2 is good for the incidence of beams.

Table 4.1 Description of the mid-infrared photomixer

Parameter	Mid-infrared photomixer
Transimpedance	AC output : 2.1×10^4 V/A; DC output: 1.9×10^3 V/A
Low cut-off frequency	AC output: 1 kHz; DC output: DC
High cut-off frequency	AC output: 100 MHz; DC output: 1MHz
Output noise density	AC output: 345 nV/ √ Hz
Voltage responsivity ±20%	AC output: 2.25×10^4 V/W
F_OV	70°
Active area	0.1×0.1 mm^2
Window	wBaF2

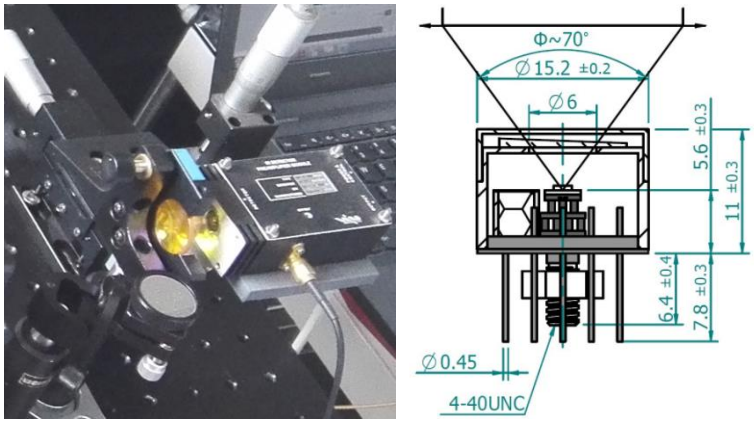

Figure 4.7 (a) Physical image of the mid-infrared photomixer; (b) The mechanical layout of the mid-infrared photomixer.

The responsivity of the mid-infrared photomixer is shown in Figure 4.8. Around the absorption line of 3.531 μm, responsivity is about 1. It is a photovoltaic detector. The integrated transimpedance amplifier (BIP-1K-100M) inside the photodetector can amplify the AC component (RF signal) in the range of [1 kHz, 150 MHz]. Under two conditions (input laser and cover the surface of photodetector), the output signals were collected by a spectrum analyzer (Agilent Technologies, N9000A), as shown in Figure 4.9. In the range of 10 MHz to 60 MHz, there is less RF noise. So, the RF filters of high pass of 10 MHz (Crystek corporation, CHPFL-0010-NC) and DC ~ 60 MHz (Mini-Circuits BLP-70+) are used to filter out the RF signal.

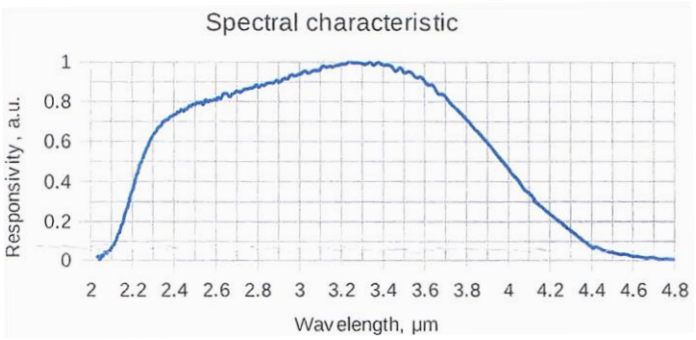

Figure 4.8 Responsivity of mid-infrared photomixer

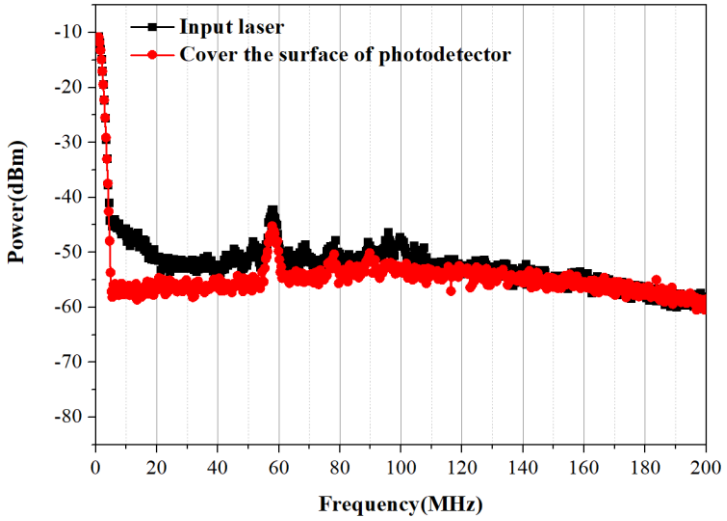

Figure 4.9 The power spectrum of the outputs from the photodetector. Conditions: red curve responds to input the laser (drive current = 30 mA); the black curve responds to the spectrum of the background signal.

4.4 Pass-band selection

4.4.1 Influence of pass-band selection

To characterize and optimize the performance of the IC-LHR, a carbon silicon rod was used as the solar radiation. Heterodyne measurements of CH_4 absorption spectra were performed in a 12-cm long single-pass cell in the laboratory (shown in Figure 4.10). Radiation from a carbon silicon rod (power of 24 V, 1385℃) is collected and collimated with an off-axis parabolic mirror (MP1) (MPD249-M01-ϕ2”, 90°, reflective focal length = 101.6 mm, parent focal length = 50.8 mm). After passing through the single-pass cell, the beam was modulated at 1300 kHz. It was then

directed to a 50%R / 95% beam splitter (in CaF). The beam would be combined with the ICL and focused by PM1 (MPD129-M01-ϕ1" 90°, reflective focal length = 50.8 mm, parent focal length = 25.4 mm) on the surface of the photomixer. The heterodyne signal translated from the beat signal in the photomixer would be demodulated by an LIA and collected to be the absorption spectrum of CH_4 in the single-pass cell. Based on this experiment, the performance of the IC-LHR can be estimated initially.

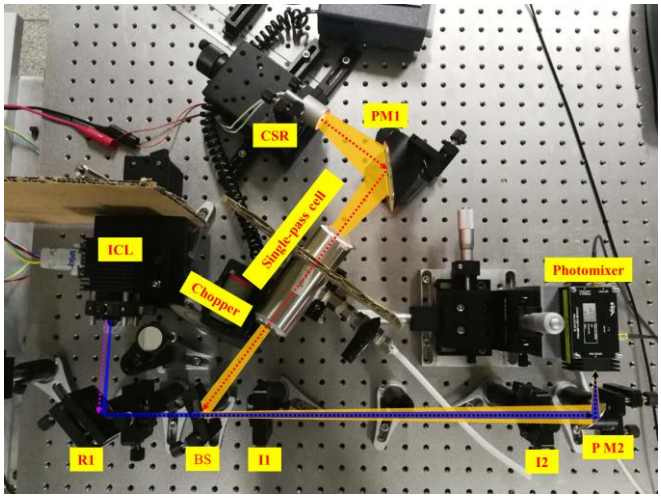

Figure 4.10 Optical path for heterodyne measurements of CH_4 absorption spectra performed in a 12 cm single-pass cell in the laboratory. PM: Parabolic mirror, CSR: carbon-silicon rod; R: reflector; BS: beam splitter; I: iris diaphragm.

In order to study the source of system noise, the outputs from LIA (integration time: 30ms, roll-off: 24dB, sensitivity: 5 μV, reference frequency 1.3 kHz) under the following six situations were collected (sampling rate: 1kHz, 8600 samples per cycle when a sine wave demodulated the laser with a cycle time of 32 s and amplitude of 200 mV): (1) outputs 1 of LIA: the light incident on the photomixer contained the power scanned laser and the CSR; (2) outputs 2 of LIA: the light incident on the photomixer contained the power fixed laser and the CSR; (3) outputs 3 of LIA: the light incident on the photomixer only contained the power scanned laser; (4) outputs 4 of LIA: the light incident on the photomixer only contained the power fixed laser; (5) outputs 5 of LIA: the light incident on the photomixer only contained the CSR; (6) outputs 6 of LIA: no light incident on the photomixer. The collected data are shown in

Figure 4.11.

The signals of outputs 3,4,5, and 6 are the background signals without heterodyne signals. By comparing these background signals, it can be seen that the laser mainly produces background noise. The background noise when the laser power was scanned is worse, and this background should be subtracted from the outputs 1 of LIA to get the heterodyne spectrum of CH_4. The SNR is calculated to be 14.

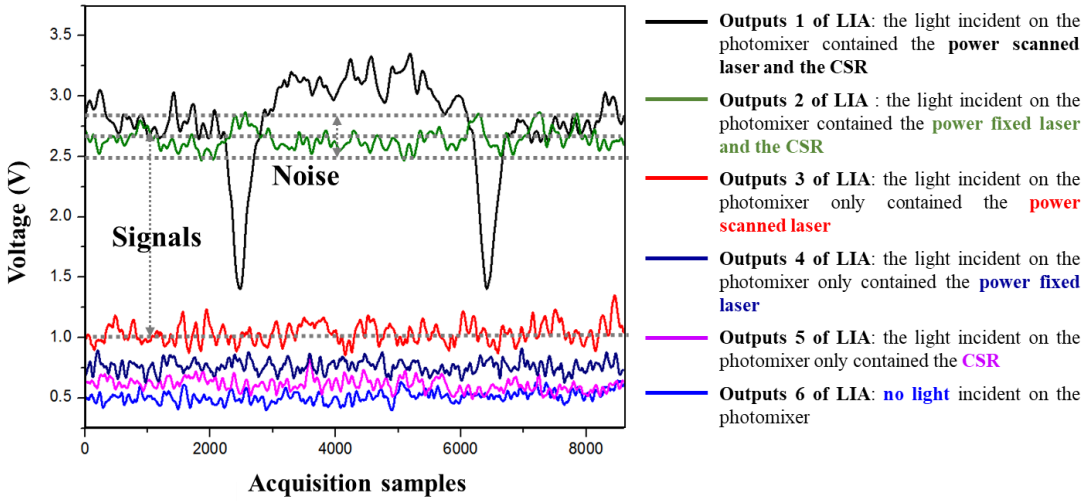

Figure 4.11 Under different input conditions, the collected heterodyne signal

The possible reason for the low SNR is that the filter bandwidth (10MHz ~150 MHz) used in the experiment contains considerable RF noise. Therefore, the outputs of LIA when using RF filters of different bandwidths were collected in Figure 4.12. It was evident that the smaller the filter bandwidth, the smaller the signal value. And the fluctuation amplitude on the signal baseline (samples points 0 ~ 1500 and 3500 ~ 8600) is relatively small. Reducing the bandwidth can reduce the RF noise but also reduce the heterodyne signal. Therefore, when choosing the RF filters and ensuring that they can filter out high-noise bands, it is also necessary to balance the bandwidth of the filters and the size of the heterodyne signal. Because the power of solar radiation is greater than that of CSR, this will increase the amplitude of the heterodyne signal. Therefore, the bandwidth can be appropriately reduced when solar radiation is used as the signal light.

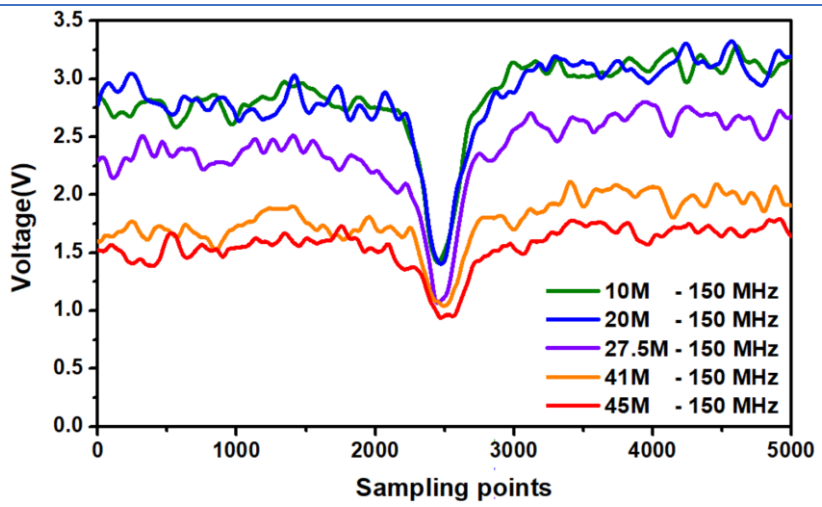

Figure 4.12 The outputs of LIA when using RF filters of different bandwidths

4.4.2 Instrument lineshape (ILS) of IC-LHR

As shown in Figure 4.13. the heterodyne signal form is dominated by the LO (ICL) signal, and the photomixer can extract the LHR signal from the background baseline below 150 MHz. However, there were several unwanted peaks between 70 MHz ~ 120 MHz, which might introduce additional noise to the LHR signal. Therefore, the 10 MHz ~60 MHz band-pass filters were chosen in the experiment, which resulted in a ~100 MHz (0.0033 cm^{-1}) double-sideband spectral resolution of the system. The inset of Figure 4.13. shows the actually used ILS for data retrieval.

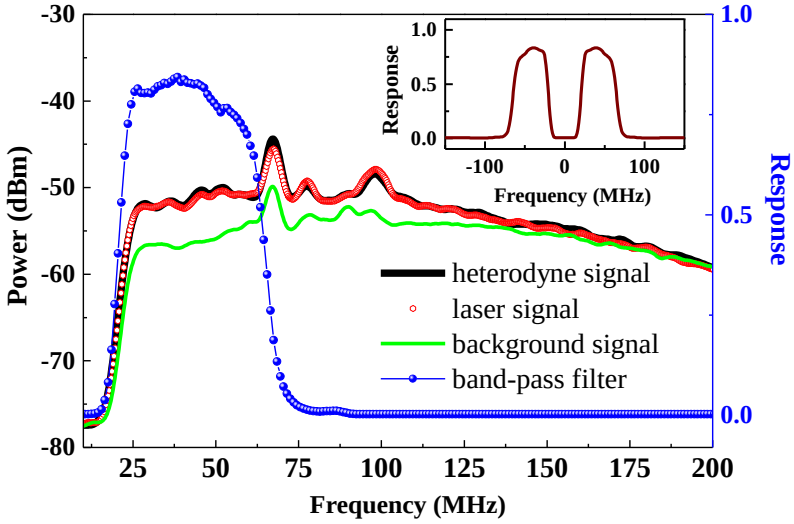

Figure 4.13 Band–pass filter used in the experiment and frequency spectrum analysis of the heterodyne, laser and background signals, the inset: the actually used instrument lineshape for data retrieval

4.5 Measurement spectrum of atmospheric CH_4 and HDO in Hefei

The experimental result, measured from our institute (Hefei, China, 31.9°N 117.166°E) on June 21th 2016, is shown in Figure 4.14 (b), where the phase compensation has processed the LHR data. In addition, the transmittance of atmospheric HDO vapor and CH_4 in the considered spectral region is calculated by using a forward model. The results are shown in Figure 4.14 (b), which were acquired at a sampling rate of 50 Hz by driving the laser current with a sinusoidal wave (0.0125 Hz (80 s), 0.5 Vpp).

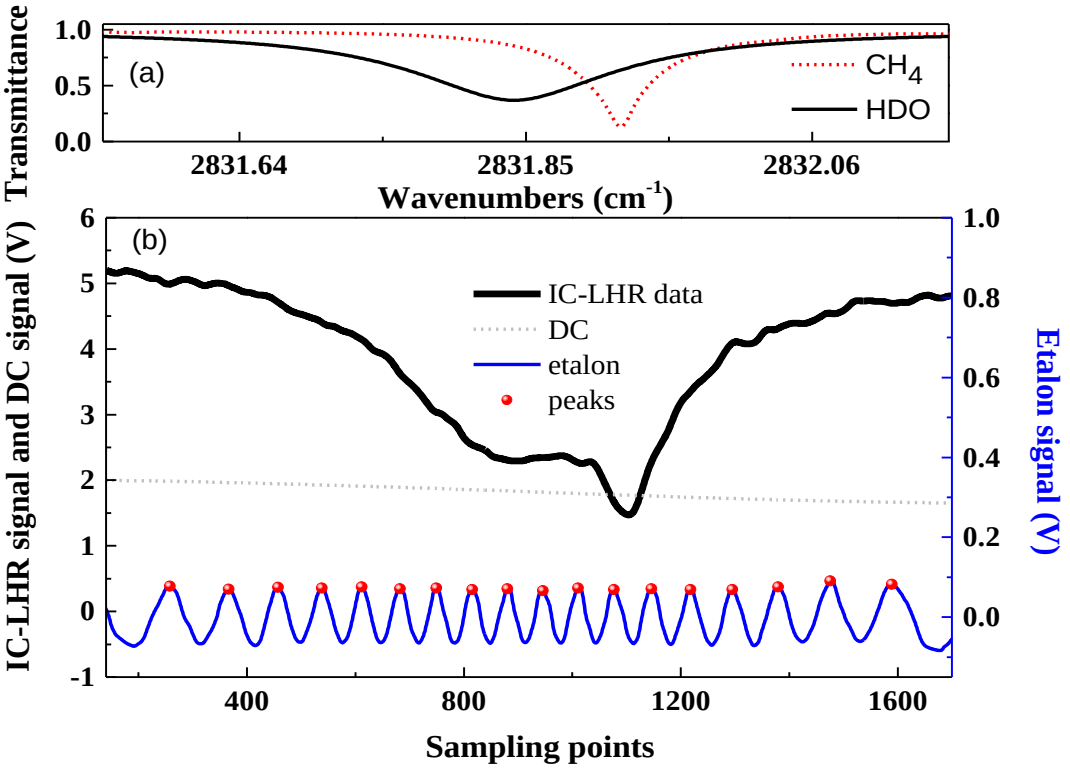

Figure 4.14 (a) Calculated transmittance of atmospheric H_2O vapor (black) and CH_4 (red dots) based on the forward model; (b) Acquired IC-LHR (black), DC (DC output of detector PD1, gray dots) and etalon signals (blue)

Before the data retrieval, the raw LHR data needs to be pre-processed. Firstly, the offset of the LHR signal, where the injection current to the ICL equals zero, was subtracted. Then the LHR signal is divided by the ICL intensity signal (DC signal) for normalization of the LHR signal. When large solar power fluctuations (more than 10% of the average of solar power intensity) occurred during the scan, the LHR data would

not be considered for further analysis. Thirdly, a frequency calibration of the LHR signal was performed with the help of relative frequencies (germanium etalon signal) and absolute frequencies from a wavemeter or the positions of the absorption lines (from the HITRAN database) [14]. In the present work, peaks of the etalon signal were fitted to a 5th order polynomial function to determine the relative frequency of the data points, and the CH_4 line position (2831.92 cm^{-1}) was employed to calibrate the absolute frequency. In addition, a scale factor and an offset were used for further frequency calibration according to the wavemeter results and the forward model calculation. Finally, the calibrated the LHR results were interpolated with the same frequency interval as the forward model, and then the processed the LHR spectrum is now ready (blue dots in Figure 4.16 (a)) for further data retrieval to inverse the LHR spectrum to the corresponding vertical concentration profiles.

4.6 Retrieval results of X_{CH4} and X_{HDO}

The main work of data retrieval was completed by G. Wang [15]. In this section, a brief introduction to the parameters and process in the data retrieval is described to verify that the measurement results of the IC-LHR can be used for the inversion of atmospheric column concentration.

The temperature and pressure profiles used in the retrieval are shown in Figure 4.15 (a) and (b), which were obtained from the China Meteorological Data Service Center (CMCC) and the European Centre for Medium-Range Weather Forecasts (ECMWF). Data below 30 km (blue dots) were interpolated from the upper air data of Anqing observation station (China, 30.53°N 117.05°E), and the data above 30 km (red dots) were interpolated from the typical zonal mean profiles in different months (obtained from ECMWF). For the methane and water vapor profiles, typical mid-latitude daytime profiles were used. Note that the atmosphere is separated into 45 layers from surface to 78 km with an altitude grid of 0.5, 1, 2, 4, and 6 km, separately.

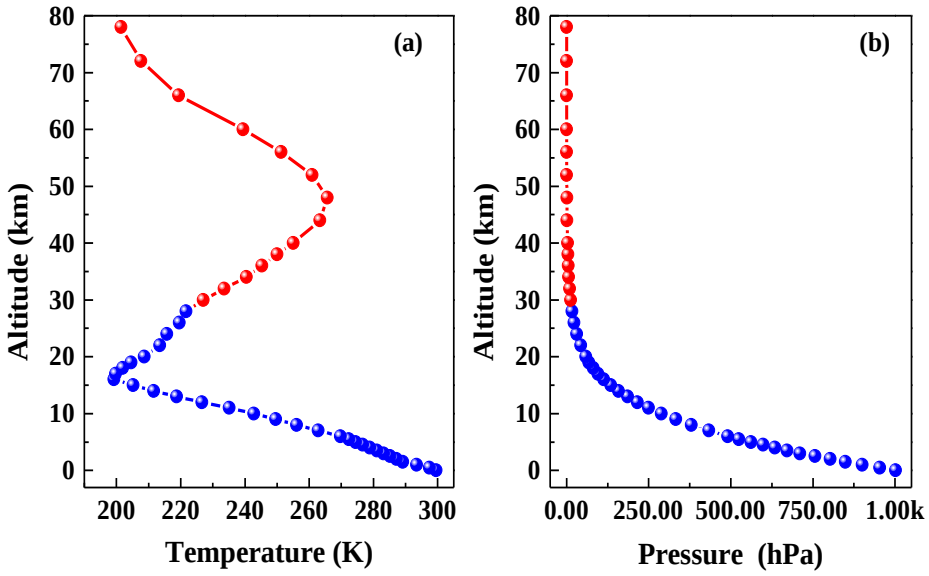

Figure 4.15 (a) Temperature and (b) pressure profiles used for the IC-LHR retrieval

The iterative solution is defined to be converged with $\Delta\chi^2/\chi^2 < 1E^{-3}$, within an upper limit of 20 iterations. In a well-conditioned retrieval, the ultimate cost function (χ^2) should be close to the size of the measurement vector (m). Figure 4.16 (a) shows the pre-processed IC-LHR data and the fitted spectrum over the spectral region of 2831.64 ~ 2832.07 cm^{-1} with an interval of 0.001 cm^{-1}. The iterative process is shown in the inset of Figure 4.16 (a), where χ^2/m equal to ~1.05 is obtained after 6 iterations. The residuals between the pre-processed data and the fitted result are shown in Figure 4.16 (b), where the random distribution indicates a well-configured fit. The retrieved CH_4 and water vapor profiles (Figure 4.16 (c) and Figure 4.16 (d)) are calculated by multiplying the retrieved scale factor with the *a priori* profile. Based on the retrieved CH_4 and water vapor profiles, the total column abundance of water vapor is calculated to be ~2868 ppm (or ~$5.8E^{+23}$ molecules/cm^2), the total column abundance of methane and its mixing ratio in dry air (X_{CH4}) are found to be ~1.875 ppm (or ~$3.8E^{+20}$ molecules/cm^2) and ~1.88 ppm (part per million), respectively.

The total retrieval error of the two-scale factors was calculated to be ~6% and ~8%, respectively. 20 consecutive measurements indicate uncertainty of 20 ppb (part per billion) and 21 ppb for the total CH_4 column abundance and X_{CH4}, respectively. For

further improvement of the measurement uncertainty, works in the near future will be focused on improving the SNR of the IC-LHR signal and determining an appropriate weight of the constraint in the retrieval so as to a 'true' profile retrieval.

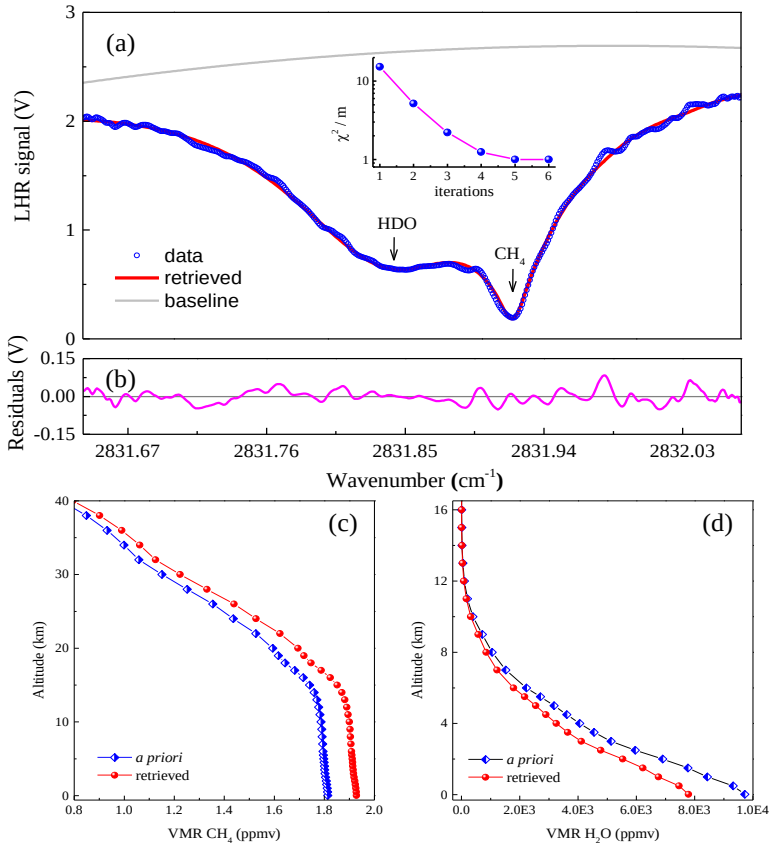

Figure 4.16 LHR data retrieval results: (a) experimental (blue) and fitted (red) LHR spectra and the convergence of the iteration process (inset); (b) the residuals (pink); (c) and (d) the retrieved vertical concentration profiles of CH_4 and water vapor, respectively.

Summary

An ICL based mid-infrared LHR has been demonstrated, for the first time, in ground-based solar occultation mode. High-resolution (0.0033 cm^{-1}) LHR spectrum near 3.53 μm were obtained for simultaneous atmospheric observations of H_2O vapor and CH_4. OEM and RFM based retrieval algorithm was developed for retrieval of the vertical profiles of H_2O and CH_4 and error analysis. The measured total CH_4 column abundance and X_{CH4} were determined to be 1.87 ± 0.02 ppm and 1.88 ± 0.02 ppm,

respectively. The IC-LHR has high potential to be developed as a compact, robust and unattended instrument for spacecraft, airborne or ground-based applications.

References

[1] G. Sonnabend, D. Wirtz, F. Schmülling, and R. Schieder. Tuneable heterodyne infrared spectrometer for atmospheric and astronomical studies, Applied Optics, 2002, 41 (15): 2978–2984.

[2] D. Weidmann and D. Courtois. Infrared 7.6-microm lead-salt diode laser heterodyne radiometry of water vapor in a CH_4-air premixed flat flame, Applied Optics, 2003, 42 (6): 1115–1121.

[3] D. Weidmann, W. J. Reburn, and K. M. Smith. Ground-based prototype quantum cascade laser heterodyne radiometer for atmospheric studies, Review of Scientific Instruments, 2007, 78 (7): 073107.

[4] D. Weidmann and G. Wysocki. High-resolution broadband (>100 cm^{-1}) infrared heterodyne spectro-radiometry using an external cavity quantum cascade laser. Optics Express, 2009, 17 (1): 248–259.

[5] D. Weidmann, B. J. Perrett, N. A. Macleod, and R. M. Jenkins. Hollow waveguide photomixing for quantum cascade laser heterodyne spectro-radiometry, Optics Express, 2011, 19 (10): 9074–9085.

[6] T. R. Tsai, R. A. Rose, D. Weidmann, and G. Wysocki. Atmospheric vertical profiles of O_3, N_2O, CH_4, CCl_2F_2, and H2O retrieved from external-cavity quantum-cascade laser heterodyne radiometer measurements, Applied Optics, 2012, 51 (36): 8779–8792.

[7] A. Hoffmann, N. A. Macleod, M. Huebner, and D. Weidmann. Thermal infrared laser heterodyne spectroradiometry for solar occultation atmospheric CO_2 measurements, Atmospheric Measurement Techniques, 2016, 9 (12): 5975–5996.

[8] D. Weidmann, A. Hoffmann, N. Macleod, K. Middleton, J. Kurtz, S. Barraclough, and D. Griffin. The methane isotopologues by solar occultation (miso) nanosatellite mission: spectral channel optimization and early performance analysis, Remote Sensing, 2017, 9 (10): 1073–1092.

[9] E. L. Wilson, M. L. McLinden, J. H. Miller, G. R. Allan, L. E. Ott, H. R. Melroy, and G. B. Clarke. Miniaturized laser heterodyne radiometer for measurements of CO_2 in the atmospheric column, Applied Physics B, 2014, 114 (3): 385–393.

[10] E. L. Wilson, A. J. Digregorio, V. J. Riot, M. S. Ammons, W. W. Bruner, D. Carter, J. P. Mao, A. Ramanathan, S. E. Strahan, L. D. Oman, C. Hoffman, and R. M. Garner. A 4 U laser heterodyne radiometer for methane (CH_4) and carbon

dioxide (CO_2) measurements from an occultation-viewing cubsat, Measurement Science and Technology, 2017, 28 (3): 035902.

[11] A. Rodin, A. Klimchuk, A. Nadezhdinskiy, D. Churbanov, and M. Spiridonov. High resolution heterodyne spectroscopy of the atmospheric methane NIR absorption, Optics Express, 2014, 22 (11): 13825–13834.

[12] J. Kurtz and S. O'Byrne. Multiple receivers in a high-resolution near-infrared heterodyne spectrometer, Optics Express, 2016, 24 (21): 23838–23848.

[13] M. Kim, C. L. Canedy, W. W. Bewley, C. S. Kim, J. R. Lindle, J. Abell, I. Vurgaftman, and J. R. Meyer. Interband cascade laser emitting at $\lambda = 3.75$ μm in continuous wave above room temperature, Applied Physics Letters, 2008, 92 (19): 191110.

[14] L. S. Rothman, I. E. Gordon, Y. Babikov, A. Barbe, D. Chris Benner, P. F. Bernath, M. Birk, L. Bizzocchi, V. Boudon, L. R. Brown, A. Campargue, K. Chance, E. A. Cohen, L. H. Coudert, V. M. Devi, B. J. Drouin, A. Fayt, J.-M. Flaud, R. R. Gamache, J. J. Harrison, J.-M. Hartmann, C. Hill, J. T. Hodges, D. Jacquemart, A. Jolly, J. Lamouroux, R. J. Le Roy, G. Li, D. A. Long, O. M. Lyulin, C. J. Mackie, S. T. Massie, S. Mikhailenko, H. S. P. Müller, O. V. Naumenko, A. V. Nikitin, J. Orphal, V. Perevalov, A. Perrin, E. R. Polovtseva, C. Richard, M. A. H. Smith, E. Starikova, K. Sung, S. Tashkun, J. Tennyson, G. C. Toon, V. G. Tyuterev, and G. Wagner. The HITRAN2012 molecular spectroscopic database, Journal of Quantitative Spectroscopy and Radiative Transfer, 2013, 130: 4–50.

Chapter 5 Wide-band near-infrared laser heterodyne radiometer

Objective

A wide-band fiber near-infrared laser heterodyne radiometer for the detection of the carbon isotope ratio of CO_2 gas in the atmosphere is demonstrated. A tunable external cavity diode laser operated in the near-infrared band is employed as the local oscillator, which makes the $^{13}CO_2$ and $^{12}CO_2$ can be measured in a wide band range. This device can provide an effective measurement method for the detection of stable isotope ratios in the atmosphere.

5.1 Introduction

Compared with the DFB lasers with a narrow output wavelength range, although the tunable external cavity diode laser has a larger volume and a higher price, its output spectral wavelength range is wide, and the intensity noise of the laser is small, the output optical power is stable, and it can be used in a wide spectral range. A series of spectral absorption peaks of CO_2 are continuously measured. Therefore, a laser heterodyne radiometer was established with a Tunable External Cavity Laser as the local oscillator source (EC-LHR), and the $^{12}CO_2$ and $^{13}CO_2$ in the atmosphere were measured in the range of 6248.5 cm^{-1} ~ 6256 cm^{-1}**.**

In the process of plants turning into petroleum, the decay of ^{14}C in their bodies is reduced. Because ^{13}C is a stable isotope, the content of ^{13}C in fossil fuels will not change over time, and because plants that form fossil fuels absorb ^{12}C instead of ^{13}C, Therefore, the ^{13}C content in fossil fuels is lower than the current ^{13}C content in atmospheric CO_2. Therefore, when fossil fuels burn, the abundance of ^{13}C in atmospheric CO_2 will decrease [1]. The influence of the combustion of chemical fuels on the atmosphere can be studied by detecting the concentration of ^{13}C in CO_2 in the atmosphere. Figure 5.1 shows the observational data of ^{12}C and ^{13}C in atmospheric CO_2 published by the World Meteorological Organization [1]. The emission of CO_2 in the atmosphere has increased year by year, as shown in Figure 5.1 (a), while the

content of 13C in atmospheric CO_2 has decreased year by year. As shown in Figure 5.1 (b), the ratio of carbon isotopes in CO_2 increases as shown in Figure 5.1 (c). Since there is no 13C in fossil fuels, it is inferred that the increase in CO_2 emissions caused by fossil fuels will reduce the content of isotopes in the atmosphere. Simultaneous observations of $^{12}CO_2$ and $^{13}CO_2$ indicate that the emission of fossil fuel combustion leads to a reduction in the ^{13}C content of atmospheric CO_2. Therefore, measuring the carbon isotope composition of CO_2 in the atmosphere can help identify and quantify the sources and sinks of CO_2.

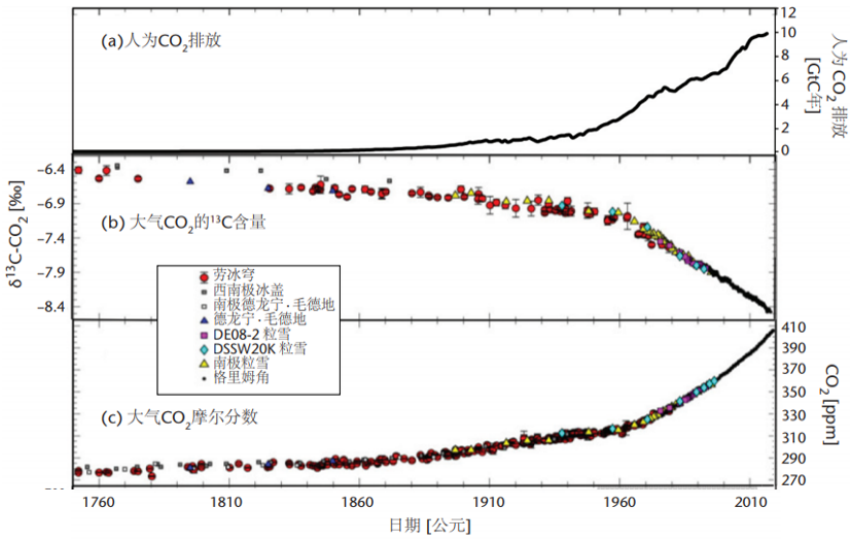

Figure 5.1 Changes in CO_2 and ^{13}C in the atmosphere [1]

The burning of fossil fuels emits CO_2 and the photosynthesis and respiration of plants leave their isotope signals in the atmosphere at different time and space scales. By detecting CO_2 gas and its isotope molecules, the sources and sinks of the atmospheric carbon cycle can be identified and measured [2]. Therefore, the use of stable carbon and oxygen isotopes of CO_2 in the atmosphere as a tracer to study the carbon cycle has become a research hotspot [3, 4]. In addition, the observational data of CO_2 and its stable isotopes can be used to speculate on the photosynthesis and respiration of plants and the contribution of fossil fuel combustion to CO_2 in the atmosphere. Remote sensing measurement technology can prevent the transmission of ground topography, boundary layer changes, and vertical air quality from affecting the

Measurement of atmospheric isotopes near the ground. Therefore, this chapter uses a wide-band external cavity laser to construct a laser heterodyne radiometer to detect $^{12}CO_2$ and $^{13}CO_2$ in the atmosphere.

5.2 LHR based on a tunable external cavity laser NIR laser (EC-LHR)

The schematic of the EC-LHR is shown in Figure 5.2. As the traditional structure of LHR, the laser and solar radiation modulated by a mechanical chopper are combined by a fiber combiner and beat in the surface of a photodetector. The current signal from the photodetector is amplified, filtered, and converted by the RF signal processing circuit, and demodulated by a lock-in amplifier. The signal of solar radiation power and the heterodyne signals are collected by an acquisition card. Solar radiation collecting structure (shown in Figure 5.3) is installed in the sun tracker and the collected power is transmitted by a single-mode fiber into the measurement system. The mechanical chopper was installed in front of the collimator with a focusing lens of 17 mm which can be adjusted by an optical adjustment frame. This structure makes the collimator and the solar tracker's lens have the same angle and follow the sun to move in unison. Then the direct sunlight can be collected into the measurement system. On a sunny day, the solar power that can be collected in the single-mode fiber can achieve 8 μW. The local oscillator is selected as the tunable external cavity laser on account of its wide working band. Its radiation is connected to the measurement system also by a single-mode fiber.

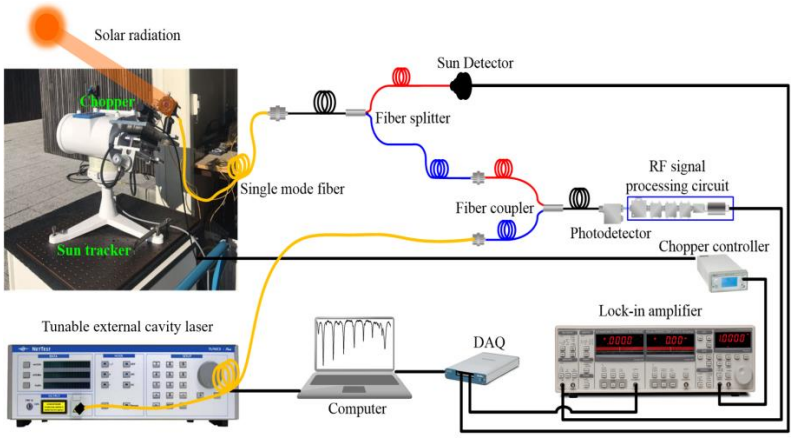

Figure 5.2 The schematic diagram of the EC-LHR

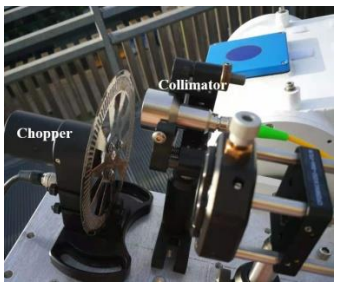

Figure 5.3 The collecting structure of solar radiation

The model of each component is shown in Table 5.1. A photodetector (InGaAs) with a responding band of 800 nm to 1700 nm is used and its electronic bandwidth (-3 dB) is 5 GHz. It can be connected by the FC/PC couple from a single-mode fiber and there is an active area diameter of 80 μm. The peak wavelength and peak responses are 1550 nm and 0.9 A/W respectively. A Bias-Tee with a bandwidth of 0.1 Hz to 4200 MHz is used to separate the DC signal and AC signal. In a fixed frequency, the insertion loss and isolation of the two inputs and the output of Bisa-Tee are approximately the same under different currents, this ensures the linearity of the response signal. Due to the selected RF frequency is around 250 MHz, the low noise amplifiers with the bandwidth of 0.1 Hz to 500 MHz and 20 MHz to 4 GHz are used to amplify the RF signal in series. When the power of 12V is applied, the gains over the measurement frequency are about 24.66 dB (292 times) and 20.1dB (102 times) respectively, so the overall gain after series connection can reach 44.76 dB (29780 times). A high pass filter with a passband of 225 MHz to 3 GHz and a low pass filter with a passband of DC to 270 MHz are used to filter the RF signal to reduce the measurement bandwidth. This can not only reduce the noise caused by the electronic measurement system but also improve the spectral resolution. The Schottky diode with a frequency range of 100 kHz to 2 GHz is used for converting the RF signal to low-frequency voltage. It is provided with a wide dynamic range of 10 μV to 5 V corresponding to the input power of -50 dBm to +20 dBm and a sensitivity of 1 mV/μW. The physical diagram of the RF signal processing circuit is fixed in a box shown in Figure 5.4. The single-mode fiber combiner with two inputs (60%: 40% for red and blue) has also been shown. The solar power detector can receive 10% of the

collecting solar radiation, and the rest is applied to be combined with the laser.

Table 5.1 Mode of components

Devices	Model
Photodetector	DET08CFC/M
Bias-Tee	ZFBT-4R2GW+
RF amplifier	ZFL-500LN+, ZX60-4016E-S+
Filters	BHP-250+, BLP-300+
Schottky diodes	DMH020BB
Lock-in amplifier	SR830
Sun power detector	DET410
Data acquisition card	IN USB-6361 (16bits)
Tunable External Cavity Laser	NetTest, TUNICS-Plus 3642 HE CL

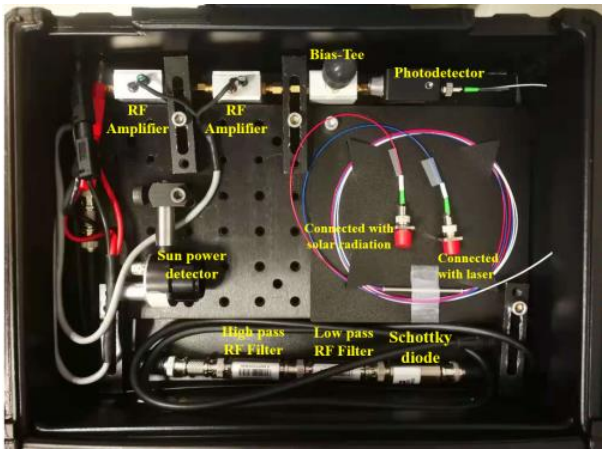

Figure 5.4 RF signal processing circuit

The output voltage from the Schottky diode is demodulated by a lock-in amplifier and is collected by a data acquisition card with an ADC resolution of 16 bits. The measurement of CO_2 in the atmosphere in a wide band mainly depends on the tunable external cavity laser (ECL: 448 × 133 × 370, 12.5 kg). The light source is composed of a laser diode installed in a Littman-Metcalf-type external cavity structure. The structure has been improved to enable the laser output wavelength to be continuously adjusted in the range of 1500 nm to 1640 nm. And the laser spectral purity can reach about 150 kHz which can be neglected compared with the electronic bandwidth (45 MHz) of the measurement system. Besides, the stability of laser power can reach ±

0.01 dB that is beneficial to calibrate measurement spectrum. The maximum power of the laser is about 5 mW. For characteristics of the laser wavelength, the absolute precision, repeatability, and resolution on a fixed wavelength are ± 0.04 nm, ± 0.005 nm, and 0.001 nm respectively.

5.3 Experimental detail

5.3.1. Choice of absorption lines

According to the working band of ECL, the reference data of CO_2 absorption lines was found in the HITRAN database. The measurement wavelength lies in 1598.3 nm ~ 1600.6 nm. In this band, the absorption line intensity is about $2.02\times e^{-25}$ cm/mol and $2.4\times e^{-23}$ cm/mol for molecules $^{13}CO_2$ and $^{12}CO_2$ respectively. The measured spectrum by Fourier transform spectrometer in this band is shown in Figure 5.5. The black font indicates the position of the absorption line of $^{12}CO_2$, and the red font indicates the position of the absorption line of $^{13}CO_2$. The laser work in this band to achieve atmospheric transmittance detection for $^{13}CO_2$ and $^{12}CO_2$.

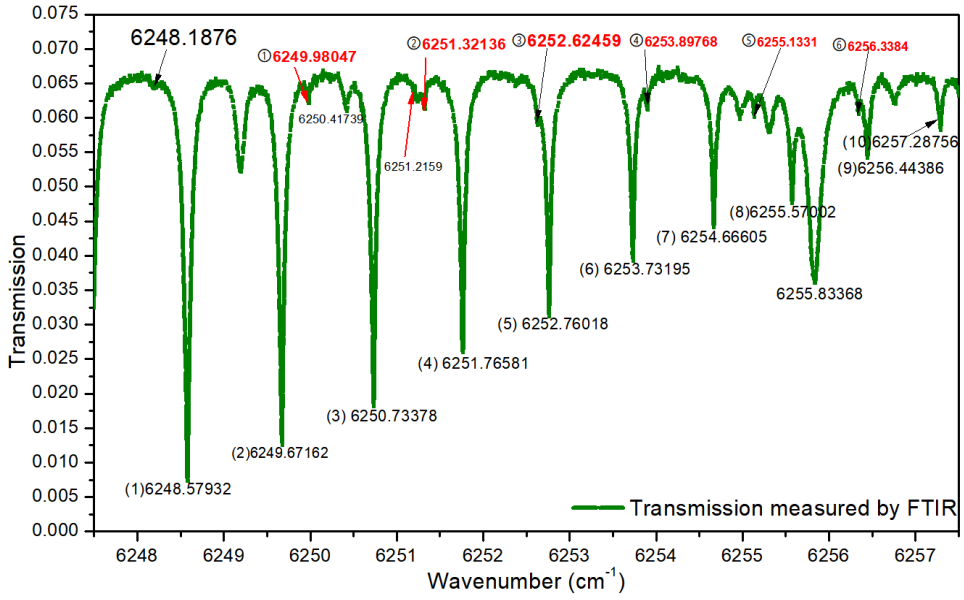

Figure 5.5 FTS measurement spectrum

5.3.2. Instrument lineshape

When the laser and sunlight were input to the measurement system, the frequency responses of RF signal were measured by a spectrum analyzer (Agilent CXA Signal Analyzer N900A) which are shown in Figure 5.6. The band of 10 MHz to 800 MHz was recorded. There is no RF filter for the black data. It can be seen that there is larger RF noise around 110 MHz. In order to filter the RF noise and diminish the electronic bandwidth, the RF filters in the range of 225 MHz ~ 270 MHz are used and the response were recorded as the red data. According to the RF response, the electronic band of 195 MHz ~ 324 MHz was retained in the measurement system and it can be transmitted into instrument lineshape(ILS) function shown in Figure 5.7. The spectral resolution of the measurement system is about 0.0086 cm^{-1}.

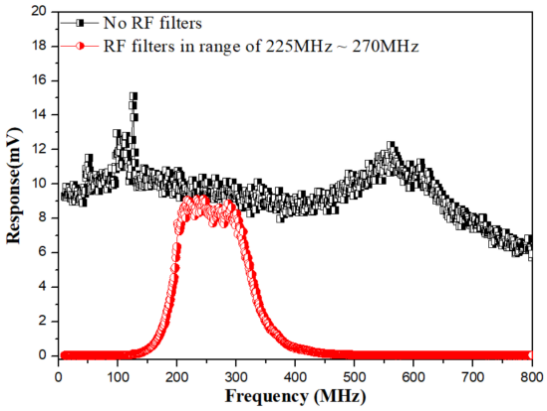

Figure 5.6 Response of RF signal

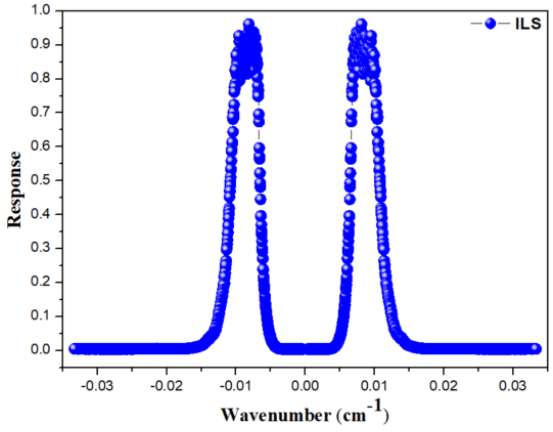

Figure 5.7 Instrument lineshape

5.4 Measurement spectrum and comparison

In the experiment, after a laser wavelength was set, there was an interval of 300 ms to wait for a stable wavelength. Then the data acquisition card collected 15000 points from the output of LIA (SR830) with a sampling rate of 20 kHz. These points were averaged in the program to one laser heterodyne signal corresponding to the current wavelength. The laser wavelength resolution and output power were set as 0.002 nm and 1.2 mW respectively. Parameters of LIA were set as integration time is 100 ms, roll-off is 24 dB, sensitivity 5 mV, and reference frequency is 588.8Hz. Each data in the spectrum is taken about 1.1 s. One of the measured atmospheric transmittances is shown in Figure 5.8 recorded at 16:00 on February 23, 2019. The experiment was conducted in Dunkirk, Northern Calais, France (51°2′6″ N, 2°22′9″ E). There were seven absorption lines of molecular $^{12}CO_2$ and five absorption lines of molecular $^{13}CO_2$ were detected in the spectrum.

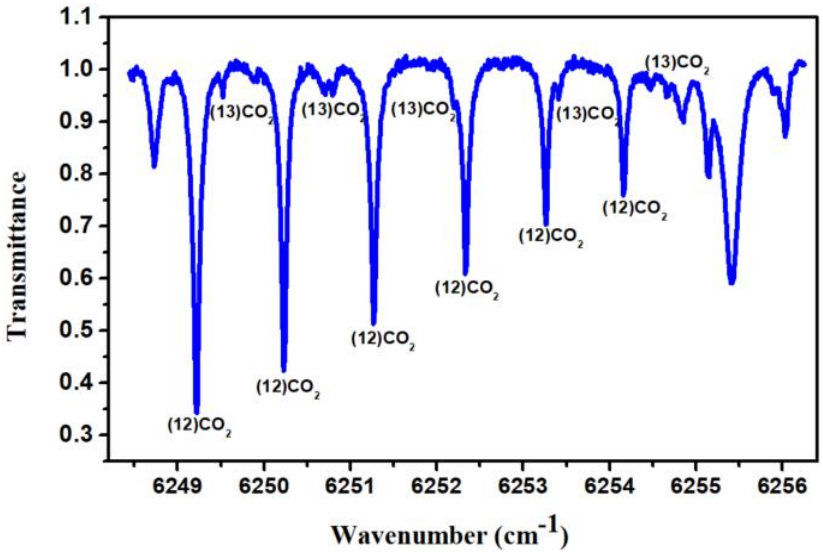

Figure 5.8 Atmospheric transmittance

The measurement spectrum (black) of the laser heterodyne radiometer is compared with the results of FTIR (red) at the TCCON observatory in Paris is shown in Figure 5.9. It can be seen that the SNR of the atmospheric transmittance spectrum obtained by EC-LHR is comparable to the FTIR.

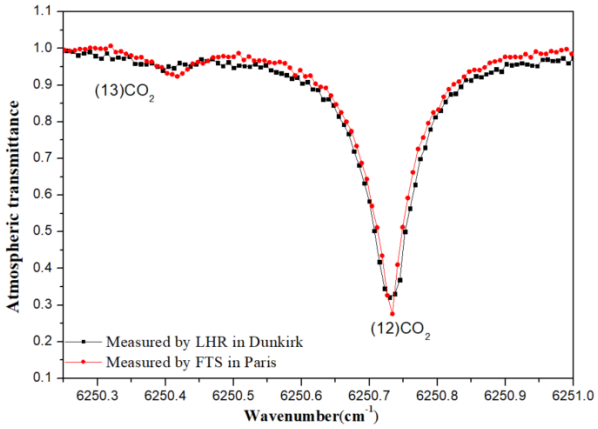

Figure 5.9 Comparison of the measured spectra of EC-LHR and FTIR

Summary

This chapter mainly introduces the device structure and measurement spectrum of EC-LHR. Achieve spectral detection of $^{12}CO_2$ and $^{13}CO_2$ in the atmosphere in the range of 6248.5 cm^{-1} ~ 6256.8cm^{-1} with a spectral resolution of 0.0086 cm^{-1}. The device provides a reference for the detection of wide-band laser heterodyne spectroscopy for the measurement of CO_2 and its isotope gases in the atmosphere.

References

[1] The State of greenhouse gases in the atmosphere based on global observations through 2018, WMO Greenhouse gas bulletin, 2019.11.25, No 15.

[2] C.Shan, W.Wang, C.Liu, X. Xu, Y. Sun, Y, Tian, W. Liu. Detection of stable isotopic ratio of atmospheric CO_2 based on Fourier transform infrared spectroscopy, Acta Physica Sinica, 2017, 66 (22): 149-157.

[3] M. Górka, D. Lewicka-Szczebak. One-year spatial and temporal monitoring of concentration and carbon isotopic composition of atmospheric CO_2 in a Wrocław (SW Poland) city area, Applied Geochemistry, 2013, 35:7-13.

[4] R. Wada, J. K. Pearce, T. Nakayama, Y. Matsumi, T. Hiyama, G. Inoue, T. Shibata. Observation of carbon and oxygen isotopic compositions of CO_2 at an urban site in Nagoya using Mid-IR laser absorption spectroscopy, Atmospheric Environment, 2011, 45 (5): 1168-1174.

Summary and perspectives

I Summary

Laser heterodyne spectroscopy detection technology has great applicant value for high spectral resolution detection of atmospheric GHGs. Based on the principle of laser heterodyne spectroscopy and the research and application of the laser heterodyne radiometer are conducted. The main works of the thesis are as follows:

(1) Use fiber optic devices which are fiber optic switch, fiber combiner, fiber splitter and single-mode fiber to establish a full-fiber NIR-LHR with a spectral resolution of 0.00442 cm^{-1}. The inversion results of the long-term observation data are well consistent with the GOSAT results and indicate that this measurement system can be used for the detection of CH_4 and CO_2 in the atmosphere.

(2) A full fiber IP-NIR-LHR is integrated, and the external field experiment was conducted in the Dachaidan, Qinghai province. In cloudless weather conditions, the atmospheric transmittance of CH_4 and CO_2 in the atmosphere with a SNR of about 250 can be obtained within 3 min.

(3) An ICL based mid-infrared LHR has been demonstrated in ground-based solar occultation mode. High-resolution (0.0033 cm^{-1}) LHR spectrum near 3.53 μm were obtained for simultaneous atmospheric observations of HDO and CH_4.

(4) Use a tunable outer cavity laser as a local oscillator light source to establish the EC-LHR with a spectral resolution of 0.0086 cm^{-1}. The absorption spectra of $^{12}CO_2$ and $^{13}CO_2$ in the whole atmosphere were measured and compare with the corresponding bands of the FTIR measurement spectrum.

II Perspectives

Due to the limitation of objective factors such as time and experimental conditions, there are still some deficiencies in the relevant research work, which requires further research, which puts forward a preliminary outlook for the future work:

（1） RF noise caused by the laser is an important factor affecting the SNR of laser heterodyne signal so that at the next step: the narrow line-wide fiber laser can be used as the local oscillator. Not it only can reduce the influence of the laser-induced RF noise on the heterodyne signal, but it also can improve the spectral resolution of the measurement system.

（2） To improve the structure design of IP-NIR-LHR. A secondary temperature control for the whole device can be designed to enable the instrument to work steadily. Establish a simple atmospheric simulation environment in the lab to verify and improve the inversion algorithm. IP-NIR-LHR should be compared repeatedly with other observation instruments to optimize the inversion algorithm.

（3） The laser heterodyne signals can be dealt with random resonance method to improve the SNR of the measured spectrum while improving the temporal resolution.

Résumé

L'augmentation de la concentration de gaz à effet de serre dans l'atmosphère entraîne un réchauffement climatique, qui a suscité une inquiétude généralisée dans la société. L'étude de l'atmosphère terrestre et la prévision des futurs changements climatiques sont étroitement liées à l'observation précise des concentrations de gaz à effet de serre. A l'heure actuelle, les instruments à haute résolution spectrale utilisés pour observer la concentration de gaz à effet de serre dans la colonne atmosphérique ont généralement de grandes tailles et de coûts élevés, ce qui ne permet pas de surveiller les gaz à effet de serre à grande échelle. Le radiomètre hétérodyne laser à haute résolution présente des avantages uniques, tels que petite taille, compact et robuste (donc portable), faible consommation d'énergie. Il est propice à la réalisation de l'observation mobile des gaz à effet de serre atmosphériques sur le terrain.

Cette thèse porte principalement sur le développement et l'application des radiomètres hétérodynes lasers fonctionnant dans l'infrarouge. Les principaux travaux et innovations de la thèse sont les suivants :

(1) Un LHR fonctionnant dans l'infrarouge prochain à double canaux tout fibré a été développé pour détecter simultanément le CH_4 et le CO_2 dans l'atmosphère. Dans le dispositif, un commutateur à fibre optique et d'autres dispositifs à fibre optique ont été utilisés pour améliorer considérablement la stabilité et la fiabilité du système de mesure. Des expériences d'observation continue ont été réalisées à Hefei, et les résultats des mesures sont approximativement cohérents avec les résultats de GOSAT. L'instrument intégré a également mené des observations sur le terrain dans la province du Qinghai. (2) Ensuite, un LHR fonctionnant dans l'infrarouge moyen utilisant un laser à cascade interbande a été démontré dans la fenêtre atmosphérique de 3-5 μm, pour la première fois, en mode d'occultation solaire au sol. Un spectre à haute résolution (0.0033 cm^{-1}) proche de 3.53 μm a été obtenu pour des observations atmosphériques simultanées de HDO et CH_4. (3) Enfin, un LHR utilisant un laser à cavité externe fonctionnant sur une large bande spectrale de 1500 à 1640 nm a été

développé pour la détection du $^{13}CO_2$ et du $^{12}CO_2$ dans l'atmosphère. Une mesure continue du spectre sur une plage de 6248.5 cm^{-1} à 6256 cm^{-1} a été réalisée. Afin d'enregistrer le spectre large bande de $^{13}CO_2$ et du $^{12}CO_2$ dans la colonne atmosphérise.

i.1 Preuve de concept radiomètre laser hétérodyne proche infrarouge (NIR-LHR)

Dans un premier temps, le développement d'une preuve de concept de radiomètre laser hétérodyne proche infrarouge basé sur deux lasers DFB (NIR-LHR) est présenté. Les modules clés (tracker solaire, commutateur à fibre optique, deux lasers DFB proche infrarouge, photomixer proche infrarouge) sont décrits et analysés. Le NIR-LHR développé a été testé à l'Institut d'optique et de mécanique fine d'Anhui, Science Island, Hefei, Chine. Des mesures au sol du CH_4 et du CO_2 dans la colonne atmosphérique ont été effectuées. (Note : Dans cette partie, pour les Figures, les tableaux et les formules, veuillez vous rappeler au Chapitre 2.)

La configuration expérimentale du NIR-LHR fibré est schématisée à la Figure 2.1. Le rayonnement solaire contenant des informations sur l'absorption atmosphérique est capté par un tracker solaire sur mesure équipé d'un collimateur à fibre (Thorlabs, FC/APC 1550), puis haché par un commutateur à fibre optique 1x2 (Angiltron, CL1x2) pour une amplification verrouillée de l'hétérodyne signaux. La précision de suivi du suiveur solaire peut atteindre 4×10^{-6} rad, ce qui est beaucoup plus petit que l'angle de divergence de la lumière solaire (9.6×10^{-3} rad). Ainsi, il peut répondre aux exigences du système de mesure laser hétérodyne. L'énergie solaire collectée qui a été produite par le collimateur à fibre peut varier de 5 W à 8 W au cours de la journée. Une fibre monomode a été utilisée pour connecter le collimateur à fibre et le commutateur à fibre optique. Un bras de sortie du commutateur optique est couplé à un oscillateur local centré à ~1.6 μm (DL1, NEL) via un coupleur de fibre (FC1), puis connecté à un photodétecteur haute vitesse (PD1, Thorlabs, DET08CFC, 5 GHz) pour la détection de CH4 hétérodyne. L'autre bras est séparé par un séparateur de fibre 5%: 95% (FS3), où la partie 5% est connectée au PD (Thorlabs, PDA20CS2)

pour suivre l'énergie solaire et génère le signal de référence, tandis que la partie restante est couplée à un oscillateur local centré à ~1.65μm (DL2, NEL) via FC2, puis connecté à un autre photodétecteur haute vitesse (PD2) pour la détection hétérodyne de CO_2. Avant que les deux faisceaux laser ne soient combinés avec le rayonnement solaire, 10% de la puissance des lasers sont divisés par les séparateurs de faisceaux à fibre (FS1, FS2) et entrent dans le mesureur de longueur d'onde (WM1, WM2) pour la longueur d'onde laser en temps réel. Les signaux de battement générés par PD1 et PD2 sont traités par deux modules de traitement de radiofréquence (RF) (RM1 et RM2), où la composante continue et la composante alternative sont extraites via un té de polarisation (mini-circuits) pour la surveillance puissances d'oscillateur local et traitement RF supplémentaire. Lors du traitement RF, les signaux RF sont d'abord amplifiés par trois amplificateurs (Mini-Circuits, ZX60), puis filtrés par un filtre passe-bande, et enfin convertis en signaux basse fréquence par une diode Schottky (HEROTE, DHM020BB) qui est démodulée au premier harmonique en utilisant un amplificateur à verrouillage (Stanford Research Systems, SR830) pour le signal hétérodyne. L'expérience du NIR-LHR primaire est illustrée à la Figure 2.2, et le suiveur solaire est installé sur le support de piste fixé à la fenêtre du laboratoire.

Contrairement au hacheur mécanique traditionnel, le commutateur à fibre optique (FOS) (Figure 2.6 (a)) présente les avantages d'une structure compacte, d'une faible consommation d'énergie, d'une longue durée de vie et d'une résistance aux chocs. Les signaux solaires modulés émis par les deux canaux du FOS sont illustrés à la Figure 2.6 (b). On constate que l'intensité de sortie des deux canaux est similaire et le taux de modulation peut atteindre plus de 90%. La puissance de sortie réelle de chaque canal est d'environ 310 nW.

LHR utilisant des lasers à diodes à rétroaction distribuée de télécommunication (DFB) en tant qu'oscillateurs locaux fonctionnant dans la région spectrale du proche infrarouge présentent leurs avantages uniques. Dans l'expérience, le contrôleur de diode laser du modèle LDC-3724B est utilisé pour contrôler la sortie de deux lasers DFB.

Le photodétecteur à grande vitesse (HS-PD, illustré à la Figure 2.8) avec une bande passante électronique de 5 GHz a été sélectionné comme mélange hétérodyne. Ses paramètres sont indiqués dans le tableau 2.1. Sa sensibilité de réponse proche de 1600 nm est d'environ 1 A/W et il a une puissance équivalente à faible bruit et un faible courant d'obscurité. Afin d'obtenir le couplage et l'adaptation maximum, le cavalier de fibre avec des connecteurs FC/APC et FC/PC a été utilisé entre le combineur de fibre et le photodétecteur à grande vitesse.

i.2 Mesures en laboratoire avec différentes résolutions

Un analyseur de spectre a été utilisé pour mesurer le spectre des signaux RF dans le système. D'après les résultats, il existe une grande quantité de bruit RF dans la bande de 10 MHz à 200 MHz, et selon l'analyse, ces bruits RF proviennent principalement du laser et le signal RF causé par le rayonnement du corps noir est minime. Ainsi, les filtres RF sont nécessaires pour supprimer le bruit RF en dessous de 200 MHz pour ce système. Selon la distribution du bruit RF, nous avons sélectionné deux types de filtres passe-bande pour les expériences.

i.2.1 Mesure avec une résolution de 0.0073 cm^{-1} et 0.0083 cm^{-1}

Lorsque les filtres passe-bande de [290, 400] MHz et [395, 520] MHz ont été utilisés dans le système, les fonctions ILS peuvent être obtenues à partir des données d'analyse spectrale des signaux RF . Sur la Figure 2.15, (a) et (b) sont les fonctions ILS pour mesurer respectivement le CH_4 et le CO_2, et les résolutions spectrales calculées sont 0.0073 cm^{-1} (CO_2) et 0.0083 cm^{-1} (CH_4). Les paramètres d'acquisition de données dans l'expérience avec la résolution de 0.0073 cm^{-1} (CO_2) et 0.0083 cm^{-1} (CH_4) sont présentés dans le tableau 2.2. Les signaux correspondants sont illustrés à la Figure 2.16, qui ont été mesurés le 17 avril 2019. Et un temps de balayage typique est d'environ 4 minutes.

i.2.2 Mesure avec une résolution de 0.00442 cm^{-1}

Lorsque les filtres passe-bande de [330, 375] MHz ont été utilisés dans le système, la bande passante électronique réelle (bande passante de 3 dB) du système de mesure est d'environ 66,3 MHz. Les fonctions ILS (illustrées à la Figure 2.17) peuvent être obtenues en fonction des données d'analyse du spectre de fréquence. Le chiffre du haut est la fonction ILS du canal de mesure CH4, et l'autre chiffre est la fonction ILS du canal de mesure CO_2. L'ordonnée est l'amplitude de réponse du système au signal RF, et l'abscisse représente la différence entre la fréquence de rayonnement dans le spectre solaire et le laser avec une fréquence de rayonnement fixe. La bande passante de réponse calculée du système est d'environ 132,6 MHz et la résolution spectrale est d'environ 0.00442 cm^{-1} pour le CH_4 et le CO_2. La puissance du signal RF dans cette bande passante est d'environ 0,15 µW, et cette puissance sera transformée en signaux basse fréquence par la diode Schottky. Graphique 2.18 montre une donnée de mesure pour le CH_4 et le CO_2 dans l'atmosphère, et les paramètres d'expérience correspondants sont dans le tableau 2.3. Les données de mesure des signaux hétérodynes de CH_4 et de CO_2 dans l'atmosphère sont présentées sur la Figure 2.18 (a) et (b). Les données de nombre d'onde correspondantes sont représentées sur les Figures 2.18 (c) et (d), respectivement. Les deux lasers DFB ont des variations de nombre d'onde de 0.97 cm^{-1} (CO_2) et de 1.83 cm^{-1} (CH_4). Lorsque le courant d'entraînement change de 0.1 mA, le nombre d'onde moyen change d'environ 0.00245 cm^{-1} (CO_2) et 0.00234 cm^{-1} (CH_4), et la résolution spectrale est plus petite (0.00442 cm^{-1}).

i.2.3 Comparatif et analyse de spectres avec différentes résolutions

On peut voir à partir de la Figure 2.16 (b) et de la Figure 2.18 (b) que lorsque la résolution spectrale est plus élevée, une structure spectrale plus fine peut être mesurée. La raie d'absorption (6056.508 cm^{-1}) du CO_2 a également été enregistrée dans le spectre de transmittance, montrant un phénomène de double pic. La position centrale du spectre solaire (6056.636 cm^{-1}) est la même que les résultats de mesure du FTS. En raison de la pression atmosphérique relativement faible dans la stratosphère, la

véritable largeur de raie du spectre d'absorption du CO_2 dans l'atmosphère est étroite. Lorsque la largeur de raie d'absorption est inférieure à la bande passante du filtre passe-bande et inférieure à la fréquence de coupure basse, les doubles pics apparaîtront dans le spectre de mesure, selon le principe du laser hétérodyne.

i.3 Résultats

Avant la récupération des données, les signaux NIR-LHR bruts doivent être prétraités, y compris la normalisation de l'intensité et l'étalonnage du nombre d'ondes. Compte tenu de l'équilibre entre SNR et résolution spectrale, les filtres passe-bande à [290, 400] MHz et [395, 520] MHz ont été choisis pour les détections de CO_2 et CH4 dans l'observation à long terme. Les nombres d'onde centraux des deux lasers DFB sont d'environ 6238.78 cm^{-1} (CO_2) et 6046.96 cm^{-1} (CH4). La partie inversion de données du travail est principalement réalisée par G. WANG.

Afin d'évaluer les résultats du NIR-LHR, des comparaisons avec les données GOSAT ont été effectuées pendant les jours ensoleillés pendant la période d'octobre 2018 à mai 2019. Les Figures 2.25 (a) et 2.25 (b) montrent la série chronologique des moyennes quotidiennes. Résultats de récupération NIR-LHR (avec écart type comme barre d'erreur) et résultats GOSAT de X_{CH4} et X_{CO2}, où les résultats GOSAT ont été sélectionnés dans un rayon de 3 degrés du site d'observation (Hefei, Chine, 31,9°N 117,16°E). Les écarts types se situent dans la plage de ppb pour X_{CH4} et pour [0.7, 2.2] ppm pour X_{CO2} pendant les mesures, ce qui correspond à une zone d'incertitude de 0.15%-0.7% pour X_{CH4} et 0.17%-0.5% pour le X_{CO2}, respectivement. Comme le montre la Figure 2.25 (a), pour les mesures de X_{CH4}, il existe un biais de ~10 ppb entre les résultats NIR-LHR et les résultats GOSAT, ce qui signifie que le X_{CH4} est sous-estimé par rapport aux mesures GOSAT. Alors que pour les mesures de X_{CO2} (illustrées à la Figure 2.25 (b)), les résultats NIR-LHR sont en bon accord avec les résultats GOSAT. À l'avenir, des analyses à plus long terme seront menées pour l'étude des variations saisonnières et annuelles du CO_2 et du CH_4 atmosphériques.

i.4 Conclusion

Un NIR-LHR entièrement fibré a été développé pour fonctionner en mode d'occultation solaire au sol. Un commutateur à fibre optique 1x2 est utilisé pour moduler le rayonnement solaire, ce qui rend le système plus stable et compact. Les spectres NIR-LHR à haute résolution du CO_2 et du CH_4 atmosphériques ont été obtenus en utilisant deux lasers DFB (1.6 μm et 1.65 μm) comme oscillateurs locaux. Après l'étalonnage de la puissance, les nombres d'onde ont été précisément étalonnés à l'aide d'une méthode de correction de corrélation. Par la suite, un algorithme d'extraction basé sur l'OEM et le RFM a été développé pour l'extraction des profils verticaux, des abondances moyennes sur colonne et des rapports de mélange dans l'air sec du CO_2 et du CH_4 atmosphériques. Enfin, les résultats NIR-LHR à long terme ont été validés en comparant les résultats GOSAT au cours de la même période, ce qui indique une région d'incertitude de 0.15%-0.7% pour X_{CH4} et 0.17%-0.5% pour X_{CO2}, respectivement. Le NIR-LHR démontré dans ce manuscrit a un grand potentiel pour être un instrument portable et à haute résolution spectrale pour la détection des gaz atmosphériques à plusieurs composants.

ii. Radiomètre hétérodyne laser proche infrarouge portable intégré (IP-NIR-LHR)

Deuxièmement, pour le développement ultérieur d'expériences sur le terrain, le développement d'un radiomètre hétérodyne à laser proche infrarouge portable intégré (IP-NIR-LHR) basé sur deux lasers DFB est présenté. Des mesures au sol du CH_4 et du CO_2 dans la colonne atmosphérique de Dachaidan (dans la province du Qinghai, Chine.) ont été effectuées. (Note : Dans cette partie, pour les Figures, les tableaux et les formules, veuillez vous rappeler au Chapitre 3.)

ii.1 Conception intégrée

Sur la base des recherches du chapitre 2, le diagramme schématique de l'IP-NIR-LHR a été conçu (illustré à la Figure 3.2). Les structures fibreuses (constituées du tracker solaire, du collimateur fibre, SMF, FOS, FS0, FS1, FC1, FS3, FC3) utilisées pour la génération du signal hétérodyne et du signal de référence sont les mêmes que celles de la Figure 2.1. Le module de traitement radiofréquence est également le même que la description du chapitre 2. Dans cette conception, afin d'intégrer tous les modules de contrôle dans un petit boîtier, deux contrôleurs à diode laser (LDC1, LDC2), deux compteurs de longueur d'onde et deux les amplificateurs de verrouillage doivent être miniaturisés.

Connectez les sorties des répartiteurs à deux faisceaux (FS2, FS4) et les entrées des combineurs à deux faisceaux (FC2, FC4), respectivement ; lorsque les longueurs des deux bras ne sont pas égales, les signaux d'interférence (IS1, IS2) liés aux longueurs d'onde de deux lasers DFB seront générés dans le photodétecteur (PD2, PD3), qui ont servi à calibrer les nombres d'onde. Sélectionnez la différence de longueur de fibre en fonction de la longueur d'onde du laser.

Deux préamplificateurs (PA1, PA2) ont été conçus pour amplifier les signaux basse fréquence des deux diodes Schottky. Les signaux de sortie (AC1, AC2) ont été collectés par la carte d'acquisition de données et traduits vers l'ordinateur personnel. Deux amplificateurs numériques verrouillables ont été programmés dans le PC pour démoduler l'AC1 et l'AC2. Les autres méthodes de traitement du signal et modes de balayage laser sont les mêmes que ceux présentés au chapitre 2. Les données du spectre d'absorption hétérodyne laser ont été collectées point par point.

La boîte intégrée (illustrée à la Figure 3.3) a été divisée en deux couches. La couche inférieure était équipée de convertisseurs de puissance, de chemins de fibre optique, d'un commutateur de fibre optique et d'un DAQ. La couche supérieure était équipée de circuits de commande laser, de lasers DFB, de deux modules de traitement radiofréquence, de deux préamplificateurs et de modules de puissance, etc. Les sorties de la fibre optique étaient connectées aux photodétecteurs correspondants sur la

couche supérieure. Chaque module sera décrit en détail ci-dessous.

ii.2 Observation de terrain à Dachaidan

Une observation de 20 jours a été menée dans le district de Dachaidan, préfecture autonome mongole-tibétaine de Haixi dans la province du Qinghai (37,7442°N, 95,3424°E). L'atmosphère dans cette zone est moins affectée par les activités humaines et peut être utilisée comme site d'observation de fond atmosphérique illustré à la Figure 3.18 (a) et (b). L'état d'observation de l'instrument dans l'expérience est illustré à la Figure 3.19. La fibre monomode transporte le rayonnement solaire collecté par le dispositif de réception de lumière du suiveur solaire dans l'IP-NIR-LHR pour la détection. Pour éviter le vent, le sable et la pluie à tout moment, l'IP-NIR-LHR est placé dans une tente pour travailler.

Après correction et filtrage du signal, le spectre d'absorption du méthane mesuré a été comparé aux résultats mesurés du FTIR. Comme le montre la Figure 3.23, comme le temps de mesure et l'emplacement des deux spectres sont incohérents, la position d'absorption du CH4 dans les deux spectres est la même et la profondeur d'absorption spectrale mesurée par FTIR est plus profonde que celle mesurée par IP-NIR- LHR. Cependant, le spectre solaire dans les deux spectres se chevauche presque, car le spectre solaire n'est pas affecté par le temps et l'emplacement, ce qui montre également la validité des données de mesure de l'instrument.

Réalisé sur le terrain selon les conditions météorologiques locales, la Figure 3.23 montre les résultats de mesure de la transmission atmosphérique du CH_4 et du CO_2 le 18 août, avant 14h00 du matin, la profondeur d'absorption du CH_4 et du CO_2 dans l'atmosphère a progressivement augmenté avec le temps, et la profondeur d'absorption des deux dans l'après-midi a progressivement diminué avec le temps. Le spectre d'absorption change lentement de 11h00 à 14h00 à midi, et change rapidement à d'autres moments. Le temps nécessaire à l'instrument pour collecter un spectre varie avec le changement d'intensité de la lumière solaire. Dans la plage de 5 min à 10 min,

le rapport signal/bruit du spectre peut être d'environ 250.

ii.3 Résultats de la récupération

La transmittance du CH_4 et du CO_2 mesurée à 9:32 le même jour a été inversée grâce à l'algorithme d'inversion. Les résultats d'ajustement des deux transmittances mesurées obtenus par calcul itératif sont illustrés à la Figure 3.25 (a),(c), respectivement. La Figure 3.25 (b),(d) est la différence résiduelle entre la transmittance mesurée du CH_4 et du CO_2 et la transmittance simulée. On peut voir que le résultat du calcul et le spectre mesuré peuvent être bien ajustés. La valeur absolue de l'erreur résiduelle est plus grande dans la zone avec le plus grand nombre d'ondes et le pic d'absorption. Cela est dû à la puissance de sortie laser plus faible dans la zone avec un nombre d'onde plus grand, ce qui réduit le rapport signal/bruit, tandis que la lumière du soleil est absorbée au pic d'absorption, le rapport signal/bruit du signal hétérodyne est ici inférieur au rapport signal sur bruit lorsqu'il n'y a pas d'absorption. D'après l'inversion du spectre mesuré du CH_4 et du CO_2, la concentration de la colonne de gaz CH_4 en dessous de 24 km est de 2.695×10^{19} moléculaire/cm^2, et la concentration de la colonne de gaz CO_2 est de 5.804×10^{21} moléculaire/cm^2. Cette partie du travail d'inversion est principalement effectuée par moi-même. Le principe et le processus d'inversion sont expliqués dans l'annexe 1 et l'annexe 2.

ii.4 Conclusion

Ce chapitre présente le développement de l'IP-NIR-LHR, conçoit le circuit de contrôle du courant de la diode laser et le circuit de contrôle de la température, combinés à l'amplificateur radiofréquence pour que la résolution spectrale du système de mesure atteigne 0.00442 cm^{-1}. La structure d'étalonnage de longueur d'onde laser est construite en utilisant le combineur de fibre optique et le séparateur de fibre optique. Le préamplificateur est conçu pour bloquer, filtrer et amplifier le signal de tension faible émis par le circuit de traitement du signal RF. Combiné avec

l'amplificateur à verrouillage numérique, le signal collecté est démodulé, et enfin le signal hétérodyne est moyenné. Lorsque le ciel est sans nuages, la totalité de la couche de transmission atmosphérique de CH_4 et de CO_2 avec un rapport signal/bruit d'environ 250 peut être obtenue toutes les 3 minutes. Cet instrument est le premier instrument de détection hétérodyne laser portable haute résolution en Chine, et sa capacité à observer sur le terrain a été vérifiée par des expériences dans la région de Dachaidan. L'étape suivante consiste à effectuer un contrôle de température secondaire sur cet instrument, à optimiser davantage la structure interne et à améliorer la stabilité de sa mesure. Améliorez le logiciel d'acquisition et de traitement des données pour permettre une observation sans surveillance.

iii. Radiomètre laser hétérodyne moyen infrarouge basé sur un laser en cascade interbande (IC-LHR)

Le développement d'un radiomètre laser hétérodyne moyen infrarouge (mid-IR) basé sur un laser en cascade interbande (IC-LHR) est présenté. L'IC-LHR développé a été testé à l'Institut d'optique et de mécanique fine d'Anhui, sur l'île des sciences, à Hefei, en Chine. Des mesures au sol du CH_4 et du HDO dans la colonne atmosphérique ont été effectuées. (Note : Dans cette partie, pour les Figures, les tableaux et les formules, veuillez vous rappeler au Chapitre 4.)

iii.1. Un IC-LHR fonctionnant à 3.53 µm

L'IC-LHR développé est représenté schématiquement sur la Figure 4.1. Et la Figure 4.2 montre l'image physique de l'IC-LHR. Il est composé d'un module de captation de la lumière solaire directe associé à un tracker solaire, un module de modulation du rayonnement solaire, et ICL, un photodétecteur, et un module d'extraction de signal hétérodyne, ainsi qu'un module de métrologie fréquentielle (dans notre cas, une longueur d'onde module de correction et les raies d'absorption du CH4 et de l'HDO extraites de la base de données Hitran ont été utilisées).

Le rayonnement solaire contenant des informations sur l'absorption atmosphérique a été capturé à l'aide d'un suiveur solaire fait maison et réfléchi dans le système par les réflecteurs (R1, R2, R3). Et puis, il a été haché à 2 kHz pour une amplification verrouillée du signal LHR par un hacheur contrôlé par un contrôleur de hacheur SR540. Les deux diaphragmes à iris (I1, I2) et deux réflecteurs (R3, R4) ont été utilisés pour marquer et ajuster le trajet de la lumière solaire afin qu'il soit colinéaire avec le trajet laser. Après un séparateur de faisceau 50T/50R (BS2), le faisceau solaire réfléchi a été dirigé vers PD3 focalisé par L3 (f = 25 mm, ZnSe) pour surveiller la fluctuation de l'intensité solaire pendant la mesure.

Un séparateur de faisceau (BS2) a été utilisé comme dispositif de mélange pour combiner le rayonnement solaire réfléchi avec le faisceau lumineux d'un ICL utilisé comme oscillateur local (LO). Le mode de sortie de l'ICL était contrôlé par un contrôleur à diode laser et un générateur de signaux. Les faisceaux combinés étaient concentrés sur un photodétecteur à haute vitesse au tellurure de mercure et de cadmium (PD1, Vigo PV-2TE-4 avec un préamplificateur personnalisé), qui avait à la fois DC ([0,1] MHz, pour surveiller la puissance ICL) et AC ([1 kHz, 100 MHz], pour la détection LHR en radiofréquence (RF)) par L1 (f = 25 mm, ZnSe). Les diaphragmes à iris de I3 et I4 ont été utilisés pour aider à ajuster la colinéarité de LO et du rayonnement solaire.

Le rayonnement solaire contenant les informations d'absorption atmosphérique a été converti dans le domaine RF via PD1, suivi d'un filtre passe-bande (constitué de F1 : [10 MHz, 3 GHz] et F2 : [DC, 60 MHz] utilisé pour déterminer la bande passante de détection RF qui définit la forme de ligne de l'instrument (ILS) du système LHR. Par la suite, le signal RF après le filtre passe-bande a été converti en un signal continu par une diode Schottky (HEROTE, DHM020BB) et démodulé au premier harmonique à l'aide d'un amplificateur de verrouillage (Stanford Research Systems, SR830) avec la fréquence de découpage comme référence. Le signal LHR peut finalement être obtenu en réglant la fréquence laser sur les raies d'absorption moléculaire cibles.

Une petite fraction du faisceau ICL réfléchi par BS1 a été utilisée pour

l'étalonnage de la longueur d'onde : un miroir à bascule (R5) a dirigé le faisceau ICL soit vers un étalon de germanium de 50.8 mm (avec une plage spectrale libre d'environ 0.0246 cm^{-1}) suivi d'un enregistrement PD2. signal de frange étalon ou à un ondemètre (Bristol Instruments, 621) pour des mesures de fréquence absolue ou pour la métrologie de fréquence relative.

Un ordinateur portable personnel équipé d'une carte DAQ (National Instruments, USB-6366) et du logiciel LabVIEW a été utilisé pour l'acquisition de données et le contrôle des instruments (contrôle du suiveur solaire, réglage de la fréquence et lecture du nombre d'ondes). Les signaux de 5 canaux ont été recodés : les sorties en phase (X) et en quadrature (Y) de l'amplificateur de verrouillage pour la compensation de phase du signal LHR en utilisant les identités de somme et de différence d'angle (identités trigonométriques), la sortie CC de PD1 pour le suivi de la puissance ICL, le signal de PD2 pour l'étalonnage de la longueur d'onde relative et le signal de PD3 pour le suivi de la variation de la puissance solaire.

iii.2 Caractéristiques des dispositifs clés impliqués dans l'IC-LHR

iii.2.1 Interband cascade laser

L'oscillateur local utilisé était un ICL à rétroaction distribuée (illustré à la Figure 4.3(a)) fonctionnant autour de 3.53 μm et monté sur le TO-66. Il y avait une lentille de collimation pour façonner le faisceau de sortie. L'image thermique du faisceau laser collimaté à une distance de 3.0 m de la facette laser est illustrée à la Figure 4.3(b). Autour de 3.53 μm, le spectre de puissance de sortie de l'ICL est illustré à la Figure 4.3(c). Ce laser peut être réglé grossièrement sur ~10 cm^{-1} en ajustant la température à un courant constant ou avec précision sur ~1 cm^{-1} en ajustant le courant d'injection à une température constante.

Les relations entre le nombre d'ondes laser, la puissance laser et le courant d'injection laser sont illustrées à la Figure 4.4. Pendant la mesure LHR, la température et le courant laser ont été réglés à 14 °C et 30 mA pour sonder les raies d'absorption

CH_4 et HDO situées autour de 2831.92 cm^{-1} (CH_4 @ 2831.9199 cm^{-1} avec une intensité de raie spectrale de 1.622 × e^{-21} cm/mol ; HDO @ 2831.841 cm^{-1} avec une intensité de raie spectrale de 3.014 × e^{-24} cm/mol. Les données sont récupérées dans la base de données HITRAN). L'accord de fréquence du laser peut être effectué en modifiant le courant laser point par point via un contrôleur laser ou en balayant le courant d'injection avec une forme d'onde de fonction commune (telle qu'une forme d'onde sinusoïdale ou triangulaire).

iii.2.2 Traqueur solaire dans l'espace de liberté

Le suiveur solaire utilisé dans IC-LHR a été conçu par T. Tan et Y. Cao. Il peut suivre le soleil de manière constante et refléter la lumière directe du soleil dans le LHR. Dans le processus de poursuite, la trajectoire du faisceau incident sur le LHR par le suiveur solaire reste inchangée. Sa précision de suivi des axes X et Y était de 0,068° et 0,06°. La Figure 4.5 (a) montre la propagation du faisceau solaire dans le suiveur solaire. Le principe de fonctionnement du tracker solaire est le suivant : Combinez l'application Labview pour obtenir l'heure locale ainsi que la longitude et la latitude locales via le module GPS externe. Selon les informations de l'heure, la latitude et la longitude, l'élévation et l'azimut du soleil sont calculés et convertis en nombre d'impulsions pour entraîner les moteurs pas à pas S1 et S2. De cette façon, la quantité de mouvement du moteur pas à pas est contrôlée séparément. Lorsque le capteur d'image CCD capte le spot solaire (comme indiqué dans l'ensemble de la Figure 4.5 (a)), le décalage de la position centrale du spot peut être obtenu grâce au traitement d'image, qui peut être converti en nombre d'impulsions à contrôler les moteurs pas à pas finement. Le suiveur solaire fait maison est illustré à la Figure 4.5 (b).

R1, R2 et R3 ont réfléchi le faisceau solaire dans le système IC-LHR. Dans l'expérience, la position du faisceau solaire doit rester fixe. Cela joue un rôle important dans le battement entre le laser et le faisceau solaire dans l'espace de liberté. Afin de vérifier la stabilité du faisceau réfléchi du suiveur solaire, un autre capteur d'image CCD (taille : 38 mm × 38 mm, pixel : 5120 × 3840) a été placé à la position

du système IC-LHR pour collecter les coordonnées de le centre de masse de la tache solaire. Nous avons utilisé ce tracker solaire pour suivre le solaire pendant deux heures et obtenu la dérive de la particule centrale du capteur CCD sur l'axe X et l'axe Y. Les résultats sont présentés à la Figure 4.6.

L'angle entre tous les deux pixels est de 0,01°. Les écarts des axes X et Y sont similaires à la distribution gaussienne et sont principalement distribués dans l'intervalle de [-0,01°, +0,01°]. Cela peut essentiellement répondre aux besoins du battement entre le laser et le rayonnement solaire.

iii.2.3 Mélangeur photo infrarouge moyen

Le Photomixer (Vigo, PC-2TE-4-0.1 × 0.1-TO8-wBaF2-70) est composé de HgCdTe, dont les descriptions sont présentées dans le tableau 4.1. Il s'agit d'un détecteur photovoltaïque doté de caractéristiques hautes performances dans la plage spectrale de 2.3 à 4.2 μm et d'un refroidissement thermoélectrique à deux étages. L'image physique et la disposition mécanique du photomélangeur infrarouge moyen sont illustrées à la Figure 4.7 (a) et (b). Le FOV de 70° et la zone active de 0.1 × 0.1 mm^2 sont bons pour l'incidence des faisceaux.

La sensibilité du photomélangeur infrarouge moyen est illustrée à la Figure 4.8. Autour de la raie d'absorption de 3.531 μm, la réactivité est d'environ 1. C'est un détecteur photovoltaïque. L'amplificateur de transimpédance intégré (BIP-1K-100M) à l'intérieur du photodétecteur peut amplifier la composante CA (signal RF) dans la plage de [1 kHz, 150 MHz]. Dans deux conditions (laser d'entrée et couvrir la surface du photodétecteur), les signaux de sortie ont été collectés par un analyseur de spectre (Agilent Technologies, N9000A), comme le montre la Figure 4.9. Dans la plage de 10 MHz à 60 MHz, il y a moins de bruit RF. Ainsi, les filtres RF passe-haut de 10 MHz (Crystek corporation, CHPFL-0010-NC) et DC ~ 60 MHz (Mini-Circuits BLP-70+) sont utilisés pour filtrer le signal RF.

iii.4. Sélection de bande passante

Comme le montre la Figure 4.13. la forme de signal hétérodyne est dominée par le signal LO (ICL), et le photomixer peut extraire le signal LHR de la ligne de base de fond en dessous de 150 MHz. Cependant, il y avait plusieurs pics indésirables entre 70 MHz et 120 MHz, ce qui pourrait introduire du bruit supplémentaire dans le signal LHR. Par conséquent, les filtres passe-bande de 10 MHz ~ 60 MHz ont été choisis dans l'expérience, ce qui a donné une résolution spectrale à double bande latérale de ~ 100 MHz (0.0033 cm^{-1}) du système. L'encart de la Figure 4.13 montre l'ILS réellement utilisé pour la récupération des données.

iii.5. Spectre de mesure du CH_4 atmosphérique et du HDO à Hefei

Le résultat expérimental, mesuré depuis notre institut (Hefei, Chine, 31,9°N 117.166°E) le 21 juin 2016, est illustré à la Figure 4.14 (b), où la compensation de phase a traité les données LHR. De plus, la transmittance de la vapeur HDO atmosphérique et du CH_4 dans la région spectrale considérée est calculée en utilisant un modèle direct. Les résultats sont présentés sur la Figure 4.14 (b), qui ont été acquis à une fréquence d'échantillonnage de 50 Hz en entraînant le courant laser avec une onde sinusoïdale (0.0125 Hz (80 s), 0.5 Vpp).

Avant la récupération des données, les données brutes LHR doivent être prétraitées. Tout d'abord, le décalage du signal LHR, où le courant d'injection vers l'ICL est égal à zéro, a été soustrait. Ensuite, le signal LHR est divisé par le signal d'intensité ICL (signal DC) pour la normalisation du signal LHR. Lorsque de grandes fluctuations de l'énergie solaire (plus de 10% de l'intensité moyenne de l'énergie solaire) se produisaient pendant le balayage, les données LHR ne seraient pas prises en compte pour une analyse plus approfondie. Dans un troisième temps, un étalonnage fréquentiel du signal LHR a été réalisé à l'aide de fréquences relatives (signal d'étalon de germanium) et de fréquences absolues d'un ondemètre ou des positions des raies d'absorption (de la base de données HITRAN). Dans le présent travail, les pics du signal étalon ont été ajustés à une fonction polynomiale d'ordre 5 pour déterminer la fréquence relative des points de données, et la position de la ligne

CH_4 (2831.92 cm^{-1}) a été utilisée pour calibrer la fréquence absolue. De plus, un facteur d'échelle et un décalage ont été utilisés pour un étalonnage de fréquence supplémentaire en fonction des résultats de l'ondemètre et du calcul du modèle direct. Enfin, les résultats calibrés du LHR ont été interpolés avec le même intervalle de fréquence que le modèle direct, puis le spectre LHR traité est maintenant prêt (points bleus sur la Figure 4.16 (a)) pour une récupération de données supplémentaire afin d'inverser le spectre LHR au profils de concentration verticaux correspondants.

Le principal travail de récupération des données a été réalisé par G. Wang. La Figure 4.16 (a) montre les données IC-LHR prétraitées et le spectre ajusté sur la région spectrale de 2831.64 à 2832.07 cm^{-1} avec un intervalle de 0.001 cm^{-1}. Le processus itératif est illustré dans l'encadré de la Figure 4.16 (a), où χ^2/m égal à ~1.05 est obtenu après 6 itérations. Les résidus entre les données prétraitées et le résultat ajusté sont illustrés à la Figure 4.16 (b), où la distribution aléatoire indique un ajustement bien configuré. Les profils de CH_4 et de vapeur d'eau récupérés (Figure 4.16 (c) et Figure 4.16 (d)) sont calculés en multipliant le facteur d'échelle récupéré par le profil a priori. Sur la base des profils de CH_4 et de vapeur d'eau récupérés, l'abondance totale de la colonne de vapeur d'eau est calculée à ~2868 ppm (ou ~$5.8E^{+23}$ molécules/cm^2), l'abondance totale de la colonne de méthane et son rapport de mélange dans l'air sec (X_{CH4}) sont respectivement de ~1.875 ppm (ou ~$3.8E^{+20}$ molécules/cm^2) et ~1.88 ppm (partie par million). L'erreur de récupération totale des facteurs à deux échelles a été calculée à ~6% et ~8%, respectivement.

iii.6. Conclusion

Un LHR moyen infrarouge basé sur ICL a été démontré, pour la première fois, en mode d'occultation solaire au sol. Un spectre LHR à haute résolution (0.0033 cm^{-1}) proche de 3.53 m a été obtenu pour des observations atmosphériques simultanées de vapeur d'H_2O et de CH_4. Un algorithme de récupération basé sur OEM et RFM a été développé pour la récupération des profils verticaux de H_2O et CH_4 et l'analyse des erreurs. L'abondance totale mesurée de la colonne CH_4 et X_{CH4} a été déterminée à

1.87 ± 0.02 ppm et 1.88 ± 0.02 ppm, respectivement. L'IC-LHR a un potentiel élevé pour être développé en tant qu'instrument compact, robuste et sans surveillance pour les engins spatiaux, les applications aéroportées ou au sol.

iv. Radiomètre laser hétérodyne à large bande proche infrarouge

Un radiomètre laser hétérodyne dans le proche infrarouge à fibre large bande pour la détection du rapport isotopique du carbone du gaz CO_2 dans l'atmosphère est démontré. Un laser à diode à cavité externe accordable fonctionnant dans la bande du proche infrarouge est utilisé comme oscillateur local, ce qui permet de mesurer le $^{13}CO_2$ et le $^{12}CO_2$ dans une large bande. Ce dispositif peut fournir une méthode de mesure efficace pour la détection de rapports isotopiques stables dans l'atmosphère. (Note : Dans cette partie, pour les Figures, les tableaux et les formules, veuillez vous rappeler au Chapitre 5.)

iv.1 LHR basé sur un laser NIR à cavité externe accordable (EC-LHR)

Le schéma de l'EC-LHR est illustré à la Figure 5.2. Comme la structure traditionnelle du LHR, le laser et le rayonnement solaire modulés par un hacheur mécanique sont combinés par un combineur de fibres et battent à la surface d'un photodétecteur. Le signal de courant provenant du photodétecteur est amplifié, filtré et converti par le circuit de traitement de signal RF, et démodulé par un amplificateur de verrouillage. Le signal de puissance de rayonnement solaire et les signaux hétérodynes sont collectés par une carte d'acquisition. La structure de collecte du rayonnement solaire (illustrée à la Figure 5.3) est installée dans le suiveur solaire et la puissance collectée est transmise par une fibre monomode au système de mesure. Le hacheur mécanique a été installé devant le collimateur avec une lentille de focalisation de 17 mm qui peut être ajustée par un cadre de réglage optique. Cette structure fait que le collimateur et la lentille du suiveur solaire ont le même angle et suivent le soleil pour se déplacer à l'unisson. Ensuite, la lumière directe du soleil peut être collectée dans le système de

mesure. Par une journée ensoleillée, l'énergie solaire qui peut être collectée dans la fibre monomode peut atteindre 8 μW. L'oscillateur local est choisi comme laser à cavité externe accordable en raison de sa large bande de travail. Son rayonnement est relié au système de mesure également par une fibre monomode.

Le modèle de chaque composante est présenté dans le tableau 5.1. Un photodétecteur (InGaAs) avec une bande de réponse de 800 nm à 1700 nm est utilisé et sa bande passante électronique (-3 dB) est de 5 GHz. Il peut être connecté par le couple FC/PC à partir d'une fibre monomode et a un diamètre de zone active de 80 μm. La longueur d'onde maximale et les réponses maximales sont respectivement de 1550 nm et 0.9 A/W. Un Bias-Tee avec une bande passante de 0.1 Hz à 4200 MHz est utilisé pou séparer le signal DC et le signal AC. A fréquence fixe, la perte d'insertion et l'isolement des deux entrées et de la sortie du Bisa-Tee sont approximativement les mêmes sous des courants différents, cela assure la linéarité du signal de réponse. Étant donné que la fréquence RF sélectionnée est d'environ 250 MHz, les amplificateurs à faible bruit avec une bande passante de 0.1 Hz à 500 MHz et de 20 MHz à 4 GHz sont utilisés pour amplifier le signal RF en série. Lorsque la puissance de 12 V est appliquée, les gains sur la fréquence de mesure sont respectivement d'environ 24.66 dB et 20.1 dB, de sorte que le gain global après connexion en série peut atteindre 44.76 dB. Un filtre passe-haut avec une bande passante de 225 MHz à 3 GHz et un filtre passe-bas avec une bande passante DC à 270 MHz sont utilisés pour filtrer le signal RF afin de réduire la bande passante de mesure. Cela peut non seulement réduire le bruit causé par le système de mesure électronique, mais également améliorer la résolution spectrale. La diode Schottky avec une plage de fréquence de 100 kHz à 2 GHz est utilisée pour convertir le signal RF en tension basse fréquence. Il est doté d'une large plage dynamique de 10 μV à 5 V correspondant à une puissance d'entrée de -50 dBm à +20 dBm et une sensibilité de 1 mV/μW. Le schéma physique du circuit de traitement du signal RF est figé dans un boîtier illustré à la Figure 5.4. Le combineur de fibre monomode à deux entrées (60% : 40% pour le rouge et le bleu) a également été présenté. Le détecteur d'énergie solaire peut recevoir 10% du

rayonnement solaire collecté, et le reste est appliqué pour être combiné avec le laser.

La tension de sortie de la diode Schottky est démodulée par un amplificateur de verrouillage et est collectée par une carte d'acquisition de données avec une résolution ADC de 16 bits. La mesure du CO_2 dans l'atmosphère dans une large bande dépend principalement du laser à cavité externe accordable (ECL : 448 × 133 × 370, 12.5 kg). La source lumineuse est composée d'une diode laser installée dans une structure à cavité externe de type Littman-Metcalf. La structure a été améliorée pour permettre à la longueur d'onde de sortie laser d'être ajustée en continu dans la plage de 1500 nm à 1640 nm. Et la pureté spectrale du laser peut atteindre environ 150 kHz ce qui peut être négligé par rapport à la bande passante électronique (45 MHz) du système de mesure. De plus, la stabilité de la puissance laser peut atteindre ± 0.01 dB, ce qui est bénéfique pour calibrer le spectre de mesure. La puissance maximale du laser est d'environ 5 mW. Pour les caractéristiques de la longueur d'onde laser, la précision absolue, la répétabilité et la résolution sur une longueur d'onde fixe sont respectivement de ± 0.04 nm, ± 0.005 nm et 0.001 nm.

iv.2 Spectre de mesure et comparaison

Selon la bande de travail de l'ECL, les données de référence des raies d'absorption du CO_2 ont été trouvées dans la base de données HITRAN. La longueur d'onde de mesure se situe entre 1598.3 nm ~ 1 600.6 nm. Dans cette bande, l'intensité de la raie d'absorption est d'environ $2.02\times e^{-25}$ cm/mol et $2.4\times e^{-23}$ cm/mol pour les molécules $^{13}CO_2$ et $^{12}CO_2$ respectivement. Le spectre mesuré par le spectromètre à transformée de Fourier dans cette bande est illustré à la Figure 5.5. La police noire indique la position de la raie d'absorption du $^{12}CO_2$, et la police rouge indique la position de la raie d'absorption du $^{13}CO_2$. Le laser fonctionne dans cette bande pour réaliser la détection de la transmittance atmosphérique pour le $^{13}CO_2$ et le $^{12}CO_2$.

Lorsque le laser et la lumière du soleil ont été entrés dans le système de mesure, les réponses en fréquence du signal RF ont été mesurées par un analyseur de spectre

(Analyseur de signal Agilent CXA N900A) qui est illustré à la Figure 5.6. La bande de 10 MHz à 800 MHz a été enregistrée. Il n'y a pas de filtre RF pour les données noires. On peut voir qu'il y a un bruit RF plus important autour de 110 MHz. Afin de filtrer le bruit RF et de diminuer la bande passante électronique, les filtres RF dans la plage de 225 MHz à 270 MHz sont utilisés et la réponse a été enregistrée en tant que données rouges. Selon la réponse RF, la bande électronique de 195 MHz ~ 324 MHz a été conservée dans le système de mesure et elle peut être transmise dans la fonction de forme de ligne de l'instrument (ILS) illustrée à la Figure 5.7. La résolution spectrale du système de mesure est d'environ 0.0086 cm^{-1}.

Dans l'expérience, après avoir défini une longueur d'onde laser, il y avait un intervalle de 300 ms pour attendre une longueur d'onde stable. Ensuite, la carte d'acquisition de données a collecté 15000 points à partir de la sortie du LIA (SR830) avec un taux d'échantillonnage de 20 kHz. Ces points ont été moyennés dans le programme à un signal laser hétérodyne correspondant à la longueur d'onde actuelle. La résolution de la longueur d'onde du laser et la puissance de sortie ont été fixées respectivement à 0.002 nm et 1.2 mW. Les paramètres de LIA ont été définis car le temps d'intégration est de 100 ms, le roll-off est de 24 dB, la sensibilité de 5 mV et la fréquence de référence est de 588,8 Hz. Chaque donnée du spectre est prise environ 1.1 s. L'une des transmissions atmosphériques mesurées est illustrée à la Figure 5.8 enregistrée à 16h00 le 23 février 2019. L'expérience a été menée à Dunkerque, dans le nord de Calais, en France (51°2′6″ N, 2°22′9″ E) . Il y avait sept raies d'absorption du $^{12}CO_2$ moléculaire et cinq raies d'absorption du $^{13}CO_2$ moléculaire ont été détectées dans le spectre.

Le spectre de mesure (noir) du radiomètre laser hétérodyne est comparé avec les résultats du FTIR (rouge) à l'observatoire TCCON à Paris est représenté sur la Figure 5.9. On constate que le SNR du spectre de transmittance atmosphérique obtenu par EC-LHR est comparable au FTIR.

iv.3 Conclusion

Ce chapitre présente principalement la structure de l'appareil et le spectre de mesure de l'EC-LHR. Réalisez la détection spectrale de $^{12}CO_2$ et $^{13}CO_2$ dans l'atmosphère dans la plage de 6248.5 cm^{-1} à 6256.8 cm^{-1} avec une résolution spectrale de 0.0086 cm^{-1}. L'appareil fournit une référence pour la détection de la spectroscopie hétérodyne laser à large bande pour la mesure du CO_2 et de ses gaz isotopiques dans l'atmosphère.

Mots clés : radiomètre hétérodyne laser ; télédétection au sol ; abondances moyennes sur colonne ; infrarouge moyen (MIR) ; proche infrarouge (NIR)

Appendix

Appendix 1 Forward model

1. Atmospheric structure

The research on atmospheric greenhouse gas measuring instruments not only needs to understand the basic theory of measurement technology but also needs to fully understand the characteristics of the measurement target so that more reasonable measurement requirements and experimental parameters can be put forward.

Generally, the atmosphere can be divided into the troposphere, stratosphere, mesosphere, thermosphere, and exosphere according to the vertical structure of the atmospheric temperature field, as shown in Figure A1.1. The troposphere is the lowest layer of the atmosphere. The height of the troposphere is approximately between 10 km and 15 km. Almost all water vapor is distributed in the troposphere, and its mass accounts for about 80% of the total mass of the earth's atmosphere. As the altitude increases, the temperature decreases. In addition, the vertical mixing process in the troposphere proceeds quickly due to convection and turbulence. Most weather phenomena occur in the troposphere and are closely related to human life. The exchange of matter and energy between the troposphere and the stratosphere has always been one of the problems to be solved in atmospheric science.

The top of the stratosphere is generally between 45 km and 55 km, and the temperature is around 270 K. Because atmospheric ozone absorbs solar ultraviolet radiation, its temperature increases with altitude, so the vertical mixing process proceeds slowly. The top of the mesosphere is generally between 80 km and 90 km, and its temperature will decrease with the increase in altitude. Its characteristics are similar to those of the troposphere, and rapid vertical mixing can also be carried out. The top of the thermosphere is about 500 km. Because N_2 and O_2 in this layer absorb the solar short-wave radiation strongly, the temperature of in thermosphere changes significantly. Therefore, the vertical mixing process carried out in it is quite fast.

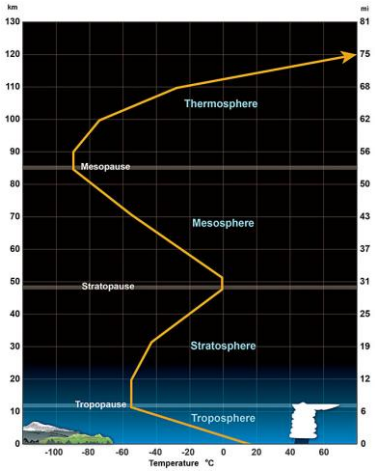

Figure A1.1 Average temperature profile for the lower layers of the atmosphere. (https://www.weather.gov/jetstream/layers)

Combining the hydrostatic formula and the ideal gas algorithm, the change of atmospheric pressure p(z) with height z can be derived [1] as:

$$\frac{\partial p(z)}{\partial z} = -\frac{M_{air}\, p(z)}{RT(z)} \tag{A1.1}$$

In the formula, Mair is the average molecular weight of air (28.97g/mol), R(g) is the molar gas constant, and T(z) is the temperature at the geometric height z. The pressure of the earth's atmosphere can change by 6 to 7 orders of magnitude.

2. Basic of molecular absorption

The absorption of various gas components in the atmosphere attenuates the radiation energy. The study of the law of gas absorption of radiation is mainly to study the influence of O_2, O_3, H_2O, CO_2, N_2O, CH_4, et al. in the atmosphere on radiation. It is generally believed that O_2, CO_2, N_2O, and CH_4 in the atmosphere are relatively stable and uniform. O_3 and H_2O have great temporal and spatial changes, and they are also the most active and vital absorption gases. The absorption of sunlight by gas molecules in the atmosphere has wavelength selectivity, and the absorption of the same atmospheric component at different wavelengths is different.

(1) Line position of molecular absorption

The value of the position of the gas absorption line is related to the motion state

and energy of the molecule [1]. The energy (E) of a molecule can be expressed as the sum of the following motion states:

$$E = E_t + E_r + E_v + E_e \quad \text{(A1.2)}$$

In the formula, E_t represents the kinetic energy of the movement of a single molecule; E_r is the rotational energy of molecules; E_v is the molecular vibrational energy; E_e is the electron orbital energy. The three forms of energy represented by the latter three are quantized, and their values are discrete. For gas molecules, the change in E_e is generally the largest, the change in E_v is in the middle, and the change in E_r is the smallest. When a molecule absorbs or emits a photon, the energy level of the molecule changes.

In the infrared and microwave spectrum, molecular absorption is caused by changes in molecular rotation and vibrational state. A spectrum has the characteristics of absorption position v, line intensity S, and line width γ. The transition wavenumber is determined by the energy E_i of the initial state and the energy E_f of the final state, expressed as the following formula:

$$\hat{v} = \frac{E_f - E_i}{hc} \quad \text{(A1.3)}$$

The most important absorbing gases in the near-infrared spectral region are H_2O, CO_2, O_2, CH_4. Each molecule has specific absorptions and emission lines due to its specific molecular structure. Table A1.1 lists the absorption bands of solar radiation by gas molecules in the atmosphere in the near-infrared band.

Table A1.1 The absorption bands of gas molecules in the atmosphere

Molecules	Center wavenumber (cm^{-1})	Spectral band (cm^{-1})
H_2O	5348	4800 ~ 6200
	7246	6400 ~ 7600
CO_2	5000	4700 ~ 5200
	6250	6100 ~ 6450
	7143	6850 ~ 7000
O_2	6329	6300 ~ 6350
CH_4	6005	5850 ~ 6100

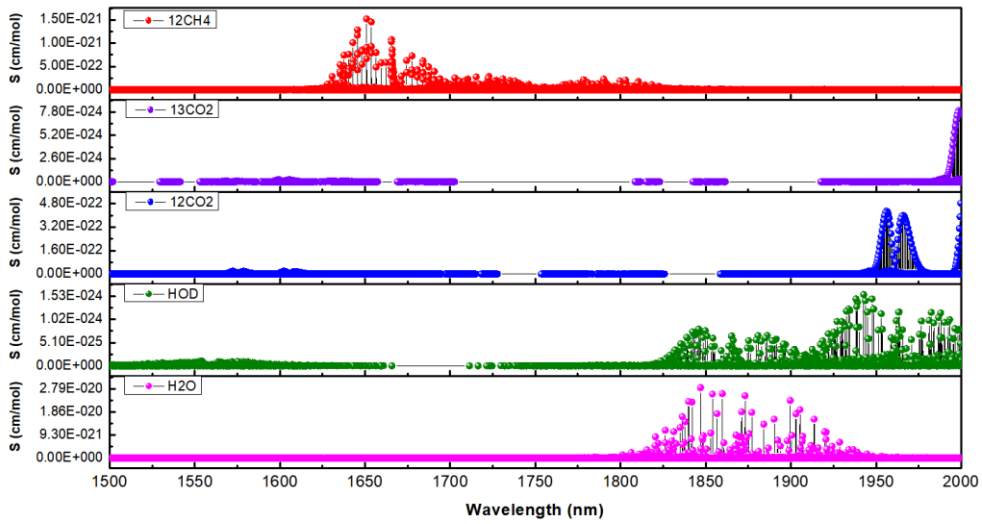

Figure A1.2 Molecular absorption line and intensity

Figure A1.2. shows the absorption line position, and corresponding absorption intensity of some molecules ($^{12}CO_2$, $^{13}CO_2$, CH_4, H_2O, HDO) downloaded from the Hitran database in the wavelength range of 1500 nm to 2000 nm.

(2) Line strength of molecule absorption

For the electric dipole transition, the line strength is determined by the square of the temperature correlation matrix elements of the electric dipole moment and other factors such as Boltzmann distribution and stimulated emission [2-4]. The line strength is expressed as:

$$S(\mathrm{T}) = \frac{8\pi^3}{3hc}\frac{g_i I_a}{Q(\mathrm{T})}\hat{\nu}e^{-E_i/kT}\left[1-e^{-hc\hat{\nu}/kT}\right]R_{if}\cdot 10^{-36} \tag{A1.4}$$

Where T is the temperature, g_i is the degeneracy of the nuclear spin in the low-energy state, I_a is the relative abundance of the isotope, Q(T) is the total number of partitions, and the R_{if} is the transition probability given by the matrix element of the electric dipole operator.

(3) Absorption broadening

In practice, a single absorption line will be broadened into a spectrum with a certain line width. The broadening of the spectral line mainly comes from the processes of natural broadening, collision broadening, and Doppler broadening. The

collision broadening in the bottom atmosphere is more important.

(3.1) Collision broadening

Collision widening is also called pressure widening. Under pressure, the absorption cross-section of a single radiation transition broadens. Generally described by the Lorentzian line type, expressed as the following formula [2, 4]:

$$g_L(v) = \frac{\gamma_L / \pi}{(v-\hat{v})^2 + \gamma_L^2} \tag{A1.5}$$

Where γ_L is the Lorentz HWHM, which is proportional to the pressure and decreases with the increase of temperature.

(3.2) Doppler broadening

The thermal motion of the molecule causes the Doppler broadening of the absorption spectrum, which is described by the Gaussian line type [2] as shown in the following formula:

$$g_D(v) = \frac{1}{\gamma_D}\left(\frac{\ln 2}{\pi}\right)^{1/2} \cdot \exp\left[-\ln 2\left(\frac{v-\hat{v}}{\gamma_D}\right)^2\right] \tag{A1.6}$$

The HWHM is determined by line position, temperature, and molecular mass.

(3.3) Compound broadening

When pressure broadening and Doppler broadening exist at the same time, it is described by the Voigt line type. The combined effect of the two expansion mechanisms can be simulated by convolution [2], which is expressed as:

$$g_v(v-\hat{v}, \gamma_L, \gamma_D) \equiv g_L \otimes g_D = \int_{-\infty}^{\infty} dv' g_L(v-v'; \hat{v}, \gamma_L) \times g_D(v'-\hat{v}; \hat{v}, \gamma_D) \tag{A1.7}$$

Where c1=1.0692, c2=0.086639 corresponds to an accuracy of 0.02%. The absorption line width of atmospheric molecules decreases as the height increases. At lower altitudes, the absorption line width is mainly determined by the pressure broadening, but when the altitude reaches a certain level, it gradually tends to Doppler broadening.

3. Atmospheric transmittance simulation

(1) Absorption cross-section

For the absorption cross-section k (v, z) of a single absorption line, it is the product of the line strength S(T) and the broadening mechanism described by the normalized linear function g(v). It can be simplified as the following formula [2]:

$$k(v, z) = S(T(z)) \cdot g(v, P(z), T(z)) \tag{A1.8}$$

Where z is the altitude. In practice, the same absorption cross-section will be affected by the absorption of multiple molecules. Generally, the sum of all absorption cross-sections [2] is taken and expressed as:

$$k_m(v, z) = \sum_i S_i^{(m)}(T(z)) \cdot g(v; \hat{v}_i^{(m)}, \gamma_i^{(m)}(P(z), T(z))) \tag{A1.9}$$

Where m represents the species of molecular, and i represents the absorption of isotopic molecules of each molecule, $\hat{v}$ represents the central wavenumber of the absorption line.

(2) Absorption coefficient

The absorption coefficient is the product of the absorption cross-section and the molecular concentration. At different altitudes, the concentration of the same gas in the atmosphere is different. Assuming that the pressure (p) and temperature (T) in the i-th layer of the atmosphere are uniformly distributed, there are m kinds of molecules and the corresponding concentration at the altitude of z_l is n_m, then the absorption coefficient [2] of this layer of atmosphere is expressed as:

$$\alpha_l(v; z) = \sum_m k^{(m)}(v, p_l, T_l) \cdot n_m(z_l) + \alpha^{(c)}(v; z) \tag{A1.10}$$

Where α(c) is the continuous absorption coefficient between molecules.

(3) Optical depth

In the l-th layer of the atmosphere, the optical thickness τ_l of the l-th layer can be obtained by integrating the path z taken by the absorption coefficient [2]:

$$\tau_l(v) = \int_{z_l}^{z_{l+1}} \alpha_l(v) dz \tag{A1.11}$$

(4) Monochromatic Transmission

From Beer's law, the monochromatic light transmittance of the medium can be

obtained [2]:

$$\mathrm{T}(v,s)=\exp(-\int_0^s \alpha(v,\mathrm{s})ds) \tag{A1.12}$$

The expression in parentheses of the e index is the optical depth.

The calculation of atmospheric transmittance in this paper is based on Py4CAts, which is a Python script used to calculate the atmospheric spectrum [2], and it is a rewrite of the infrared radiation transmission code written in Fortran. The computationally intensive code part uses python's highly optimized numerical processing. Each step of infrared or microwave radiation transmission calculation is executed in a separate script, so molecular lines in any spectral range can be extracted. The absorption cross-section can be calculated by line-by-line integration based on the actual pressure and temperature.

The first is to obtain the absorption information (such as the position of the absorption line, the intensity of the absorption line at different temperatures, etc.) of the target molecule within the specified wavelength range from the Hitran or Geisa database. Combining the vertical profile of atmospheric temperature and pressure shared by ECMWF, the molecular absorption cross-section in a specific wavelength range can be calculated layer by layer. In the case of ignoring continuous absorption, the absorption coefficient of each layer of molecules is calculated using the product of the gas concentration profile and the absorption cross-section. The optical depth is obtained by integrating the absorption coefficient of each layer according to the path. Finally, take the e index for the optical depth to calculate the atmospheric transmittance.

References

[1] M. Wendisch,P. Yang. Theory of atmospheric radiative transfer, First Edition. Weinheim, Germany: Wiley-VCH,2012.

[2] F. Schreier, S. Gimeno García, P. Hochstaffl, S. Städt. Py4CAtS-python for computational atmospheric spectroscopy, Atmosphere, 2019, 10 (5): 262.

[3] R. H. Norton, C. P. Rinsland. Atmos data processing and science analysis method,

Applied Optics, 1991, 30 (4): 389-400.

[4] A. Dudhia. The Reference Forward Model (RFM), Journal of Quantitative Spectroscopy & Radiative Transfer, 2017, 186: 243-253.

Appendix 2 Retrieval method

1. Understanding of the retrieval problem

According to the basic theory of atmospheric transmittance simulation introduced in Appendix 1, the atmospheric absorption spectrum under certain conditions can be approximately calculated. The absorption spectrum detected by the laser heterodyne measurement device is affected by the noise in the measurement process, so there is an error between the real spectrum and the measured spectrum, so an error term ε needs to be introduced between the simulated spectrum and the measured spectrum. The forward model [1] for simulating atmospheric transmittance can be expressed as:

$$\exp(-A\cdot X)\cdot(a+bv+cv^2)+\varepsilon = Y(\mathrm{X},a,b,c,v) \quad \text{(A2.1)}$$

Where Y = $(y_1, y_2,\cdots y_j, \cdots y_m)^T$, (j = 1,2,3...m), y_j represents the spectral value at each wavenumber; X = $(x_1, x_2,\cdots x_i, \cdots x_n)^T$, (i=1,2,3...n), x_i represents the concentration of gas in each layer of the atmosphere; A = αij, (i=1,2,3…m; j=1,2,3…n), αij represents the absorption coefficient at each wavenumber in each layer of the atmosphere. v represents the wavenumber, and the introduction of a, b, and c is to describe the laser power. The concentration profile is inverted using the inversion algorithm developed by D. Weidoman [1-3] et al.

This algorithm is based on the best estimation method (OEM) [4] to determine the cost function and uses the Levenberg-Marquardt method to solve the concentration profile iteratively to minimize the cost function finally and obtain the optimal solution.

2. Approximate linear problems solving

Suppose there is a set of measured values **y** = $(y_0, y_1, y_2,\ldots, y_m)$ and a set of values **x** = $(x_0, x_1, x_2, \ldots, x_n)$ to be inverted. Assuming that the relationship between the **x** and **y** is linear. Then the linear equation can be expressed in the form of a matrix as:

$$\boldsymbol{y} = \mathbf{K}\boldsymbol{x} \quad \text{(A2.2)}$$

Where K is a matrix composed of equation coefficients, $\mathbf{y}^{\mathbf{T}} = (y_0, y_1, \ldots, y_m)$, $\mathbf{x}^{\mathbf{T}} = (x_0, x_1, \ldots, x_n)$. When n = m and K^{-1} exists, the solution of the equation is $K^{-1}y$. When K^{-1} does not exist, K is a singular matrix. When n > m, The equation has many possible solutions. When n < m, the number of equations is greater than the number of unknowns. This problem is over-determined. There are enough channels in the spectrum measurement to formulate the equation to make m > n.

For this over-determined problem, there is no exact solution, and the best solution (**x)** needs to be found. Define the error corresponding to the best solution **x** as **e** = **y**-**Kx**, and the sum of squares of the error represents the cost function:

$$\chi^2 = \boldsymbol{e}^{\mathrm{T}}\boldsymbol{e}=(\boldsymbol{y}-\mathbf{K}\boldsymbol{x})^{\mathrm{T}}(\boldsymbol{y}-\mathbf{K}\boldsymbol{x}) \tag{A2.3}$$

When a set of solutions minimizes χ^2, then this set of solutions is the best solution. This method is called the least-squares method, and the function that needs to be minimized is called the cost function (or penalty function). Differentiate the above formula to get the following formula:

$$\mathbf{K}^{\mathrm{T}}\mathbf{K}\boldsymbol{x}=\mathbf{K}^{\mathrm{T}}\boldsymbol{y} \tag{A2.4}$$

This equation is the ordinary equation and can be solved by the usual methods.

When **x** and **y** are linear approximations, the relationship between the two can be written as:

$$\boldsymbol{y} = F(\boldsymbol{x}) \tag{A2.5}$$

Where F is called the forward model.

Due to errors in measurement and calculation, each element in **x** and **y** can be regarded as a random variable. They can be described by Probability Density Function (PDF) [4]. Assume that the PDF of **x** and **y** before measurement are P(**x**) and P(**y**), respectively. The PDF of **x** after the measurement is P(**x**|**y**). Then according to Bayesian theory, we can get:

$$P(\boldsymbol{x}|\,\boldsymbol{y}) = \frac{P(\boldsymbol{y}|\,\boldsymbol{x})P(\boldsymbol{x})}{P(\boldsymbol{y})} \tag{A2.6}$$

P(y|x) can be obtained by using the forward model and measurement instrument. When $\hat{\boldsymbol{x}}$ is found to maximize P(x|y), then $\hat{\boldsymbol{x}}$ is the optimal solution of **x**. This method is called the Maximum A-posteriori Probability (MAP) method.

In order to perform the next calculation, it is necessary to guess the PDF of the random variable. Suppose **v** is a random variable in vector form, N is the number of measurements, and the j-th measurement value is $\mathbf{v}_j$, and the mean square value of **v** is defined as:

$$\bar{\boldsymbol{v}} = \frac{1}{N}\sum_{j=1}^{N}\boldsymbol{v}_j \tag{A2.7}$$

The covariance matrix (**S**) of **v** is used to measure the change of the sampling points relative to its average value. It can be expressed as follows:

$$\boldsymbol{S} = \frac{1}{N-1}\sum_{j=1}^{N}(\boldsymbol{v}_j - \bar{\boldsymbol{v}})(\boldsymbol{v}_j - \bar{\boldsymbol{v}})^{\mathbf{T}} \tag{A2.8}$$

Each diagonal element of the covariance matrix is the variance of each element in **v**, and each off-diagonal element is the covariance of every two different elements in **v**. It is generally assumed that the PDF of the random vector **v** is normally distributed, which can be expressed as follows:

$$P\ \bar{\boldsymbol{v}}\ = \frac{1}{(2\pi)^{\frac{n}{2}}|\boldsymbol{S}|^{\frac{1}{2}}}\exp\left(-\frac{1}{2}(\boldsymbol{v}-\bar{\boldsymbol{v}})^{\mathbf{T}}\boldsymbol{S}^{-1}(\boldsymbol{v}-\bar{\boldsymbol{v}})\right) \tag{A2.9}$$

Where $\bar{\boldsymbol{v}}$ is the average value of **v**, **S** is the covariance matrix of **v**, and P(**v**) can also be expressed as:

$$-2\ln P(\boldsymbol{v}) = (\boldsymbol{v}-\bar{\boldsymbol{v}})^{\mathbf{T}}\boldsymbol{S}^{-1}(\boldsymbol{v}-\bar{\boldsymbol{v}}) + \boldsymbol{c}_1 \tag{A2.10}$$

Among them, **c**1 is a constant that does not correlate with **v**. When **v** is equal to the average value, P(**v**) has the maximum value.

Similarly, for a random vector **x**, P(**x**) can be expressed as follows:

$$-2\ln P(\boldsymbol{x}) = (\boldsymbol{x}-\boldsymbol{x}_a)^{\mathbf{T}}\boldsymbol{S}_a^{-1}(\boldsymbol{x}-\boldsymbol{x}_a) + c_2 \tag{A2.11}$$

Where $\mathbf{x}_a$ is the prior profile of **x**, and it is the best-estimated profile before measurement. P(y|x) is expressed [4] as:

$$-2\ln P(\boldsymbol{y}|\boldsymbol{x}) = (\boldsymbol{y}-F(\boldsymbol{x}))^{\mathbf{T}}\boldsymbol{S}_y^{-1}(\boldsymbol{y}-F(\boldsymbol{x}))+\boldsymbol{c}_3 \quad \text{(A2.12)}$$

The meaning of P(**y**|**x**) is to find the possibility of **y** given **x**. The variation range of **y** is determined by the covariance matrix $\mathbf{S_y}$ of the measurement error. According to Bayesian theory, combining the above formulas, the equation about P(**x**|**y**) is [4]:

$$-2\ln P(\boldsymbol{x}|\boldsymbol{y})+\boldsymbol{c}_4 = (\boldsymbol{x}-\boldsymbol{x}_a)^T\boldsymbol{S}_a^{-1}(\boldsymbol{x}-\boldsymbol{x}_a)+(\boldsymbol{y}-F(\boldsymbol{x}))^{\mathbf{T}}\boldsymbol{S}_y^{-1}(\boldsymbol{y}-F(\boldsymbol{x})) \quad \text{(A2.13)}$$

Where **c**4 contains **c**2, **c**3, and P(**y**), to find the solution of MAP is to find the solution that minimizes the cost function on the right side of the above formula. The $\mathbf{z^TMz}$ form is called the quadratic form, and the quadratic form on the right side of the above equation can also be written as the following equation [4]:

$$-2\ln P(\boldsymbol{x}|\boldsymbol{y})+\boldsymbol{c}_4 = (\boldsymbol{x}-\hat{\boldsymbol{x}})^{\mathbf{T}}\hat{\boldsymbol{S}}^{-1}(\boldsymbol{x}-\hat{\boldsymbol{x}}) \quad \text{(A2.14)}$$

Among them $\hat{\boldsymbol{x}}$ is the MAP profile to be searched, and $\hat{\boldsymbol{S}}$ is the covariance matrix. When the forward model is linear, the equation for the best-estimated value $\hat{\boldsymbol{x}}$ can be found. The above formula can be rewritten as [4]:

$$(\boldsymbol{x}-\hat{\boldsymbol{x}})^{\mathbf{T}}\hat{\boldsymbol{S}}^{-1}(\boldsymbol{x}-\hat{\boldsymbol{x}}) = (\boldsymbol{x}-\boldsymbol{x}_a)^{\mathbf{T}}\boldsymbol{S}_a^{-1}(\boldsymbol{x}-\boldsymbol{x}_a)+(\boldsymbol{y}-\mathbf{K}\boldsymbol{x})^{\mathbf{T}}\boldsymbol{S}_y^{-1}(\boldsymbol{y}-\mathbf{K}\boldsymbol{x}) \quad \text{(A2.15)}$$

Expanding the above formula, the corresponding equations about **x** is:

$$\boldsymbol{x}^{\mathbf{T}}\hat{\boldsymbol{S}}^{-1}\boldsymbol{x} = \boldsymbol{x}^{\mathbf{T}}\boldsymbol{S}_a^{-1}\boldsymbol{x}+\boldsymbol{x}^{\mathbf{T}}\mathbf{K}^{\mathbf{T}}\boldsymbol{S}_y^{-1}\mathbf{K}\boldsymbol{x} \quad \text{(A2.16)}$$

The covariance of the MAP profile is obtained as:

$$\hat{\boldsymbol{S}}^{-1} = \boldsymbol{S}_a^{-1}+\mathbf{K}^{\mathbf{T}}\boldsymbol{S}_y^{-1}\mathbf{K} \quad \text{(A2.17)}$$

Through further calculation, the MAP profile [4] is:

$$\hat{\boldsymbol{x}} = (\boldsymbol{S}_a^{-1}+\mathbf{K}^{\mathbf{T}}\boldsymbol{S}_y^{-1}\mathbf{K})^{-1}(\boldsymbol{S}_a^{-1}\boldsymbol{x}_a+\mathbf{K}^{\mathbf{T}}\boldsymbol{S}_y\boldsymbol{y}) \quad \text{(A2.18)}$$

$$\text{or} \quad \hat{\boldsymbol{x}} = \boldsymbol{x}_a+(\boldsymbol{S}_a^{-1}+\mathbf{K}^{\mathbf{T}}\boldsymbol{S}_y^{-1}\mathbf{K})^{-1}\mathbf{K}^{\mathbf{T}}\boldsymbol{S}_y^{-1}(\boldsymbol{y}-\mathbf{K}\boldsymbol{x}_a) \quad \text{(A2.19)}$$

Generally, the contribution function (**D**) [4] is defined as:

$$D = \frac{d\hat{\boldsymbol{x}}}{d\boldsymbol{y}} \quad \text{(A2.20)}$$

For the MAP solution, it can be expressed by **D** as:

$$\hat{\boldsymbol{x}} = \boldsymbol{x}_a+\boldsymbol{D}(\boldsymbol{y}-\mathbf{K}\boldsymbol{x}_a) \quad \text{(A2.21)}$$

Then the expression of the contribution function can be written as [4]:

$$\boldsymbol{D} = \boldsymbol{S}_a \mathbf{K}^{\mathbf{T}} (\mathbf{K}\boldsymbol{S}_a \mathbf{K}^{\mathbf{T}} + \boldsymbol{S}_y)^{-1} \tag{A2.22}$$

3. Non-linear problem solving

When the forward model is nonlinear, the cost function can be derived from Bayesian theory by using the method similar to solving linear problems, and the following form is obtained [4]:

$$\boldsymbol{\chi}^2(\boldsymbol{x}) = (\boldsymbol{x} - \boldsymbol{x}_a)^{\mathbf{T}} \boldsymbol{S}_a^{-1} (\boldsymbol{x} - \boldsymbol{x}_a) + (\boldsymbol{y} - F(\boldsymbol{x}))^{\mathbf{T}} \boldsymbol{S}_y^{-1} (\boldsymbol{y} - F(\boldsymbol{x})) \tag{A2.23}$$

When it is assumed that the prior profile has Gaussian statistics, the first term on the right side of the equation has no nonlinearity, and the second term can introduce nonlinearity F(**x**). In the nearly linear case, using $\mathbf{y}_L$+**K**(**x**-$\mathbf{x}_L$) to approximate F(**x**), the cost function can be rewritten as [4]:

$$\boldsymbol{\chi}^2(\boldsymbol{x}) = (\boldsymbol{x} - \boldsymbol{x}_a)^{\mathbf{T}} \boldsymbol{S}_a^{-1} (\boldsymbol{x} - \boldsymbol{x}_a) + (\boldsymbol{y} - \boldsymbol{y}_L - \mathbf{K}(\boldsymbol{x} - \boldsymbol{x}_L))^{\mathbf{T}} \boldsymbol{S}_y^{-1} (\boldsymbol{y} - \boldsymbol{y}_L - \mathbf{K}(\boldsymbol{x} - \boldsymbol{x}_L)) \tag{A2.24}$$

The cost function takes the partial derivative of **x** and sets it to 0 to obtain the MAP profile [4] as:

$$\hat{\boldsymbol{x}} = \boldsymbol{x}_a + (\boldsymbol{S}_a^{-1} + \mathbf{K}^{\mathbf{T}} \boldsymbol{S}_y^{-1} \mathbf{K})^{-1} \mathbf{K}^{\mathbf{T}} \boldsymbol{S}_y^{-1} (\mathbf{y} - \mathbf{y}_L - K(\boldsymbol{x}_a - \boldsymbol{x}_L)) \tag{A2.25}$$

When the problem is moderately non-linear, the $\hat{\boldsymbol{x}}$ calculation using the above formula is not enough to minimize the cost function. But in many cases, the above formula can make the cost function smaller. So, the expression of $\hat{\boldsymbol{x}}$ can be used to find a new solution in a loop to make the cost function gradually becomes smaller.

Use the last calculated solution $\mathbf{x}_i$ instead of $\mathbf{x}_L$ to recalculate $\mathbf{y}_L$ and **K**. Then, the next iterative solution can be recalculated. For such a loop solving process, it is possible to find a solution that minimizes the cost function. The iterative solution [4] is expressed as follows:

$$\boldsymbol{x}_{i+1} = \boldsymbol{x}_a + (\boldsymbol{S}_a^{-1} + \mathbf{K}_i^{\mathbf{T}} \boldsymbol{S}_y^{-1} \mathbf{K}_i)^{-1} \mathbf{K}_i^{\mathbf{T}} \boldsymbol{S}_y^{-1} (\boldsymbol{y} - F(\boldsymbol{x}_i) - \mathbf{K}_i(\boldsymbol{x}_a - \boldsymbol{x}_i)) \tag{A2.26}$$

This method is called the Gauss-Newton method or the Inverse Hessian method. Another form of this iterative solution [4] can be expressed as:

$$\boldsymbol{x}_{i+1} = \boldsymbol{x}_i + (\boldsymbol{S}_a^{-1} + K_i^{\mathrm{T}} \boldsymbol{S}_y^{-1} K_i)^{-1} (K_i^{\mathrm{T}} \boldsymbol{S}_y^{-1} (\boldsymbol{y} - F(\boldsymbol{x}_i)) - \boldsymbol{S}_a^{-1} (\boldsymbol{x}_i - \boldsymbol{x}_a)) \quad \text{(A2.27)}$$

The steepest descent method is generally combined with the Newton iteration formula to obtain the following formula [4]:

$$\boldsymbol{x}_{i+1} = \boldsymbol{x}_i - (\gamma + \nabla g(\boldsymbol{x}_i))^{-1} g(\boldsymbol{x}_i) \quad \text{(A2.28)}$$

This formula is the Levenberg-Marquardt formula. After substituting the cost function into the Newton Gaussian iterative formula, the form of the iterative solution [4] is:

$$\boldsymbol{x}_{i+1} = \boldsymbol{x}_i + (\boldsymbol{S}_a^{-1} + \mathbf{K}_i^{\mathrm{T}} \boldsymbol{S}_y^{-1} \mathbf{K}_i + \gamma \boldsymbol{D})^{-1} (\mathbf{K}_i^{\mathrm{T}} \boldsymbol{S}_y^{-1} (\boldsymbol{y} - F(\boldsymbol{x}_i)) - \boldsymbol{S}_a^{-1} (\boldsymbol{x}_i - \boldsymbol{x}_a)) \quad \text{(A2.29)}$$

Where **D** is a scaling matrix in order to make γ dimensionless and to ensure that this term has the same unit as $\boldsymbol{S}_a^{-1}$. Generally, $\boldsymbol{S}_a^{-1}$ is chosen as **D**, which can slightly simplify the iterative formula. When γ is relatively small, this formula approaches the Inverse Hessian method and approaches the steepest descent method conversely. The steepest descent method is more stable to find the optimal solution, but the convergence speed is slow. When a solution $\mathbf{x}_{i+1}$ can reduce the cost function, it means that the calculation direction is correct, then replace $\mathbf{x}_i$ with the $\mathbf{x}_{i+1}$, and reduce γ to continue the next cycle calculation. On the contrary, if the solution $\mathbf{x}_{i+1}$ increases the cost function, it means that the calculation direction is wrong, so keep **x**i unchanged and increase γ to recalculate.

4. Retrieval steps

According to the theory of inversion algorithm, the parameters needed before calculation are atmospheric pressure profile **P**(z) and temperature profile **T**(**z**) (**z** is the altitude), the concentration prior profile **X**a, prior parameters a0, b0 , C0, a priori covariance matrix **S**a, molecular absorption information in the GEISA database, longitude and latitude of the measurement location and measurement time, measurement of transmittance, measurement of the covariance matrix, instrument linear function and the initial value of each calculation parameter. The inversion

process is shown in Figure A2.1. PyCats is used to calculate the absorption cross-section (cs(**z,v**)) corresponding to each layer of atmosphere at a given temperature profile, pressure profile, and within the range of measured wavenumbers(v represents the wavenumber). The atmospheric transmittance is calculated using the concentration profile $\boldsymbol{X}$i, ai, bi, ci, absorption cross-section and layered path, and then convolved with the instrument line function to simulate the transmittance detected by LHR. Use the above parameters to calculate the Jacobian matrix $\boldsymbol{K}$i. Bring the relevant parameters into the iterative formula to find the solution $\boldsymbol{X}_{i+1}$ of this cycle and also calculate the cost function. Compare the cost function calculated this time with the last time. If it decreases, then decrease γ and assign this solution to the initial value of the next cycle to continue the cycle operation. If it increases, judge whether γ is less than 20. If it is greater than 20, decrease it by four times, otherwise increase it by two times. Then find whether the change value of the cost function divided by the value calculated in this loop is less than 0.001. If it is, the optimal value is obtained. Otherwise, the loop is continued.

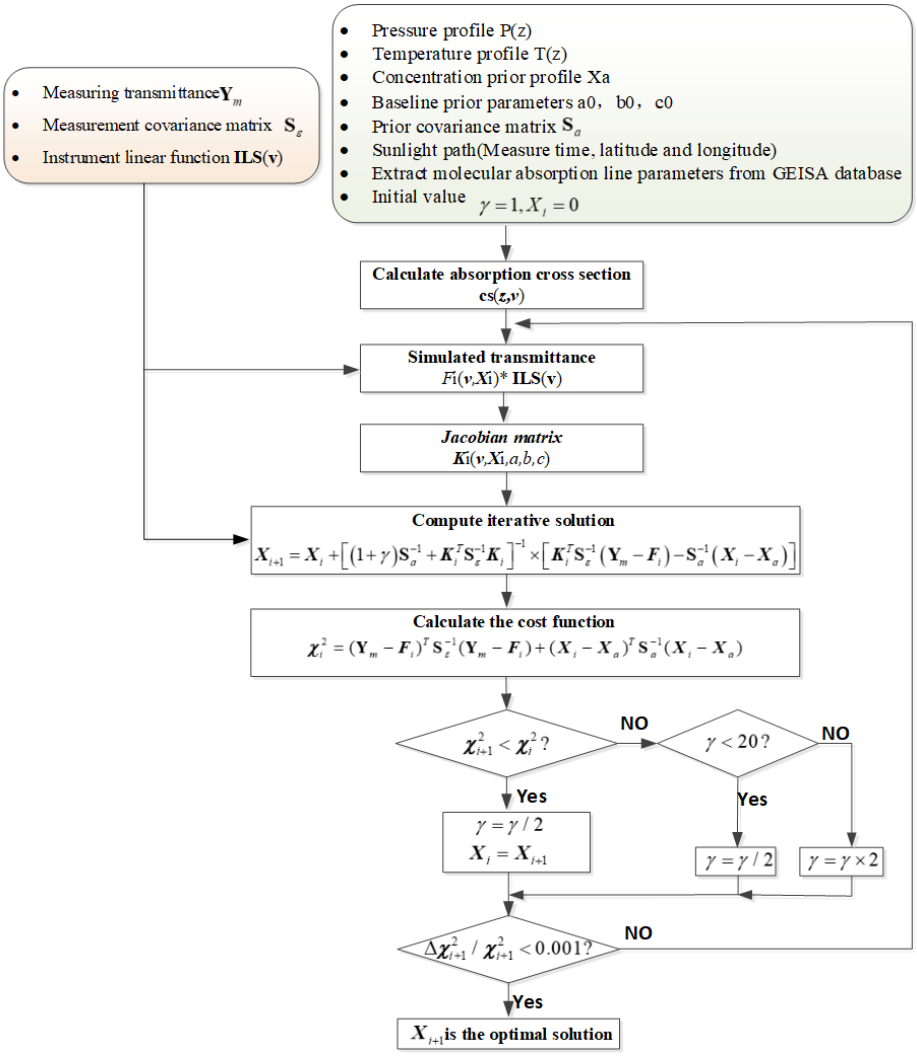

Figure A2.1 Inversion flow chart

References

[1] D. Weidmann, G. Wysocki. High-resolution broadband (>100 cm^{-1}) infrared heterodyne spectro-radiometry using an external cavity quantum cascade laser, Optics Express, 2009, 17 (1): 248-259.

[2] D, Weidmann, W, J, Reburn, K, M, Smith. Retrieval of atmospheric ozone profiles from an infrared quantum cascade laser heterodyne radiometer results and analysis, Applied Optics, 2007, 46 (29): 7162-7171.

[3] T. R.Tsai, R. A. Rose, D. Weidmann, G, Wysocki. Atmospheric vertical profiles of O_3, N_2O, CH_4, CCl_2F_2, and H_2O retrieved from external-cavity quantum-cascade laser heterodyne radiometer measurements, Applied Optics, 2012, 51(36):

8779-8792.

[4] Rodgers C D. Inverse Methods for Atmospheric Sounding: Theory and Practice. Second Edition. Singapore: World Scientific, 2004.

Appendix 3 Article: Mid-infrared laser heterodyne radiometer (LHR) based on a 3.53 μm room-temperature interband cascade laser

Research Article | Vol. 27, No. 7 | 1 Apr 2019 | OPTICS EXPRESS 9610
Optics EXPRESS

Mid-infrared laser heterodyne radiometer (LHR) based on a 3.53 μm room-temperature interband cascade laser

J. WANG,[1] G. WANG,[1,*] T. TAN,[1,3] G. ZHU,[1] C. SUN,[1] Z. CAO,[1] W. CHEN,[2] AND X. GAO[1]

[1]*Anhui Institute of Optics and Fine Mechanics, Chinese Academy of Sciences, 230031 Hefei, China*
[2]*Laboratoire de Physicochimie de l'Atmosphère, Université du Littoral Côte d'Opale, 59140 Dunkerque, France*
[3]*tantu@aiofm.ac.cn*
[*]*gswang@aiofm.ac.cn*

Abstract: The performance of an interband cascade laser based laser heterodyne radiometer (LHR) is demonstrated in ground-based solar occultation mode. High-resolution (0.0033 cm^{-1}) transmission spectra near 3.53 μm were obtained for simultaneous atmospheric observations of H_2O and CH_4. Combined with the preprocessed measurement data (acquired at Hefei, China, on June 21th 2016), an optimal estimation method based retrieval algorithm is developed for data retrieval and error analysis. By considering the corrected atmospheric parameters, vertical profiles of H_2O and CH_4 are retrieved. Finally, the measured total column abundance and X_{CH4} were calculated to be 1.87 ± 0.02 ppm and 1.88 ± 0.02 ppm, respectively. The interband cascade laser-based laser heterodyne radiometer that is demonstrated in this manuscript has high potential for use in the development of compact, robust, and unattended LHR for spacecraft, airborne or ground-based atmospheric sensing.

1. Introduction

Laser heterodyne radiometer (LHR), as a radio receiver (using the Sun or interstellar medium as light source and a laser as local oscillator), has already been successfully used for remote sensing of earth atmosphere and astronomy since the 1970s [1–4]. Initial LHRs, employed carbon dioxide (CO_2) gas lasers as local oscillators, focused in the 8-12 μm atmospheric window, where numerous important atmospheric species exhibit fundamental rotational-vibrational absorptions. However, the CO_2 lasers suffered from line-tuned spectral tunability. As an alternative, lead-salt diode lasers offered better frequency choice and frequency tuning ability, but lacking reliability and optical powers, and suffering from the requirement of LN2 temperature cooling [5,6]. The quick development of quantum-cascade lasers (QCLs) offers an ideal alternative to the traditional local oscillators in the mid-infrared region with the merits of room temperature operation, wide spectral tuning range, compactness, and robustness. Over the last decade, the QC-LHR applications for atmospheric observation have been successfully developed [7–12]. At the same period, the application of LHR for passive sensing of atmospheric CO_2 and CH_4 in the shortwave infrared band (around 1.6 μm) is also investigated, where telecommunication distributed feedback lasers are employed as the local oscillators. Combined with single-mode optical fibers, couplers and attenuators, the system can be made small, low-power consumption, compact and robust [13–16].

The atmospheric window of 3-5 μm is another attractive spectral region for mid-infrared atmospheric sounding, however commercially available QCLs operate generally in the 4-12 μm spectral region, which led to a "mid-infrared gap" in the QC-LHR applications. Since the first demonstration in 2008 [17], interband cascade lasers (ICLs), lasing in continuous wave (cw) mode at room temperature at the spectral region between 3 and 6 μm, open a new

#361302 https://doi.org/10.1364/OE.27.009610
Journal © 2019 Received 28 Feb 2019; revised 14 Mar 2019; accepted 14 Mar 2019; published 19 Mar 2019

Research Article | Vol. 27, No. 7 | 1 Apr 2019 | OPTICS EXPRESS 9611
Optics EXPRESS

spectral window for mid-infrared sensing. ICLs offer room temperature operation, compactness, high spectral purity with much lower electrical power consumption compared with QCLs.

In this paper, an ICL based LHR (IC-LHR) for atmospheric sounding is demonstrated for the first time (for our best knowledge). Simultaneous heterodyne detection of atmospheric water vapor (H_2O) and methane (CH_4) near 3.53 μm has been performed in ground-based solar occultation mode. The experimental details, as well as data retrieval and result analysis will be presented and discussed.2. Experimental details

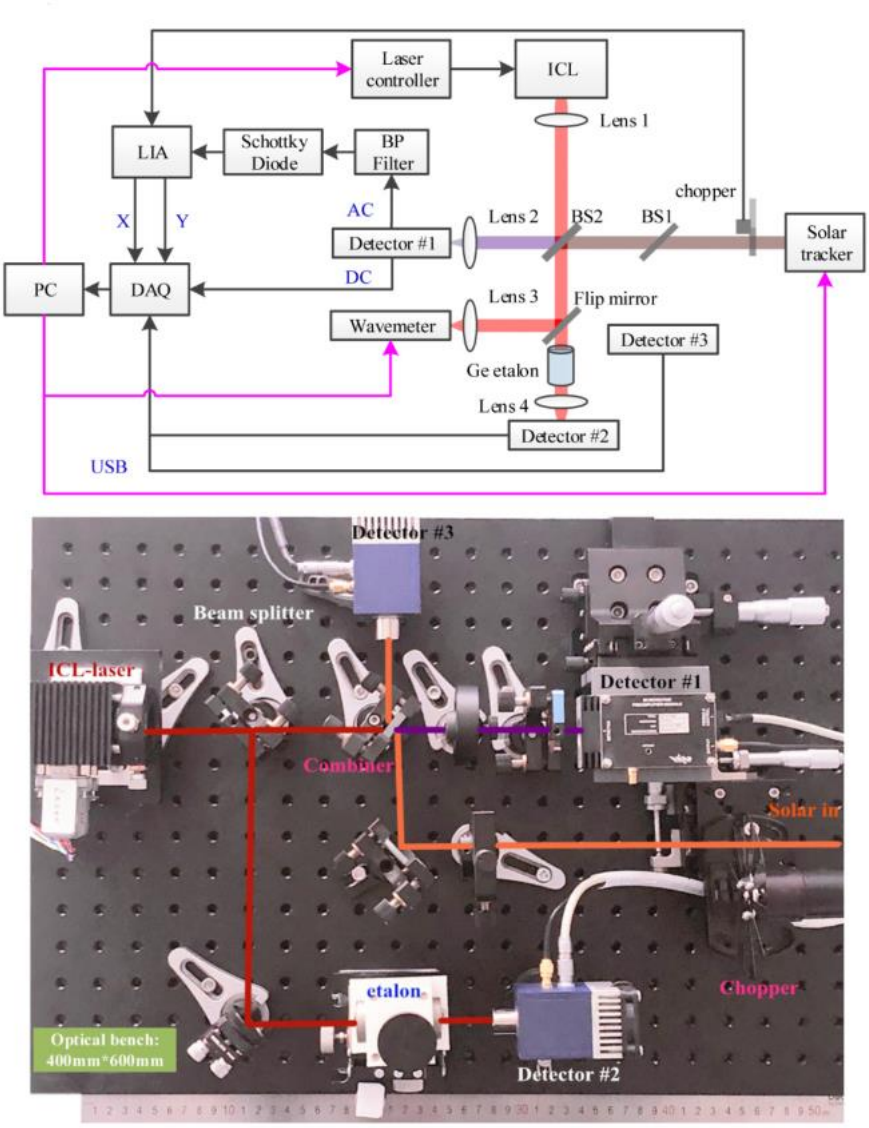

Fig. 1. Schematic diagram of the IC-LHR setup and photo of the optical module. ICL: interband cascade laser; BS: beam splitter; LIA: lock-in amplifier; BP Filter: band-pass filter; USB: Universal Serial Bus.

Research Article | Vol. 27, No. 7 | 1 Apr 2019 | OPTICS EXPRESS 9612
Optics EXPRESS

The experimental LHR setup is schematically shown in Fig. 1. Solar radiation containing atmospheric absorption information was captured with the help of a home-made solar tracker, then chopped at 2 kHz for lock-in amplification of the LHR signal. After a 50T/50R beam splitter (BS1), the reflected solar beam was directed to detector #3 for monitoring solar intensity fluctuation during the measurement. Beam splitter BS2 was employed as a mixing device to combine the transmitted solar radiance with the light beam from an ICL used as local oscillator (LO). The combined beams were imaged on a high-speed mercury cadmium telluride detector (detector #1, Vigo PV-2TE-4 with a custom preamplifier), which had both DC (0-1 MHz, for monitoring the ICL power) and AC (1 kHz –100 MHz, for LHR detection at radio-frequency (RF)). A small fraction of the ICL beam transmitted through BS2 was used for frequency calibration: a flip mirror directed the ICL beam either to a wavemeter (Bristol Instruments, 621) for absolute frequency measurements or to a 50.8 mm germanium etalon (with a free spectral range of ~0.0246 cm^{-1}) followed by detector #2 recording etalon fringe signal for relative frequency metrology.

The used local oscillator was a TO-66 mounted distributed feedback (DFB) ICL operating around 3.53 μm (nanoplus). The used ICL was coarsely tuned ~10 cm^{-1} by tuning the temperature at a constant current or precisely tuned over ~1 cm^{-1} by tuning the injection current at a constant temperature. The relationships between laser wavenumber, laser power and laser injection current are shown in Fig. 2. During LHR measurement, the laser temperature and current were set at 14°C and 30mA (ILX Lightwave, LDC-3724) to probe the CH_4 and HDO absorption lines located around 2831.92 cm^{-1}. The frequency tuning of the laser could be performed by changing the laser current point-by-point via laser controller or scanning the injection current with a common function waveform (such as sinusoidal or triangle waveform).

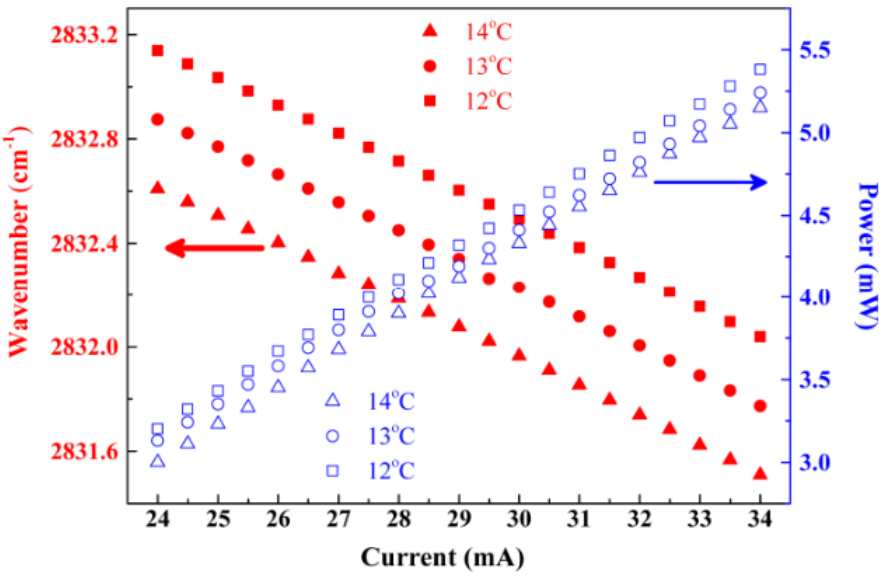

Fig. 2. Relationships between laser wavenumber (red solid symbols), power (blue hollow symbols) and laser injection current.

The solar radiation containing atmospheric absorption information was down-converted to the RF domain via detector #1, followed by a band-pass filter employed to determine RF detection bandwidth which defines the instrument lineshape (ILS) of the LHR system. In order to choose an appropriate band-pass filter, frequency spectrum analysis of the

Research Article | Vol. 27, No. 7 | 1 Apr 2019 | OPTICS EXPRESS 9613
Optics EXPRESS

heterodyne, laser and background (without laser and solar) signals were performed by using a RF signal analyzer (Agilent Technologies, N9000A).

As shown in Fig. 3, the heterodyne signal form is dominated by the LO (ICL) signal, and the detector can extract LHR signal from the background baseline below 150 MHz. However, there were several unwanted peaks between 70 and 120 MHz, which might introduce additional noise to the LHR signal. Therefore, a 10–60 MHz band-pass filter was chosen in the experiment, which resulted in a ~100 MHz (0.0033 cm^{-1}) double-sideband spectral resolution of the system. The inset of Fig. 3 shows the actually used ILS for data retrieval. Subsequently, the RF signal after the band-pass filter was converted to a DC signal by a Schottky diode (HEROTE, DHM020BB) and demodulated at first harmonic using lock-in amplifier (Stanford Research Systems, SR830) with the chopping frequency as reference. LHR signal can be ultimately obtained by tuning the laser frequency across the target molecular absorption lines.

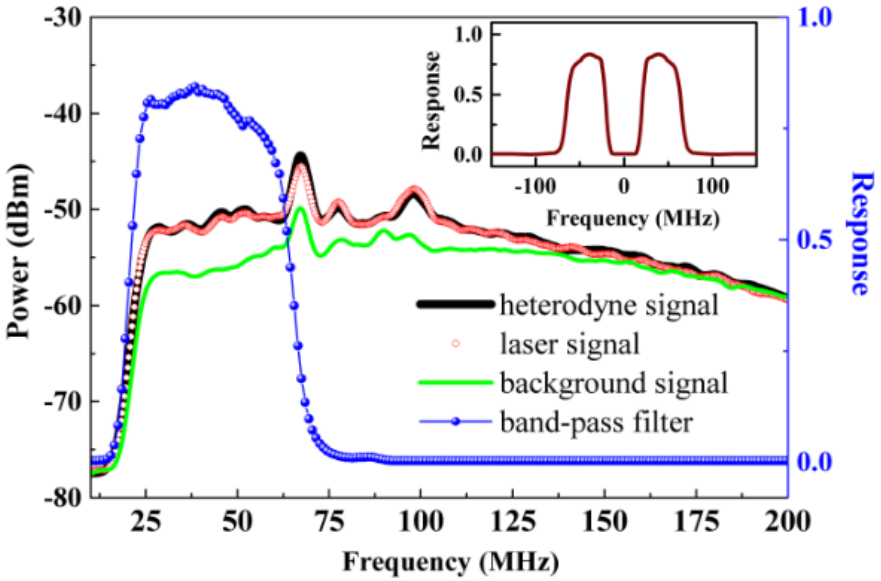

Fig. 3. Band–pass filter used in the experiment and frequency spectrum analysis of the heterodyne, laser and background signals, the inset: the actually used instrument lineshape for data retrieval.

A personal laptop equipped with a DAQ card (National Instruments, USB-6366) and LabVIEW software was employed for data acquisition and instrument control (solar tracker controlling, frequency tuning and wavenumber reading). Signals from 5 channels were recoded: the in-phase (X) and quadrature (Y) outputs of the lock-in amplifier for phase compensation of the LHR signal by using the angle sum and difference identities (trigonometric identities), the DC output of detector #1 for tracking the ICL power, the signal from detector #2 for the relative frequency calibration, and the signal from detector #3 for tracking the solar power variation.

The experimental result, measured from our institute (Hefei, China, 31.9°N 117.166°E) on June 21th 2016, is shown in Fig. 4(b), where the LHR data has been processed by the phase compensation. In addition, transmittance of atmospheric H_2O vapor and CH_4 in the considered spectral region are calculated by using a forward model (introduced in detail in section 3). It should be noted that, when tuning the laser frequency in "point-by-point" mode, an acquisition interval longer than 3 times of the lock-in integration time was used to avoid deformation of lineshape of the LHR signal. Otherwise, the ILS of the LHR system would no longer be determined by the band-pass filter but by the lock-in amplifier. A typical scan time

Research Article | Vol. 27, No. 7 | 1 Apr 2019 | OPTICS EXPRESS 9614
Optics EXPRESS

is at an order of minutes, which depends on the current intervals, acquisition time and acquisition intervals. While the scan time is determined, a corresponding "function waveform scan" mode can be employed as an alternative to the "point-by-point" mode, where no obvious difference is found between the two scan methods. It should be noted that, the results shown in Fig. 4(b) are acquired at a sampling rate of 50 Hz by driving the laser current with a sinusoidal wave (0.0125 Hz, 0.5 Vpp).

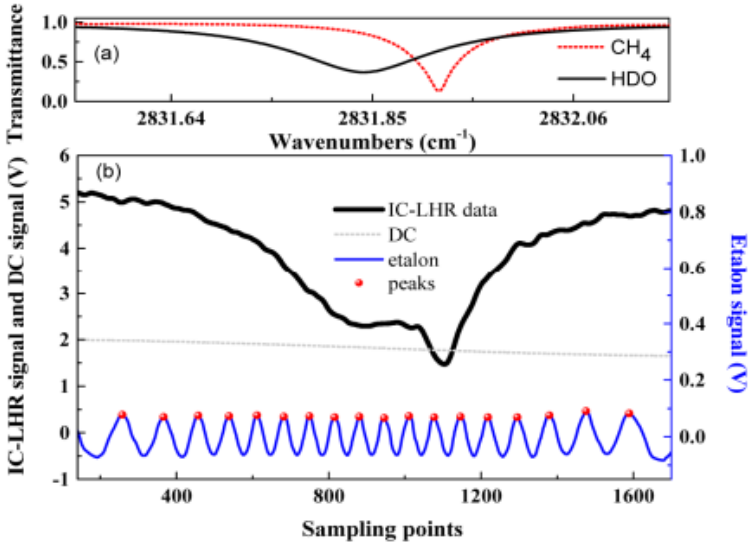

Fig. 4. (a) Calculated transmittance of atmospheric H_2O vapor (black) and CH_4 (red dots) based on the forward model; (b) Acquired IC-LHR (black), DC (DC output of detector #1, gray dots) and etalon signals (blue).

Before the data retrieval, the raw LHR data needs to be pre-processed. Firstly, the offset of the LHR signal, where the injection current to the ICL equals zero, was subtracted. Then the LHR signal is divided by the ICL intensity signal (DC signal) for normalization of the LHR signal, When large solar power fluctuations (more than 10% of the average of the solar power intensity) occurred during the scan, the LHR data would not be considered for further analysis. Thirdly, a frequency calibration of the LHR signal was performed with the help of relative frequencies (germanium etalon signal), and absolute frequencies from a wavemeter or the positions of the absorption lines (from the HITRAN database) [18]. In the present work, peaks of the etalon signal were fitted to a 5th order polynomial function to determine relative frequency of the data points, and the CH_4 line position (2831.92 cm^{-1}) was employed to calibrate the absolute frequency. In addition, a scale factor and an offset were used for further frequency calibration according to the wavemeter results and the forward model calculation. Finally, the calibrated LHR results were interpolated with the same frequency interval as the forward model and then the processed LHR spectrum is now ready (blue dots in Fig. 7(a)) for further data retrieval to inverse the LHR spectrum to the corresponding vertical concentration profiles.

3. Data retrieval and results analysis

The LHR data retrieval was performed employing the optimal estimation method (OEM), introduced by Rodgers [19]. The applications of the OEM to a LHR based atmospheric sounding has already been described in detail by Weidmann [20]. Here, only a brief recall is presented. The atmospheric transmission spectrum of the solar radiance can be calculated using a radiative transfer model (***F***). The relationship between pre-processed LHR data and the atmospheric state vectors is described as:

Research Article | Vol. 27, No. 7 | 1 Apr 2019 | OPTICS EXPRESS 9615
Optics EXPRESS

$$y_m = F(x,a,b,c) + \varepsilon. \quad (1)$$

where $\boldsymbol{y_m}$ is the measurement vector, $\boldsymbol{x}$ is the state vector considered in the forward calculation, and $\boldsymbol{\varepsilon}$ is the error vector. A second order polynomial baseline (with coefficients of a, b and c) represents the non-selective absorption and uncorrected power contributions in the target spectral region. The OEM-based data retrieval is a Levenberg–Marquardt (LM) iterative process, using Bayesian statistics with Gaussian probability density functions, to minimize the cost function (χ^2):

$$\chi^2 = (y-F)^T S_\varepsilon^{-1}(y-F) + (x_i - x_a)^T S_a^{-1}(x_i - x_a). \quad (2)$$

where $\boldsymbol{x_a}$ is *a priori* state vector with an *a priori* covariance matrix $\boldsymbol{S_a}$, and $\boldsymbol{S_\varepsilon}$ is the error covariance matrix. The iterative state vector $\boldsymbol{x_{i+1}}$ is calculated using the following equation:

$$\begin{aligned} x_{i+1} &= x_i + \left[(1+\gamma)S_a^{-1} + K_i^T S_\varepsilon^{-1} K_i\right]^{-1} \\ &\times \left[K_i^T S_\varepsilon^{-1}(y_m - F_i) - S_a^{-1}(x_i - x_a)\right]. \end{aligned} \quad (3)$$

where $\boldsymbol{K}$ is the Jacobian matrix (or weighting functions), and γ is the Levenberg–Marquardt (LM) parameter.

The flow chart of the LHR data retrieval is shown in Fig. 5, which mainly consists of a forward calculation program and an iterative inverse program. Crucially, the forward model employed in this study is based on the reference forward model (RFM, version 4.34), which is a fast and high-resolution line-by-line algorithm developed by Dudhia [21]. In the forward calculation program, atmospheric transmission spectrum ($\boldsymbol{y}$) combined with a baseline and the corresponding Jacobian matrix ($\boldsymbol{K}$) are calculated with the input atmospheric parameters (profiles of pressure, temperature, and atmospheric species), ILS, *a priori* state vector and solar position (zenith angle for ray trace path calculation). In the inverse program, the forward model is iteratively called to minimize the cost function (Eq. (2)) following LM algorithm (Eq. (3)). Table 1 defines the used state vector in the data retrieval, which consists of two scale factors of the considered atmospheric species (CH_4 and H_2O) and three polynomial coefficients of the baseline. It should be noted that, when the scale factor x is exchanged with VMRs (volume mixing ratios) at different altitudes, the inverse program will yield a 'real' profiles retrieval. Here, the scale factor of *a prior* profile is retrieved in this manuscript.

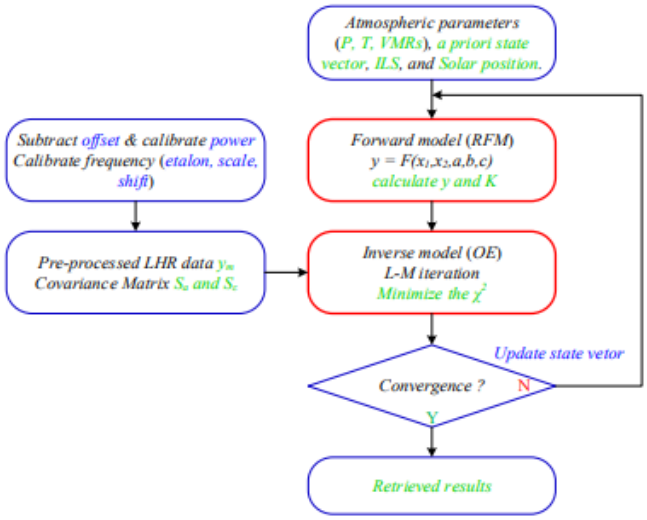

Fig. 5. Flow chart of the data retrieval. VMRs: volume mixing ratios; ILS: instrument lineshape; L-M: Levenberg–Marquardt.

Research Article | Vol. 27, No. 7 | 1 Apr 2019 | OPTICS EXPRESS 9616
Optics EXPRESS

Table 1. Definition of the state vector used in the data retrieval.

State vector	*a priori*	Error	Description
$x1$ (CH_4)	1	30%	Scale factor of a priori profile (ECMWF 45 levels).
$x2$ (H_2O)	1	30%	Scale factor of a priori profile (ECMWF 45 levels).
a	a0	100%	Polynomial coefficients of the baseline, a0, b0, and c0 are calculated by using a 2nd order polynomial fitting of the ratio of pre-processed LHR signal and model result (after eliminating the absorption part).
b	b0	100%	
c	c0	100%	

The temperature and pressure profiles used in the retrieval are shown in Fig. 6, which were obtained from the China Meteorological Data Service Center (CMCC) and the European Centre for Medium-Range Weather Forecasts (ECMWF). Data below 30 km (blue dots) were interpolated from the upper air data of Anqing observation station (China, 30.53°N 117.05°E), and the data above 30 km (red dots) were interpolated from the typical zonal mean profiles in different months (obtained from ECMWF). For the methane and water vapor profiles, typical mid-latitude daytime profiles were used. Note that the atmosphere is separated to 45 layers from surface to 78 km with an altitude grid of 0.5, 1, 2, 4 and 6 km, separately.

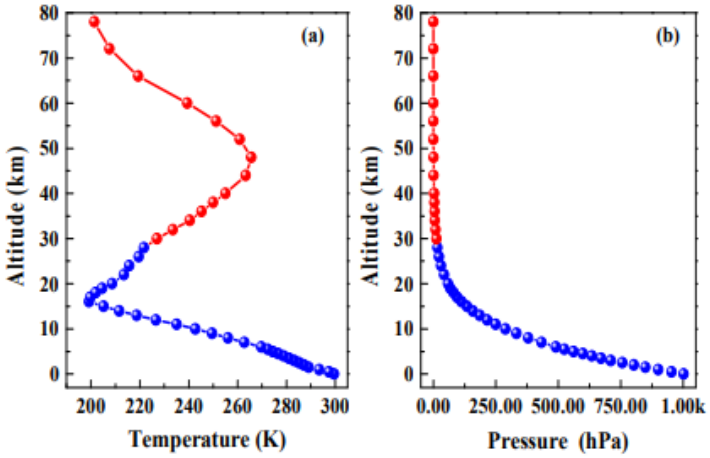

Fig. 6. Temperature (a) and pressure (b) profiles used for the IC-LHR retrieval.

The covariance matrices ($\boldsymbol{S}_a$ and $\boldsymbol{S}_\varepsilon$) were set to be diagonal, where $\boldsymbol{S}_\varepsilon$ was built based on the standard deviation of the measurement vector ($\boldsymbol{y}_m$), while $\boldsymbol{S}_a$ was built based on the error definitions shown in Table 1. The iterative solution is defined to be converged with $\Delta\chi^2/\chi^2 <$ 1E-3, within an upper limit of 20 iterations. In a well-conditioned retrieval, the ultimate cost function (χ^2) should be close to the size of the measurement vector (m). Figure 7(a) shows the pre-processed LHR data and the fitted spectrum over the spectral region of 2831.64 - 2832.07 cm^{-1} with an interval of 0.001 cm^{-1}. The iterative process is shown in the inset of Fig. 7(a), where χ^2/m equal to ~1.05 is obtained after 6 iterations. The residuals between the pre-processed data and the fitted result are shown in Fig. 7(b), where the random distribution indicates a well configured fit. The retrieved CH_4 and water vapor profiles (Figs. 7(c) and 7(d)) are calculated by multiplying the retrieved scale factor with the *a priori* profile. Based on the retrieved CH_4 and water vapor profiles, the total column abundance of water vapor is calculated to be ~2868ppm (or ~5.8E + 23 molecules/cm^2), the total column abundance of methane and its mixing ratio in dry air (X_{CH4}) are found to be ~1.875 ppm (or ~3.8E + 20 molecules/cm^2) and ~1.88 ppm (part per million), respectively.

Research Article | Vol. 27, No. 7 | 1 Apr 2019 | OPTICS EXPRESS 9617
Optics EXPRESS

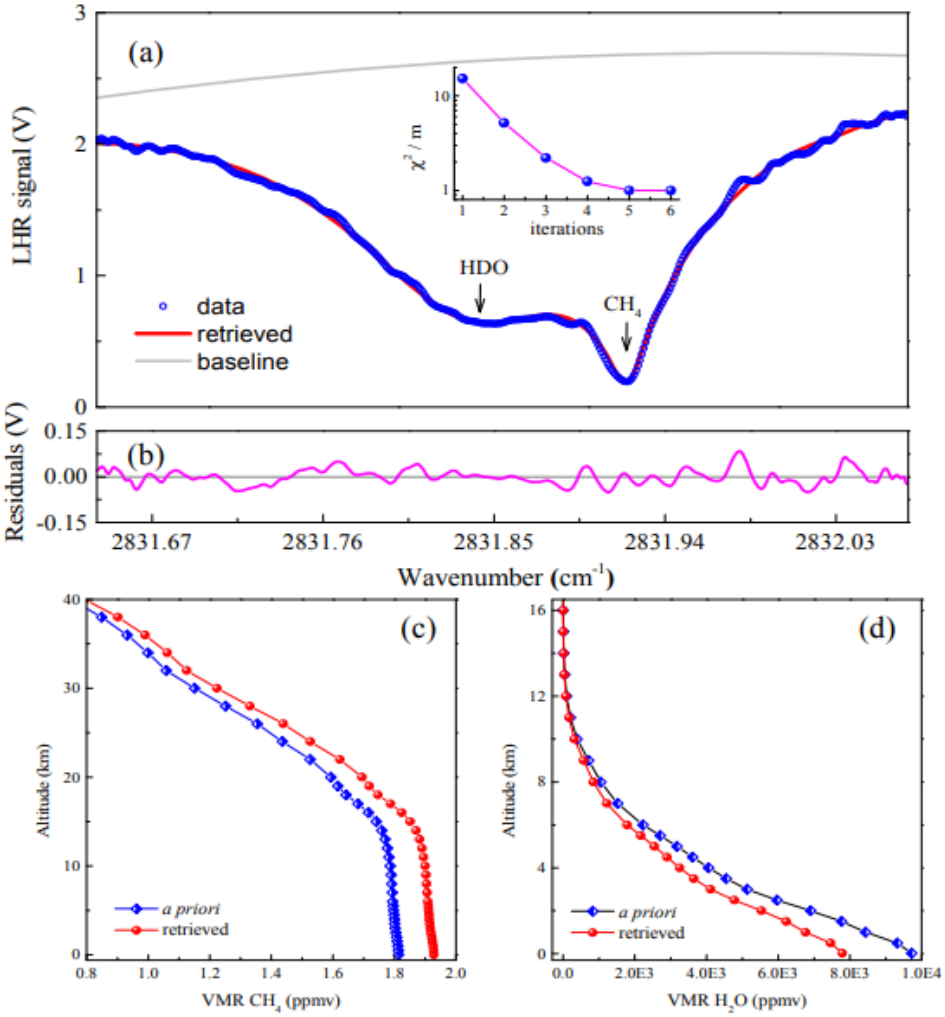

Fig. 7. LHR data retrieval results: (a) experimental (blue) and fitted (red) LHR spectra and the convergence of the iteration process (inset); (b) the residuals (pink); (c) and (d) the retrieved vertical concentration profiles of CH_4 and water vapor, respectively.

In order to perform an error analysis, the smoothing error $\boldsymbol{S_s}$ and the measurement error $\boldsymbol{S_m}$ are considered. In our case, the retrieval error is dominated by smoothing error. The $\boldsymbol{S_s}$ and $\boldsymbol{S_m}$ can be calculated by using the following equation [19]:

$$S_m = GS_\varepsilon G^T, S_s = (I_n - A)S_a(I_n - A)^T. \quad (4)$$

$$\boldsymbol{A} = \frac{\partial \hat{\boldsymbol{x}}}{\partial \boldsymbol{x}} = \boldsymbol{GK} = \left[\left(\boldsymbol{K}^T S_\varepsilon^{-1}\boldsymbol{K} + \boldsymbol{S}_a^{-1}\right)^{-1}\boldsymbol{K}^T S_\varepsilon^{-1}\right]\boldsymbol{K}. \quad (5)$$

where $\boldsymbol{G}$ and $\boldsymbol{A}$ are the gain matrix and averaged kernel matrix. The total retrieval error of two scale factors were calculated to be ~6% and ~8%, respectively. 20 consecutive measurements indicate an uncertainty of 20 ppb (part per billion) and 21 ppb for the total CH_4 column abundance and X_{CH4}, respectively. For further improvement of the measurement uncertainty, works in the near future will be focused on improving the signal to noise ratio of the IC-LHR signal and determining an appropriate weight of the constraint in the retrieval, so as to a 'true' profile retrieval.

Research Article | Vol. 27, No. 7 | 1 Apr 2019 | OPTICS EXPRESS 9618
Optics EXPRESS

4. Conclusions

An ICL based mid-infrared LHR has been demonstrated in ground-based solar occultation mode. High-resolution (0.0033 cm^{-1}) LHR spectrum near 3.53 μm were obtained for simultaneous atmospheric observations of H_2O vapor and CH_4. OEM and RFM based retrieval algorithm was developed for retrieval of the vertical profiles of H_2O and CH_4 and error analysis. The measured total CH_4 column abundance and X_{CH4} were determined to be 1.87 ± 0.02 ppm and 1.88 ± 0.02 ppm, respectively. The IC-LHR has high potential to be developed as a compact, robust and unattended instrument for spacecraft, airborne or ground-based applications.

Funding

National Key Research and Development Program of China (2017YFC0209700, 2016YFC0303900), Key Project of the National Natural Science Foundation of China (41730103) and National Natural Science Foundation of China (41405022, 41805018).

Acknowledgments

The authors are grateful to Damien Weidmann from Rutherford Appleton Laboratory and Gerard Wysocki from Princeton University for their technical guidance of LHR. They are also very grateful to Anu Dudhia from University of Oxford and Yao Veng TE from Pierre and Marie Curie University for providing RFM source codes and guidance of retrieval algorithm.

References

1. R. T. Menzies and R. K. Seals, Jr., "Ozone monitoring with an infrared heterodyne radiometer," Science **197**(4310), 1275–1277 (1977).
2. M. A. Frerking and D. J. Muehlner, "Infrared heterodyne spectroscopy of atmospheric ozone," Appl. Opt. **16**(3), 526–528 (1977).
3. M. M. Abbas, T. Kostiuk, M. J. Mumma, D. Buhl, V. G. Kunde, and L. W. Brown, "Stratospheric ozone measurement with an infrared heterodyne spectrometer," Geophys. Res. Lett. **5**(4), 317–320 (1978).
4. D. Deming, F. Espenak, D. Jennings, T. Kostiuk, M. Mumma, and D. Zipoy, "Observations of the 10-μm natural laser emission from the mesospheres of Mars and Venus," Icarus **55**(3), 347–355 (1983).
5. G. Sonnabend, D. Wirtz, F. Schmülling, and R. Schieder, "Tuneable heterodyne infrared spectrometer for atmospheric and astronomical studies," Appl. Opt. **41**(15), 2978–2984 (2002).
6. D. Weidmann and D. Courtois, "Infrared 7.6-microm lead-salt diode laser heterodyne radiometry of water vapor in a CH4-air premixed flat flame," Appl. Opt. **42**(6), 1115–1121 (2003).
7. D. Weidmann, W. J. Reburn, and K. M. Smith, "Ground-based prototype quantum cascade laser heterodyne radiometer for atmospheric studies," Rev. Sci. Instrum. **78**(7), 073107 (2007).
8. D. Weidmann and G. Wysocki, "High-resolution broadband (>100 cm-1) infrared heterodyne spectro-radiometry using an external cavity quantum cascade laser," Opt. Express **17**(1), 248–259 (2009).
9. D. Weidmann, B. J. Perrett, N. A. Macleod, and R. M. Jenkins, "Hollow waveguide photomixing for quantum cascade laser heterodyne spectro-radiometry," Opt. Express **19**(10), 9074–9085 (2011).
10. T. R. Tsai, R. A. Rose, D. Weidmann, and G. Wysocki, "Atmospheric vertical profiles of O3, N2O, CH4, CCl2F2, and H2O retrieved from external-cavity quantum-cascade laser heterodyne radiometer measurements," Appl. Opt. **51**(36), 8779–8792 (2012).
11. A. Hoffmann, N. A. Macleod, M. Huebner, and D. Weidmann, "Thermal infrared laser heterodyne spectroradiometry for solar occultation atmospheric CO₂ measurements," Atmos. Meas. Tech. **9**(12), 5975–5996 (2016).
12. D. Weidmann, A. Hoffmann, N. Macleod, K. Middleton, J. Kurtz, S. Barraclough, and D. Griffin, "The methane isotopologues by solar occultation (miso) nanosatellite mission: spectral channel optimization and early performance analysis," Remote Sens. **9**(10), 1073–1092 (2017).
13. E. L. Wilson, M. L. McLinden, J. H. Miller, G. R. Allan, L. E. Ott, H. R. Melroy, and G. B. Clarke, "Miniaturized laser heterodyne radiometer for measurements of CO2 in the atmospheric column," Appl. Phys. B **114**(3), 385–393 (2014).
14. E. L. Wilson, A. J. Digregorio, V. J. Riot, M. S. Ammons, W. W. Bruner, D. Carter, J. P. Mao, A. Ramanathan, S. E. Strahan, L. D. Oman, C. Hoffman, and R. M. Garner, "A 4 U laser heterodyne radiometer for methane (CH4) and carbon dioxide (CO2) measurements from an occultation-viewing cubsat," Meas. Sci. Technol. **28**(3), 035902 (2017).
15. A. Rodin, A. Klimchuk, A. Nadezhdinskiy, D. Churbanov, and M. Spiridonov, "High resolution heterodyne spectroscopy of the atmospheric methane NIR absorption," Opt. Express **22**(11), 13825–13834 (2014).

Research Article | Vol. 27, No. 7 | 1 Apr 2019 | OPTICS EXPRESS 9619
Optics EXPRESS

16. J. Kurtz and S. O'Byrne, "Multiple receivers in a high-resolution near-infrared heterodyne spectrometer," Opt. Express **24**(21), 23838–23848 (2016).
17. M. Kim, C. L. Canedy, W. W. Bewley, C. S. Kim, J. R. Lindle, J. Abell, I. Vurgaftman, and J. R. Meyer, "Interband cascade laser emitting at λ = 3.75 μm in continuous wave above room temperature," Appl. Phys. Lett. **92**(19), 191110 (2008).
18. L. S. Rothman, I. E. Gordon, Y. Babikov, A. Barbe, D. Chris Benner, P. F. Bernath, M. Birk, L. Bizzocchi, V. Boudon, L. R. Brown, A. Campargue, K. Chance, E. A. Cohen, L. H. Coudert, V. M. Devi, B. J. Drouin, A. Fayt, J.-M. Flaud, R. R. Gamache, J. J. Harrison, J.-M. Hartmann, C. Hill, J. T. Hodges, D. Jacquemart, A. Jolly, J. Lamouroux, R. J. Le Roy, G. Li, D. A. Long, O. M. Lyulin, C. J. Mackie, S. T. Massie, S. Mikhailenko, H. S. P. Müller, O. V. Naumenko, A. V. Nikitin, J. Orphal, V. Perevalov, A. Perrin, E. R. Polovtseva, C. Richard, M. A. H. Smith, E. Starikova, K. Sung, S. Tashkun, J. Tennyson, G. C. Toon, V. G. Tyuterev, and G. Wagner, "The HITRAN2012 molecular spectroscopic database," J. Quant. Spectrosc. Radiat. Transf. **130**, 4–50 (2013).
19. C. D. Rodgers, "Inverse Methods for Atmospheric Sounding: Theory and Practice (World Scientific, 2000).
20. D. Weidmann, W. J. Reburn, and K. M. Smith, "Retrieval of atmospheric ozone profiles from an infrared quantum cascade laser heterodyne radiometer: results and analysis," Appl. Opt. **46**(29), 7162–7171 (2007).
21. A. Dudhia, "The reference forward model (RFM)," J. Quant. Spectrosc. Radiat. Transf. **186**, 243–253 (2017).

Appendix 4 Article: A fibered near-infrared laser heterodyne radiometer for simultaneous remote sensing of atmospheric CO_2 and CH_4

Optics and Lasers in Engineering 129 (2020) 106083

Contents lists available at ScienceDirect

Optics and Lasers in Engineering

journal homepage: www.elsevier.com/locate/optlaseng

A fibered near-infrared laser heterodyne radiometer for simultaneous remote sensing of atmospheric CO_2 and CH_4

Jingjing Wang[a,b,1], Chunyan Sun[a,b,1], Guishi Wang[a,*], Mingmin Zou[c], Tu Tan[a], Kun Liu[a], Weidong Chen[d], Xiaoming Gao[a,b]

[a] Anhui Institute of Optics and Fine Mechanics, Chinese Academy of Sciences, Hefei 230031, China
[b] University of Science and Technology of China, Hefei 230026, China
[c] Institute of Remote Sensing and Digital Earth, Chinese Academy of Sciences, Beijing 100101, China
[d] Laboratoire de Physicochimie de l'Atmosphère, Université du Littoral Côte d'Opale, Dunkerque 59140, France

A B S T R A C T

The performance of an all fibered near-infrared laser heterodyne radiometer (NIR-LHR) is demonstrated in ground-based solar occultation mode. A 1 × 2 fiber optical switch is employed as an alternative modulator to traditional chopper, which makes the system more stable and compact. Two distribute feedback (DFB) lasers centered at 1.6 μm and 1.65 μm, are employed as local oscillators to probe absorption lines of CO_2 and CH_4, respectively. After data processing and retrieval, column-averaged abundances and the mixing ratio of atmospheric CO_2 and CH_4 are determined based on the measurement of over six months in our laboratory (Hefei, China, 31.9°N 117.16°E). Finally, the results are validated by comparison with the GOSAT results during the same time period. The reported all fibered laser heterodyne radiometer in this manuscript has great potential to be a portable and high spectral resolution instrument for atmospheric remote sensing of multi-component gases.

1. Introduction

Carbon dioxide (CO_2) and methane (CH_4) are key greenhouse gases emitted by human activities, accounting for ~76% and ~16% of total greenhouse gases emissions at the global scale [1]. However, current knowledge about the sources and sinks of both gases is still insufficient for reliable climate predictions. Current space-based observations (such as GOSAT [2], OCO-2 [3] and TANSAT [4]), though useful for quantification of the sources and sinks on large scales, suffer from limited precision, limited density of observations, and biases related to details of atmospheric scattering properties [5]. Whilst ground-based observations (such as TCCON [6]), usually equipped with Fourier transform spectrometer (Bruker, IFS125HR) with ~0.01 cm^{-1} spectral resolution, can provide column-averaged abundances with high precision and accuracy, however the shortfalls (such as large dimensions and high cost of maintenance) limit further expansion of the observing network. Over the last decade, portable FTIR spectrometers (Bruker, EM27/SUN) with 0.5/0.2 cm^{-1} spectral resolution, which sacrifices the spectral resolution for portability, have proven to be a promising complement to the ground-based observations [7-9]. With the objective to develop a portable instrument maintained with high spectral resolution (< 0.01 cm^{-1}), a high-resolution laser heterodyne radiometer (LHR) for ground-based atmospheric remote sensing is reported in this paper.

LHR, which extracts absorption information from a broadband light source (such as the Sun or interstellar medium) by beating with a narrow-band local oscillator on a high speed detector, has been successfully applied for remote sensing of earth atmosphere and astronomy since the 1970s [10–13]. Early LHR based applications, employing carbon dioxide (CO_2) gas lasers or lead-salt diode lasers as the local oscillators [14,15] for the mid-infrared spectral region, where many important atmospheric species exhibit fundamental rotational-vibrational absorptions. More recently, quantum cascade lasers (QCLs) and interband cascade lasers (ICLs) offered more reliable alternatives to traditional local oscillators in the mid-infrared region with the merits of room temperature operation, wide spectral tuning range, compactness, and robustness. Over the past decade, the QC-LHR and IC-LHR have been successfully developed for atmospheric observations of different species [16–23]. However, limited by the lack of matured fiber optical components or optical waveguides in the mid-infrared spectral region, further integration of the optical module is currently difficult. LHRs using telecommunication distributed feedback (DFB) diode lasers as local oscillators operating in the near-infrared spectral region exhibit their unique advantages. Combined with single-mode optical fibers, couplers and attenuators, the NIR-LHR can be made small, low-power consumption, compact and robust, which make it a promising instrument for ground-based observations [24–28].

In the present work, an all fibered NIR-LHR is demonstrated in ground-based solar occultation mode. A 1 × 2 fiber optical switch is employed as an alternative modulator to traditional chopper, which

* Corresponding author.
E-mail address: gswang@aiofm.a.c.cn (G. Wang).
[1] Co-first authors of the article.

https://doi.org/10.1016/j.optlaseng.2020.106083
Received 14 January 2020; Received in revised form 15 February 2020; Accepted 27 February 2020

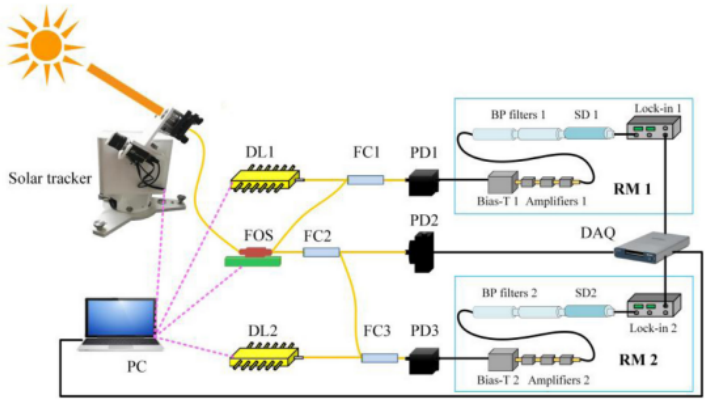

Fig. 1. Schematic diagram of the experimental setup, DL: diode laser; FOS: fiber optical switch; FC: fiber coupler; PD: photo-detector; RM: Radio frequency processing module; BP filters: Band-pass filters; SD: Schottky diode; DAQ: data acquisition card; PC: personal computer.

makes the system more stable and compact. By employing two DFB lasers (1.6 μm and 1.65 μm) as the local oscillators, measurements of column-averaged abundances and mixing ratio in dry air of atmospheric CO_2 and CH_4 were performed over six months in our laboratory (Hefei, China, 31.9°N 117.16°E). The experimental details, data processing, as well as analysis results and validation through comparison with GOSAT results will be presented and discussed.

2. Experimental details

The experimental setup of the fibered NIR-LHR is schematically shown in Fig. 1. Solar radiation containing atmospheric absorption information is captured by a custom-made solar tracker equipped with a fiber collimator (Thorlabs, FC/APC 1550), then chopped with a 1 × 2 fiber optical switch (Angiltron, CL1×2) at 250 Hz for lock-in amplification of the NIR-LHR signal. One output arm of the optical switch is coupled with a local oscillator centered at ~1.6 μm (DL1, NEL, 10 mW, 2 MHz) through a fiber coupler (FC1), and then connected to a high speed photo-detector (PD1, Thorlabs, DET08CFC, 5 GHz) for CH_4 heterodyne detection. The other arm is separated by a 5:95 fiber splitter (FC2), where the 5% part is connected to PD2 (Thorlabs, PDA20CS2) for tracking the solar power, while the rest part is coupled with a local oscillator centered at ~1.65 μm (DL2, NEL, 10 mW, 2 MHz) through FC3, and then connected to another high speed photo-detector (PD3) for CO_2 heterodyne detection. Subsequently, the beat signals generated from PD1 and PD3 are processed by two Radio frequency (RF) processing modules (RM1 and RM2), where the DC component and AC component (RF signal) are extracted through a bias-T (Mini-Circuits) for monitoring local oscillator powers and further RF processing. During RF processing, the RF signal is first amplified by three amplifiers (Mini-Circuits, ZX60), then filtered by a band-pass filter, and finally converted to a DC signal by a Schottky diode (HEROTE, DHM020BB) and demodulated at first harmonic using a lock-in amplifier (Stanford Research Systems, SR830).

For data acquisition and instrumental control (solar tracker, optical switch, wavelength meter and laser controllers), a personal computer (PC) equipped with a DAQ card (National Instruments, USB-6366) and LabVIEW software was employed. During the measurements, signals from 7 channels were recorded (Fig. 2(a)–(d)): the in-phase (X) and quadrature (Y) outputs of two lock-in amplifiers for phase compensation of two NIR-LHR signals, the DC components of PD1 and PD3 for tracking the power of the two local oscillators, and the signal from PD2 for tracking the solar power variations. In one scan, the temperatures of the two local oscillators were first set at 28 °C and 21.5 °C, respectively, to probe the CO_2 and CH_4 absorption lines located around 6238.78 cm^{-1} and 6046.96 cm^{-1}, then the currents were tuned in a point-by-point mode (0–100 mA, 0.1 mA interval) to cover the target absorption features via laser controllers (ILX Lightwave, LDC-3724). Note that, when tuning the laser working currents, an acquisition time interval (~3 times of the lock-in integration time) were set to avoid distortion of the NIR-LHR spectral forms, and one typical scan time is about 4 min.

The instrument line-shape (ILS) is a key parameter for LHR data retrieval, which entirely determined by electronic filter bandwidth in the point-by-point scanning mode [23]. In order to choose an appropriate pass-band, frequency spectrum analysis of the heterodyne, laser and background (without laser and solar) signals were performed to isolate the NIR-LHR signal from unwanted noises by using a RF signal analyzer (Agilent Technologies, N9000A). Considering the balance between signal-to-noise ratio and spectral resolution, band-pass filters with 290–400 MHz and 395–520 MHz were chosen for the detections of CO_2 and CH_4 in the present work, which resulted in ~220 MHz (0.0073 cm^{-1}) and ~250 MHz (0.0083 cm^{-1}) double-sideband spectral resolution for the two detection channels, respectively. The respective finally used ILS for the NIR-LHR data retrievals are shown in Fig. 3(a) and (b), where the single-sideband line-shapes were determined by employing a white noise source and the RF signal analyzer. In particular, a wavelet denoising method is employed in the data processing to avoid introducing additional noises to the data retrieval.

3. Data processing

Before data retrievals, the raw NIR-LHR signals need to be preprocessed, including intensity normalization and wavenumber calibration. For intensity normalization, the offset of the NIR-LHR signal is first subtracted, which equals to the mean value of the NIR-LHR signal before the laser emitting light. Then, the NIR-LHR signal is divided by the DC signal ((a) / $(c)_{blue}$ and (b) / $(c)_{red}$ in Fig. 2) to normalize the power variations caused by the local oscillator. It should be noted that, if large solar power fluctuations appeared in the scan, the NIR-LHR data would no longer be considered for further analysis.

Since the laser currents are scanned in the point-by-point mode, it is convenient to calibrate the wavenumber by using a wavelength meter (Bristol, 621B). However, the laser wavenumber may slightly change during the measurements (Fig. 4(a)). In order to accurately identify the wavenumber shift, as shown in Fig. 4(b), the correlation coefficient of the reference signal (calculated using the forward model) and the real signal is calculated by moving the real signal, where the moving step can be defined as an arbitrarily small length by using interpolation method. Finally, the wavelength shift can be precisely determined by the location of the maximum correlation coefficient (inset of Fig. 4(b)). Specially, the

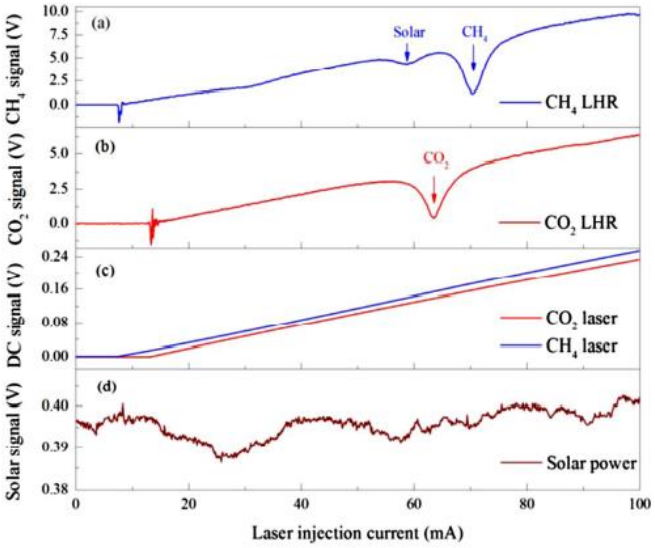

Fig. 2. Example of raw signals acquired in one scan on April 17, 2019. (a), (b) CH_4 and CO_2 NIR-LHR signals after phase compensation; (c) DC components of PD1 and PD3 for monitoring the power of the two local oscillators (lasers for CO_2 in red, for CH_4 in blue); (d) Amplitudes of the signals from PD2 for tracking the solar power.

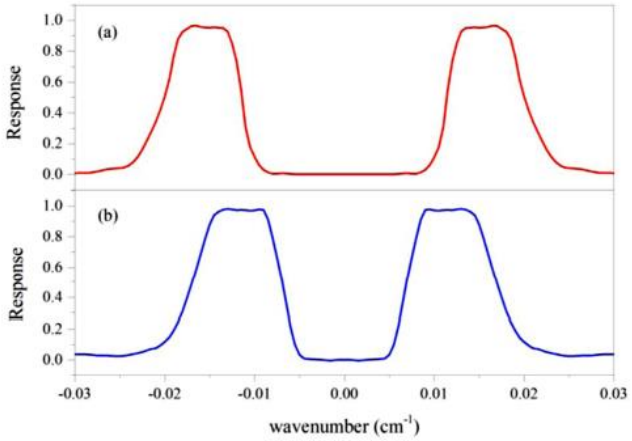

Fig. 3. Finally used ILS for the data retrievals, (a) The ILS used for CH4 retrieval (395–520 MHz); (b) The ILS used for CO_2 retrieval (290–400 MHz).

proposed correlation method still works at low signal to noise ratios. After intensity normalization and wavenumber calibration, the processed data is now ready for data retrievals.

4. Data retrieval

Data retrievals were performed using the optimal estimation method (OEM), described by Rodgers [29] and it was applied to the LHR data retrievals by Weidmann [30]. A brief recall and some necessary modifications needed in our case are presented as below. The atmospheric transmission spectrum of the solar radiance can be calculated by calling a radiative transfer forward model ($\boldsymbol{F}$), where $\boldsymbol{F}$ is built based on the reference forward model (RFM, version 4.34), which is a fast line-by-line radiative transfer model developed by Dudhia [31]. The relationships between the processed NIR-LHR data and the forward model $\boldsymbol{F}$ are described as:

$$y_m\big|_{CO_2} = F(x, a, b, c) + \varepsilon. \quad (1)$$

$$y_m\big|_{CH_4} = F(x, a, b, c, S_1, S_2, S_3, S_4) + \varepsilon. \quad (2)$$

where $\boldsymbol{y_m}$ is the measurement vector, the state vector $\boldsymbol{x}$ is the vertical profile of atmospheric CO_2 or CH_4, and $\boldsymbol{\varepsilon}$ is the error vector. A second order polynomial baseline (with coefficients a, b and c) is used to represent the non-selective absorption and uncorrected power contributions. Specially, in the CH_4 retrieval, a Gaussian like line-shape function (with coefficients S_1, S_2, S_3 and S_4) is employed to describe the solar emission spectrum. The OEM based data retrieval is a Levenberg–Marquardt (LM) iterative process, using Bayesian statistics with Gaussian probability density functions, to minimize the cost function (χ^2):

$$\chi^2 = (y - F)^T S_\varepsilon^{-1}(y - F) + (x_i - x_a)^T S_a^{-1}(x_i - x_a). \quad (3)$$

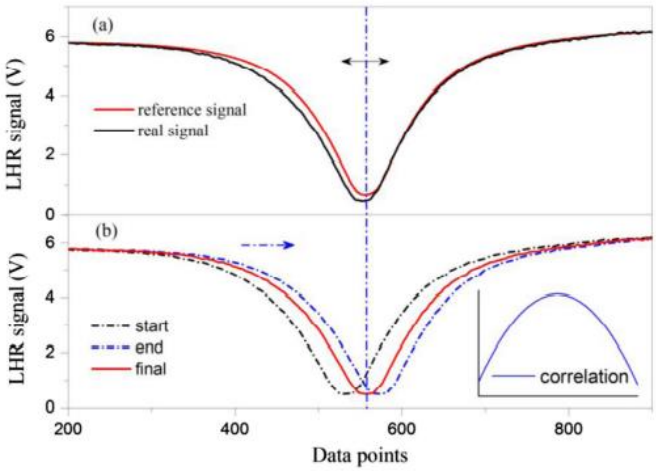

Fig. 4. Principle of the wavenumber shift identification. (a) Wavenumber shift between the reference signal and real signal; (b) The process of calculating the wavenumber shift, the inset shows the result of correlation coefficients.

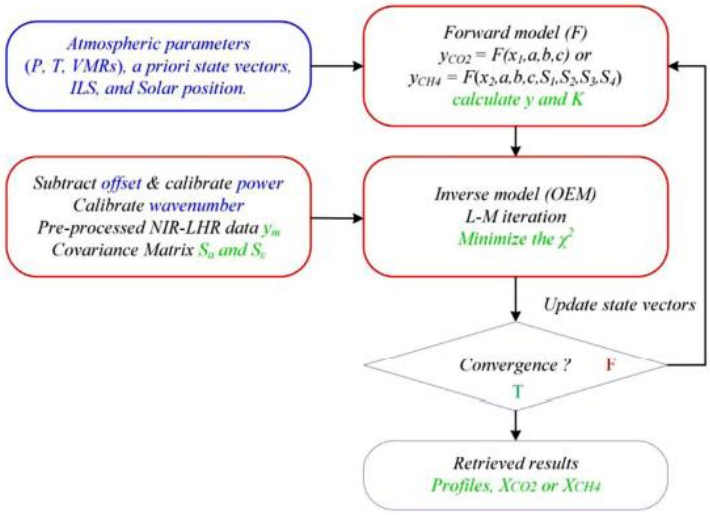

Fig. 5. Flow-chart of the data retrieval. VMRs: volume mixing ratios; ILS: instrument line-shape; L-M: Levenberg–Marquardt.

where $\boldsymbol{x_a}$ is *a priori* CO_2 (or CH_4) profile with an *a priori* covariance matrix $\boldsymbol{S_a}$, and $\boldsymbol{S_\varepsilon}$ is the error covariance matrix. The iterative state vector $\mathbf{x_{i+1}}$ is calculated using the following equation:

$$x_{i+1}=x_i+\left[(1+\gamma)S_a^{-1}+K_i^T S_\varepsilon^{-1} K_i\right]^{-1}\times\left[K_i^T S_\varepsilon^{-1}\left(y_m-F_i\right)-S_a^{-1}\left(x_i-x_a\right)\right]. \quad (4)$$

where $\boldsymbol{K}$ is the Jacobian matrix (or weighting functions), and γ is the Levenberg–Marquardt parameter.

The flow-chart of the NIR-LHR data retrieval is shown in Fig. 5, which mainly consists of a data pre-processing program, a forward calculation program and an iterative inverse program. In the data pre-processing program, the power and wavenumber are calibrated, and the covariance matrices ($\boldsymbol{S_a}$ and $\boldsymbol{S_\varepsilon}$) are set to be diagonal based on the error definitions (shown in Table 1) and the standard deviation of

program, the forward spectrum ($\boldsymbol{y_{CO2}}$ or $\boldsymbol{y_{CH4}}$) and Jacobian matrix ($\boldsymbol{K}$) are calculated with corresponding input parameters, including atmospheric parameters (profiles of the pressure, temperature, and atmospheric species), ILS, and solar position (zenith angle). In the inverse program, the forward calculation program is iteratively called to minimize the cost function (Eq. (3)) following LM algorithm (Eq. (4)). The state vectors are defined in Table 1, which are the information need to be retrieved in the present study.

In order to describe the data retrieval process more clearly, the data acquired on April 17, 2019 are chosen as a representative. The pressure and temperature profiles used for the data retrieval are shown in Fig. 6, which were obtained from China Meteorological Data Service Center (CMCC), National Centers for Environmental Prediction (NCEP) and the European centre for Medium-Range Weather Forecasts (ECMWF). Data from 0.2 km to 55 km (blue dots) were interpolated from the data of

Table 1
Definition of the state vector used in the data retrieval.

State vector	*a priori*	Error	Description
$x1$ (CH_4)	1	10%	Scale factor of the *a prior* profile for CH_4 retrieval.
$x2$ (CO_2)	1	10%	Scale factor of the *a prior* profile for CO_2 retrieval.
a	a0	100%	Polynomial coefficients of the baseline, where a0, b0, and c0 are calculated by using
b	b0	100%	a second-order polynomial fit of the ratio of the pre-processed NIR-LHR signal
c	c0	100%	to the forward-calculated spectrum (after removing the absorption part).
S_1	Sa0	10%	Parameters for describing the Gaussian like solar spectrum in CH_4 retrieval,
S_2	Sb0	10%	where S_1 defines the peak height, S_2 defines the peak position, S_3 defines
S_3	Sc0	10%	the peak width, and S_4 defines the offset.
S_4	Sd0	10%	

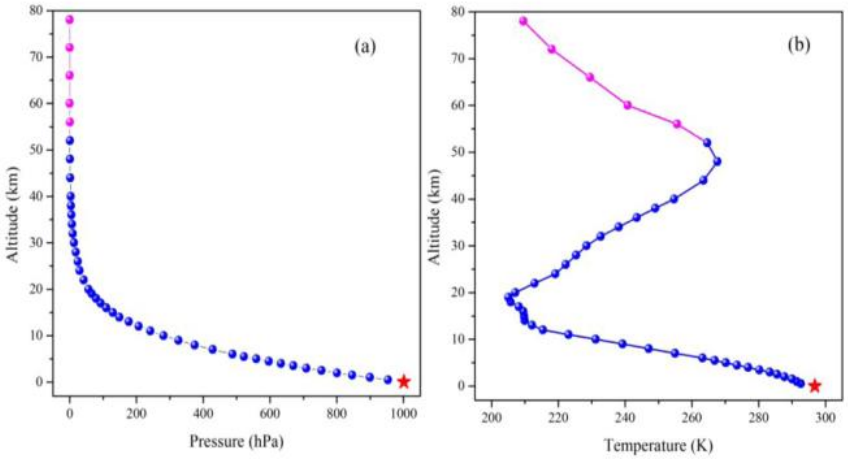

Fig. 6. Pressure (a) and temperature (b) profiles used for the data retrieval on April 17, 2019, which are interpolated based on the data from CMCC (red star), NDACC (blue dots) and ECMWF (pink dots).

Hefei observation station (NECP), while the data above 55 km (pink dots) were interpolated from the typical zonal mean profiles in April (obtained from ECMWF), and the surface data (red star) were obtained from CMCC. Note that the atmosphere is separated to 45 layers from surface (30 m altitude) to 78 km with an altitude grid of 0.5, 1, 2, 4 and 6 km, separately. For the *a prior* profiles of CO_2 and CH_4, typical mid-latitude daytime profiles were used in the retrieval, while the water vapor profile was interpolated from the upper air data from CMCC. Besides the atmospheric parameters, a solar position calculation program is also compiled to determine the real-time solar zenith angle, and the relative deviation was found to be less than 0.1% by comparison with the NOAA (National Oceanic and Atmospheric Administration) solar calculator.

The LM iterative process is considered to be converged when $\Delta\chi^2/\chi^2 < 1E{-}3$ within an upper limit of 20 iterations. In a well-conditioned retrieval, the ultimate cost function (χ^2) should be close to the size of the measurement vector (m). The retrieval results of CO_2 and CH_4 are shown in Fig. 7(a)–(b) and Fig. 8(a) and (b), respectively, where the pre-processed NIR-LHR data, the fitted spectrum, baseline and residuals are presented with an interval of 0.001 cm^{-1}. The iterative processes are shown in the inset of Figs. 7(a) and 8(a), where χ^2/m equals to ~1 is obtained after 7 and 6 iterations, respectively. After the iterations, the retrieved CH_4 and CO_2 profiles are calculated by multiplying the retrieved scale factor with relative *a priori* profile. Based on the retrieved CH_4 and CO_2 profiles, the total column abundance of CH_4 and CO_2 is calculated to be ~412.7 ppm (or ~8.2E21 molecules/cm^2) and ~1.886 ppm (or ~3.74E19 molecules/cm^2), respectively. By using the water vapor profile obtained from CMCC, the mixing ratio in dry air (X_{CH4} and X_{CO2}) are calculated to be ~415 ppm and ~1.897 ppm, respectively. For calculating the X_{CH4} and X_{CO2} more accurately, real-time retrieval of NIR-LHR spectrum of the water vapor will be performed in the future.

5. Results analysis and validation

The consecutive measurement results on April 17, 2019 shown in Fig. 9(a) and (b) indicate a standard deviation of ~6 ppb (part per billion) for X_{CH4} and ~1 ppm (part per million) for X_{CO2}, respectively. It should be noted that, only the measurement results from 11:00 am to 13:00 pm were analyzed in this study, because the timestamp of NCEP and CMCC data was 12:00, and the atmospheric parameters were considered stable during this time period. The factors affecting the detection accuracy of the NIR-LHR can be sorted as errors resulted from system noises and retrieval errors. For further improvement of the measurement accuracy, efforts will be focused on improving the signal to noise ratio of the NIR-LHR signals, building appropriate covariance matrices, so as to employing more reasonable *a priori* profiles for the data retrievals.

In order to evaluate the results of the NIR-LHR, comparisons with GOSAT data were performed in the sunny days during the period from October 2018 to May 2019. Fig. 10(a) and (b) show the time series of the daily averaged NIR-LHR retrieval results (with standard deviation as

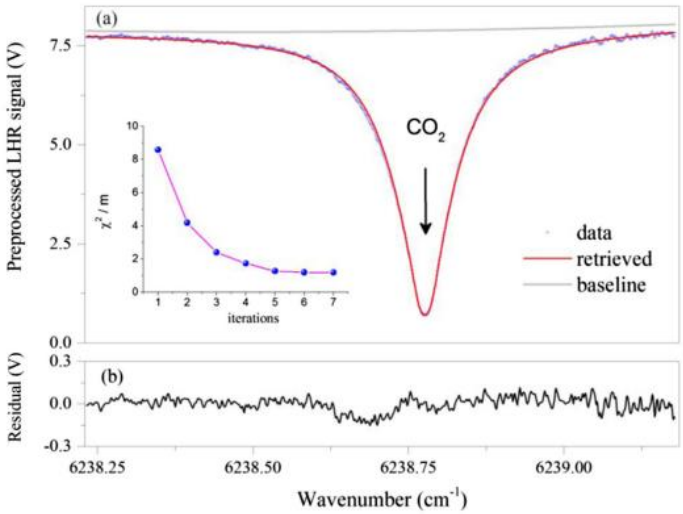

Fig. 7. Retrieval results of CO2 on April 17, 2019. (a) Preprocessed (blue dots), baseline (gray line) and fitted (red line) NIR-LHR spectra and the iteration process (inset); (b) the residuals.

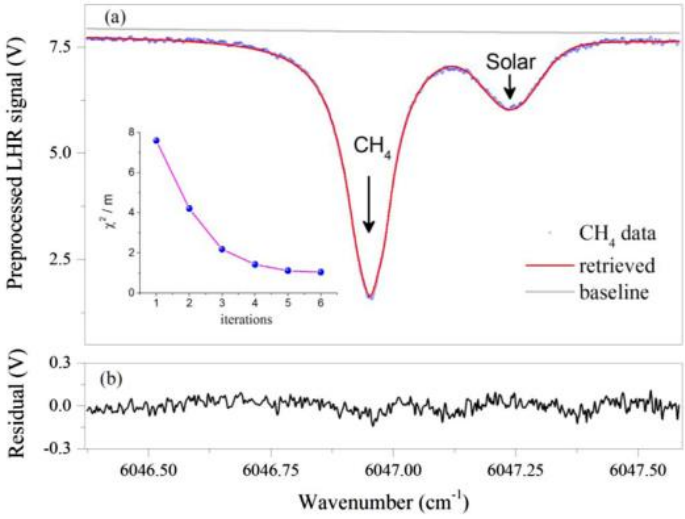

Fig. 8. Retrieval results of CH4 on April 17, 2019. (a) Preprocessed (blue dots) and fitted (red line) NIR-LHR spectra, baseline (gray line) and the convergence of the iteration process (inset); (b) the residuals.

the error bar) and GOSAT results of X_{CH4} and X_{CO2}, where the GOSAT results were selected within a 3° radius of the observation site (Hefei, China, 31.9°N 117.16°E). The standard deviations are found to be in the range of 3–17 ppb for X_{CH4} and for 0.7–2.2 ppm for X_{CO2} during the measurements, which correspond to an uncertainty region of 0.15–0.7% for X_{CH4} and 0.17–0.5% for X_{CO2}, respectively. As seen from the Fig. 10(a), for the measurements of X_{CH4}, there is a bias of ~10 ppb between the NIR-LHR results and GOSAT results, which means that the X_{CH4} is underestimated from the GOSAT measurements. The probable reason may be the existence of methane sources around the observation site. While for the measurements of X_{CO2} (shown in Fig. 10(b)), the NIR-LHR results are in good agreement with the GOSAT results. In the future, longer term analysis will be carried out for the study of seasonal and annual variations of atmospheric CO_2 and CH_4. In addition, A FPGA-based integrated circuits will be employed in place of the laser controllers and lock-in amplifiers in the system [32].

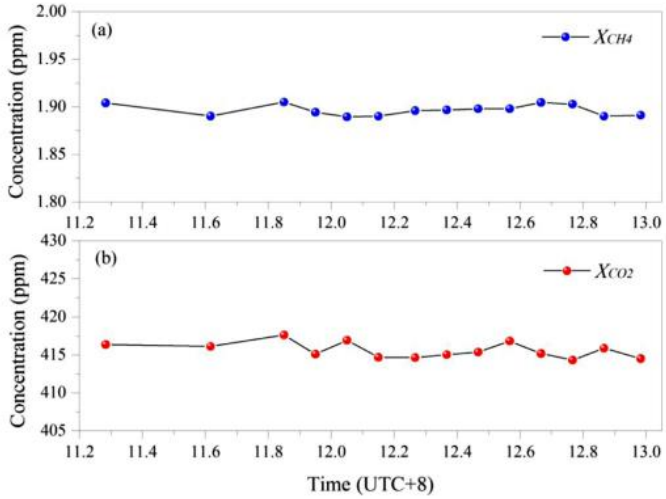

Fig. 9. Retrieval results of the X_{CH4} and X_{CO2} from 11:00 to 13:00 on April 17, 2019. (a) X_{CH4} results versus time; (b) X_{CO2} results versus time.

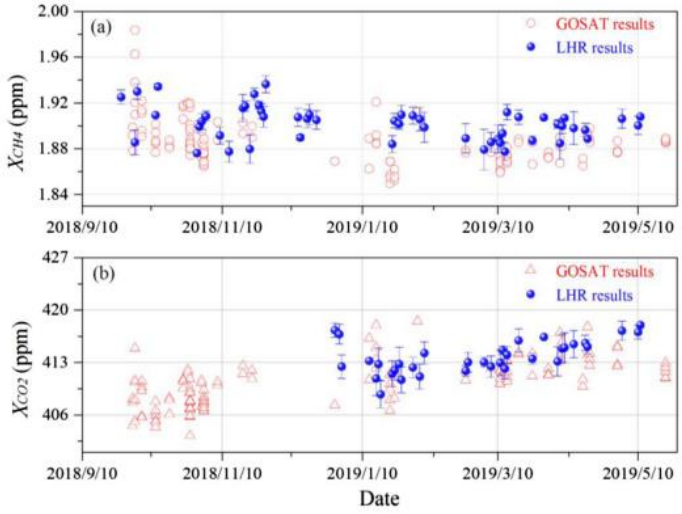

Fig. 10. Time series of the NIR-LHR data retrieval results and GOSAT results. (a) NIR-LHR results (blue sphere) and GOSAT results (circle) of X_{CH4}; (b) NIR-LHR results (blue sphere) and GOSAT results (up triangle) of X_{CO2}.

6. Conclusions

An all fibered NIR-LHR has been developed for operation in ground-based solar occultation mode. A 1 × 2 fiber optical switch is employed to modulate solar radiation, which makes the system more stable and compact. High resolution NIR-LHR spectra of atmospheric CO_2 and CH_4 were obtained by employing two DFB lasers (1.6 μm and 1.65 μm) as the local oscillators. After power calibration, the wavenumbers were precisely calibrated using a correlation correction method. Subsequently, an OEM and RFM based retrieval algorithm was developed for retrieval of the vertical profiles, column-averaged abundances and mixing ratios in dry air of atmospheric CO_2 and CH_4. Finally, the long term NIR-LHR results were validated by comparing the GOSAT results during the same time period, which indicates a uncertainty region of 0.15–0.7% for X_{CH4} and 0.17–0.5% for X_{CO2}, respectively. The NIR-LHR demonstrated in this manuscript has great potential to be a portable and high spectral resolution instrument for atmospheric multi-component gases sensing.

Author contributions

Jingjing Wang: established the detection system. Chunyan Sun: acquired the experimental data. Guishi Wang: methodology, software, data retrieval, Writing Original draft preparation. Mingmin Zou: Validation. Tu Tan: methodology. Kun Liu: Supervision, Writing Reviewing

and Editing. Weidong Chen: Writing Reviewing and Editing. Xiaoming Gao: Supervision, Funding acquisition.

Declaration of Competing Interest

The authors declare that they have no known competing financial interests or personal relationships that could have appeared to influence the work reported in this paper.

Acknowledgments

This work was supported by Key Project of the National Natural Science Foundation of China (Grant no. 41730103), National Key Research and Development Program of China (2017YFC0209700), and National Natural Science Foundation of China (Grant nos. 41805018 and 41405022).

References

[1] Edenhofer O, Pichs-Madruga R, Sokona Y, Farahani E, Kadner S, Seyboth K, Adler A, Baum I, Brunner S, Eickemeier P, Kriemann B, Savolainen J, Schlömer S, von Stechow C, Zwickel T, Minx JCIPCC. Climate change 2014: mitigation of climate change. Contribution of working group III to the fifth assessment report of the intergovernmental panel on climate change, Cambridge, United Kingdom and New York, NY, USA: Cambridge University Press; 2014. 2015. doi:10.1017/CBO9781107415416.

[2] Kuze A, Suto H, Nakajima M, Hamazaki T. Thermal and near infrared sensor for carbon observation Fourier-Transform spectrometer on the Greenhouse Gases Observing Satellite for greenhouse gases monitoring. Appl Opt 2009;48(35):6716–33. doi:10.1364/ao.48.006716.

[3] Frankenberg C, Pollock R, Lee RAM, Rosenberg R, Blavier J-F, Crisp D, et al. The orbiting carbon observatory (OCO-2): spectrometer performance evaluation using pre-launch direct sun measurements. Atmos Meas Tech 2015;8(1):301–13. doi:10.5194/amt-8-301-2015.

[4] Yang D, Liu Y, Cai Z, Chen X, Yao L, Lu D. First global carbon dioxide maps produced from tansat measurements. Adv Atmos Sci 2018;35(6):621–3. doi:10.1007/s00376-018-7312-6.

[5] Hase F, Frey M, Blumenstock T, Groß J, Kiel M, Kohlhepp R, Mengistu Tsidu G, Schäfer K, Sha MK, Orphal J. Application of portable FTIR spectrometers for detecting greenhouse gas emissions of the major city Berlin. Atmos Meas Tech 2015;8(7):3059–68. doi:10.5194/amt-8-3059-2015.

[6] Wunch D, Toon GC, Blavier J-FL, Washenfelder RA, Notholt J, Connor BJ, et al. The total carbon column observing network. Philos Trans R Soc A 2011;369(1943):2087–112. doi:10.1098/rsta.2010.0240.

[7] Frey M, Hase F, Blumenstock T, Groß J, Kiel M, Mengistu Tsidu G, Schäfer K, Sha MK, Orphal J. Calibration and instrumental line shape characterization of a set of portable FTIR spectrometers for detecting greenhouse gas emissions. Atmos Meas Tech 2015;8(7):3047–57. doi:10.5194/amt-8-3047-2015.

[8] Gisi M, Hase F, Dohe S, Blumenstock T, Simon A, Keens A. XCO_2-measurements with a tabletop FTS using solar absorption spectroscopy. Atmos Meas Tech 2012;5(11):2969–80. doi:10.5194/amt-5-2969-2012.

[9] Tian Y, Sun Y, Liu C, Xie P, Chan K, Xu J, Wang W, Liu C. Characterization of urban CO_2 column abundance with a portable low resolution spectrometer (PLRS): comparisons with GOSAT and GEOS-Chem model data. Sci Total Environ 2018;612:1593–609. doi:10.1016/j.scitotenv.2016.12.005.

[10] Menzies RT, Seals RK. Ozone monitoring with an infrared heterodyne radiometer. Science 1977;197(4310):1275–7. doi:10.1126/science.197.4310.1275.

[11] Frerking MA, Muehlner DJ. Infrared heterodyne spectroscopy of atmospheric ozone. Appl Opt 1977;16(3):526–8. doi:10.1364/ao.16.000526.

[12] Abbas MM, Kostiuk T, Mumma MJ, Buhl D, Kunde VG, Larry W. B. Stratospheric ozone measurement with an infrared Heterodyne spectrometer. Geophys Res Lett 1978;5(4):317–20. doi:10.1029/gl005i004p00317.

[13] Deming D, Espenak F, Jennings D, Kostiuk T, Mumma M, Zipoy D. Observations of the 10-μm natural laser emission from the mesospheres of Mars and Venus. Icarus 1983;55(3):347–55. doi:10.1016/0019-1035(83)90107-0.

[14] Sonnabend G, Wirtz D, Schmülling F, Schieder R. Tuneable Heterodyne Infrared Spectrometer for atmospheric and astronomical studies. Appl Opt 2002;41(15):2978–84. doi:10.1364/ao.41.002978.

[15] Weidmann D, Courtois D. Infrared 7.6-μm lead-salt diode laser heterodyne radiometry of water vapor in a CH4-air premixed flat flame. Appl Opt 2003;42(6):1115–21. doi:10.1364/ao.42.001115.

[16] Weidmann D, Reburn WJ, Smith KM. Ground-based prototype quantum cascade laser heterodyne radiometer for atmospheric studies. Rev Sci Instrum 2007;78(7):073107. doi:10.1063/1.2753141.

[17] Weidmann D, Wysocki G. High-resolution broadband (>100 cm˜-1) infrared heterodyne spectro-radiometry using an external cavity quantum cascade laser. Opt Express 2008;17(1):248–59. doi:10.1364/oe.17.000248.

[18] Weidmann D, Perrett BJ, Macleod NA, Jenkins RM. Hollow waveguide photomixing for quantum cascade laser heterodyne spectro-radiometry. Opt Express 2011;19(10):9074–85. doi:10.1364/oe.19.009074.

[19] Tsai TR, Rose RA, Weidmann D, Wysocki G. Atmospheric vertical profiles of O_3, N_2O, CH_4, CCl_2F_2, and H_2O retrieved from external-cavity quantum-cascade laser heterodyne radiometer measurements. Appl Opt 2012;51(36):8779–92. doi:10.1364/ao.51.008779.

[20] Hoffmann A, Macleod NA, Huebner M, Weidmann D. Thermal infrared laser heterodyne spectroradiometry for solar occultation atmospheric CO_2 measurements. Atmos Meas Tech 2016;9(12):5975–96. doi:10.5194/amt-9-5975-2016.

[21] Weidmann D, Hoffmann A, Macleod N, Middleton K, Kurtz J, Barraclough S, Griffin D. The methane isotopologues by solar occultation (MISO) nanosatellite mission: spectral channel optimization and early performance analysis. Remote Sens 2017;9(10):1073–92. doi:10.3390/rs9101073.

[22] Martín-Mateos P, Genner A, Moser H, Lendl B. Implementation and characterization of a thermal infrared laser heterodyne radiometer based on a wavelength modulated local oscillator laser. Opt Express 2019;27(11):15575–84. doi:10.1364/oe.27.015575.

[23] Wang J, Wang G, Tan T, Zhu G, Sun C, Cao Z, Chen W, Gao X. Mid-infrared laser heterodyne radiometer (LHR) based on a 353 μm room-temperature interband cascade laser. Opt Express 2019;27(7):9610–19. doi:10.1364/oe.27.009610.

[24] Wilson EL, McLinden ML, Miller JH, Allan GR, Ott LE, Melroy HR, Clarke GB. Miniaturized laser heterodyne radiometer for measurements of CO_2 in the atmospheric column. Appl Phys B 2013;114(3):385–93. doi:10.1007/s00340-013-5531-1.

[25] Wilson EL, DiGregorio AJ, Riot VJ, Ammons MS, Bruner WW, Carter D, Mao JP, Ramanathan A, Strahan S E, Oman LD, Hoffman C, Garner RM. A 4U laser heterodyne radiometer for methane (CH4) and carbon dioxide (CO_2) measurements from an occultation-viewing CubeSat. Meas Sci Technol 2017;28(3):035902. doi:10.1088/1361-6501/aa5440.

[26] Rodin A, Klimchuk A, Nadezhdinskiy A, Churbanov D, Spiridonov M. High resolution heterodyne spectroscopy of the atmospheric methane NIR absorption. Opt Express 2014;22(11):13825–34. doi:10.1364/oe.22.013825.

[27] Kurtz J, O'Byrne S. Multiple receivers in a high-resolution near-infrared heterodyne spectrometer. Opt Express 2016;24(21):23838–48. doi:10.1364/oe.24.023838.

[28] Martín-Mateos P, Bonilla-Manrique OE, Gutiérrez-Escobero C. Wavelength modulation laser heterodyne radiometry. Opt Lett 2018;43(12):3009–12. doi:10.1364/ol.43.003009.

[29] Rodgers CD. Inversion methods in atmospheric remote sounding. Elsevier; 1977. doi:10.1016/b978-0-122-08450-8.x5001-2.

[30] Weidmann D, Reburn WJ, Smith KM. Retrieval of atmospheric ozone profiles from an infrared quantum cascade laser heterodyne radiometer: results and analysis. Appl Opt 2007;46(29):7162–71. doi:10.1364/ao.46.007162.

[31] Dudhia A. The Reference Forward Model (RFM). J Quant Spectrosc Radiat Transf 2017;186:243–53. doi:10.1016/j.jqsrt.2016.06.018.

[32] Guo X, Zheng F, Li C, Yang X, Li N, Liu S, Wei J, Qiu X, He Q. A portable sensor for in-situ measurement of ammonia based on near-infrared laser absorption spectroscopy. Opt Laser Eng 2019;115:243–8. doi:10.1016/j.optlaseng.2018.12.005.

Publications

[1] **J.Wang**, G.Wang, T.Tan, G.Zhu, C.Sun, Z.Cao, W.Chen and X.Gao. Mid-infrared laser heterodyne radiometer (LHR) based on a 3.53 um room-temperature interband cascade laser. Optics Express, 2019.27(7): 9610-9619.

[2] **J.Wang**, C.Sun, G.Wang, M. Zou, T. Tan, K. Liu, W. Chen, X. Gao. A fibered near-infrared laser heterodyne radiometer for simultaneous remote sensing of atmospheric CO_2 and CH_4. Optics and Lasers in Engineering, 2020, 129: 106083.

[3] J.Wang, T. Tan, G. Wang, G. Zhu, Z. Xue, J. Li, X. Liu, X. Gao. Research on All-Fiber Dual-Channel Atmospheric Greenhouse Gas Laser Heterodyne Dtector Technology. Spectroscopy and Spectral Analysis, 2021, 41(1).

Conferences

[1] **Jingjing Wang**, Fengjiao Shen, Tu Tan, Zhensong Cao, Xiaoming Gao, Pascal Jeseck, Yao-Veng Te, Eric Fertein, Weidong Chen. "Infrared laser heterodyne radiometers for ground-based measurements of greenhouse gases in the atmospheric column (poster)". JSM-Créteil, France, 21-23 May 2019.

[2] **Jingjing Wang**, Fengjiao Shen, Tu Tan, Zhensong Cao, Xiaoming Gao, Pascal Jeseck, Yao Te and Weidong Chen. "Laser heterodyne radiometers (LHR) for in situ ground-based remote sensing of greenhouse gases in the atmospheric column(poster)". European Geosciences Union General Assembly 2020, Online, 4-6 May 2020.

[3] **Jingjing Wang**, Tu Tan, Xiaoming Gao. "Application of infrared laser heterodyne technology in atmospheric greenhouse gas detection(report)". The 4th Laser Spectroscopy Conference, Jinghua China, 29 Nov.2020.